Supercapacitive Properties of Nanocarbons Modified with Manganese Oxide Nanoparticles and Metallotetrapyrazinoporphyrazines

By

Joel Ntotole Lekitima

Submitted in fulfilment of the requirements of the degree

Magister Scientiae

In the Faculty of Natural and Agricultural Sciences

University of Pretoria

Pretoria

Supervisor: Prof. K.I. Ozoemena

July 2013

DECLARATION

I, Lekitima Joel Ntotole declare that the dissertation which I hereby submit for the degree Master of Science at the University of Pretoria, is my own work and has not previously been submitted by me for a degree at this or any other tertiary institution. Secondary materials used have been carefully acknowledged and referenced in compliance with plagiarism policies of the University.

……………………………………………….

Date ……………………………………..

DEDICATION

This dissertation is dedicated to my children,

Motlhodi and Thoriso

Who always said “daddy is working hard”

ACKNOWLEDGEMENTS

Above all, To God almighty, without His grace, strength, protection and wisdom I could not have come this far. “I am what I am by the grace of the Lord” (I Cor. 15:10).

My sincerest gratitude and appreciation goes to the following:

Prof. K.I. Ozoemena, my supervisor and mentor. Thank you for an opportunity to study under your tutelage. Many thanks from the bottom of my heart for all your time, guidance, persistent help and accommodative heart for all these years. The seed you have sown will surely yield results. It was not in vain.

My sincere gratitude goes to the UP electrochemistry research team, amongst others Alfred, Katlego, Bolade and Bose for your valuable inputs.

UP chemistry department, for the valuable time they allowed me to pursue my studies.

I would like to thank my dearest wife, Coretta for your understanding and love throughout these years. Thank you for been there when I needed comfort and courage.

My gratitude goes to microscopy and microanalysis unit, University of Pretoria for assistance with SEM and TEM analysis. Lastly I would like to thank the University of Pretoria and the NRF/DST Nanotechnology Flagship programme for financial support

ABSTRACT

This dissertation describes the electrochemical properties of nanocarbons (multi-walled carbon nanotubes (MWCNTs) and graphene oxide (GO)) incorporated with manganese dioxide (MnO_2) and metallotetrapyrazinoporphyrazines (MTPyzPz, where M = Co, Fe) as electrochemical capacitors. Supercapacitive properties of the composites formed were investigated using cyclic voltammetry (CV), galvanostatic charge-discharge and electrochemical impedance spectroscopy (EIS) in both three- and two-electrode systems using 1.0 M H_2SO_4 and 1.0 M Na_2SO_4 as electrolytes. This study showed that acid functionalized MWCNTs (MWCNTaf) enormously increased the specific capacitance of MnO_2 from 45 $F.g^{-1}$ to 1209 $F.g^{-1}$. Supercapacitive properties of nanocarbons modified with cobalt(II)tetrapyrazino-porphyrazine(CoTPyzPz) and Iron(II)tetrapyrazino-porphyrazine (FeTPyzPz) were explored. MWCNTaf modified with CoTPyzPz and FeTPyzPz gave higher capacitances than phenylamine-functionalised MWCNTs ($MWCNTPhNH_2$) modified MTPyzPz nanocomposites in acidic electrolyte. The specific capacitance obtained for MWCNTaf-CoTPyzPz at 1 $A.g^{-1}$ was 1642 $F.g^{-1}$ in 1.0 M H_2SO_4 while 410 $F.g^{-1}$ was obtained for MWCNTaf-FeTPyzPz at 3 $A.g^{-1}$. This large specific capacitance was attributed to the protonation and deprotonation of the porphyrazine macromolecule. FeTPyzPz nanocomposites gave higher specific capacitance in acid electrolyte than in a neutral electrolyte.

An asymmetric capacitor cell (coin cell) was made to further investigate the suitability of MTPyzPz compounds as electrode capacitor material. A novel asymmetric electrochemical capacitor (AEC) using functionalised MWCNTs and MTPyzPz nanocomposite as the positive electrode and functionalised MWCNTs and carbon black (CB) as the negative electrode in a neutral aqueous Na_2SO_4 electrolyte was investigated. CoTPyzPz//CB-MWCNTaf was the best AEC with specific capacitance of 70 F.g^{-1}. This AEC cell exhibited energy density and power density of 8.5 kW.kg^{-1} and 4.3 KW.kg^{-1} respectively. A novel AEC with high energy and power densities was successfully developed using GO/CoTPyzPz as the positive electrode and GO/CB as the negative electrode in 1.0 M Na_2SO_4. The excellent energy and power densities (44 Wh.kg^{-1} and 31 kW.kg^{-1} obtained at high current density, 2.4 A.g^{-1}) coupled with excellent long cycle life, short response time, and low equivalent series resistance (ESR) clearly indicate that this asymmetric electrochemical capacitor has a considerable potential in developing low-cost and green energy storage devices that operate at high energy and power densities. Interestingly, the energy density of the GO/CoTPyzPz//GOCB based AEC falls within the range usually seen for nickel metal hydride (NiMH) batteries (30 – 100 Wh.kg^{-1}), but, more importantly, has a much better power performance than NiMH batteries (0.25 – 1 kW.kg^{-1}) widely used in hybrid vehicles such as Toyota Prius and Honda Insight. In summary, the findings in this work clearly indicate that CoTPyzPz and FeTPyzPz are potentially useful in developing low-cost and 'green' electrochemical energy storage devices with high capacitance, energy and power densities. The work has indeed opened a door of opportunity that will permit the study of other MTPyzPz complexes for the development of electrochemical capacitors.

TABLE OF CONTENTS

LIST OF ABBREVIATIONS

AC	Activated carbon
Ag/AgCl	Silver/silver chloride reference electrode
BPPGE	Basal plane pyrolytic graphite
CB	Carbon black
c-d	Charge-discharge
CNFs	Carbon nanofibers
CNTs	Carbon nanotubes
CoTPyzPz	Tetrapyrazinopophyrazine Cobalt (II)
CV	Cyclic voltammetry
DTG	Differential thermogravimetry
EC	Electrochemical capacitor
EDLC	Electrochemical double layer capacitor
EDX	Energy dispersive X-ray spectroscopy
EIS	Electrochemical impedance spectroscopy
ESD	Energy storage devices
ESR	Equivalent series resistance
FESEM	Field emission scanning electron microscopy
FeTPyzPz	Tetrapyrazinopophyrazine Iron (II)

FTIR	Fourier transform infrared spectroscopy
GO	Graphene oxide
IHP	Inner Helmholtz plane
MWCNTaf	Acid functionalized multiwalled carbon nanotube
MWCNTPhNH$_2$	Phenylamine functionalized multiwalled carbon nanotube
MWCNTs	Multiwalled carbon nanotubes
NEC	Nippon Electric company
OHP	Outer Helmholtz plane
PVDF	Polyvinylidene fluoride
P-XRD	Powder X-ray diffraction
SEM	Scanning electron microscope
SOHIO	Standard oil of Ohio
TG	Thermogravimetry
TGA	Thermogravimetry analysis
UV-Vis	Ultraviolet-visible
PEDOT	poly-3,4-ethylenedioxythiophene
PMMA	polymethyl methacrylate
PPV	polyphenylenevinylene

LIST OF FIGURES

LIST OF TABLES

CHAPTER 1

INTRODUCTION

1.1 General Overview

Global warming, one of the biggest threats to human life today is caused by man’s dependency on fossil fuels for energy production. Energy demand due to modernisation has been increasing in an alarming rate. The demand of energy is associated with environmental concerns such as pollution. As energy production is scaled up to meet energy demand, nations worldwide are beginning to explore renewable energy sources such as solar and wind energy. The focus of research in energy today is on improving efficiency in energy production and storage processes. The current methods for energy production and storage are less efficient and increase the CO_2 concentration in the atmosphere. Currently fuel cells, batteries and electrochemical capacitors are explored as alternatives to traditional methods of energy production, conversion and storage.

Electrochemical capacitor (EC), sometimes referred to as supercapacitor, is an electric energy storage device that fills the gap between conventional capacitors such as electrolytic capacitors and batteries in terms of energy density and power density (1). This device can be discharged at a higher rate. The fast energy delivery and durability (high cycle number) of the electrochemical capacitors (ECs) makes them attractive energy storage devices. ECs can be used in various applications, among others, hybrid electric vehicles (2, 3), aircraft emergency door (4), electronic devices (5) and back-up power storage (6). One of the drawbacks of EC in the utilizing carbon as its electrode material is low energy density. The makeup of an electrode determines how much energy can be stored by the EC. More research on carbon as an electrode material in ECs has been done (7-12). Carbon nanotubes have been studied extensively as electrode materials (1, 13-18) and carbon nanotubes capacitance can be enhanced by functionalization (19, 20). Acid functionalization of carbon nanotubes increases capacitance of the carbon nanotubes by 3-20 folds. This enhancement of capacitance is due to psuedocapacitance from the functional groups introduced on carbon atoms. Carbon materials have lower energy density. The lower conductivity of metal oxides (26) is a greater challenge to it been utilized for ECs. Due to lower energy and power density of carbon materials and metal oxides, scientists have been exploring hybrid capacitors from composite material electrodes (27) in order to increase energy and power density of the multiwalled carbon nanotubes (MWCNTs). Metal oxide (21-23) and polymer (1, 24, 25) electrode materials have been extensively researched, and they were found to be electrochemically unstable. South Africa has large reserves of manganese ore. MnO_2 due to its theoretical high capacitance (23), less toxicity and environmental friendliness, is an excellent alternative to the expensive and toxic RuO_2.

There is a continual effort to investigate electroactive materials as potential electrodes for hybrid supercapacitors with high energy density. Recently, Chidembo *et al* (28) reported NiTAPc/MWCNT nanocomposite with superior supercapacitive behaviour as a promising electrode for supercapacitors. In their paper, they attributed this supercapacitive behaviour to nitrogen containing groups on the phthalocyanine ring. It was reported (29, 30) that capacitance increase in acidic electrolyte is proportional to an increase of nitrogen content in the graphene layer of carbon. It was found that nitrogen content increases the capacitance of carbon materials. Despite a considerable number of nitrogens on its pyrazine ring and increasing basicity of its ring, there are no reports on the capacitive behaviour of metallo-porphyrazine macrocycle compounds.

However, the literature on the use of porphyrazine macrocycle compounds and their composites for supercapacitive studies is limited.

1.2 Aims and objectives.

The main aim of this project is to utilize electrochemical techniques, which are cyclic voltammetry (CV), chronopotentiometric galvanostatic charge-discharge and electrochemical impedance spectroscopy (EIS) to investigate the supercapacitive behaviour of:

i) MWCNT-MnO_2 Nanocomposites

ii) MWCNTaf-MTPyzPz composites immobilised onto basal plane pyrolytic graphite electrode in neutral and acidic electrolyte.

iii) MWCNTPhNH_2-MTPyzPz composites immobilised onto basal plane pyrolytic graphite electrode in neutral and acidic electrolyte.

iv) Asymmetric capacitors made from MWCNTs, Carbon black and MTPyzPz.

v) Graphene oxide-metallotetrapyrazinoporphyrazino nanocomposites.

1.3 Outline of the dissertation

Chapter 1 outlines the rationale of the thesis and also present the aims and objectives of this study. This chapter also gives a detailed review of supercapacitors -

their history, classification, storage mechanism as well as their performance criteria. General review of electrochemistry is also discussed as well as physico-chemical characterisation of supercapacitor electrode materials.

Chapter 2 describes the experimental work, the equipment used and electrode modification and fabrication.

Chapter 4, 5 and 6 presents the results and discussion of synthesised materials and prepared modified electrodes with MWCNTs, MnO_2 and MTPyzPz materials. These chapters will give the detailed electrochemical and physical characterisations of various electrode materials under study.

1.4 References

1. Kötz R, Carlen M. Principles and applications of electrochemical capacitors. Electrochimica Acta. 2000;45(15-16):2483-98.

2. Pandolfo AG, Hollenkamp AF. Carbon properties and their role in supercapacitors. Journal of Power Sources. 2006;157(1):11-27.

3. Stoller MD, Park S, Zhu Y, An J, Ruoff RS. Graphene-Based Ultracapacitors. Nano Letters. 2008;8(10):3498-502.

4. Zhang LL, Zhao XS. Carbon-based materials as supercapacitor electrodes. Chemical Society Reviews. 2009;38(9):2520-31.

5. Arbizzani C, Mastragostino M, Soavi F. New trends in electrochemical supercapacitors. Journal of Power Sources. 2001;100(1-2):164-70.

6. Chang J-K, Chen Y-L, Tsai W-T. Effect of heat treatment on material characteristics and pseudo-capacitive properties of manganese oxide prepared by anodic deposition. Journal of Power Sources. 2004;135(1-2):344-53.

7. Salitra G, Soffer A, Eliad L, Cohen Y, Aurbach D. Carbon Electrodes for Double-Layer Capacitors I. Relations Between Ion and Pore Dimensions. Journal of The Electrochemical Society. 2000;147(7):2486-93.

8. Frackowiak E, Béguin F. Electrochemical storage of energy in carbon nanotubes and nanostructured carbons. Carbon. 2002;40(10):1775-87.

9. Huang Q, Wang X, Li J. Characterization and performance of hydrous manganese oxide prepared by electrochemical method and its application for supercapacitors. Electrochimica Acta. 2006;52(4):1758-62.
10. Obreja VVN. On the performance of supercapacitors with electrodes based on carbon nanotubes and carbon activated material-A review. Physica E: Low-Dimensional Systems and Nanostructures. 2008;40(7):2596-605.
11. Frackowiak E. Carbon materials for supercapacitor application. Physical Chemistry Chemical Physics. 2007;9(15):1774-85.
12. Inagaki M, Konno H, Tanaike O. Carbon materials for electrochemical capacitors. Journal of Power Sources. 2010;195(24):7880-903.
13. Frackowiak E, Béguin F. Carbon materials for the electrochemical storage of energy in capacitors. Carbon. 2001;39(6):937-50.
14. Frackowiak E, Delpeux S, Jurewicz K, Szostak K, Cazorla-Amoros D, Béguin F. Enhanced capacitance of carbon nanotubes through chemical activation. Chemical Physics Letters. 2002;361(1-2):35-41.
15. Béguin F, Szostak K, Lota G, Frackowiak E. A Self-Supporting Electrode for Supercapacitors Prepared by One-Step Pyrolysis of Carbon Nanotube/Polyacrylonitrile Blends. Advanced Materials. 2005;17(19):2380-4.
16. Frackowiak E, Metenier K, Bertagna V, Béguin F. Supercapacitor electrodes from multiwalled carbon nanotubes. Applied Physics Letters. 2000;77(15):2421-3.

17. Liu CG, Liu M, Li F, Cheng HM. Frequency response characteristic of single-walled carbon nanotubes as supercapacitor electrode material. Applied Physics Letters. 2008;92(14):143108--3.

18. Pan H, Li J, Feng Y. Carbon Nanotubes for Supercapacitor. Nanoscale Research Letters. 2010;5(3):654-68.

19. Ye J-S, Liu X, Cui HF, Zhang W-D, Sheu F-S, Lim TM. Electrochemical oxidation of multi-walled carbon nanotubes and its application to electrochemical double layer capacitors. Electrochemistry Communications. 2005;7(3):249-55.

20. Liu CG, Fang HT, Li F, Liu M, Cheng HM. Single-walled carbon nanotubes modified by electrochemical treatment for application in electrochemical capacitors. Journal of Power Sources. 2006;160(1):758-61.

21. Trasatti S, Buzzanca G. Ruthenium dioxide: a new interesting electrode material. Solid states structure and electrochemical behaviour. Journal of Electroanalytical Chemistry. 1971;29(2):A1-A5.

22. Zhang H, Cao G, Wang Z, Yang Y, Shi Z, Gu Z. Growth of Manganese Oxide Nanoflowers on Vertically-Aligned Carbon Nanotube Arrays for High-Rate Electrochemical Capacitive Energy Storage. Nano Letters. 2008;8(9):2664-8.

23. Toupin M, Brousse T, Bélanger D. Influence of microstucture on the charge storage properties of chemically synthesized manganese dioxide. Chemistry of Materials. 2002;14(9):3946-52.

24. Wang Y, Yuan A, Wang X. Pseudocapacitive behaviors of nanostructured manganese dioxide/carbon nanotubes composite electrodes in mild aqueous

electrolytes: effects of electrolytes and current collectors. Journal of Solid State Electrochemistry. 2008;12(9):1101-7.

25. Zheng JP, Huang J, Jow TR. The Limitations of Energy Density for Electrochemical Capacitors. Journal of The Electrochemical Society. 1997;144(6):2026-31.

26. Hall PJ, Mirzaeian M, Fletcher SI, Sillars FB, Rennie AJR, Shitta-Bey GO, et al. Energy storage in electrochemical capacitors: designing functional materials to improve performance. Energy & Environmental Science. 2010;3(9):1238-51.

27. Wang Y-g, Yu L, Xia Y-y. Electrochemical Capacitance Performance of Hybrid Supercapacitors Based on Ni(OH)2/Carbon Nanotube Composites and Activated Carbon. Journal of The Electrochemical Society. 2006;153(4):A743-A8.

28. Chidembo AT, Ozoemena KI, Agboola BO, Gupta V, Wildgoose GG, Compton RG. Nickel(ii) tetra-aminophthalocyanine modified MWCNTs as potential nanocomposite materials for the development of supercapacitors. Energy & Environmental Science. 2010;3(2):228-36.

29. Frackowiak E, Lota G, Machnikowski J, Vix-Guterl C, Béguin F. Optimisation of supercapacitors using carbons with controlled nanotexture and nitrogen content. Electrochimica Acta. 2006;51(11):2209-14.

30. Hulicova D, Kodama M, Hatori H. Electrochemical Performance of Nitrogen-Enriched Carbons in Aqueous and Non-Aqueous Supercapacitors. Chemistry of Materials. 2006 2011/12/03;18(9):2318-26.

CHAPTER 2

LITERATURE REVIEW

2.1 Electrochemical supercapacitors

Capacitors can be classified into three categories namely: electrostatic capacitors, electrolytic capacitors and electrochemical capacitors (1). Electrostatic capacitors or sometimes called conventional capacitors are energy storage devices that are made of two metal plates separated by a dielectric which might be a vacuum or a medium like air as illustrated in Figure 2.1. When potential is applied to a capacitor, two layers of opposite charges accumulate on the two electrodes separated by a dielectric. Thus, capacitance C is given by the equation:

$$ - \tag{2.1} $$

where, ε_r is the dielectric of the medium, ε_0 is the dielectric of a vacuum, A is the area of the capacitor and D is the distance between the electrodes

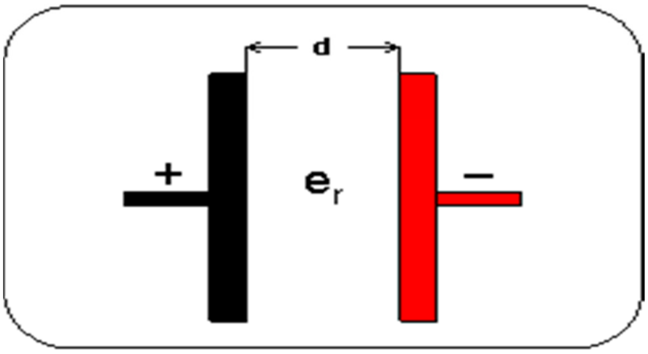

Figure 2.1: A typical electrostatic capacitor diagram.

Electrolytic capacitors as shown in Figure 2.2 are energy storage devices made of two metal plates that are separated by a thin dielectric which is an oxide layer. Electrochemical capacitors are devices that store electric charges in the interface between the electrode and the electrolyte by non faradaic processes and/or non faradaic processes.

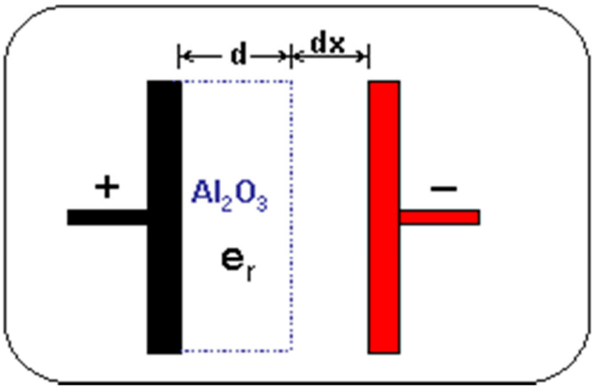

Figure 2.2: A typical electrolytic capacitor diagram.

Electrochemical capacitors due to their charge storage mechanism can be divided into two categories namely: Electrochemical double layer capacitor (EDLC) or pseudocapacitor. Figure 2.3 shows a basic design of an electrochemical capacitor. Electrochemical capacitors, known by many names such as double layer capacitors, supercapacitors, gold capacitors, ultra capacitors, power capacitors or cache capacitors.

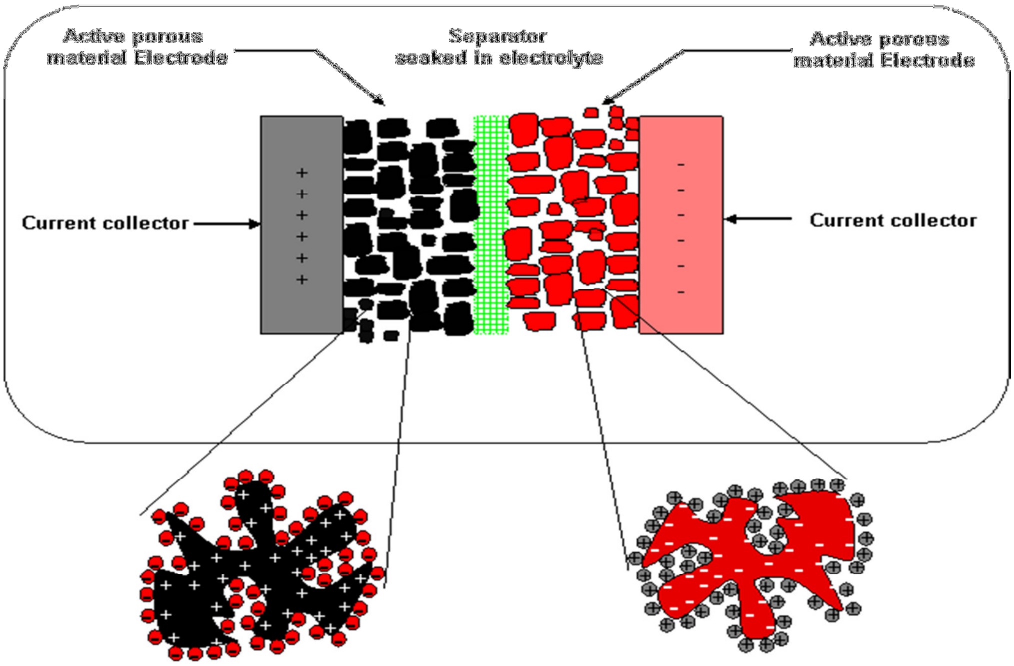

Figure 2.3: A typical EDLC schematic diagram

2.1.1 Historical background

Electrical charge storage on surfaces was discovered from rubbing of naturally occurring amber phenomena (2). In the seventeenth century, a Swedish professor Johan Carl Wicke developed an electrophorus. Electrophorus is a capacitive generator used to produce electrostatic charge via a process of electrostatic induction (3). This electric machine was improved and popularized by Allesandro Volta who made the first electric battery in 1800 (4). Wimshurst machine, an electrostatic device for generating high voltages was developed by James Wimshurst between 1880 and 1883. From this development together with those of Michael Faraday's dielectric concept an electric condenser, Leyden jar was invented (5, 6). Leyden jar which stores electrostatic electricity between two surfaces was later referred to as a "capacitor". Work by some researchers (7), (8) led to the proposal that an electron charge is equivalent to Faraday's constant.

The Work by Sommerfeld (9), Schröendinger (10), and Heisenberg (11) on electron energy states in atoms and molecules coupled with key conclusion on Faraday's laws by Hermann Von Helmholtz (12) brought about the full understanding of the charging and discharging processes in the atomic level. He developed a double layer concept. The understanding that electrical energy could be stored led to a first patent by Becker (13) at General electric in 1957. In the patent, he outlined that electrical energy storage is due to the charges arrangement at the double layer between the porous carbon and aqueous electrolyte. Years later SOHIO (14) patented an EC that had high area carbon materials and non-aqueous tetraalkylammonium salt electrolyte.

Nippon Electric company (15) introduced the first EC products in 1957 after obtaining the license for the technology from SOHIO. In 1970, SOHIO had obtained another patent of a disk shaped capacitor based on carbon paste. NEC (16) was the first company to launch a double layer capacitor under the name "supercapacitor" after obtaining their license from SOHIO. Table 2.1 gives the list of manufacturers who are producing capacitors commercially.

Table 2.1: A summary of the commercialized ECs (1, 17, 18).

Company Name	Device name	Country	Voltage range	Capacitance/F
AVX	Bestcap	USA	3.5-1.2	0.022-0.56
Cap XX	Super capacitor	Australia	2.25-4.5	0.09-2.8
Copper	Power stor	USA	2.5-5.0	0.47-50
ELNA	Dyna cap	USA	2.5-6.8	0.033-100
ESMA	Capacitor modules	Russia	12-52	100-8000
EPCOS	Ultracapacitor	USA	5.5,11	5-5000
Evans	Capattery	USA	5.5,11	0.01-1.5
Kold Ban	Kapower	USA	12	1000
Maxwell	Super capacitor	USA	2.5	1.6-2600
Nesscap	EDLC	South Korea	2.7	0.01-6.5
Panasonic	Gold capacitor	Japan	2.3-5.5	0.1-2000

2.1.2 Principles of Electrochemical capacitors

Electrochemical capacitors store their energy in the form of electric charge using principles similar to conventional capacitors. Capacitance is a measure of an amount of electrical energy stored for a given potential. Energy can be stored on the capacitor through a non-faradaic process or a faradaic process or both processes. Two methods of energy storage, namely, electrochemical double layer capacitance and pseudocapacitance will be discussed.

2.1.2.1 Electrochemical double layer capacitance

EDLC is the name that describes the fundamental charge storage principle of this kind of electrochemical capacitors. The separation of charged particles or electronic charges at the interfaces of metal electrodes and ionic solutions give rise to the so-called double layer. The capacitance due to this capacitor behaviour is dependent on the large interfacial area and the atomic range of charge separation distances. An EDLC consists of two such double layers, each exhibiting its own non faradaic capacitive behaviour. The interface structure at electrode surfaces has been developed over years. First Helmholtz (19) in 1853 adopted a model where there is an array layer of positive or negative charges on the electrode surface and an array of opposite sign charges accumulated in the electrolyte. The distance between this double layer of charges was between 0.05 nm and 0.2 nm. As illustrated in Figure 2.4(a), the layer of charges in the electrolyte is fixed and there is a linear drop of potential from the electrode to the layer of charges. According to Boltzmann principle (20), it was found that the ions (both positive and negative) on the solution side of the double layer will not remain static but will be distributed throughout the electrolyte. Gouy (21, 22) used this principle to propose a model where ions were assumed to be point charges distributed in the electrolyte. Gouy point charge model (figure 2.4(b)) resulted in large capacitance been predicted and also gave a wrong potential profile. The layer of distributed charges as proposed by Gouy was referred to as Gouy diffuse layer. In 1924, Stern (23) proposed a model as illustrated in Figure 2.4(c) as a solution to the overestimation of capacitance by Gouy model. His model was a combination of Helmholtz and Gouy double layer models. As illustrated in Figure 2.4(c), the difference in potential extends beyond the immediate layer of solvated ions in compact (Helmholtz) through the OHP into the diffuse layer.

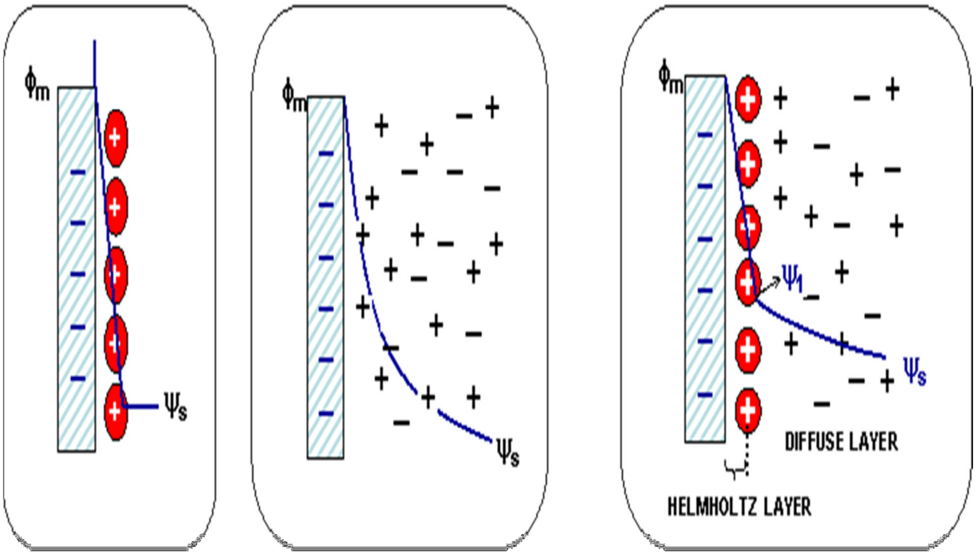

(a) (b) (c)

Figure 2.4: (a) Helmholtz (b) Gouy and (c) Stern.(24)

From this model, the overall capacitance, C_{dl} (double layer capacitance) is given by the equation:

$$\text{—} \qquad \text{—} \qquad \text{——} \tag{2.2}$$

where, C_H is the capacitance from the Helmholtz layer or compact layer and C_{diff} is the capacitance from the diffuse layer. Figure 2.5 illustrate the model as proposed by Grahame (25), it consists of three regions where the Helmholtz layer is divided into inner and outer plane. The inner Helmholtz plane (IHP) is the closest to the electrode and contains solvent molecules and specifically adsorbed ions. The outer Helmholtz plane is the next region after IHP and consists of solvated ions at their closest approach to the electrode. The last region is the diffuse or Gouy layer. The determination of EDL behaviour at planar electrode is influenced by the following factors (26):

(i) The electric field across the electrode.

(ii) Types of the electrolyte ions.

(iii) Solvent in which the electrolyte ions are dissolved.

(iv) Chemical affinity between the adsorbed ions and electrode surface.

In 1963 Bockris *et al (27)* proposed a model (Figure 2.6) that takes into account the influence of the water interactions in the interphase (2). He outlined that dielectric constant increase as you move away from the polarised electrode.

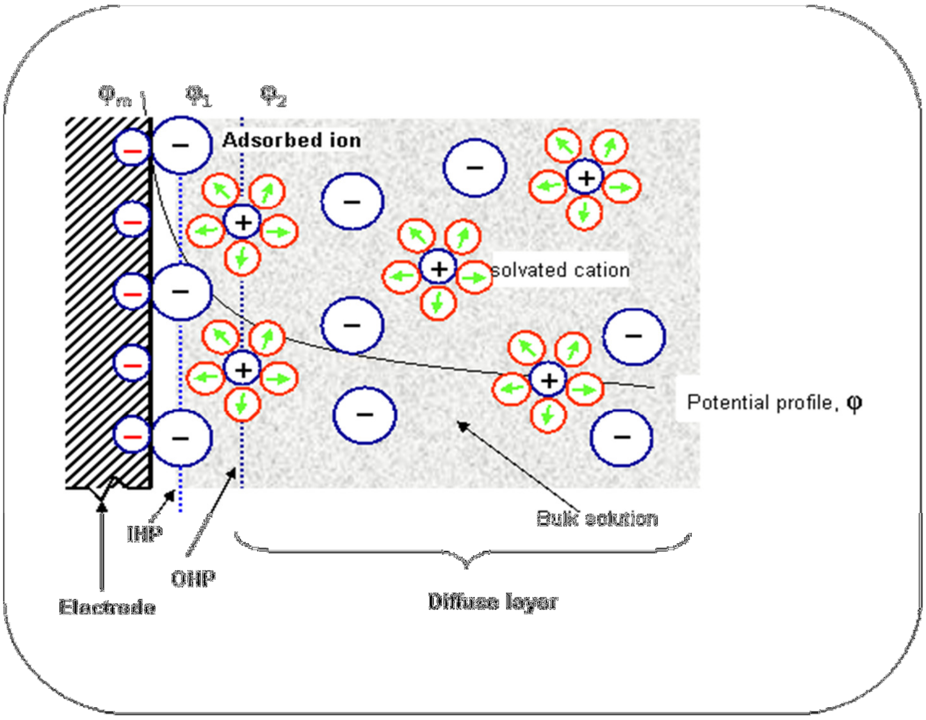

Figure 2.5: Schematic representation of the Grahame model of the electrical double layer (28).

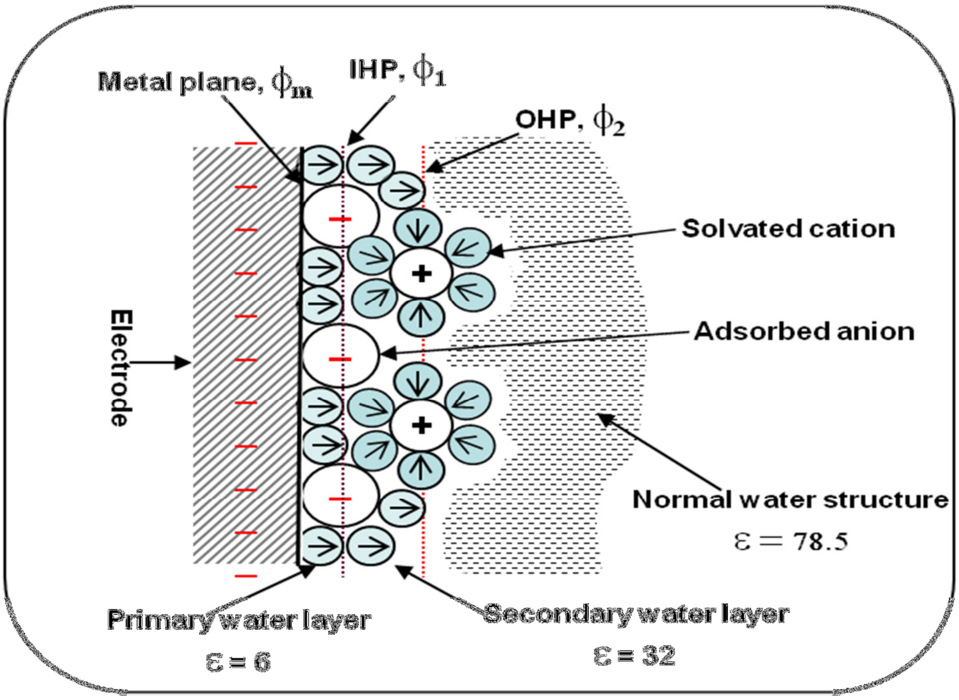

Figure 2.6: Double layer model including layers of solvent (27).

2.1.2.2 Pseudocapacitance

Pseudocapacitor was initially investigated in Conway's laboratory by a Continental group (29). Pseudocapacitance arises when applied potential induces faradaic current from processes such as electrosorption and/or oxidation-reduction of the electro-active materials. It should be noted that pseudocapacitance is Faradaic in origin and that it is potential dependent. There are two types of psuedocapacitance namely: adsorption/electrosorption pseudocapacitance and redox pseudocapacitance (29).

(i) Adsorption/electrosorption pseudocapacitance

Electrosorption pseudocapacitance is a reversible process where ions are deposited onto an electrode surface to form a monolayer resulting in a Faradaic charge transfer, and hence gives rise to pseudocapacitance. The surface reaction equation for adsorption/desorption (29, 30) is given by the following equation:

(2.3)

where, A is the ionic species, S is the substrate, c is the concentration of deposited ions, A_{ads} is the adsorbed species A, 1-θ_A is the fractional free surface area available for adsorption, θ_A is a coverage and V is the electrode potential (31).

From Langmuir adsorption equation the electrode surface coverage will be given by (26, 29):

$$\frac{\quad}{\quad} \qquad \frac{\quad}{\quad} \tag{2.4}$$

where, K is an electrochemical equilibrium constant for chemisorption with charge transfer. Differentiating the above equation yields a pseudocapacitive relation, C_φ (pseudocapacitance) represented by (29):

(2.5)

where, q_1 is the faradaic charge required for the complete formation or dispersion of the monolayer, V is the electrode potential, R is the gas constant, T is the absolute temperature and F is the faraday's constant.

(ii) Redox pseudocapacitance

A reversible redox process given in equation 2.6 involves an electron transfer process between an oxidized species, Ox and a reduced species, Red.

$$Ox + ze^{-} \qquad Red \tag{2.6}$$

From equation 2.6, the potential, E is given by the Nernst equation 2.7:

2.7)

where, E^0 is the standard potential and $\mathfrak{R}$ is relative fractions of oxidation and reduction activities defined as [ox]/([ox]+[red]). Differentiating equation 2.7 yields a redox capacitance quantity (C_φ) as shown in equation 2.8:

(2.8)

It should be noted that redox pseudocapacitance gives “mirror image” cyclic voltammograms as shown in Figure 2.7. Capacitors are categorised into three main classes in accordance with their storage mechanism (30):

- Electrochemical double layer capacitor
- Pseudocapacitor
- Hybrid capacitor.

EDLC uses the non-faradaic separation of charges at the double layer while pseudocapacitor utilizes the faradaic charge transfer processes. Hybrid capacitors use both mechanisms for energy storage.

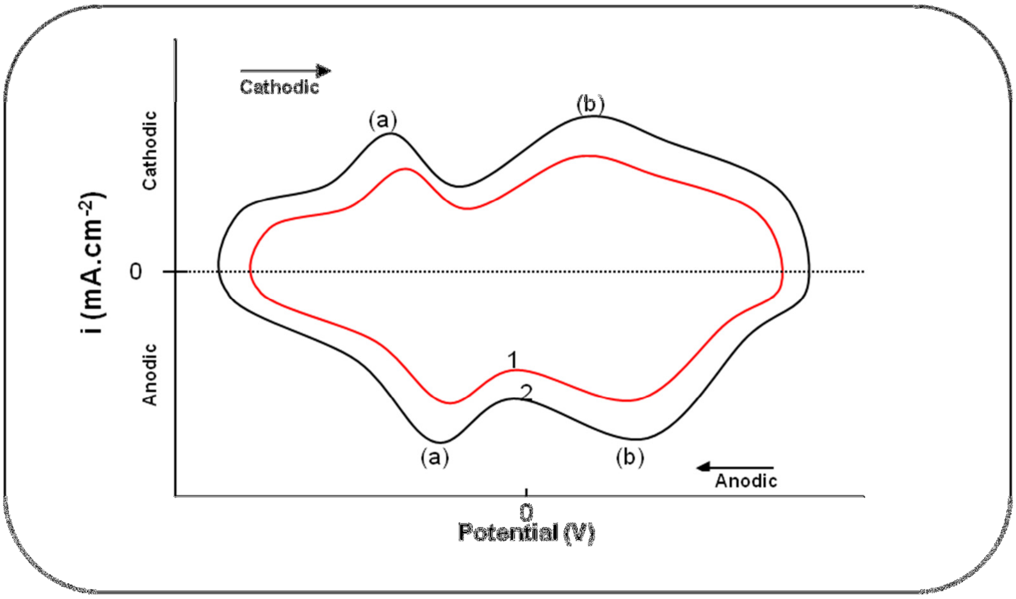

Figure 2.7: Example of a typical cyclic voltammogram for a redox process

Figure 2.8 illustrates the classification and outlines the materials that are utilized for the different electrodes used to make capacitors.

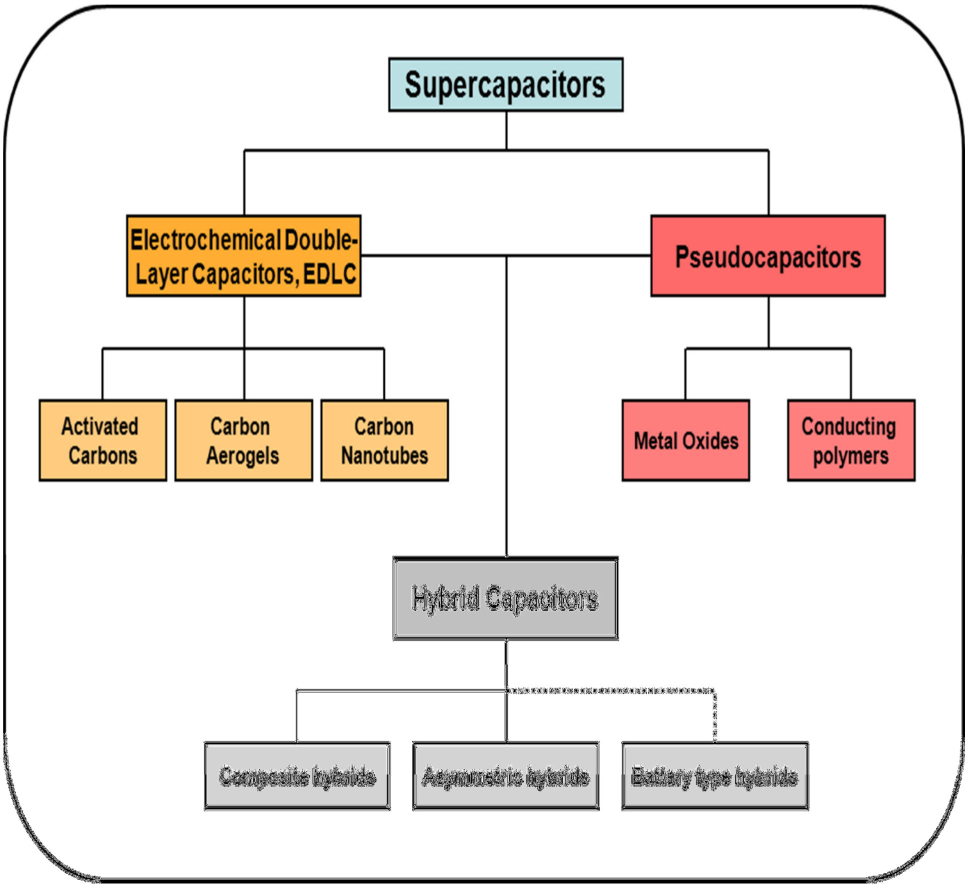

Figure 2.8: Classification of electrochemical capacitors (31).

2.1.2.3 Electrochemical double layer capacitors

Carbon is the material of choice for electrode fabrication in EDLCs. Carbon exists in several allotropic forms and possesses desirable properties for double layer capacitance. Carbon is mostly used because of its chemical stability, good conductivity, high surface area, low cost, good polarizability and pore size. Activated carbons, carbide-derived carbons, carbon nanofibers, templated carbons, carbon aerogels and carbon nanotubes (24, 32-34) are the most used carbon materials for EDLCs.

Activated carbons (34) (ACs) are produced from physical (thermal) activation and or chemical activation (impregnation with chemical activating agents like KOH, HNO_3 and $ZnCl_2$) of carbon materials. Activated carbons have a surface area (34) as high as $3000 m^2.g^{-1}$. ACs due to different pore sizes can (35), (36), (37) have capacitance ranging between 94 $F.g^{-1}$ and 413 $F.g^{-1}$. Pore size is one of the important properties of ACs that has an impact on capacitance. ACs have a broad distribution pore sizes consisting of micropores (< 2 nm), mesopores (2 nm - 50 nm) and macropores (> 50 nm). ACs give better capacitance in aqueous electrolytes (100 $F.g^{-1}$ - 300 $F.g^{-1}$) than in organic electrolytes (< 150 $F.g^{-1}$) (38). Salitra group (39) have reported that pore sizes above 0.4 nm are ideal for EDLC charging in aqueous electrolytes. Béguin *et al* (40) have concluded that there is a correlation between pore size and capacitance. They hypothesised that a particular pore size is related to a particular electrolyte used, either aqueous or organic. They found that optimal capacitance is obtained when a pore size is between 0.7 nm and 0.8 nm for aqueous and organic electrolytes respectively.

Carbide-derived carbons (CDC) are produced by chlorination of the metallic carbide. Chmiola *et al* reported that the best CDC materials are derived from TiC (41). TiC-derived carbons (41, 42) have a surface area of about 1600 m^2g^{-1}, an average micropore width of 0.7 nm and have shown capacitances of between 130 $F.g^{-1}$ and 190 $F.g^{-1}$.

Carbon nanofibers (CNFs) also called graphite nanofibers or carbon filaments are catalytically vapour grown carbon fibres with diameters between 50 nm and 500 nm and average pore size of 3 nm - 20 nm (34). Some multibranched CNFs were found to have capacitance of about 50 $F.g^{-1}$ at high current density (43) while some researchers (44) reported a high capacitance of 297 $F.g^{-1}$. CNFs are unlikely materials to be used for electrode making because they are expensive and have high equivalent series resistance (ESR).

Template derived carbons are produced by impregnating the inorganic matrix with a carbon precursor (e.g. sucrose, propylene, and pitch or polymer solutions). Template derived carbon can be tailor made with desired pore volume, pore size and surface area (34). Sevilla *et al* (45) reported that these carbons can have a surface area of 1500 m^2g^{-1} – 1600 m^2g^{-1}, thus limiting the theoretical capacitance to between 200 $F.g^{-1}$ and 220 $F.g^{-1}$ in aqueous electrolytes and less in organic electrolytes. Zeolite Y templated carbon (46), (47) can have a gravimetric capacitance of up to 340 $F.g^{-1}$. This carbon exhibits good recyclability in excess of 10 000 cycles.

Carbon aerogels (CAGs) were first made by Pekala (48, 49). CAGs are three dimensional mesoporous network of carbon nanoparticles prepared by a sol-gel process. Some CAGs are derived from organic aerogels such as resorcinol-formaldehyde (RF), phenol-furfural (PF), and melamine-formaldehyde (MF) with subsequent pyrolysis in inert atmosphere (50). CAGs such as high surface area, good polarizability, superior electrical conductivity and high porosity (51) makes them good EDLC electrode materials. High production costs, presence of functional groups, difficulty in mass production and inaccessibility of micropores makes CAGs less desirable for EDLC purposes (52). Escribano *et al* (53) reported CAGs with specific capacitance of between 70 $F.g^{-1}$ and 150 $F.g^{-1}$ for pore diameters between 3 nm and 13 nm.

Recently carbon nanotubes have been extensively researched for supercapacitance behaviour due to their intrinsic properties. Carbon nanotubes are thoroughly reviewed in section 2.5.

2.1.2.4 Pseudocapacitors.

Materials mostly used for electrode fabrication of pseudocapacitors are metal oxides and conducting polymers. These materials exhibit faradaic reactions that are essential for this kind of supercapacitors. Metal oxides have been receiving a considerable attention in research since the study of ruthenium oxide (RuO_2) electrode gave the highest capacitance as compared to carbon based supercapacitors. Metal oxides are of immense interest for use in supercapacitors due to their high conductivity and redox activity properties. A hydrous RuO_2 prepared by a sol-gel process was found to have specific capacitance of 740 $F.g^{-1}$ (54). Specific capacitance as high as 1170 $F.g^{-1}$ and 1580 $F.g^{-1}$ have been obtained from composites of RuO_2 (55-57). The high cost of RuO_2 has made researchers to look for an alternative metal oxide that is cheap and less toxic which can yield capacitance results comparable to RuO_2. Several metal oxides such as Co_3O_4 (58), NiO (59), Fe_3O_4 (60), SnO_2 (61), V_2O_5 (62), MnO_2 (63-65), Bi_2O_3 (66) and In_2O_3 (67) have been studied. Metal oxides' serious drawback for use as electrode materials in supercapacitors are their small potential window and short term stability during cycling. Recently research on metal oxides has shifted from bulk conventional materials to nano-structured materials. Nano-structured material electrodes offer high capacitance because of the enhanced surface area and better ion conductivity.

Deng *et al* (68) have reported nano CoO electrode with a specific capacitance of 2200 F.g^{-1}, which is ten times the capacitance of the bulk CoO. It was recently (69) reported that thin metal oxide films give superior capacitance values as compared to their bulk and composite metal oxide electrodes.

Electroconducting polymers (ECPs) have been considered alternative electrode materials for capacitance due to their high conductivity, high capacitance, good reversibility and low cost (70). ECPs exhibit pseudocapacitive behaviour since their energy storage mechanism is due to faradaic processes emanating from p- and n-doping (25). From literature several ECPs such as polyaniline (PANI) (71), polythiophene(Pth) (72), polypyrrole (PPy) (73), (PEDOT) (74), (PMMA) (75) and (PPV) (76) with specific capacitance ranging from 250 F.g^{-1} to 775 F.g^{-1} have been reported. The drawback of ECPs are their lack of long term stability due to swelling or shrinking during charging and discharging process (32). Capacitive results and intrinsic properties of PANI make it a highly desirable electrode material. Mastragostino *et al* (77) reported the challenge of inefficiently n-doped ECPs.

2.1.2.5 Hybrid capacitors

High energy and high power density at high rates are not simultaneously achievable by either EDLCs or pseudocapacitors. To achieve high performance, hybrid capacitors integrate both energy storage mechanisms in their operation. They utilize both the faradaic and non-faradaic processes to store charges. Hybrid capacitors are subdivided into three classes, namely composite, asymmetric and battery-type hybrids. Hybrid capacitors are tailor made to meet the following requirements for a high performance ECs namely: good electron conductivity, highly accessible specific surface area and efficient mass transport (78).

Composite hybrid capacitor consists of electrodes which contain a carbon material that is incorporated into a conducting polymer or metal oxide material. Li and co-workers (79) reported a specific capacitance of 587 $F.g^{-1}$ for PANI/AC composite electrode which is higher than of AC and PANI individually. Other composites studied were $RuO_2{\cdot}xH_2O$/CNT (1143 $F.g^{-1}$) (80), NiO/CNTs (1329 $F.g^{-1}$) (81), PPy/CAG (433 $F.g^{-1}$) (82). The incorporation of MWCNTs into metal oxides helps to circumvent the lack of electrical conductivity in metal oxides. For polymers, the formation of composites has shown to counteract the swelling and shrinking of the electrodes during charging and discharging process. Composite hybrids are formed in order to enhance EC performance, due to synergistic properties from a combination of two or more materials.

Asymmetric hybrid capacitors sometimes referred to as capacitor-type/capacitor-type capacitor are capacitors with a different positive and negative electrode. These capacitors usually have a high operating potential window that accounts for an increase in the EC performance (83). From literature, mostly carbon materials are used for a negative electrode while pseudocapacitive materials and composites are utilized for the positive electrode (84-86). Cheng *et al* (87) reported an optimized nano structured asymmetric hybrid capacitor with excellent power and energy density of 50.3 $kW.kg^{-1}$ and 25.5$Wh.kg^{-1}$, respectively.

Battery type hybrid capacitors are referred to sometimes as battery-type/capacitor type capacitor. These capacitors are also asymmetric and their negative electrode is similar to an anode lithium ion battery anode.

2.1.3 Performance of supercapacitors

The characteristics of electrode materials and the electrolyte used in the cell determine supercapacitor performance. For better performance, electrode materials that give maximum capacitance are preferred, and for the electrolyte, minimum resistivity is desirable. Power density (35) and energy density (88) are the two main characteristic parameters that are used to evaluate cell performance. Energy density is calculated from the formula:

$$\frac{}{} \tag{2.9}$$

where, C is the capacitance, m is active mass of the electrode and V is the potential. Power density is calculated from the formula:

$$\frac{}{} \tag{2.10}$$

where, P_{max} is the power density, V_i is the potential, R_{ESR} is the equivalent series resistance.

The comparison of power density and energy density is graphically well illustrated by a Ragone plot (Figure 2.9). A Ragone plot is used to evaluate the performance of a capacitor (32). Energy storage devices (ESD) are characterized by the energy and the power available for a load. Figure 2.9 illustrate that supercapacitors must have more power density than batteries and more energy than conventional capacitors.

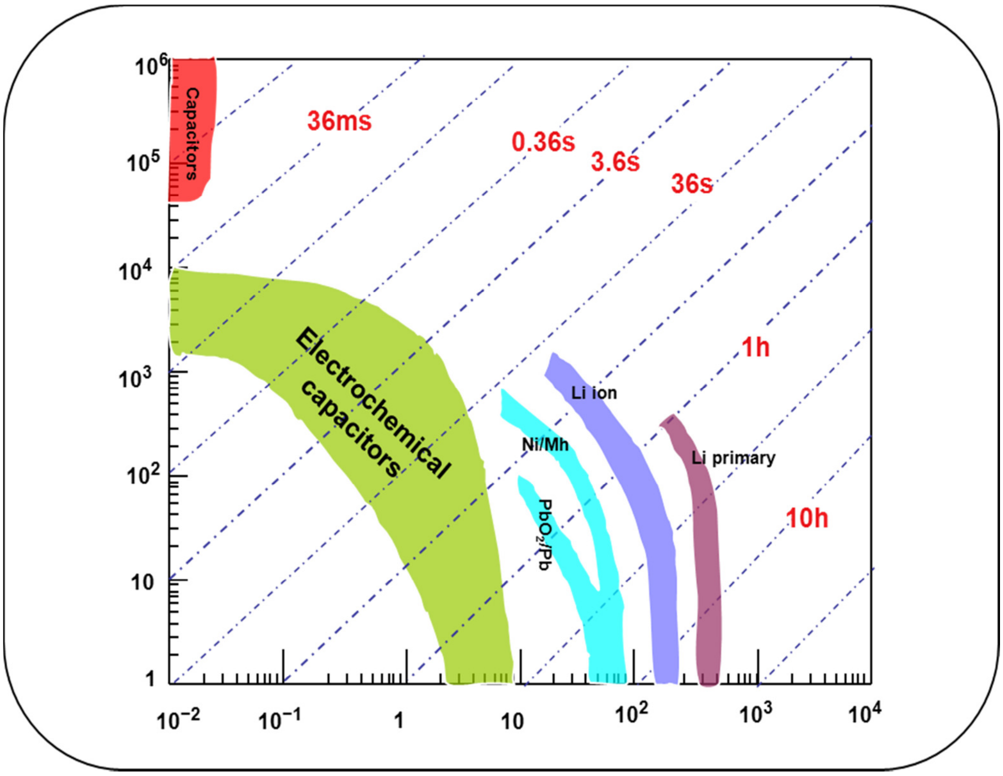

Figure 2.9: Ragone plot of various energy storage devices (21).

2.2 Carbon nanotubes.

Carbon nanotubes (CNTs) are tubular nanostructures made of sp^2 hybridized carbon atoms. They are made of graphite sheets that are rolled into cylindrical shaped seamless tubes and capped at the end with fullerene-type hemispheres. They are categorized into two main types: single-walled nanotube (Figure 2.10a) and multi-walled nanotube (Figure 2.10b). Further classification of the carbon nanotubes is based on how the graphite sheet that consists of the sp^2 carbon atoms is rolled.

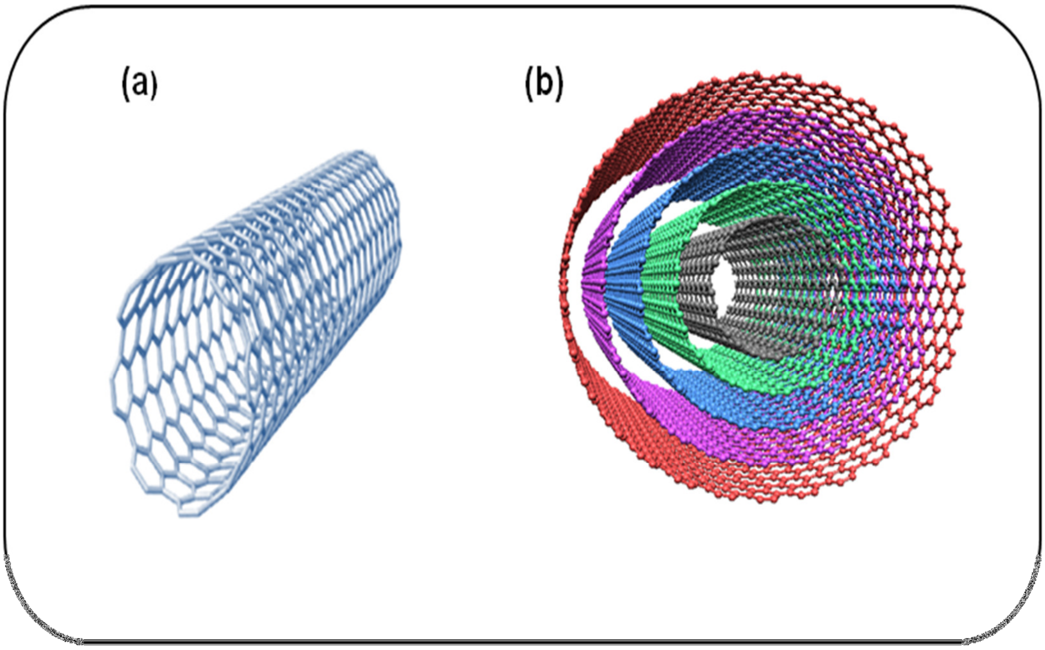

Figure 2.10: Images of (a) single-wall carbon nanotube and (b) multi-walled carbon nanotubes.

Carbon nanotubes can further be described in shorthand notation by two indices (n,m). The radius and chiral angle of the carbon nanotubes can be estimated from Equations 2.11 (89) and 2.12 (89):

$$\frac{\quad - }{\qquad\qquad} \tag{2.11}$$

$$- \tag{2.12}$$

CNTs (Figure 2.11) can further be described as zigzag, armchair or chiral structure. Since their discovery by Iijima (90), carbon nanotubes have attracted a lot of interest in research due to their outstanding physical and chemical properties.

Carbon nanotubes are widely used as electrode material for supercapacitors due to their excellent properties. CNTs have high conductivity, high mechanical strength, large specific surface area, high chemical stability, low resistivity and low mass density.

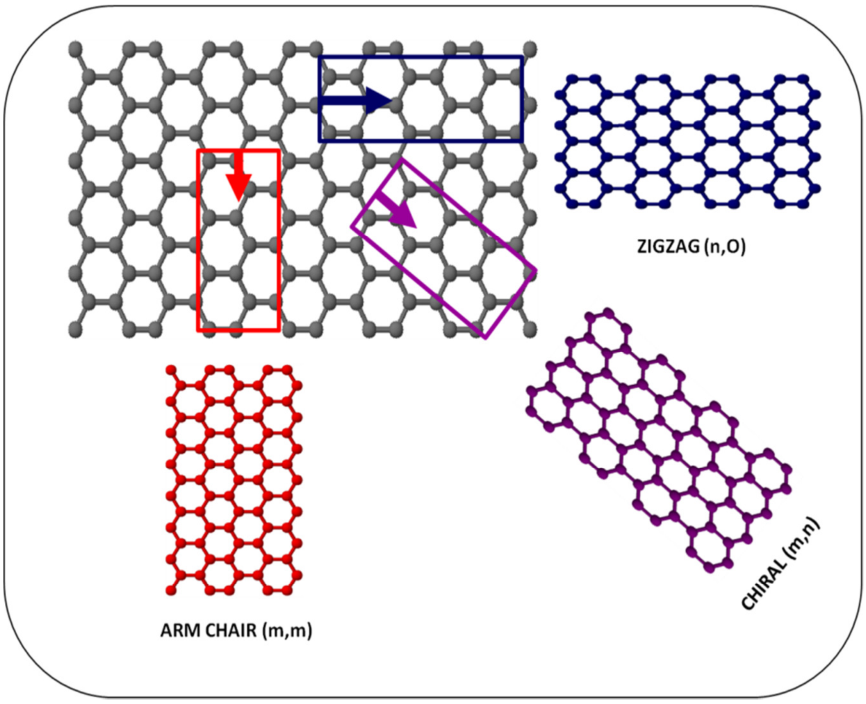

Figure 2.11: The diagram of graphene layer rolled into armchair, chiral and zigzag nanotube.

CNTs possess strong Van der Waals interactions between the atoms. CNTs are highly conductive due to π-electrons delocalization in the carbon framework. Entanglement and bundling of CNTs caused by high aspect ratio, decreases their dispersion in solvents contributing to low capacitance values (91). Capacitance and dispersion of CNTs can be increased by chemical or mechanical activation, functionalization and heat and surface treatment. CNTs can be functionalized either by non covalent or covalent modification approaches (92). Covalent functionalization introduces redox active surface functional groups such as carboxyl, hydroxyl, amine, fluorine and many more on the CNTs (93). The covalent functionalization of the CNTs alters their properties and introduces redox active sites which contribute to the increase of capacitance through faradaic reactions.

Functionalized CNTs are more chemical stable than non-covalent functionalized CNTs. The interactions between CNT's graphite surface and the aromatic component of redox material are weak since there are either due to Van der Waals, electrostatic interactions or π-π interactions. Niu *et al* (93) were the first to report the specific capacitance of functionalized CNTs (102 $F.g^{-1}$) in H_2SO_4. Ahn *et al* (94) reported that capacitance is indirectly proportional to diameter of the CNTs. The introduction of surface carboxyl groups enhances capacitance three fold due to the increased hydrophilicity of MWCNTs in an aqueous electrolyte. In contrast, the introduction of alkyl groups resulted in a marked decrease in capacitance. Notably, the complete disappearance of capacitance for samples functionalized with longer alkyl groups, indicated the perfect block of proton access to the carbon nanotubes surfaces by extreme hydrophobicity (95, 96). The carbon nanotube is a nonpolar material and easily aggregates in a polar solvent. Aggregation leads to difficulty in fabricating CNT electrodes for energy storage, and this results in the decrease in the performance of the electrodes (97). High performance ECs are obtained by combining electrode materials that give rise to pseudocapacitance and EDLC storage mechanisms. The psuedocapacitance due to functionalization on the CNTs contributes little to the overall SC of the CNTs electrode. Recently composites that combine CNTs and electroactive materials are of considerable interest. The carbon based composites are seen as best candidates that can give high power and larger energy density.

2.3 Graphene oxide

Graphene oxide (GO) is an analogue of graphene and also an intermediate during the oxidation and exfoliation of graphite (98-100). GO is a single sheet of graphite oxide that bears different kinds of oxygen–containing functional groups on the basal and edge plane of the carbon framework (98, 101-103). GO can be prepared by several methods such as Staudenmaier method, Hummers method and Offeman method (100, 104). Several models of GO (Figure 2.12) have been proposed, and Lerf-Klinowski's model and Dekany's model are the most used models (101, 102).

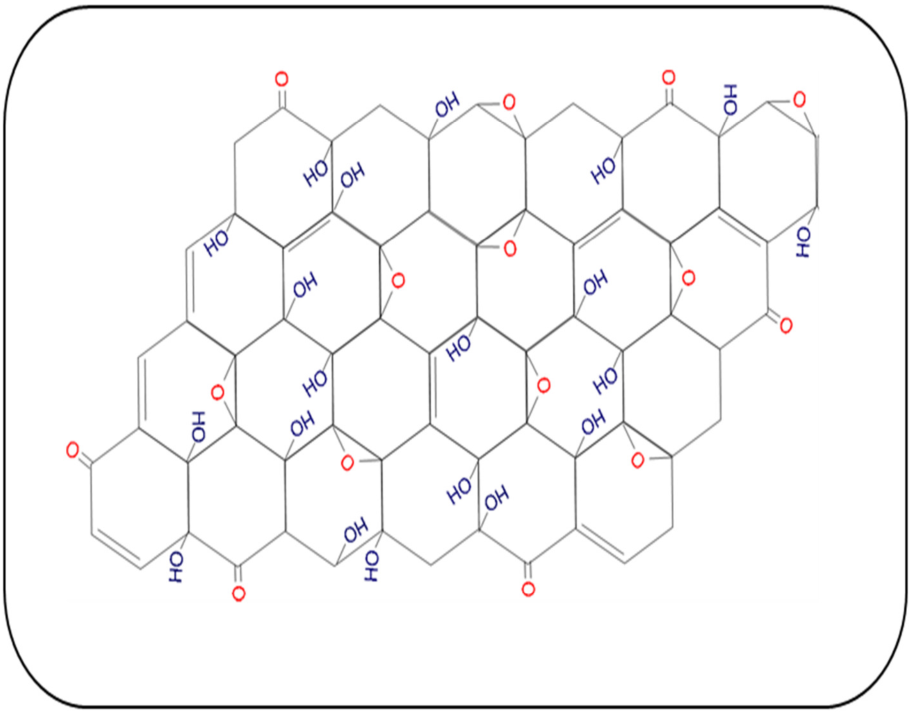

Figure 2.12: The diagram of graphene oxide model as proposed by Lee *et al* (103).

Hybrid materials are easily formed between GO and organic and inorganic materials via non covalent, covalent and/or ionic interactions due to oxygen functional groups on GO and π electrons found in GO carbon framework (98, 100). Xu *et al* (99) have reported that GO has a small ESR, higher capacitance of up to 189 $F.g^{-1}$, good cycle stability. They also found that GO's rate performance is comparable to graphene. Several graphene oxide composites like GO-MnO_2 (211 $F.g^{-1}$) (105), GO/PANI (555 $F.g^{-1}$) (106), GO/PPy (633 $F.g^{-1}$) (107) and RGO/RuO (471 $F.g^{-1}$) (108) have been found to be good capacitive materials.

2.4 Manganese Oxides

Manganese is one of the transition metals that are abundant in the earth's crust (109). It occurs in various forms such as pyrolusite (MnO_2), rhodochrosite ($MnCO_3$) and manganite MnO(OH) in nature. Divalent Mn^{2+} is the most stable oxidation state. Beadouret *et al* (110) have reported that MnO_2 is the best performing electrode material as compared to $Mn(OH)_2$, Mn_2O_3 and Mn_3O_4. The theoretical capacitance of MnO_2 is in the range 1100 $F.g^{-1}$ – 1300 $F.g^{-1}$ attributable to EDLC and pseudocapacitance storage mechanisms (111). Manganese oxides are widely used in batteries since they are less toxic, environmentally friendly, and less expensive. Methods like Chemical vapour deposition, thermal vapour transport, laser assisted catalysis, and electrochemical deposition and condensation are amongst well known synthetic methods of MnO_2. All these different methods are an attempt to find a suitable MnO_2 material with desirable supercapacitive properties. MnO_2 can be found in one, two or three dimensional structural shapes. Manganese dioxide of various shapes have been studied, namely nanospheres (112), nanotubes (113), nanowires (114), helices (115), microspheres (116) and core-shell structures (117). Amongst the various MnO_2 compounds reported we have (113):

- α-MnO_2 (the best supercapacitive material)
- ε- MnO_2
- γ- MnO_2
- δ- MnO_2
- β- MnO_2
- λ- MnO_2

Forming a MnO_2 composite is the ideal way to counteract lack of conductivity and electrochemical stability of MnO_2. For most supercapacitor applications, MnO_2 is usually mixed with a carbon material like graphene to improve the conductivity of MnO_2. The hydrated form of MnO_2 has been found to yield satisfactory results. It was reported that in an aqueous electrolyte like Na_2SO_4, the energy storage mechanism is faradaic not non-faradaic. Table 2.2 summarises some of the research done on the capacitive behaviour of MnO_2 in different electrolytes. The best MnO_2 material that satisfies all the supercapacitor performance requirements has not been found yet. This makes the study of the supercapacitive behaviour of MnO_2 an area of research still to be explored.

Table 2.2: Published data on MnO2 and its carbon based composites.

Electrode	Electrolyte	Potential window/ V	Scan rate / $mV.s^{-1}$	current density	Mass specific capacitance/ ($F.g^{-1}$)	Reference Electrode	Reference
MnO_2	6M KOH	-0.8 – 0.8	-	2 $A.g^{-1}$	460	SCE	(118)
MnO_2	1M Na_2SO_4	0 – 0.9	50	-	322	SCE	(119)
CNT/MnO_2	1M $LiClO_4$ /PC	1.5 – 4.0	10	-	491	Li foil	(120)
Mn/C	1M KCl		10	-	271	SCE	(121)
γ-MnO_2	0.5M Na_2SO_4	0.0 – 1.0	5	-	344	SHE	(122)
MnO_2	2M $(NH_4)_2SO_4$	-0.2 – 0.8	5	-	310	SCE	(123)
MnO_2/C	1M Na_2SO_4	-0.8 – 0.8	10	-	410	SCE	(124)
MWCNT/MnO_2	1M $(NH_4)_2SO_4$	0.0 1.0	-	2$mA.cm^{-2}$	298	SCE	(125)
MnO_2	0.1M K_2SO_4	-0.05 – 0.85	2	-	112	Ag/AgCl	(110)
MnO_2/PPy	0.1M Na_2SO_4	-0.5 – 0.5	5	-	620	SCE	(126)
MWCNT/MnO_2	0.5M H_2SO_4 – 0.5M Na_2SO_4	-0.1 – 1.0	-	2.5$mA.cm^{-2}$	384	SCE	(127)
ε-MnO_2	1M Na_2SO_4	0.0 – 1.0	20	-	320	Ag/AgCl	(128)
MnO_2/CNT	1M Na_2SO_4	0.0 –1.0	-	1$mA.cm^{-2}$	586	SCE	(129)
α-MnO_2	1M $NaSO_4$	0.0 – 0.8	5	-	220	Ag/AgCl	(130)
MnO_2	1M LiOH	0.0 1.0	-	10$A.g^{-1}$	200	Hg/HgO	(131)
CP-CNT-MnO2	0.65M K_2SO_4	-0.3 – 0.7	1	-	322	Hg/HgSO4	(132)

2.5 Macrocyclic compounds

Metalloporphyrins (MPo), metallophthalocyanines (MPc) and metalloporphyrazines (MPz) (Figure 2.13) are tetrapyrrollic macrocyclic systems with a metal central atom. The macrocycles differ with respect to the atoms on the meso positions (133). Though metalloporphyrazine and metallophthalocyanine have the same atoms on the meso positions, they differ with regard to the presence of a benzene ring (134). Macrocycles are of potential interest for a variety of applications such as photodynamic therapy (PDT) (135) and catalysis (136). Porphyrazines are tetraazaporphyrins where the meso carbon atoms of the porphyrinic macrocycles are replaced with nitrogen atoms. Porphyrazines absorb stronger in the Q band region and have broad soret bands between 300 nm and 400 nm due to π-π* and n-π* transitions (137, 138). MPz have a higher electronegativity than MPc due to the aza bridge that contains nitrogen atoms (139). The presence of the aza bridges make porphyrazines (Pzs) strong σ donors, much stronger than porphyrins.

The synthetic method by Linstead and Fisher (the cyclocondensation(140) of fumaronitrile or maleonitrile) is still the preferred method of porphyrazine synthesis. Pzs can also be synthesised by reductive deselenation of TSePyMg with H_2S followed by ring closure (141). The porphyrazine macrocycle may be annulated with heterocyclic rings containing different heteroatoms (N, S, Se.) (142). The incorporation of the heterocyclic rings makes the porphyrazine macrocycle to be electron deficient (143). The electrochemical and optical properties depend on the metal centre on the macrocycle as well as the peripheral modification of the Pzs substituted on the β positions with either the heteroatoms or with six or seven membered rings (144). Tuncer *et al* (145) have reported that Pz complexes show well defined redox couples ascribed to metal and ring-based processes.

Porphyrazines have been investigated for photodynamic therapy (146), metal ion and gas sensing (147), optical data recording systems, electrochromic displays, and magnetic (148), electronic and conductive materials for nanotechnology (141, 149-151).

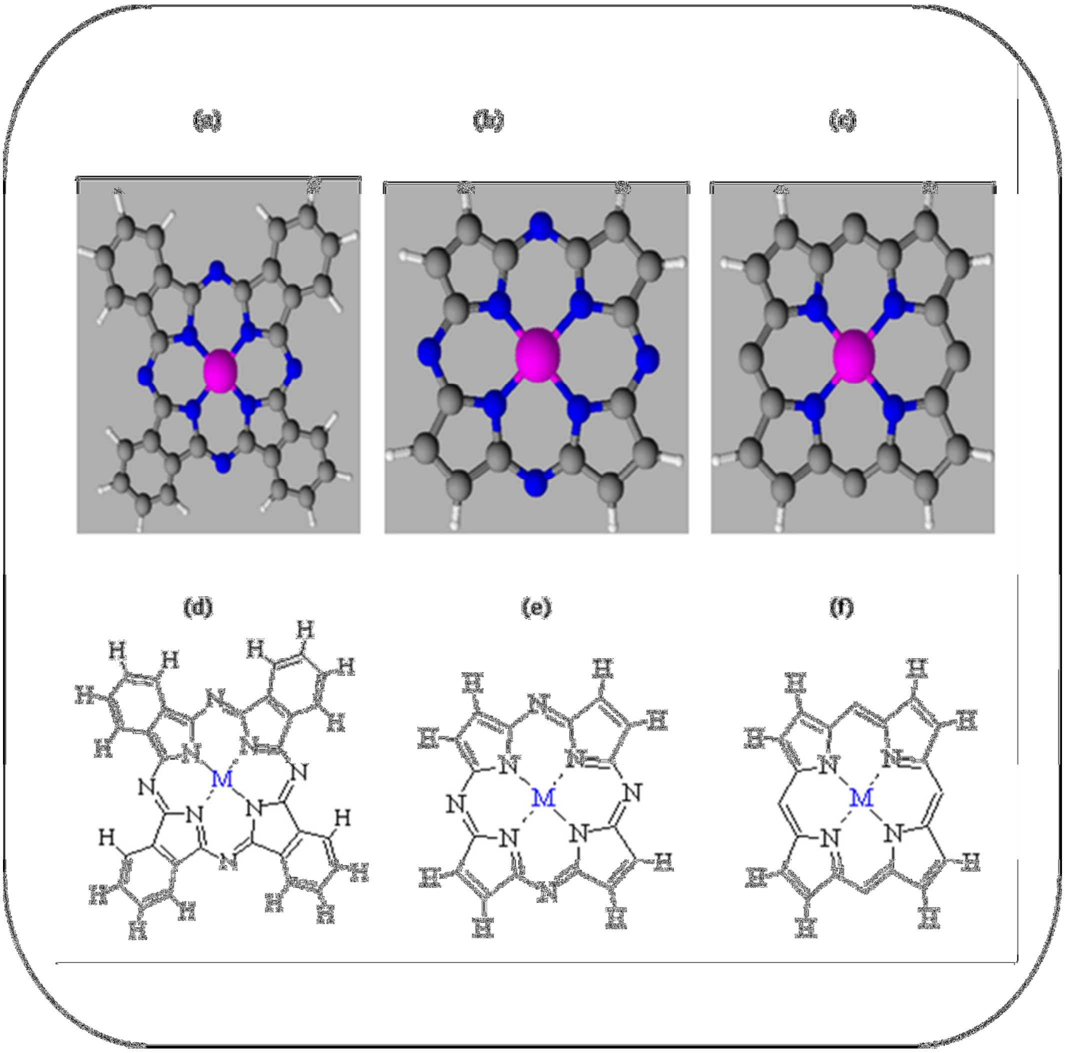

Figure 2.13: Macrocycles of (a and d) phthalocyanine, (b and e) porphyrazine and (c and f) Porphyrins (152).

2.5.1 Metallopyrazino porphyrazine

Metallotetrapyrazinoporphyrazines (MTPyzPzs) as shown in Figure 2.14 are aza-analogues of well-known phthalocyanine (Pc) macrocycles (153). They are symmetrical tetrapyrrollic macrocycles with a six membered heterocyclic ring. Kobayashi *et al* (154) found that the energy level of $1b_{1u}(\pi^*)$ orbital of H_2TPyzPz is lower than that of phthalocyanines. Kobayashi *et al* (154) also reported that protonation occurs on the nitrogen atoms of a pyrazine ring in CoTPyzPz and FeTPyzPz in concentrated H_2SO_4. Petrik *et al* (155) reported that in acidic medium, TPyzPz can exhibit various protonated forms depending on the strength of the acid. Villano *et al*(142) have shown that properties of TPyzPz are significantly influenced by the presence of the external N atoms. The π- delocalization on MTPyzPz enhances the possibility π-π interactions.

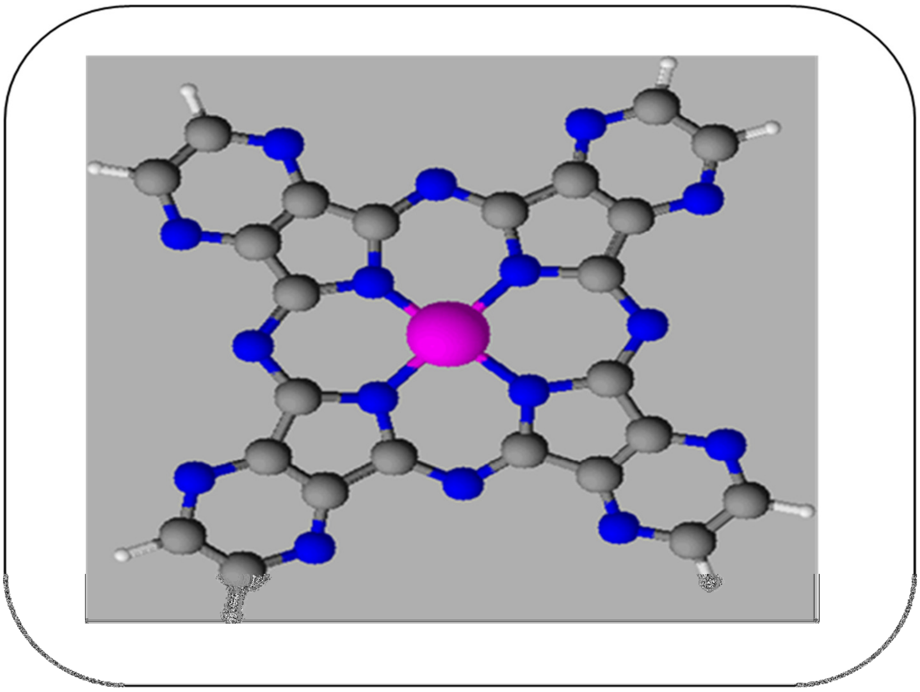

Figure 2.14: Ball and stick model of metallopyrazinoporphyrazine

Linstead macrocyclization of cyclic maleonitriles is the preferred method of synthesising MTPyzPz (156). The synthetic scheme of MTPyzPz is shown in Scheme 1.

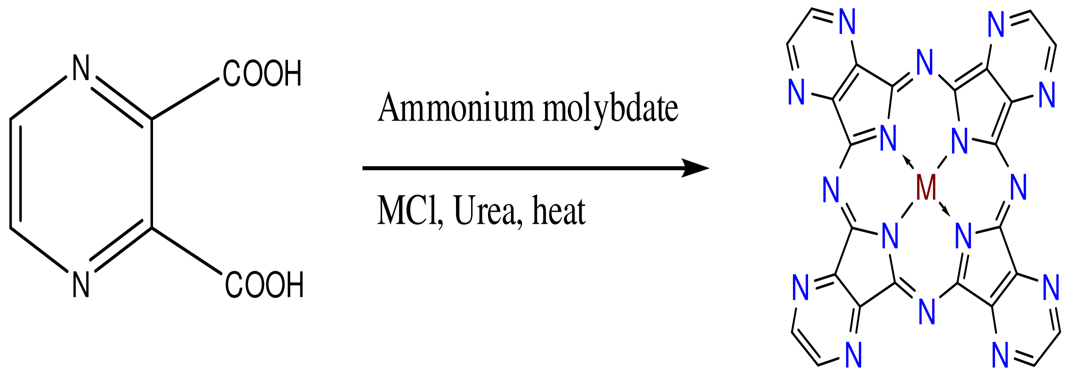

Scheme 1: Synthetic method of metallopyrazinoporphyrazine (156).

2.6 Electrochemistry of Supercapacitors

Electrochemistry is the study of what happens at the electrode-electrolyte interface and the processes involved at the interface of phases that conduct ions or conducts charges (157). Electrochemistry interrogates the interrelationship between chemical changes and electrical phenomena. Electrochemistry is applied in natural and life sciences (24). Electrochemistry has been utilized a lot in energy generation and storage concepts since the discovery of the Volta pile by Alessandro Volta. The measurement of potential, current and time in electrochemical systems provides valuable information on what happens at the interface of the electrode (phase that involves the conduction of charges) and the electrolyte (phase that involves the conduction of ions) (25). Electrochemistry has been widely used in the area of Batteries and supercapacitors. Electroanalytical tools (158) used in electrochemistry are cyclic voltammetry (CV), differential pulse voltammetry (DPV), linear sweep voltammetry (LSV), square wave voltammetry (SWV), chronoamperometry (CA), chronopotentiometry (CP) and chronocoulometry (CC). The work described in this dissertation involves the usage of cyclic voltammetry and chrono potentiometry (galvanostatic) which is also called galvanostatic charge-discharge.

2.6.1 Cyclic Voltammetry

Cyclic voltammetry is an electroanalytical technique that is used to provide qualitative information about electrochemical processes that happen at the electrode-electrolyte interface (24, 159). This method among others is used for the quick screening of materials to identify their potential as electrode material for energy storage (25). The relationship between the measured current and the applied potential describe the nature of the process that happens at the interface of the electrode and the electrolyte. In supercapacitors, this method is hugely valuable as it outlines how the current is dependent on voltage. From the acquired measurements, a reaction or process can be described as faradaic or non-faradaic. To acquire data, a potentiostat connected to three-electrode system (Figure 2.15) or two-electrode system (Figure 2.16) is used. A three-electrode system consists of a working electrode (WE), counter electrode (CE) and reference electrode (RE). The working electrode is an electrode made of inert materials on which the electrochemical reaction to be studied occurs. Working electrodes are usually made from gold, platinum and carbon materials. Reference electrode is an electrode which has stable and known electrode potential and is usually used as a point of reference in the determination of the potential of a WE. RE such as silver/silver chloride and saturated calomel electrode are commonly used in a three electrode system. Counter electrode is an electrode that completes an electrochemical circuit cell and is usually made of inert materials such as platinum, gold and glassy carbon.

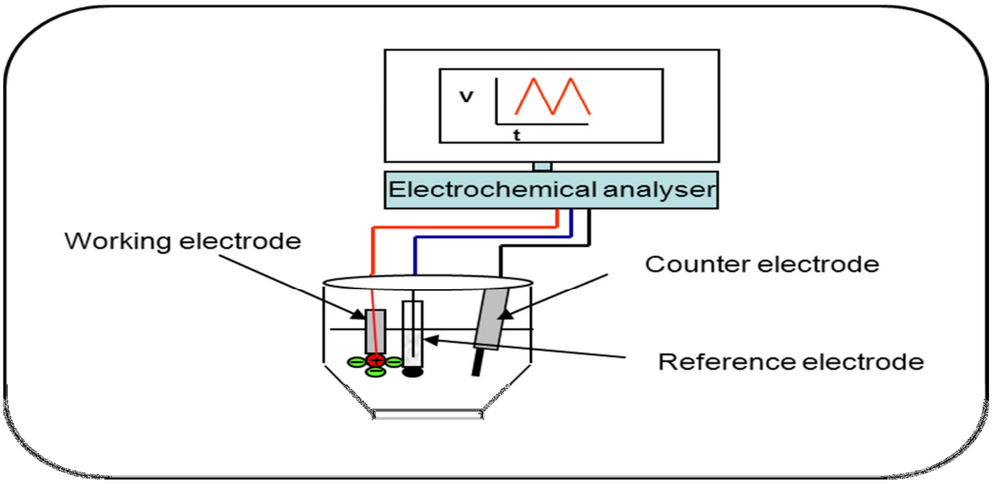

Figure 2.15: Schematic diagram of the three electrode system connected to an electrochemical analyser.

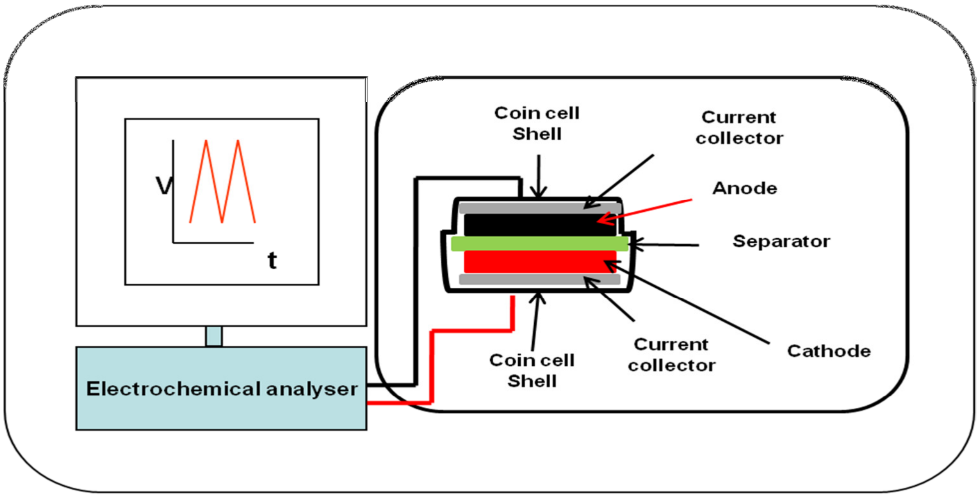

Figure 2.16: Schematic diagram of the two-electrode system connected to an electrochemical analyser.

A counter electrode with a higher surface area to WE is usually used to make it non-contributory to the kinetics of electrochemical processes in a cell.

Typical cyclic voltammograms of electrochemical double layer and pseudocapacitive behaviour of electrode are shown in Figure 2.17. The cyclic voltammograms of the ideal electric double layer capacitance are rectangular in shape (25, 160). This outlines that the charge storage is purely double layer capacitance which is due to non-faradaic processes (28). One prominent observation from this kind of behaviour is that applied current is independent of applied voltage (25). The reverse scan of an ideal electric double layer material is a mirror image of the forward scan.

A parallelogram shape as shown in Figure 2.17 indicates that there is resistance to the transfer of charges between an electrode and the electrolyte. Electrode materials that exhibit faradaic processes give cyclic voltammogram that deviate from a rectangular shape. The charge accumulated on the capacitor is dependent on the applied potential. For pseudocapacitors, the cyclic voltammograms have redox peaks that show the involvement of faradaic reactions (161). Cyclic Voltammetry is a powerful analytical tool that provides information on the thermodynamics of redox processes, kinetics of heterogeneous electron transfer reactions and adsorption processes (25). From the cyclic voltammograms, one can then distinguish which storage mechanism is utilized by a particular electrode material. The electron transfer processes can be labelled reversible, irreversible or quasi-reversible and Table 2.3 gives summary of the diagnostic criteria for evaluating these processes.

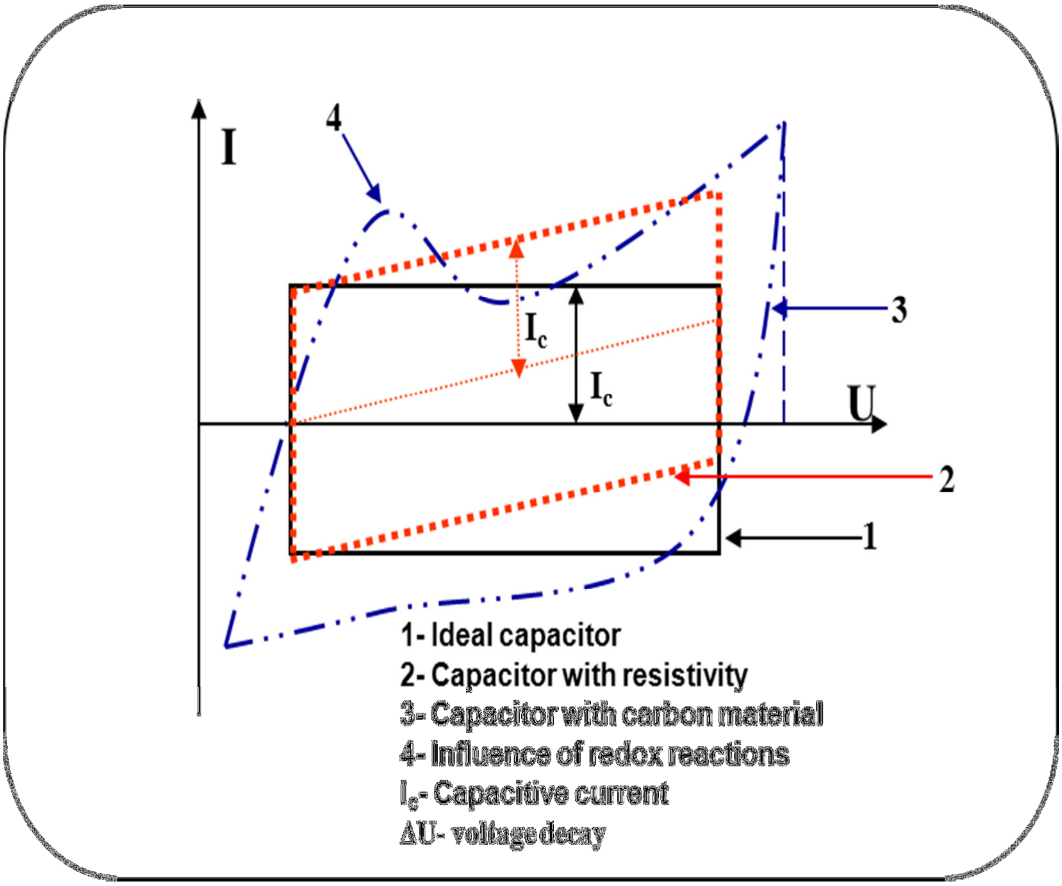

Figure 2.17: Typical cyclic voltammograms of different capacitive electrodes (162).

Specific capacitance can be calculated from the cyclic voltammograms using the Equation 2.13 (163):

$$\frac{\quad}{\quad} \qquad (2.13)$$

where *i* is the current (A), is the scan rate (V.s^{-1}) and m is the mass of active electrode (g).

Table 2.3: The diagnostic criteria for the reversible, irreversible and quasi-reversible cyclic voltammetric processes (25, 28, 164, 165).

Parameter	Cyclic Voltammetry Process		
	Reversible	Irreversible	Quasi-reversible
E_p	Independent of	Shifts cathodically by 30/αn mV for a 10-fold increase in V	Shifts with
E_{pc}-E_{pa}	~59/n mV at 25°C ΔE independent of but slightly increase with due to solution increase	Not applicable	$>\frac{59}{n}mV$ ΔE increases as increases
$\frac{i_p}{v^{1/2}}$	Constant (linear plot)	Constant	Virtually independent of (non-linear plot)
$\frac{i_{pa}}{i_{pc}}$	Equals 1	No current on the reverse side	Equals 1 only for α = 0.5

2.6.2 Chronopotentiometry (Galvanostatic charge-discharge)

Chronopotentiometry is an electroanalytical technique that measures the potential of the working electrode against a reference electrode as a function of time at a constant current during electrode polarization (166). This technique was used extensively in applications ranging from analysis to measurement of kinetics, adsorption, and transport properties (166). Chronopotentiometry is classified into four controlled current techniques depending on the excitation criteria namely (163): constant current, linearly increasing current, current reversal and cyclic chronopotentiometry.

Figure 2.18(a) shows typical discharge profiles of a battery, an ideal capacitor and EC. These devices exhibit different discharge profiles when current is applied. Battery takes the longest to discharge while an ideal capacitor discharges very fast. Figure 2.18(b), curve ii shows charge-discharge (c-d) profiles of an ideal supercapacitor which are a mirror image of each other. Figure 2.18(a) illustrates that the relationship between potential and time for the EDLC capacitor is linear. For pseudocapacitors, the relationship between measured voltage and time is non-linear (25), and the charge-discharge curves are not mirror images of each other. The charge-discharge curves of pseudocapacitive material have at least one hump to depict the redox activity of the material as shown by curve i in Figure 2.18(b). Curve iii in Figure 2.18(b) shows an ohmic potential (IR) drop that depicts the uncompensated resistance due to either an electrolyte or electrode.

Varying the current density gives information about the ability of the electrode material to retain capacitance and its power performance. The power of the electrode material will be considerably increased when charge-discharge measurements are done at higher current density and the electrode is stable. The following equation is used to calculate gravimetric specific capacitance (C_s) (162, 163) in three electrode system.

- —— (2.14)

where, i is the discharge current (A), Δt is the discharge time (s), m is the active mass of the electrode (g) and ΔE is the potential difference (V).

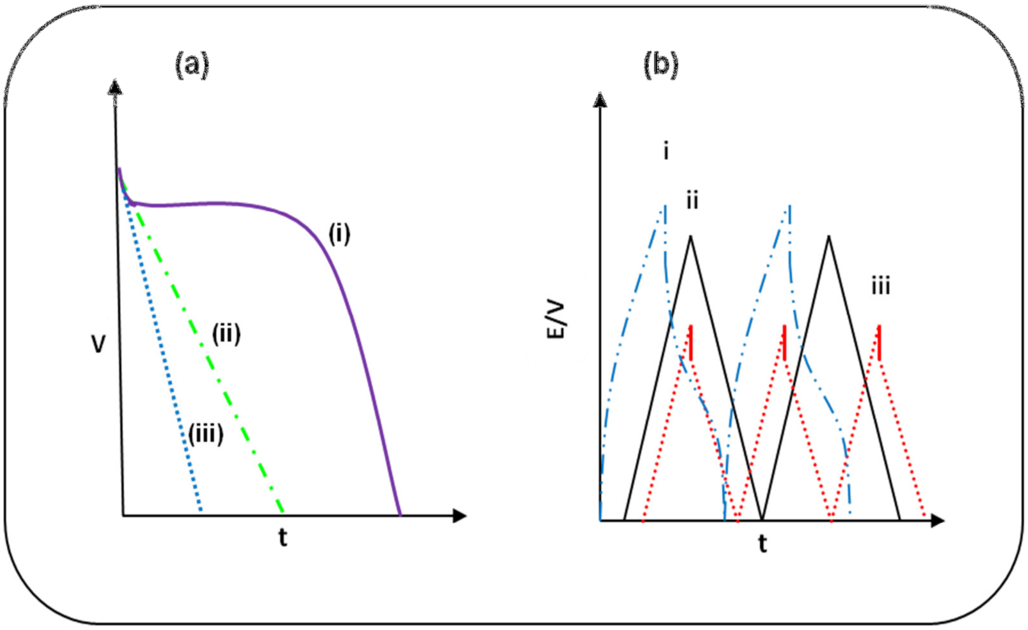

Figure 2.18: (a) Typical charge-discharge curves of a (i) battery, (ii) EC and (iii) Capacitor (b) typical (i) pseudocapacitive, (ii) EDLC and (iii) EDLC with iR drop charge-discharge curves (25).

Specific capacitance can also be expressed in terms of volume with units F.cm^{-3} using the following equation:

—— (2.15)

where, i, Δt, ΔE are as outlined above and V is the volume of the electrode (cm^3).

Specific capacitance can also be expressed per unit area of the electrode material by the equation:

—— (2.16)

where, A is a unit area of the electrode material (cm^2).

The columbic efficiency “*η*” is a measure of the efficiency with which charge is transferred in a system facilitating an electrochemical reaction. The energy deliverable efficiency is calculated by the equation(16):

— (2.17)

where t_d is the discharge time and t_c is the charging time.

One important aspect of supercapacitors is that they must have longer cycle life. The stability of the supercapacitors must be in the order of thousands of cycles. For a two-electrode system gravimetric capacitance is calculated by the equation (167-169):

— ——— (2.18)

where *-dv/dt* is the slope of the discharge curve, whereas m is the total mass of active material in a positive and negative electrode. Kötz and Carlen (32) reported that the total capacitance of a three electrode system is four times the total capacitance of a two electrode system.

2.6.3 Electrochemical Impedance spectroscopy

Electrochemical impedance spectroscopy (EIS) is one of the analytical tools frequently used to analyse the dynamic behaviour of supercapacitors. EIS has been used in understanding electrochemical systems (149), including those involved in corrosion, electrodeposition (170, 171), batteries (172) and fuel cells (129). Impedance is measured by applying a small sinusoidal AC voltage (between 2V and 10 V) and measuring a sinusoidal current response (173). The impedance of a system can be measured using various techniques (27):

- Ac bridges
- Lissajous curves
- Phase sensitive detection
- Fast Fourier transform
- Frequency response analysis.

For frequency response modulation the in-phase current response gives the real (resistive) component of the impedance while the out-of-phase current response gives the imaginary (capacitive) component (164). When AC voltage (V) is applied to a capacitor C (Figure 2.19), instantaneous charge (q) on the capacitor will be given by the formula (164):

(2.19)

The corresponding charging current will be

— (2.20)

where t is time, ω is the angular frequency, and I is the charging current. The impedance behaviour of a fast charge transfer reaction under diffusion control at a planar electrode is shown on the Complex impedance plane (Figure 2.20). R_s is the solution resistance that exists between the working electrode surface and reference electrode. R_f or R_{ct} is charge transfer resistance. The diffusional process happening in the reaction is represented by Warburg impedance element ω. ESR is the equivalent series resistance, and it comprises of solution resistance, resistance within the porous layer and contact resistance between current collector and an electrode. EDR is the equivalent distributed resistance in the Warburg region when the Warburg has a slope of 45°.

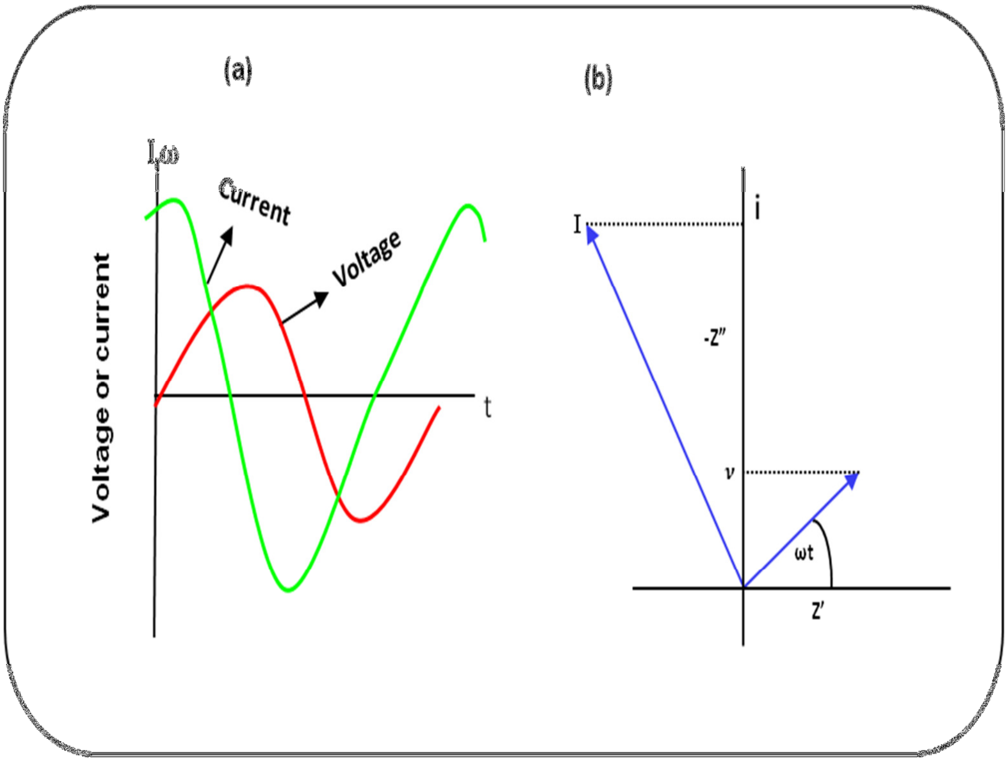

Figure 2.19:(a) Two graphs showing a current response curve from an applied sinusoidal voltage curve. (b) Vector representation of real and imaginary impedance (24).

For an ideal capacitor the impedance plane plot is parallel to the imaginary axis while that of EDLC, at high frequency it makes a 45° angle while at low frequency is nearly parallel to the imaginary axis of the complex plane impedance plot. Randles equivalent circuit of a simple charge transfer reaction which involves diffusion is presented in Figure 2.21.

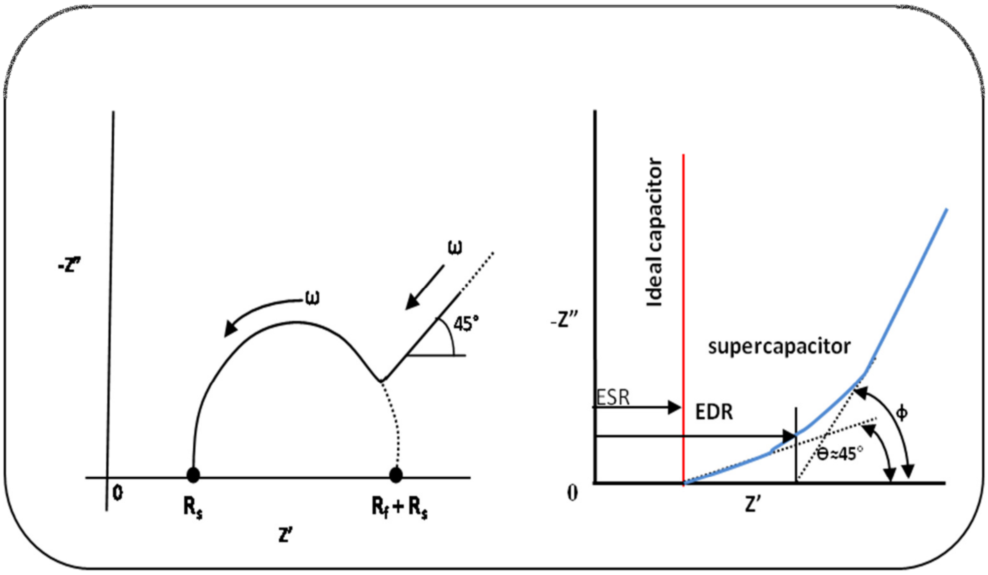

Figure 2.20: Complex-plane impedance (Nyquist) plot of diffusion controlled faradaic process and complex plane of ideal and EDLC (25, 129, 164).

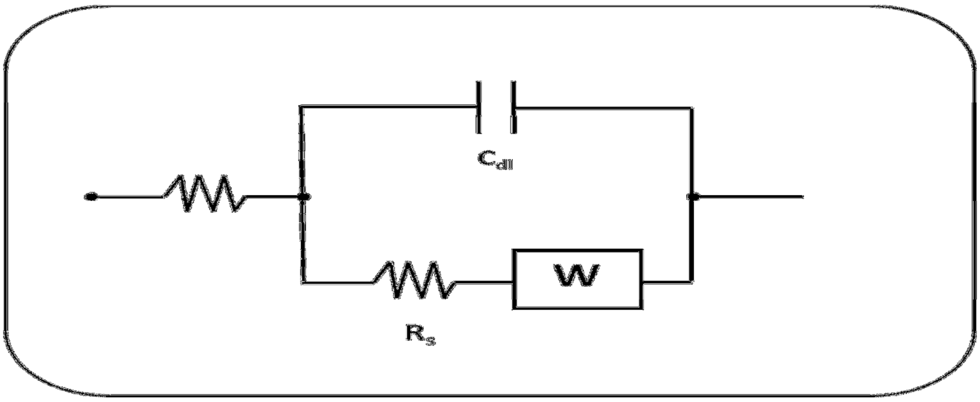

Figure 2.21: Randles equivalent circuit of fast charge transfer reaction that involves diffusion (129).

The impedance plot can be divided into two or more regions in relation to frequency. We have high and low frequency and the area where these two meet is called knee frequency.

From the Randles circuit the impedance of the capacitance is given by the following equation (174):

(2.21)

where, i = - , ω is the angular frequency and C is the capacitance

Impedance of the CPE can be expressed by (174):

(2.22)

where, T_{CPE} is the capacitance when $\alpha_{CPE} = 1$ and α_{CPE} is the constant phase exponent (0≤ α_{CPE} ≤1. When $\alpha_{CPE} = 0$, CPE becomes a resistor.

At low frequency the maximum specific capacitance is given by the equation (115):

(2.23)

where, Z” is the imaginary part of the impedance, f the frequency and C is the capacitance.

Data from impedance can be presented in several ways to show the relationship between frequency and impedance. Amongst the methods of data presentation we have Nyquist and bode plots. Nyquist plot (Figure 2.20) is the complex-plane impedance and admittance plot.

In bode plot (Figure 2.22), when the phase angle is ±90, the phenomenon depicts an ideal capacitor. When ϕ = 0 then the material becomes a pure resistor.

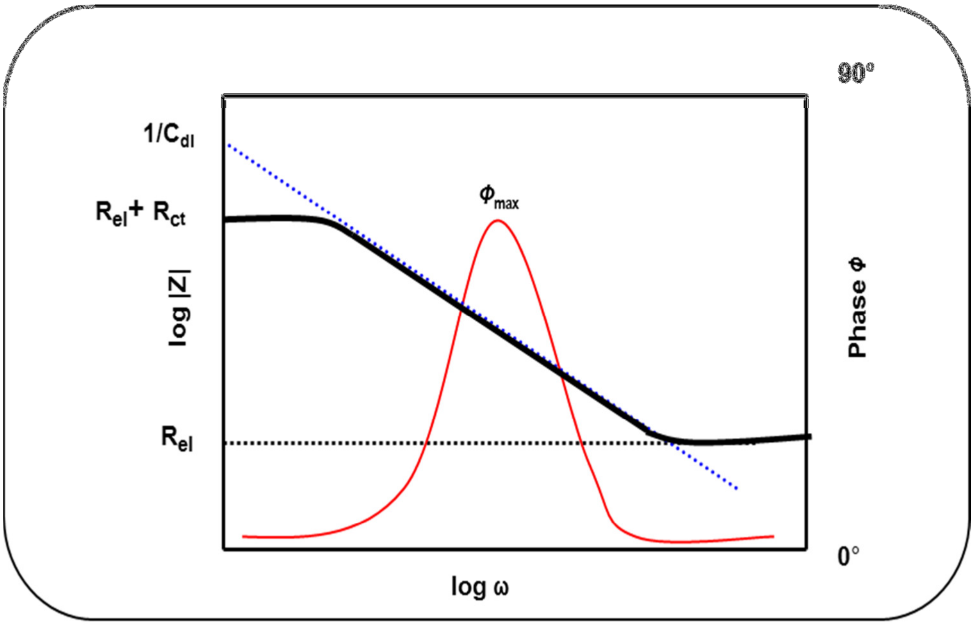

Figure 2.22: Typical Bode plot of an electrode.

2.7 Microscopic, spectroscopic and thermal techniques of electrode materials

Several techniques have been utilized to acquire physicochemical properties of the electrode materials. The properties of the electrode surface are very significant since they affect what happens at the electrode-electrolyte interface. Material surface composition can be correlated to the electronic structure and electrocatalytic activity of the material (175, 176). Some of the microscopic and spectroscopic techniques used in this study are scanning electron microscope (SEM), Fourier transform infrared spectroscopy (FT-IR), ultra-violet absorption spectroscopy UV-Vis, energy dispersive X-ray spectroscopy (EDX), powder X-ray diffraction spectroscopy (PXRD) and thermogravimetry(TG). The abovementioned techniques are briefly explained below.

2.7.1 Scanning electron microscopy.

SEM is one of the powerful characterisation tools used in nano materials research today. SEM is an imaging technique that uses backscattered and/or secondary electrons from the interaction of electron beam and specimen surface (Figure 2.23) to determine surface characteristics (morphology and topography features) and chemical composition of the specimen (177, 178).

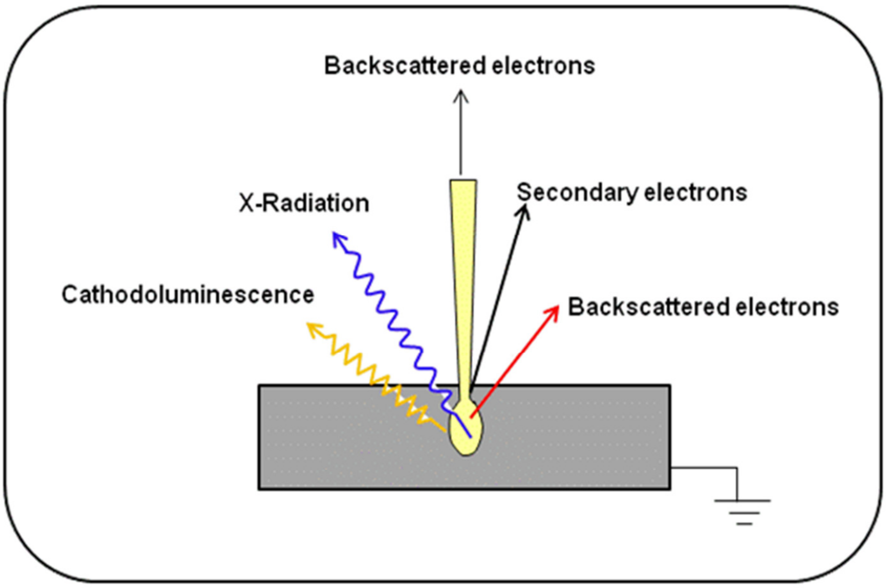

Figure 2.23: Schematic representation of the types of emissions from the interaction of the electron beam and specimen surface (178).

The interaction of emitted characteristic X-rays and from the electron beam's interaction with the specimen surface is used to identify material chemical composition. SEM micrographs can depict material characteristics like entanglement, porosity, vertically alignment and agglomeration of nanocarbons and the other electrode materials.

2.7.2 Energy dispersive X-ray spectroscopy

Energy dispersive X-ray spectroscopy (EDX), sometimes referred to as EDS or EDAX is an analytical tool used to determine elemental composition in material specimen. A characteristic photon radiation is produced after an inelastic scattering of beam electrons when an outer shell electron occupies an inner core shell vacancy left by the ejection of the inner shell electron (Figure 2.24) (178).

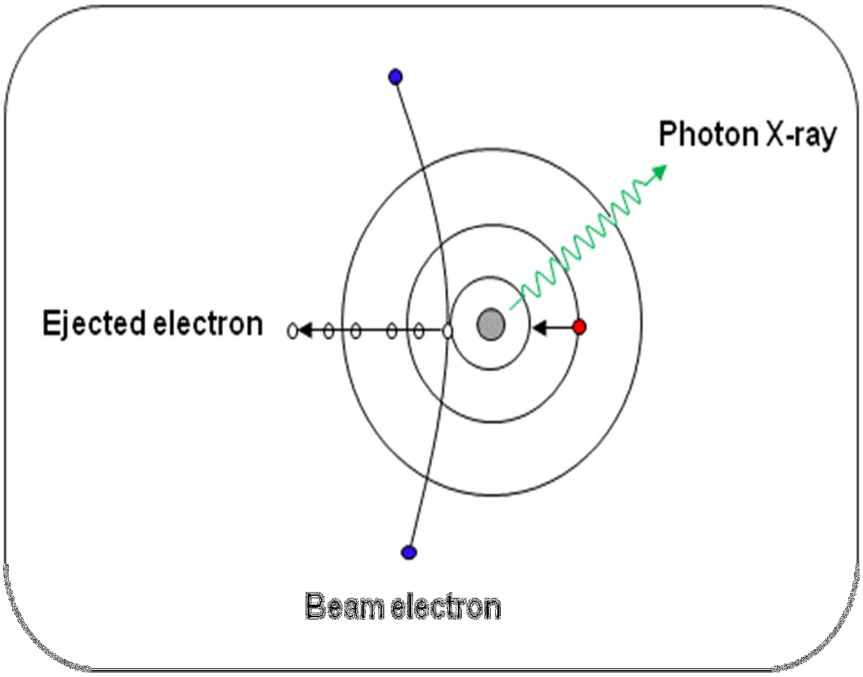

Figure 2.24: Schematic representation of the photon X-ray emission process (178).

The emitted photon X-ray radiation depends on the kind of atom involved (177). Each element exhibit a characteristic radiation peaks. Thus EDX is a valuable tool for elemental composition determination. A spectrum with elemental peaks is generated from the EDX data acquired. This technique is mostly used as attachments to SEM and TEM instrumentation.

2.7.3 Infrared Spectroscopy.

Infra-red spectroscopy is a qualitative analytical tool used for organic and inorganic compounds identification. An infra-red spectrum is obtained when an infra-red radiation of a continuous wavelength pass through a sample is absorbed by the vibrating molecules at a specific wavelength giving rise to an absorption peak at the same wavelength (179). The various molecular vibrations in a sample produce vast number of absorptions which are uniquely characteristic of the functional groups of that molecule. FT-IR spectrometers are highly sensitive instruments that have good resolutions (158). Spectral data acquisition is in the order of seconds. This method has been used in the confirmation of the carbon nanotube functionalization (180-182). Again the functional groups in porphyrazine molecules have been confirmed by this technique (143, 153).

2.7.4 Powder X-ray diffraction spectroscopy

Powder X-ray diffraction is a technique mostly used to characterize crystalline powder materials. This technique is also useful for unit cell dimensions, sample purity and crystallinity determination (177-179). This technique is derived from Bragg's law (179) where diffraction occurs when a condition for a constructive interference (from incident beams) from planes with spacing d is satisfied. XRD data is recorded as a plot of x-ray intensity versus a diffraction angle, 2θ. This technique has been widely used to determine whether the energy materials used for supercapacitors are amorphous or crystalline (64, 183).

2.7.5 Thermogravimetry

Thermogravimetry is a method used for the determination of the material thermal's stability and composition. In TG changes to a known amount of a material weight is recorded as a function of temperature or time under inert or reactive atmosphere. This technique has been used to determine the quality of the MWCNTs. Mirershadi *et al* found that the acid treatment of the MWCNTs enhances their thermal stability (184).

2.7.6 Other Characterisation techniques

UV-Vis technique was used to determine the molecular electronic transitions in materials such as porphyrazine. It has been observed that the splitting of the Q band in porphyrazine is associated with molecular symmetry.(142, 153)

2.8 References

1. Sharma P, Bhatti TS. A review on electrochemical double-layer capacitors. Energy Conversion and Management. 2010;51(12):2901-12.

2. Conway BE. Electrochemistry Encyclopedia. Electrochemical Supercapacitors: Their Nature, Function and Applications; 2003. Available from: http://electrochem.cwru.edu/encycl/art-c03-elchem-cap.htm

3. Pacaldi G. Volta:Science and culture in the Age of enlightment. 1 ed. New Jersey: Princeton University press; 2003.

4. Scrosati B. Technology: Charging towards the superbattery. Nature. 2011;473(7348):448-9.

5. Zalk van M. In between matters, interfaces in complex oxides. Enschede; 2009.

6. Wimshurst J. A new form of influence-machine. Proceedings of the Physical Society of London. 1892;12(1):403-6.

7. Serrano E, Rus G, García-Martínez J. Nanotechnology for sustainable energy. Renewable and Sustainable Energy Reviews. 2009;13(9):2373-84.

8. Townsend JS, Tizard HT. The Motion of Electrons in Gases. Proceedings of the Royal Society of London Series A, Containing Papers of a Mathematical and Physical Character; 1913. The Royal Society; 1913. p. 336-47.

9. Sommerfeld A. Concerning the Shape of the Compton Lines (From a Letter to A. H. Compton). Physical Review. 1936;50(1):38-40.

10. Schrodinger E. An Undulatory Theory of the Mechanics of Atoms and Molecules. Physical Review. 1926;28(6):1049-70.

11. Heisenberg W. Z Phys. 1927;43:172.

12. Kimble GA, Wertheimer M. Portraits of Pioneers in Psychology. Taylor and Francis; 2000.

13. Becker HI, inventor Low voltage electrolytic capacitor. United States. 1957.

14. Boos DL, inventor Electrolytic capacitor having carbon paste electrodes. United states patent 3536963. 1970.

15. Bagotsky V. Fuel cells, batteries, and the development of electrochemistry. Journal of Solid State Electrochemistry. 2011;15(7):1559-62.

16. Endo M, Maeda T, Takeda T, Kim YJ, Koshiba K, Hara H, et al. Capacitance and Pore-Size Distribution in Aqueous and Nonaqueous Electrolytes Using Various Activated Carbon Electrodes. Journal of The Electrochemical Society. 2001;148(8):A910-A4.

17. Obreja VVN. On the performance of supercapacitors with electrodes based on carbon nanotubes and carbon activated material-A review. Physica E: Low-Dimensional Systems and Nanostructures. 2008;40(7):2596-605.

18. Obreja VVN, editor. On the performance of commercial supercapacitors as storage devices for renewable electrical energy sources. International conference on renewable energies and power quality; 2007; Sevilla.

19. Gouy G. Annals of Physics. 1917;7:129.

20. Belhachemi F, Rael S, Davat B, editors. A physical based model of power electric double-layer supercapacitors. Industry Applications Conference, 2000 Conference Record of the 2000 IEEE; 2000 2000.

21. Zhang LL, Zhao XS. Carbon-based materials as supercapacitor electrodes. Chemical Society Reviews. 2009;38(9):2520-31.

22. Torrie GM, Valleau JP. Electrical double layers. 4. Limitations of the Gouy-Chapman theory. The Journal of Physical Chemistry. 1982;86(16):3251-7.

23. Stern O. Z Eleckrochem. 1924;30:508.

24. Wang J. Analytical electrochemistry. 3 ed. New York: John Wiley and sons Inc; 2006.

25. Conway BE. Electrochemical supercapacitors: scientific fundamentals and technological applications. Plenum Press; 1999.

26. Conway BE, Gileadi E. Kinetic theory of pseudo-capacitance and electrode reactions at appreciable surface coverage. Transactions of the Faraday Society. 1962;58:2493-509.

27. Bockris JOM, Conway BE, White RE. Modern Aspects of Electrochemistry. Kluwer Academic/Plenum Publishers; 1999.

28. Conway BE, Birss V, Wojtowicz J. The role and utilization of pseudocapacitance for energy storage by supercapacitors. Journal of Power Sources. 1997;66(1-2):1-14.

29. Conway BE. Electrochemical surface science: The study of monolayers of ad-atoms and solvent molecules at charged metal interfaces. Progress in Surface Science. 1984;16(1):1-137.

30. Arbizzani C, Biso M, Cericola D, Lazzari M, Soavi F, Mastragostino M. Safe, high-energy supercapacitors based on solvent-free ionic liquid electrolytes. Journal of Power Sources. 2008;185(2):1575-9.

31. Peng C, Zhang S, Jewell D, Chen GZ. Carbon nanotube and conducting polymer composites for supercapacitors. Progress in Natural Science. 2008;18(7):777-88.

32. Kötz R, Carlen M. Principles and applications of electrochemical capacitors. Electrochimica Acta. 2000;45(15-16):2483-98.

33. Inagaki M, Konno H, Tanaike O. Carbon materials for electrochemical capacitors. Journal of Power Sources. 2010;195(24):7880-903.

34. Hall PJ, Mirzaeian M, Fletcher SI, Sillars FB, Rennie AJR, Shitta-Bey GO, et al. Energy storage in electrochemical capacitors: designing functional materials to improve performance. Energy & Environmental Science. 2010;3(9):1238-51.

35. Shi H. Activated carbons and double layer capacitance. Electrochimica Acta. 1996;41(10):1633-9.

36. Qu D, Shi H. Studies of activated carbons used in double-layer capacitors. Journal of Power Sources. 1998;74(1):99-107.

37. Frackowiak E, Béguin F. Carbon materials for the electrochemical storage of energy in capacitors. Carbon. 2001;39(6):937-50.

38. Hu Z, Srinivasan MP. Mesoporous high-surface-area activated carbon. Microporous and Mesoporous Materials. 2001;43(3):267-75.

39. Salitra G, Soffer A, Eliad L, Cohen Y, Aurbach D. Carbon Electrodes for Double-Layer Capacitors I. Relations Between Ion and Pore Dimensions. Journal of The Electrochemical Society. 2000;147(7):2486-93.

40. Raymundo-Piñero E, Kierzek K, Machnikowski J, Béguin F. Relationship between the nanoporous texture of activated carbons and their capacitance properties in different electrolytes. Carbon. 2006;44(12):2498-507.

41. Chmiola J, Yushin G, Dash R, Gogotsi Y. Effect of pore size and surface area of carbide derived carbons on specific capacitance. Journal of Power Sources. 2006;158(1):765-72.

42. Largeot C, Portet C, Chmiola J, Taberna P-L, Gogotsi Y, Simon P. Relation between the Ion Size and Pore Size for an Electric Double-Layer Capacitor. Journal of the American Chemical Society. 2008;130(9):2730-1.

43. Merino C, Soto P, Vilaplana-Ortego E, Gomez de Salazar JM, Pico F, Rojo JM. Carbon nanofibres and activated carbon nanofibres as electrodes in supercapacitors. Carbon. 2005;43(3):551-7.

44. Tao XY, Zhang XB, Zhang L, Cheng JP, Liu F, Luo JH, et al. Synthesis of multi-branched porous carbon nanofibers and their application in electrochemical double-layer capacitors. Carbon. 2006;44(8):1425-8.

45. Sevilla M, Álvarez S, Centeno TA, Fuertes AB, Stoeckli F. Performance of templated mesoporous carbons in supercapacitors. Electrochimica Acta. 2007;52(9):3207-15.

46. Ania CO, Khomenko V, Raymundo-Piñero E, Parra JB, Béguin F. The Large Electrochemical Capacitance of Microporous Doped Carbon Obtained by Using a Zeolite Template. Advanced Functional Materials. 2007;17(11):1828-36.

47. Zhao XS, Su F, Yan Q, Guo W, Bao XY, Lu L, et al. Templating methods for preparation of porous structures. Journal of Materials Chemistry. 2006;16(7):637-48.

48. Pekala RW. Organic aerogels from the polycondensation of resorcinol with formaldehyde. Journal of Materials Science. 1989;24(9):3221-7.

49. Pekala RW, Alviso CT, Kong FM, Hulsey SS. Aerogels derived from multifunctional organic monomers. Journal of Non-Crystalline Solids. 1992;145(C):90-8.

50. Pekala RW, Farmer JC, Alviso CT, Tran TD, Mayer ST, Miller JM, et al. Carbon aerogels for electrochemical applications. Journal of Non-Crystalline Solids. 1998;225(0):74-80.

51. Bordjiba T, Mohamedi M, Dao LH. New Class of Carbon-Nanotube Aerogel Electrodes for Electrochemical Power Sources. Advanced Materials. 2008;20(4):815-9.

52. Wang J, Zhang SQ, Guo YZ, Shen J, Attia SM, Zhou B, et al. Morphological Effects on the Electrical and Electrochemical Properties of Carbon Aerogels. Journal of The Electrochemical Society. 2001;148(6):D75-D7.

53. Escribano S, Berthon, S., Ginoux, J.L., Archard, P., editor. Characterization of carbon aerogels. Extended abstracts. Eurocarbon '98 Strasbourg; 1998; France.

54. Zheng JP, Cygan PJ, Jow TR. Hydrous Ruthenium Oxide as an Electrode Material for Electrochemical Capacitors. Journal of The Electrochemical Society. 1995;142(8):2699-703.

55. Kim I-H, Kim J-H, Lee Y-H, Kim K-B. Synthesis and Characterization of Electrochemically Prepared Ruthenium Oxide on Carbon Nanotube Film Substrate for Supercapacitor Applications. Journal of The Electrochemical Society. 2005;152(11):A2170-A8.

56. Hu C-C, Chen W-C. Effects of substrates on the capacitive performance of $RuO_x \cdot nH_2O$ and activated carbon-RuO_x electrodes for supercapacitors. Electrochimica Acta. 2004;49(21):3469-77.

57. Hu C-C, Chen W-C, Chang K-H. How to Achieve Maximum Utilization of Hydrous Ruthenium Oxide for Supercapacitors. Journal of The Electrochemical Society. 2004;151(2):A281-A90.

58. Srinivasan V, Weidner JW. Capacitance studies of cobalt oxide films formed via electrochemical precipitation. Journal of Power Sources. 2002;108(1-2):15-20.

59. Zheng YZ, Ding HY, Zhang Ml. Preparation and electrochemical properties of nickel oxide as a supercapacitor electrode material. Materials Research Bulletin. 2009;44(2):403-7.

60. Wang S-Y, Ho K-C, Kuo S-L, Wu N-L. Investigation on Capacitance Mechanisms of Fe3O4 Electrochemical Capacitors. Journal of The Electrochemical Society. 2006;153(1):A75-A80.

61. Prasad KR, Miura N. Electrochemical synthesis and characterization of nanostructured tin oxide for electrochemical redox supercapacitors. Electrochemistry Communications. 2004;6(8):849-52.

62. Kim I-H, Kim J-H, Cho B-W, Lee Y-H, Kim K-B. Synthesis and Electrochemical Characterization of Vanadium Oxide on Carbon Nanotube Film Substrate for Pseudocapacitor Applications. Journal of The Electrochemical Society. 2006;153(6):A989-A96.

63. Wang Y, Yuan A, Wang X. Pseudocapacitive behaviors of nanostructured manganese dioxide/carbon nanotubes composite electrodes in mild aqueous electrolytes: effects of electrolytes and current collectors. Journal of Solid State Electrochemistry. 2008;12(9):1101-7.

64. Ragupathy P, Vasan HN, Munichandraiah N. Synthesis and Characterization of Nano-MnO_2 for Electrochemical Supercapacitor Studies. Journal of The Electrochemical Society. 2008;155(1):A34-A40.

65. Staiti P, Lufrano F. Study and optimisation of manganese oxide-based electrodes for electrochemical supercapacitors. Journal of Power Sources. 2009;187(1):284-9.

66. Gujar TP, Shinde VR, Lokhande CD, Han S-H. Electrosynthesis of Bi_2O_3 thin films and their use in electrochemical supercapacitors. Journal of Power Sources. 2006;161(2):1479-85.

67. Chang J, Lee W, Mane RS, Cho BW, Han S-H. Morphology-Dependent Electrochemical Supercapacitor Properties of Indium Oxide. Electrochemical and Solid-State Letters. 2008;11(1):A9-A11.

68. Chang B-Y, Park S-M. Electrochemical Impedance Spectroscopy. Annual Review of Analytical Chemistry. 2010;3(1):207-29.

69. Lokhande CD, Dubal DP, Joo O-S. Metal oxide thin film based supercapacitors. Current Applied Physics. 2011;11(3):255-70.

70. Mastragostino M, Arbizzani C, Soavi F. Polymer-based supercapacitors. Journal of Power Sources. 2001;97-98(0):812-5.

71. Gupta V, Miura N. High performance electrochemical supercapacitor from electrochemically synthesized nanostructured polyaniline. Materials Letters. 2006;60(12):1466-9.

72. Laforgue A, Simon P, Sarrazin C, Fauvarque J-Fo. Polythiophene-based supercapacitors. Journal of Power Sources. 1999;80(1-2):142-8.

73. Fan L-Z, Maier J. High-performance polypyrrole electrode materials for redox supercapacitors. Electrochemistry Communications. 2006;8(6):937-40.

74. Xu Y, Wang J, Sun W, Wang S. Capacitance properties of poly(3,4-ethylenedioxythiophene)/polypyrrole composites. Journal of Power Sources. 2006;159(1):370-3.

75. Gao HJ, Xue ZQ, Wu QD, Pang SJ. 2D fractal pattern in fullerene doped polymer. Solid State Communications. 1996;97(7):579-82.

76. Ago H, Petritsch K, Shaffer MSP, Windle AH, Friend RH. Composites of Carbon Nanotubes and Conjugated Polymers for Photovoltaic Devices. Advanced Materials. 1999;11(15):1281-5.

77. Arbizzani C, Mastragostino M, Meneghello L. Polymer-based redox supercapacitors: A comparative study. Electrochimica Acta. 1996;41(1):21-6.

78. Yuan CZ, Gao B, Shen LF, Yang SD, Hao L, Lu XJ, et al. Hierarchically structured carbon-based composites: Design, synthesis and their application in electrochemical capacitors. Nanoscale.3(2):529-45.

79. Agarwal P, Orazem ME, Garcia-Rubio LH. Measurement Models for Electrochemical Impedance Spectroscopy. Journal of The Electrochemical Society. 1992;139(7):1917-27.

80. Gao B, Hao L, Fu Q, Su L, Yuan C, Zhang X. Hydrothermal synthesis and electrochemical capacitance of RuO2·xH2O loaded on benzenesulfonic functionalized MWCNTs. Electrochimica Acta. 2010;55(11):3681-6.

81. Lin P, She Q, Hong B, Liu X, Shi Y, Shi Z, et al. The Nickel Oxide/CNT Composites with High Capacitance for Supercapacitor. Journal of The Electrochemical Society. 2010;157(7):A818-A23.

82. An H, Wang Y, Wang X, Zheng L, Wang X, Yi L, et al. Polypyrrole/carbon aerogel composite materials for supercapacitor. Journal of Power Sources. 2010;195(19):6964-9.

83. Li J, Gao F. Analysis of electrodes matching for asymmetric electrochemical capacitor. Journal of Power Sources. 2009;194(2):1184-93.

84. Ma S-B, Nam K-W, Yoon W-S, Yang X-Q, Ahn K-Y, Oh K-H, et al. A novel concept of hybrid capacitor based on manganese oxide materials. Electrochemistry Communications. 2007;9(12):2807-11.

85. Wang Y-g, Xia Y-y. A new concept hybrid electrochemical surpercapacitor: Carbon/$LiMn_2O_4$ aqueous system. Electrochemistry Communications. 2005;7(11):1138-42.

86. Park JH, Park OO. Hybrid electrochemical capacitors based on polyaniline and activated carbon electrodes. Journal of Power Sources. 2002;111(1):185-90.

87. Chen P-C, Shen G, Shi Y, Chen H, Zhou C. Preparation and Characterization of Flexible Asymmetric Supercapacitors Based on Transition-Metal-Oxide Nanowire/Single-Walled Carbon Nanotube Hybrid Thin-Film Electrodes. ACS Nano. 2010;4(8):4403-11.

88. Osaka T, Liu X, Nojima M, Momma T. An Electrochemical Double Layer Capacitor Using an Activated Carbon Electrode with Gel Electrolyte Binder. Journal of The Electrochemical Society. 1999;146(5):1724-9.

89. Iijima S. Helical microtubules of graphitic carbon. Nature. 1991;354(6348):56-8.

90. Iijima S, Ichihashi T. Single-shell carbon nanotubes of 1-nm diameter. Nature. 1993;363(6430):603-5.

91. Lu W, Qu L, Henry K, Dai L. High performance electrochemical capacitors from aligned carbon nanotube electrodes and ionic liquid electrolytes. Journal of Power Sources. 2009;189(2):1270-7.

92. Tans SJ, Verschueren ARM, Dekker C. Room-temperature transistor based on a single carbon nanotube. Nature. 1998;393(6680):49-52.

93. Niu C, Sichel EK, Hoch R, Moy D, Tennent H. High power electrochemical capacitors based on carbon nanotube electrodes. Applied Physics Letters. 1997;70(11):1480-2.

94. Ahn H-J, Sohn JI, Kim Y-S, Shim H-S, Kim WB, Seong T-Y. Electrochemical capacitors fabricated with carbon nanotubes grown within the pores of anodized aluminum oxide templates. Electrochemistry Communications. 2006;8(4):513-6.

95. Pan H, Li J, Feng Y. Carbon Nanotubes for Supercapacitor. Nanoscale Research Letters. 2010;5(3):654-68.

96. Kim Y-T, Ito Y, Tadai K, Mitani T, Kim U-S, Kim H-S, et al. Drastic change of electric double layer capacitance by surface functionalization of carbon nanotubes. Applied Physics Letters. 2005;87(23):234106-3.

97. Lee JY, An KH, Heo JK, Lee YH. Fabrication of Supercapacitor Electrodes Using Fluorinated Single-Walled Carbon Nanotubes. The Journal of Physical Chemistry B. 2003;107(34):8812-5.

98. Loh KP, Bao Q, Eda G, Chhowalla M. Graphene oxide as a chemically tunable platform for optical applications. Nat Chem. 2010;2(12):1015-24.

99. Xu B, Yue S, Sui Z, Zhang X, Hou S, Cao G, et al. What is the choice for supercapacitors: graphene or graphene oxide? Energy & Environmental Science. 2011;4(8):2826-30.

100. Dreyer DR, Park S, Bielawski CW, Ruoff RS. The chemistry of graphene oxide. Chemical Society Reviews. 2010;39(1):228-40.

101. Lerf A, He H, Forster M, Klinowski J. Structure of Graphite Oxide Revisited. The Journal of Physical Chemistry B. 1998;102(23):4477-82.

102. He H, Klinowski J, Forster M, Lerf A. A new structural model for graphite oxide. Chemical Physics Letters. 1998;287(1-2):53-6.

103. Lee DW, De Los Santos V L, Seo JW, Felix LL, Bustamante D A, Cole JM, et al. The Structure of Graphite Oxide: Investigation of Its Surface Chemical Groups. The Journal of Physical Chemistry B. 2010;114(17):5723-8.

104. Compton OC, Nguyen ST. Graphene Oxide, Highly Reduced Graphene Oxide, and Graphene: Versatile Building Blocks for Carbon-Based Materials. Small. 2010;6(6):711-23.

105. Chen S, Zhu J, Wu X, Han Q, Wang X. Graphene Oxide-MnO_2 Nanocomposites for Supercapacitors. ACS Nano. 2010;4(5):2822-30.

106. Xu J, Wang K, Zu S-Z, Han B-H, Wei Z. Hierarchical Nanocomposites of Polyaniline Nanowire Arrays on Graphene Oxide Sheets with Synergistic Effect for Energy Storage. ACS Nano. 2010;4(9):5019-26.

107. Li J, Xie H. Synthesis of graphene oxide/polypyrrole nanowire composites for supercapacitors. Materials Letters. 2012;78(0):106-9.

108. Chen Y, Zhang X, Ma Y. Synthesis of Reduced Graphene Oxide and Reduced Graphene Oxide/Ruthenium Oxide for Supercapacitors. Meeting Abstracts; 2011. ECS; 2011. p. 562.

109. Taylor SR, McLennan SM. The geochemical evolution of the continental crust. Rev Geophys. 1995;33(2):241-65.

110. Beaudrouet E, Le Gal La Salle A, Guyomard D. Nanostructured manganese dioxides: Synthesis and properties as supercapacitor electrode materials. Electrochimica Acta. 2009;54(4):1240-8.

111. Xu M, Kong L, Zhou W, Li H. Hydrothermal Synthesis and Pseudocapacitance Properties of α-MnO_2 Hollow Spheres and Hollow Urchins. The Journal of Physical Chemistry C. 2007;111(51):19141-7.

112. Chen H, He J. Facile Synthesis of Monodisperse Manganese Oxide Nanostructures and Their Application in Water Treatment. The Journal of Physical Chemistry C. 2008;112(45):17540-5.

113. Ding YS, Shen XF, Gomez S, Luo H, Aindow M, Suib SL. Hydrothermal Growth of Manganese Dioxide into Three-Dimensional Hierarchical Nanoarchitectures. Advanced Functional Materials. 2006;16(4):549-55.

114. Wang X, Li Y. Synthesis and Formation Mechanism of Manganese Dioxide Nanowires/Nanorods. Chemistry – A European Journal. 2003;9(1):300-6.

115. Giraldo OSL. Spontaneous formation of inorganic helices. Nature. 2000;405(6782):38.

116. Zhang L-C, Liu Z-H, Lv H, Tang X, Ooi K. Shape-Controllable Synthesis and Electrochemical Properties of Nanostructured Manganese Oxides. The Journal of Physical Chemistry C. 2007;111(24):8418-23.

117. Zhai Y, Zhai J, Zhou M, Dong S. Ordered magnetic core-manganese oxide shell nanostructures and their application in water treatment. Journal of Materials Chemistry. 2009;19(38):7030-5.

118. Liu EH, Li W, Li J, Meng XY, Ding R, Tan ST. Preparation and characterization of nanostructured NiO/MnO_2 composite electrode for electrochemical supercapacitors. Materials Research Bulletin. 2009;44(5):1122-6.

119. Digby D M. Reflections on the history of electrochemical impedance spectroscopy. Electrochimica Acta. 2006;51(8-9):1376-88.

120. Nam K-W, Lee C-W, Yang X-Q, Cho BW, Yoon W-S, Kim K-B. Electrodeposited manganese oxides on three-dimensional carbon nanotube substrate: Supercapacitive behaviour in aqueous and organic electrolytes. Journal of Power Sources. 2009;188(1):323-31.

121. Yoon S, Lee C, Oh SM, Park Y-K, Choi WC. Preparation of mesoporous carbon/manganese oxide materials and its application to supercapacitor electrodes. Journal of Non-Crystalline Solids. 2009;355(4-5):252-6.

122. Zolfaghari A, Ataherian F, Ghaemi M, Gholami A. Capacitive behavior of nanostructured MnO_2 prepared by sonochemistry method. Electrochimica Acta. 2007;52(8):2806-14.

123. Huang Q, Wang X, Li J. Characterization and performance of hydrous manganese oxide prepared by electrochemical method and its application for supercapacitors. Electrochimica Acta. 2006;52(4):1758-62.

124. Liu EH, Meng XY, Ding R, Zhou JC, Tan ST. Potentiodynamical co-deposited manganese oxide/carbon composite for high capacitance electrochemical capacitors. Materials Letters. 2007;61(16):3486-9.

125. Fan Z, Qie Z, Wei T, Yan J, Wang S. Preparation and characteristics of nanostructured MnO_2/MWCNTs using microwave irradiation method. Materials Letters. 2008;62(19):3345-8.

126. Sharma RK, Rastogi AC, Desu SB. Manganese oxide embedded polypyrrole nanocomposites for electrochemical supercapacitor. Electrochimica Acta. 2008;53(26):7690-5.

127. Yuan C, Su L, Gao B, Zhang X. Enhanced electrochemical stability and charge storage of MnO_2/carbon nanotubes composite modified by polyaniline coating layer in acidic electrolytes. Electrochimica Acta. 2008;53(24):7039-47.

128. Xiao W, Xia H, Fuh J-Y-H, Lu L. Electrochemical Synthesis and Supercapacitive Properties of e-MnO_2 with Porous/Nanoflaky Hierarchical Architectures. Journal of The Electrochemical Society. 2009;156(7):A627-A33.

129. Suni II. Impedance methods for electrochemical sensors using nanomaterials. TrAC Trends in Analytical Chemistry. 2008;27(7):604-11.

130. Xiao W, Xia H, Fuh JYH, Lu L. Growth of single-crystal α-MnO_2 nanotubes prepared by a hydrothermal route and their electrochemical properties. Journal of Power Sources. 2009;193(2):935-8.

131. Yuan A, Wang X, Wang Y, Hu J. Textural and capacitive characteristics of MnO_2 nanocrystals derived from a novel solid-reaction route. Electrochimica Acta. 2009;54(3):1021-6.

132. Bordjiba T, Belanger D. Direct Redox Deposition of Manganese Oxide on Multiscaled Carbon Nanotube/Microfiber Carbon Electrode for Electrochemical Capacitor. Journal of The Electrochemical Society. 2009;156(5):A378-A84.

133. Lee S, White AJP, Williams DJ, Barrett AGM, Hoffman BM. Synthesis of Near-IR Absorbing/Emitting Porphyrazine Derivatives with Tunable Solubility. The Journal of Organic Chemistry. 2000;66(2):461-5.

134. Theodoridis A, Maigut J, Puchta R, Kudrik EV, van Eldik R. Novel Iron(III) Porphyrazine Complex. Complex Speciation and Reactions with NO and H_2O_2. Inorganic Chemistry. 2008;47(8):2994-3013.

135. Bonnett R. Photosensitizers of the porphyrin and phthalocyanine series for photodynamic therapy. Chemical Society Reviews. 1995;24(1):19-33.

136. Garramone G, Pietrangeli D, Ricciardi G, Conoci S, Guascito MR, Malitesta C, et al. Electrochemical and Spectroscopic Behavior of Iron(III) Porphyrazines in Langmuir-Schäfer Films. The Journal of Physical Chemistry B. 2008;112(37):11517-28.

137. Keskin B, Köseoğlu Y, Avciata U, Gül A. Synthesis and EPR studies of porphyrazines with bulky substituents. Polyhedron. 2008;27(4):1155-60.

138. Onay H, Esat B, Öztrük R. The symmetrical porphyrazine with annulated six membered rings. Polyhedron. 2010;29(4):1314-6.

139. Liao M-S, Scheiner S. Comparative study of metal-porphyrins, -porphyrazines, and -phthalocyanines. Journal of Computational Chemistry. 2002;23(15):1391-403.

140. Fitzgerald JP, Haggerty BS, Rheingold AL, May L, Brewer GA. Iron octaethyltetraazaporphyrins: synthesis, characterization, coordination

chemistry, and comparisons to related iron porphyrins and phthalocyanines. Inorganic Chemistry. 1992;31(11):2006-13.

141. Goslinski T, Zhong C, Fuchter MJ, Stern CL, White AJP, Barrett AGM, et al. Porphyrazines as Molecular Scaffolds: Flexible Syntheses of Novel Multimetallic Complexes. Inorganic Chemistry. 2006;45(9):3686-94.

142. Villano M, Amendola V, Sandonà G, Donzello MP, Ercolani C, Meneghetti M. Excited State Dynamics and Nonlinear Absorption of a Pyrazinoporphyrazine Macrocycle Carrying Externally Appended Pyridine Rings. The Journal of Physical Chemistry B. 2006;110(48):24354-60.

143. Bergami C, Donzello MP, Ercolani C, Monacelli F, Kadish KM, Rizzoli C. Tetra-2,3-pyrazinoporphyrazines with Externally Appended Pyridine Rings. 3. A New Highly Electron-Deficient Octacationic Macrocycle: Tetrakis-2,3-[5,6-di{2-(N-methyl)pyridiniumyl}pyrazino]porphyrazine, $[(2\text{-Mepy})_8\text{TPyzPzH2}]^{8+}$. Inorganic Chemistry. 2005;44(26):9852-61.

144. Montalban AG, Jarrell W, Riguet E, McCubbin QJ, Anderson ME, White AJP, et al. Bis(dimethylamino)porphyrazines: Synthetic, Structural, and Spectroscopic Investigations. The Journal of Organic Chemistry. 2000;65(8):2472-8.

145. Tuncer S, Koca A, Gül A, Avciata U. Synthesis, characterization, electrochemistry and spectroelectrochemistry of novel soluble porphyrazines bearing unsaturated functional groups. Dyes and Pigments. 2009;92(1):610-8.

146. Sakellariou EG, Montalban AG, Meunier HG, Rumbles G, Phillips D, Ostler RB, et al. Peripherally Metalated Secoporphyrazines: A New Generation of Photoactive Pigments. Inorganic Chemistry. 2002;41(8):2182-7.

147. Lange SJ, Sibert JW, Barrett AGM, Hoffman BM. Synthesis and coordination chemistry of unsymmetrical tetraazaporphyrins containing single oxathia- and thiacrown substituents. Tetrahedron. 2000;56(38):7371-7.

148. Vesper BJ, Salaita K, Zong H, Mirkin CA, Barrett AGM, Hoffman BM. Surface-Bound Porphyrazines:Controlling Reduction Potentials of Self-Assembled Monolayers through Molecular Proximity/Orientation to a Metal Surface. Journal of the American Chemical Society. 2004;126(50):16653-8.

149. Michel SLJ, Goldberg DP, Stern C, Barrett AGM, Hoffman BM. Solitaire and Gemini Metallocene Porphyrazines. Journal of the American Chemical Society. 2001;123(20):4741-8.

150. Hochmuth Detlev H, Michel Sarah LJ, White Andrew JP, Williams David J, Barrett Anthony GM, Hoffman Brian M. Ci Symmetric and Non-Centrosymmetric Crystalline Complexes of [60]Fullerene with Octakis(dimethylamino)porphyrazinato-Copper(II) and -Nickel(II). European Journal of Inorganic Chemistry. 2000;2000(4):593-6.

151. Koca A, Şahin M, Gül A, Uslu RZ. Electrochemical Investigation of Metal-Free and Nickel-Containing Porphyrazines Carrying Eight Tosylaminoethylthia Groups. Monatshefte für Chemie / Chemical Monthly. 2002;133(8):1135-45.

152. Sorokin A, Meunier B. Oxidation of Polycyclic Aromatic Hydrocarbons Catalyzed by Iron Tetrasulfophthalocyanine FePcS: Inverse Isotope Effects and Oxygen Labeling Studies. European Journal of Inorganic Chemistry. 1998;1998(9):1269-81.

153. Kudrik EV, van Eldik R, Makarov SV. Kinetics and mechanism of water substitution in the low-spin Fe(ii) complex of 4-octasulfophenylpyrazinoporphyrazine. Dalton Transactions. 2004(3):429-35.

154. Kobayashi N, Adachi, A., Osa, T. Some Spectroscopic, Electrochemical and Spectroelectrochemical Properties of Tetrapyrazinoporphyrazine and Its Iron and Cobalt Complexes. Analytical Sciences. 1990;6(3):449-53.

155. Petrik P, Zimcik, P., Kopecky, K., Musil, Z., Miletin, M., Loukotova, V. Protonation and deprotonation of nitrogens in tetrapyrazino-porphyrazine macrocycles. Journal of Porphyrins and Phthalocyanine. 2007;11(7):487-95.

156. Kudrevich SV, Van Lier JE. Azaanalogs of phthalocyanine: Syntheses and properties. Coordination Chemistry Reviews. 1996;156:163-82.

157. Hibbert DB. Introduction to electrochemistry. London: The Macmillan Press Ltd; 1993.

158. Skoog DA, West, Donald M., Holler, F. James, Crouch, Stanley R. Fundamentals of analytical chemistry. 8 ed. Califonia: Thomson-Brooks/Cole; 2004.

159. Schmickler W, Santos E. Interfacial Electrochemistry. New York: Springer; 2010.

160. Kötz R, Stucki S. Stabilization of RuO_2 by IrO_2 for anodic oxygen evolution in acid media. Electrochimica Acta. 1986;31(10):1311-6.

161. Conway BE, Pell WG. Double-layer and pseudocapacitance types of electrochemical capacitors and their applications to the development of hybrid devices. Journal of Solid State Electrochemistry. 2003;7(9):637-44.

162. Frackowiak E, Béguin F. Electrochemical storage of energy in carbon nanotubes and nanostructured carbons. Carbon. 2002;40(10):1775-87.

163. Reddy ALM, Ramaprabhu S. Nanocrystalline Metal Oxides Dispersed Multiwalled Carbon Nanotubes as Supercapacitor Electrodes. The Journal of Physical Chemistry C. 2007;111(21):7727-34.

164. Bard AJ, Faulkner LR. Electrochemical methods: fundamentals and applications. 2 ed. New York: Wiley; 2001.

165. Monk PMS. Fundamentals of electroanalytical chemistry. Wiley; 2001.

166. Olmstead ML, Nicholson RS. Influence of double-layer charging in chronopotentiometry. The Journal of Physical Chemistry. 1968;72(5):1650-6.

167. Shaijumon MM, Ou FS, Ci L, Ajayan PM. Synthesis of hybrid nanowire arrays and their application as high power supercapacitor electrodes. Chemical Communications. 2008(20):2373-5.

168. Pushparaj VL, Shaijumon MM, Kumar A, Murugesan S, Ci L, Vajtai R, et al. Flexible Energy Storage Devices Based on Nanocomposite Paper. Proceedings of

the National Academy of Sciences of the United States of America. 2007;104(34):13574-7.

169. Chen P-C, Shen G, Sukcharoenchoke S, Zhou C. Flexible and transparent supercapacitor based on In_2O_3 nanowire/carbon nanotube heterogeneous films. Applied Physics Letters. 2009;94(4):043113-3.
170. Hasannejad H, Shahrabi T, Jafarian M, Rouhaghdam AS. EIS study of nano crystalline Ni-cerium oxide coating electrodeposition mechanism. Journal of Alloys and Compounds. 2011;509(5):1924-30.
171. Florian M. Electrochemical impedance spectroscopy (EIS) as a new tool for investigating methods of corrosion protection. Electrochimica Acta. 1990;35(10):1533-44.
172. Buller S, Thele M, Karden E, De Doncker RW. Impedance-based non-linear dynamic battery modeling for automotive applications. Journal of Power Sources. 2003;113(2):422-30.
173. Hughes M, Chen GZ, Shaffer MSP, Fray DJ, Windle AH. Electrochemical capacitance of a nanoporous composite of carbon nanotubes and polypyrrole. Chemistry of Materials. 2002;14(4):1610-3.
174. Sugimoto W, Iwata H, Yokoshima K, Murakami Y, Takasu Y. Proton and Electron Conductivity in Hydrous Ruthenium Oxides Evaluated by Electrochemical Impedance Spectroscopy:The Origin of Large Capacitance. The Journal of Physical Chemistry B. 2005;109(15):7330-8.

175. Vayssieres L, Hagfeldt A, Lindquist SE. Purpose-built metal oxide nanometarials. The emergence of a new generation of smart materials. Pure and Applied Chemistry. 2000;72(1):47-52.

176. Wang D, Kou R, Choi D, Yang Z, Nie Z, Li J, et al. Ternary Self-Assembly of Ordered Metal Oxide- Graphene Nanocomposites for Electrochemical Energy Storage. ACS Nano. 2010;4(3):1587-95.

177. Guo Z, Tan L. Fundamentals and Applications of Nanomaterials. Norwood, MA, USA: Artech House; 2009.

178. Zhang S, Li L, Kumar A. Materials characterization techniques. 1 ed. Boca Raton: CRC Press; 2009.

179. Willard HH, Merritt LL, Dean JA. Instrumental methods of analysis. Van Nostrand; 1974.

180. Goyanes S, Rubiolo GR, Salazar A, Jimeno A, Corcuera MA, Mondragon I. Carboxylation treatment of multiwalled carbon nanotubes monitored by infrared and ultraviolet spectroscopies and scanning probe microscopy. Diamond and Related Materials. 2007;16(2):412-7.

181. Bahr JL, Tour JM. Highly Functionalized Carbon Nanotubes Using in Situ Generated Diazonium Compounds. Chemistry of Materials. 2001;13(11):3823-4.

182. Hsieh C-T, Teng H, Chen W-Y, Cheng Y-S. Synthesis, characterization, and electrochemical capacitance of amino-functionalized carbon nanotube/carbon paper electrodes. Carbon. 2010;48(15):4219-29.

183. Devaraj S, Munichandraiah N. Effect of Crystallographic Structure of MnO_2 on Its Electrochemical Capacitance Properties. The Journal of Physical Chemistry C. 2008;112(11):4406-17.

184. Mirershadi S, Mortazavi SZ, Reyhani A, Moniri N, Novinrooz AJ. Effective Condition for Purification of Multi-Walled Carbon Nanotubes by Nitric Acid. Synthesis and Reactivity in Inorganic, Metal-Organic, and Nano-Metal Chemistry. 2009;39(4):204-8.

CHAPTER 3

EXPERIMENTAL

3.1 Materials and Reagents

All the reagents were used without further purification unless otherwise stated. Ultra-pure water (deionised) of resistivity 18.2 MΩ.cm obtained from Milli Q water system (Millipore Corp., Bedford, MA, USA) was used for all experiments. Ultra-pure N_2 gas (99.998%, Afrox) was used for purging the electrolytes before electrochemical analysis. The porphyrazine complexes (CoTPyzPz and FeTPyzPz) were donated by Prof. Nagao Kobayashi (Tohoku University, Japan). Graphene Oxide was donated by Prof. Shaowei Chen (University of California, USA). All reagents used, their purity and suppliers are tabulated in table 3.1.

3.2 Synthesis

3.2.1. Synthesis of manganese dioxide

Manganese dioxide nanoparticles were synthesised from slight modification of the method used by Ragupathy *et al* (1). 1.00 ml of aniline was added dropwise to a vigorously stirred solution of 0.100 M $KMnO_4$ over the period of 20 min, and a brownish black precipitate was formed. The brownish black precipitate was ultra-centrifuged and washed numerously with deionised water until neutral. The obtained precipitate was finally rinsed with acetone. A shiny crystalline brownish black powder (1.616 g) was obtained after vacuum drying overnight.

Table 3.1: List of reagents and chemical suppliers used.

Reagent	Supplier
Potassium permanganate, $KMnO_4$ (99.0%, univAR)	Saarchem
Aniline, C_6H_7N (99.5%, ACS reagent)	Sigma-Aldrich
Acetone, $C_2H_4O_2$, (99.5%, univAR)	Saarchem
MWCNT (95%, ℓ = 5-10µm, diameter = 15±5 nm	Nanolab Inc.
Nitric Acid, HNO_3 (65%,Analar)	BDH chemicals
Sulphuric Acid, H_2SO_4(98%, univAR)	Merck
Hydrogen peroxide, H_2O_2 (30%, univAR)	Saarchem
N,N-Dimethylformamide, C_3H_7NO (99.8%, ACS, distilled)	Sigma-Aldrich
N,N-Dimethylformamide, C_3H_7NO (99.8%, Uvasol, spectroscopy grade)	Merck
Sodium sulphate anhydrous, Na_2SO_4 (99.0%, univAR)	Saarchem
Sodium Nitrite, $NaNO_2$(99.0%, GR)	Merck
1,4-Benzenediamine dihydrochloride, $C_6H_4(NH_2)_2.2HCl$ (99%, AT)	Aldrich
Polyvinylidene fluoride (Average mw~534 000)	Sigma-Aldrich
Carbon Black (EQ-LiB-super)	MTI

3.2.2. Synthesis of MWCNT(x%)-MnO2

MWCNT(15%)-MnO_2 was synthesised by adapting the established method (1, 2). Approximately 0.0474 g acid functionalized MWCNT was added to 20 ml of 0.100 M $KMnO_4$ solution, followed by a dropwise addition of approximately 0.15 ml aniline while stirring (for 20 min). The resultant brownish black mixture was stirred for an additional 30 min. Thereafter the brownish black solution was sonicated for 30 min and a black powder was collected after filtration. The obtained precipitate was washed several times with copious amount of deionised water until pH 7. After washing with acetone, a black shiny crystalline powder was obtained. The black crystalline was vacuum oven dried (30 °C, 0.54 mBar) overnight. Yield = 0.256 g

The above procedure was repeated with approximately 0.0948 g of acid functionalised MWCNT to give 0.226 g of MWCNT(30%)-MnO_2 powder.

3.3 Functionalization of MWCNT

3.3.1. Acid functionalization

The acid functionalization (Figure 3.1) was done according to the established method by Liu and co-workers.(3) A mixture of MWCNT (0.501 g) and 250 ml of approximately 2.6 M HNO_3 was refluxed for 48 h. The mixture was filtered with 0.45 µm polycarbonate filter paper. The Black precipitate was washed and thereafter dispersed in a piranha mixture H_2SO_4:H_2O_2 (4:1) and sonicated for 24 h. The reaction was quenched with deionised water and centrifuged until the pH of the filtrate was neutral. The black powder was vacuum dried (0.54 mBar, 30 °C). Yield of 64 % was obtained. FTIR (KBr) **V_{max}**(cm^{-1}): 3437 (O-H str.), 2917 (C-H symm. str.), 2849 (C-H antisymm. str.) and 1627 (COO-bend).

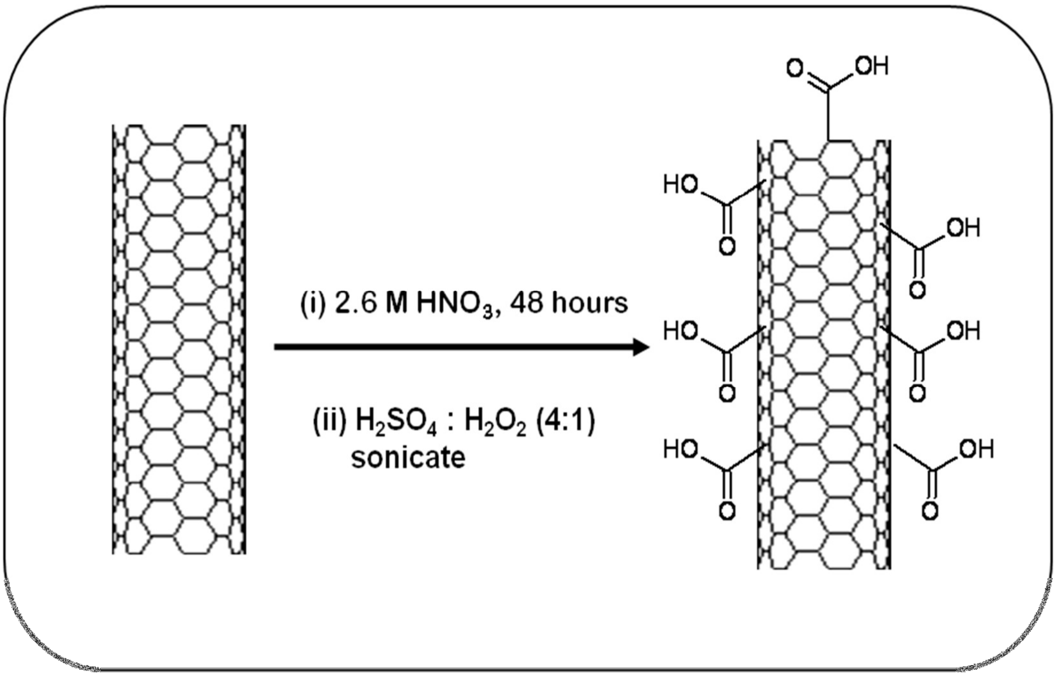

Figure 3.1: Acid functionalization of MWCNT.

3.3.2. Phenylamine functionalization

Functionalization of MWCNT with phenylamine (Figure 3.2) was done by following the method of one step process synthesis developed by Ellison and co-workers (4) for SWCNTs. Approximately 0.052 ml of concentrated H_2SO_4 was added dropwise to a stirred mixture of purified MWCNT (0.0604 g), $NaNO_2$ (0.3308 g) and $C_6H_4(NH_2)_2{\cdot}2HCl$ (0.1197 g). To the mixture, 4.0 ml of DMF was added, and the mixture was heated for I hour at 55 °C. A black solid precipitate was obtained after filtration. The obtained precipitate was dispersed and sonicated in DMF several times until pH 7. Approximately 0.267 g of black solid powder was obtained after drying overnight at 60 °C.

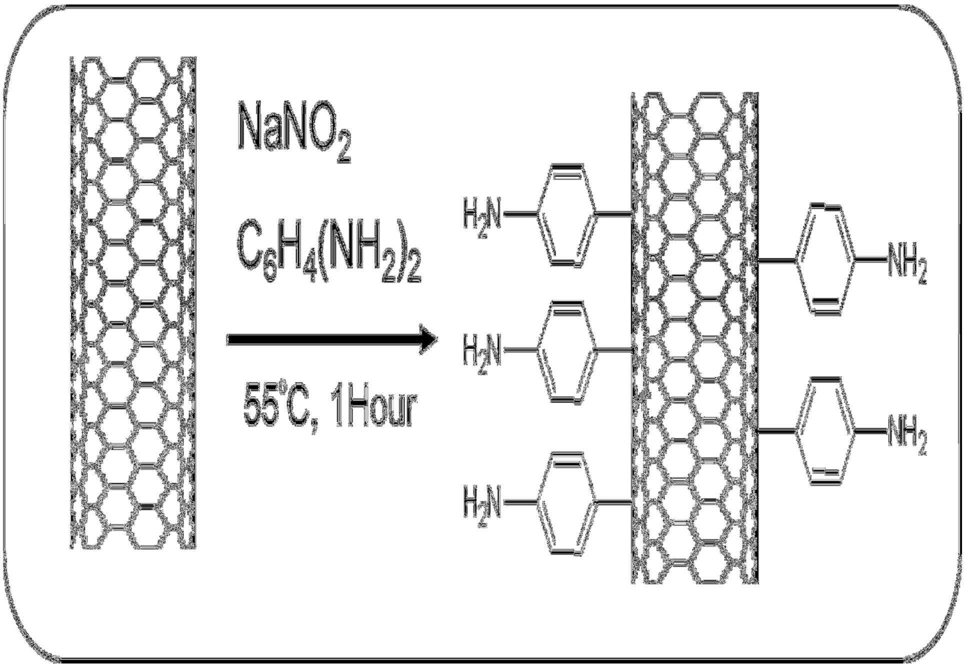

Figure 3.2: Functionalization of MWCNT with phenylamine.

3.4 Composite formation

3.4.1. Formation of CoTPyzPz composites

MWCNT-CoTPyzPz composite was prepared by grinding equal amounts of MWCNTaf and CoTPyzPz (1:1 mass ratio) using an agate mortar and pestle for 20 min until an even blend of the solids was obtained. The resultant composite was dissolved in 2 ml DMF at a ratio of 1:1 (mass: volume ratio). The mixture was sonicated for one hour using ultrasonic bath at room temperature. A green MWCNTaf-CoTPyzPz solution was obtained after sonication. The above procedure was also used to prepare MWCNTPhNH_2 -CoTPyzPz.

3.4.2. Formation of FeTPyzPz composites

MWCNTaf-FeTPyzPz composites were prepared by grinding equal amounts of MWCNTaf and FeTPyzPz (1:1 mass ratio) using an agate mortar and pestle for 20 minutes until an even blend of the solids was obtained. The resultant composite was dissolved in approximately 2ml DMF at a ratio of 1:1 (mass: volume ratio). A brown uniform MWCNTaf-FeTPyzPz solution was obtained after sonication. The above procedure was also used to prepare MWCNTPhNH$_2$-FeTPyzPz.

3.4.3. Formation of GO/CoTPyzPz

The GO-CoTPyzPz hybrid was obtained by milling an equal amount of CoTPyzPz and GO (1:1 mass ratio), dissolved in DMF, ultra-sonicated for 30 min and finally dried. The same procedure was used for MWCNTaf-CoTPyzPz, MWCNTPhNH$_2$-CoTPyzPz, MWCNTaf-FeTPyzPz and MWCNTPhNH$_2$-FeTPyzPz composites used in the two-electrode system.

3.5 Electrode modification

Before electrochemical measurements were done, electrodes were either modified or made as outlined below.

3.5.1. Electrode pre-treatment

BPPGE was first cleaned in accordance to the method reported by Compton’s group. First, BPPGE was gentle polished on a p1200C Norton carborundum paper, followed by peeling the electrode layers with sellotape to expose a new layer of the electrode.

Finally, the electrode was rinsed in acetone to remove any adhesives and impurities. Prior to use, the nickel foam (current collector) was cleaned in a 1 M HCl solution, washed with a copious amount of de-ionized water, and dried under vacuum.

3.5.2. Electrode modification with MWCNTaf

Basal plane pyrolytic graphite (BPPG) disc encased in Teflon, with copper as current collector was used as a bare electrode. The drop dry method was utilized in electrode modification. Approximately 20 µL of sonicated MWCNTaf solution was dropped on bare BPPGE, and the electrode was oven dried at 50 °C for 10 min (Figure 3.3).

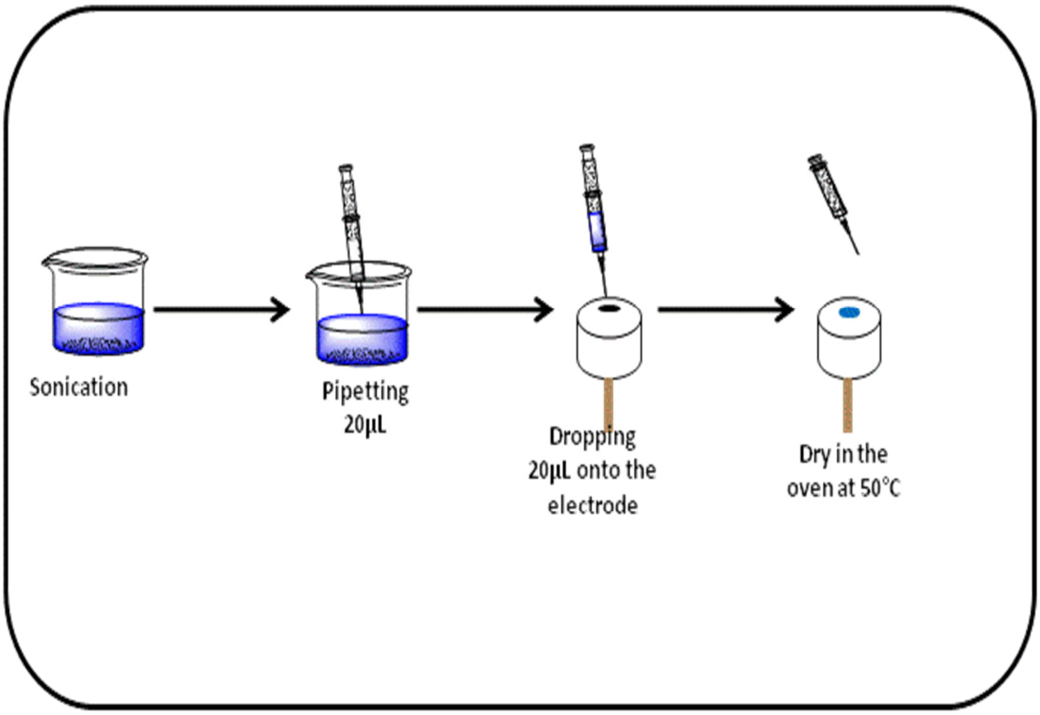

Figure 3.3: Schematic representation of BPPG electrode modification using drop dry method.

Mass of the active material on the electrode was assumed to be 20 μg. The above procedure was used in modifying the electrode with the following materials MnO_2, MWCNT(15%)-MnO_2, MWCNT(30%)-MnO_2, CoTPyzPz, FeTPyzPz, MWCNTaf-CoTPyzPz, MWCNTPhNh_2-CoTPyzPz, MWCNTaf-FeTPyzPz and MWCNTPhNh_2-FeTPyzPz. These modified electrodes were used in the three-electrode system.

3.5.3. Positive electrode preparation

For the two electrode system, the following procedure was used to make a positive electrode (cathode). The positive electrode (MWCNTs-CoTPyzPz hybrid) was prepared by mixing CoTPyzPz, MWCNTs, carbon black (CB) and polyvinylidene fluoride (PVDf) in a mass ratio of 4:4:1:1 using a pestle and mortar and dispersing in a few drops of anhydrous N-methyl-2-pyrrolidone to produce a homogeneous paste. The CB and PVDf served as the conductive agent and binder, respectively. The resulting slurry was coated onto the nickel foam substrate (201 cm^2) with a spatula. The electrode was then dried at 80 ^oC for 8 h in a vacuum oven, and pressed to a thickness of about 0.5 mm. The same procedure was used to prepare GO-CoTPyzPz positive electrode. (mass of active materials in the electrodes are tabled in the appendix)

3.5.4. Negative electrode preparation

The negative electrode or an anode (CB-MWCNTs) was prepared by mixing carbon black (CB), MWCNTs and polyvinylidene fluoride (PVDf) in a mass ratio of 8:1:1 using a pestle and mortar and dispersing in a few drops of anhydrous N-methyl-2-

pyrrolidone to produce a homogeneous paste. PVDF served as the conductive agent and binder, respectively. The resulting slurry was coated onto the 15mm diameter nickel foam substrate (201 cm^2) with a spatula. The electrode was then dried at 80 °C for 8 h in a vacuum oven, and pressed to a thickness of 0.5 mm. CB-GO was prepared by using the same procedure for making CB-MWCNTs negative electrode.

3.6 Asymmetric cell preparation

An asymmetric cell was assembled in a coin cell (Figure 3.4). An anode and a cathode were separately immersed in an electrolyte for 24 h. Firstly, the cathode was placed in a bottom coin cell casing facing upward, then a 16mm diameter separator disk made from Whatman no 1 filter paper was placed on top of the cathode.

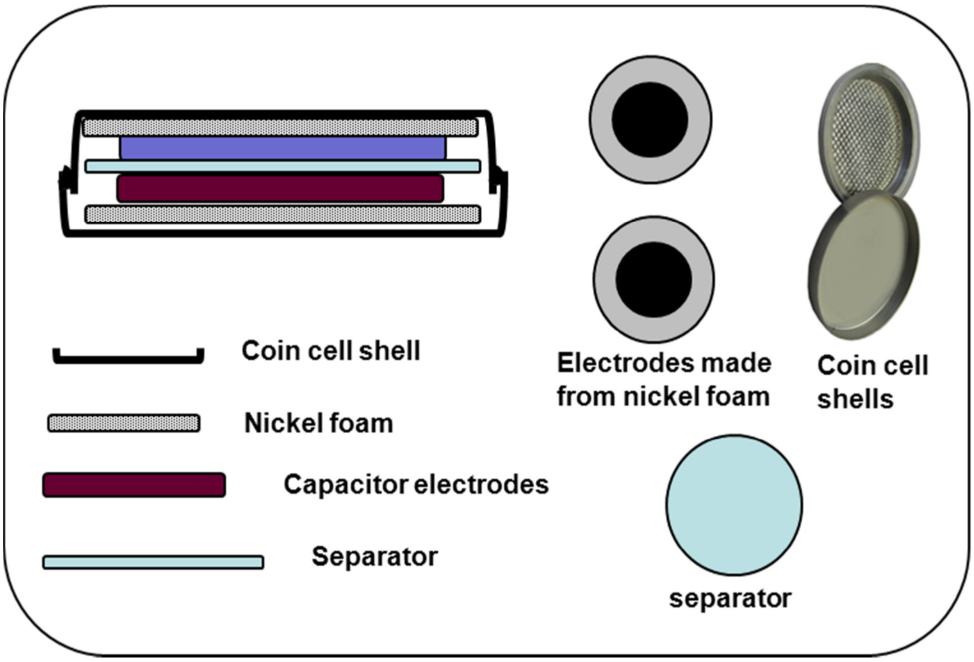

Figure 3.4: Schematic representation of coin cell fabrication.

An electrolyte was poured on top of the separator to ensure sufficient wetting of the separator. An anode was placed on top of the separator facing downwards. A coin cell spring was placed on top of the anode before closing the coin cell with a top casing. 1.0 M Na_2SO_4 aqueous electrolyte was poured into the casing before they were sealed.

3.7 Equipment and characterization

Thermogravimetric analysis (TGA) data of the composite materials were collected on a Mettler Telodo 851e instrument. Approximately 10 ± 2 mg of a sample was placed in an open 70 μL alumina pan. The samples were heated from room temperature to 1000 °C at a heating rate of 10 °C min^{-1}. Data was collected in air at a flow rate of 50 ml min^{-1}.

Fourier transform infrared spectroscopy (FTIR) data were collected using a Perkin Elmer spectrum RX I FTIR spectrometer with pure anhydrous potassium bromide (KBr) as the background. Sample pellets were prepared from a mixture of active material and KBr (1% of material in KBr). Background corrected spectra were recorded at room temperature in the wavenumber region 4000-400 cm^{-1} at a resolution of 2 cm^{-1}.

The UV–visible spectra were recorded using a Cary 300 UV–Visible Spectrophotometer, utilising Varian software (version 3.0). A spectrophotometer DMF grade solvent was used to prepare solutions for UV analysis.

Ultrahigh resolution field emission scanning electron microscope (FESEM) images were captured using JEOL JSM 6000 F Japan at an accelerating voltage of 2 KeV.

Samples for FESEM morphological analysis were prepared by drop drying samples on an aluminium plate thereafter the plate was coated with carbon twice using Polaron h/v coater

Scanning electron microscope (SEM) images and Energy dispersive x- ray spectroscopy (EDX) analysis were captured on JEOL 5800 LV at an accelerating voltage of 5 KeV and 20 KeV respectively. Samples for SEM analysis were prepared as follows: A small amount of the sample was placed on a carbon sticky tape. Excess powder was removed by blasting with air. The samples were gold plated twice with SEM auto coating unit, E2500 Polaron LTD sputter. Transmission electron microscopy (TEM) imaging analysis were carried out using JEOL JEM-2100

Powder X-ray diffraction patterns (XRD) analyses were recorded using PANlytical X-pert pro diffractometer with variable divergence and receiving slits and X'celerator detector using Fe filtered Co-Kα radiation operating with X'pert high score plus software with powder samples

Basal plane pyrolytic graphite electrode (BPPGE) fabricated in-house from BPPG plate was used as a working electrode for electrochemical studies in this project. A 5.0 mm diameter disk of BPPG was connected to a copper wire and held in place with conducting silver vanish. Teflon was used as the casing for the fabricated electrode.

All electrochemical experiments were performed with Autolab potentiostat PGSTAT 20 (Eco Chemie, Utrecht, Netherlands) controlled by General Purpose Electrochemical Systems data processing software (GPES, version 4.9) using a conventional three-electrode system. Ag/AgCl (sat'd KCl) and platinum rod were used as a reference and counter electrode respectively. The same equipment was used for two electrode system measurements.

Electrochemical impedance spectroscopy (EIS) measurements were performed with an Autolab Potentiostat PGSTAT instrument using Frequency Response Analyser software. Measurements were taken between 10 mHz and 100 kHz, while some between 10 mHz and 10 kHz using a 5 mV rms sinusoidal modulation.

3.8 References

1. Ragupathy P, Vasan HN, Munichandraiah N. Synthesis and Characterization of Nano-MnO$_2$ for Electrochemical Supercapacitor Studies. Journal of The Electrochemical Society. 2008;155(1):A34-A40.

2. Toupin M, Brousse T, Bélanger D. Charge Storage Mechanism of MnO$_2$ Electrode Used in Aqueous Electrochemical Capacitor. Chemistry of Materials. 2004;16(16):3184-90.

3. Liu J, Rinzler AG, Dai H, Hafner JH, Bradley RK, Boul PJ, et al. Fullerene Pipes. Science. 1998:1253-6.

4. Ellison MD, Gasda PJ. Functionalization of Single-Walled Carbon Nanotubes with 1,4-Benzenediamine Using a Diazonium Reaction. The Journal of Physical Chemistry C. 2007;112(3):738-40.

CHAPTER 4

MULTI-WALLED CARBON NANOTUBES MODIFIED WITH MANGANESE DIOXIDE NANOPARTICLES

4.1. Surface characterisation MWCNT-MnO_2

Surface characterisation of electrode materials is of great importance since capacitance is affected by physical attributes of materials like crystallinity. Thermogravimetry is a tool that can be used to estimate adsorbed water, predict stability, and confirm the stoichiometry of a compound as well as to study decomposition reactions. Figure 4.1 (a) and (b) shows the TG and DTG curves of MnO_2, MWCNT and MWCNTs-MnO_2 composites measured in air. The total mass loss of the electrode materials are as follows:

MWCNT(30%)-MnO_2 **(57%)** > MWCNT(15%)-MnO_2 **(35%)** > MnO_2 **(22%)** > MWCNTaf **(15%)**

Thermogravimetric curves show that MWCNTs has better thermal stability compared to the MnO_2. From DTG curves, four major weight losses can be observed for the composites while three could be observed for MnO_2. The incorporation of MWCNTs with MnO_2 to form a composite enhanced the thermal stability of MnO_2. A significant mass loss of about 14 % between 0 °C and 400 C was associated with the liberation of water by both the composites and pure MnO_2. This indicates that both MnO_2 and its MWCNTs composites are hydrated. The amorphous nature of the materials is also confirmed by SEM micrographs. The loss of water crystallization from the synthesized materials is essential for the movement of charges and contributes to the increase in capacitance (1). A sharp peak between 400 °C and 500 °C is associated with the loss of oxygen atoms from octahedral framework as Mn^{4+} turns to Mn^{3+}. A sharp peak at 885°C for MWCNT(15%)-MnO_2, MWCNT(30%)-MnO_2 and MnO_2 is attributed to the phase change of MnO_2 to Mn_3O_4 (2) due to the release of O_2 during the conversion. From the graphs in Figure 4.1, it is evident that there is a phase transition from MnO_2 to Mn_2O_3 since there is a small peak at around 600°C.(1, 3)

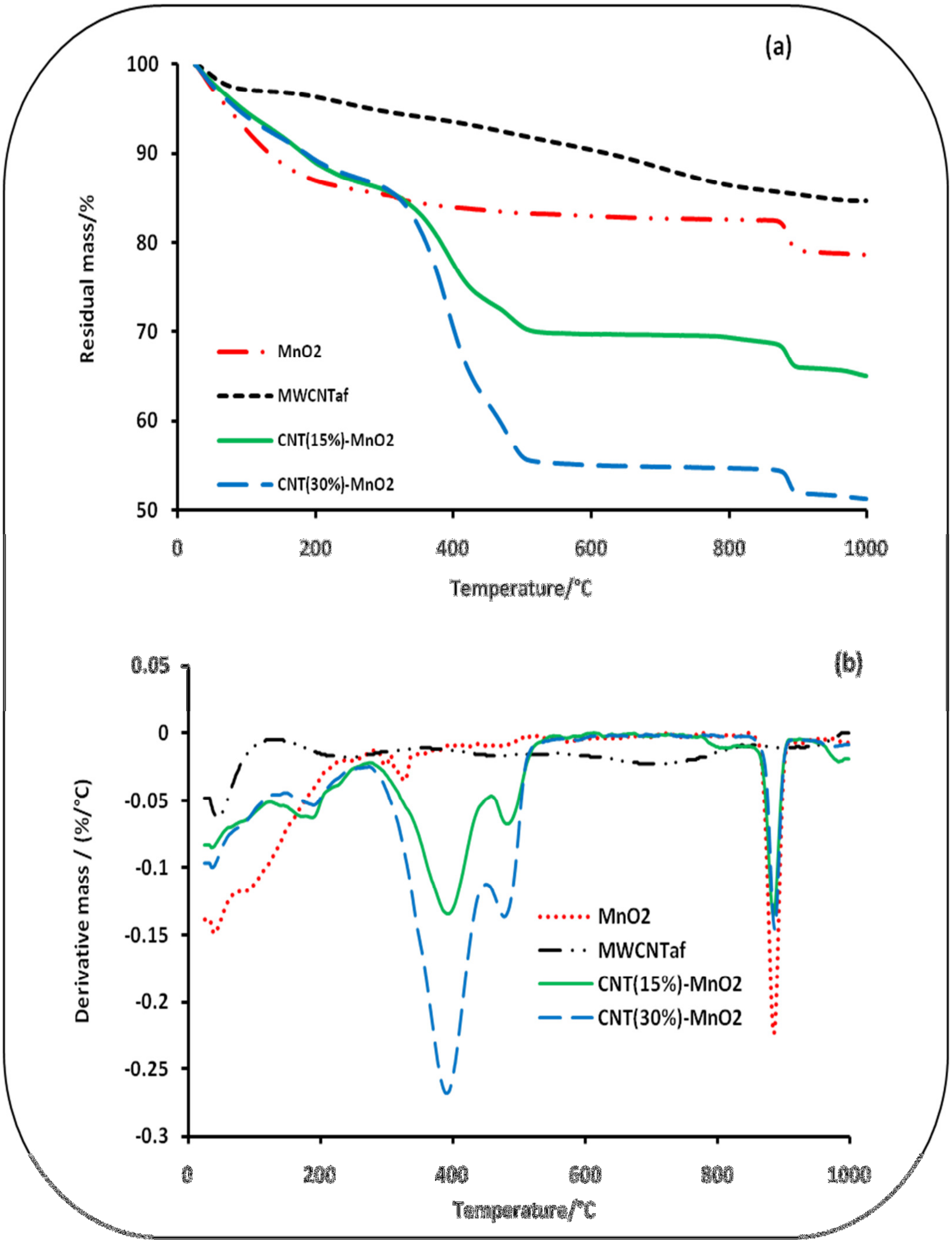

Figure 4.1: Thermogravimetric analyses (a) and derivative thermogravimetric analyses (b) curves of MnO_2, MWCNTaf, MWCNT(15%)-$MnO_2$and MWCNT(30%)-MnO_2 composite

X-ray diffraction (XRD) patterns of synthesised MWCNT(15%)-MnO_2 and MWCNT(30%)-MnO_2 are shown in Figure 4.2. The synthesized MnO_2 and composites are poorly crystalline and thus are presumed to be amorphous since no distinctive peaks can be observed. Additionally, the peaks feature a broad background which is an indication of the amorphous nature of these MnO_2 and its composites.

The XRD pattern of the acid functionalised MWCNT shows peaks at $2\Theta = 30°$, 51° and 63°. The latter peak is characteristic of metal impurities in MWCNT (3-5).

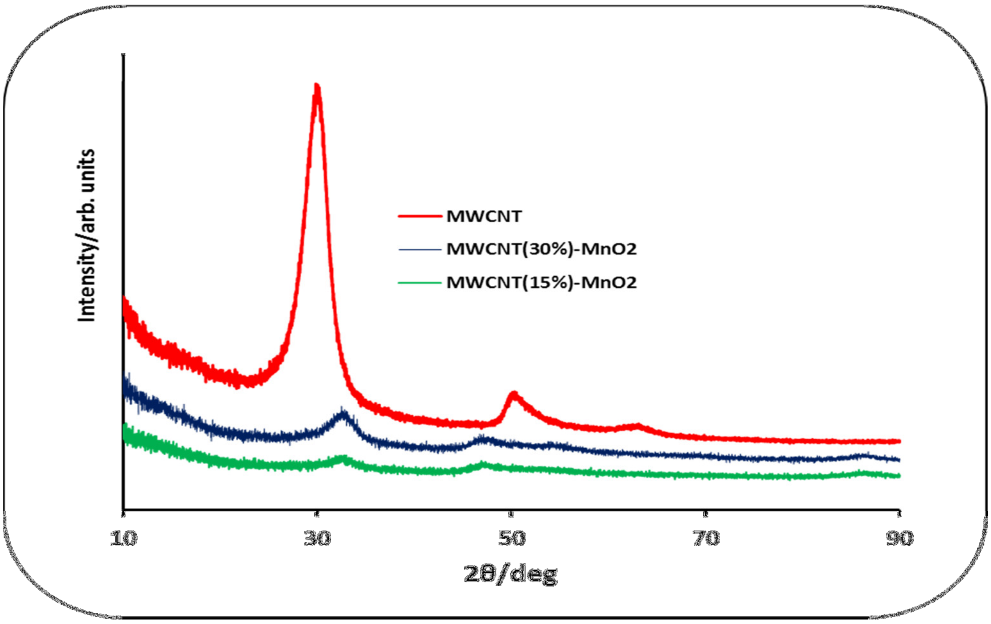

Figure 4.2: XRD pattern of MWCNT(15%)MnO_2, MWCNT(30%)MnO_2 and MWCNT

The FTIR spectra of MnO_2, acid functionalized MWCNT and MWCNT(30%)-MnO_2 were measured in the range 400 cm^{-1} – 4000 cm^{-1} using KBr. The broad absorption band at approximately 3482 cm^{-1} appears in all spectra as shown in Figure 4.3. This band is attributable to the hydroxyl stretching frequency. This confirms that the materials are hydrated as seen from TG curves. Carboxylation of MWCNT is confirmed by the carbonyl stretching frequency at 1648 cm^{-1}. Peak at around 600 cm^{-1} is attributable to Mn-O stretching frequency in MnO_6 octahedra. The peak at around 1654 cm^{-1} is due to C=C stretch from the CNTs and appears in all the spectra. This confirms that the composite consists of MnO_2 and functionalised MWCNT.

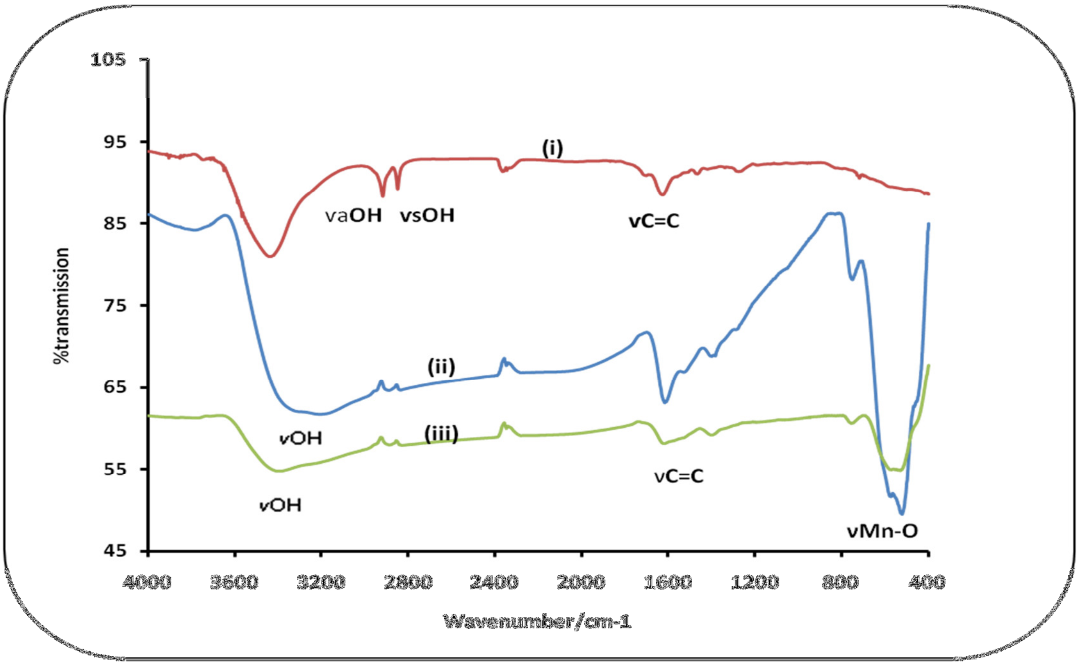

Figure 4.3: The FTIR spectra of (i) MWCNTaf, (ii) MnO_2 and (iii) MWCNT (30%)-MnO_2

The morphology of the electrode material is depicted in Figure 4.4. The images show that there is an agglomeration of the MnO_2 particles. This agglomeration was previously been reported (3) and it is caused by particle-particle collisions. There is no particular particle shape observable for MnO_2 and the composites. Ragupathy *et al* (1) reported an amorphous MnO_2 that exhibited highly clustered granules.

The EDX plots confirm the elemental composition of the synthesised materials. From the plots it is evident by the peak intensities that the carbon content in the composites is not the same. It is also evident that the synthesised material contains the K atom.

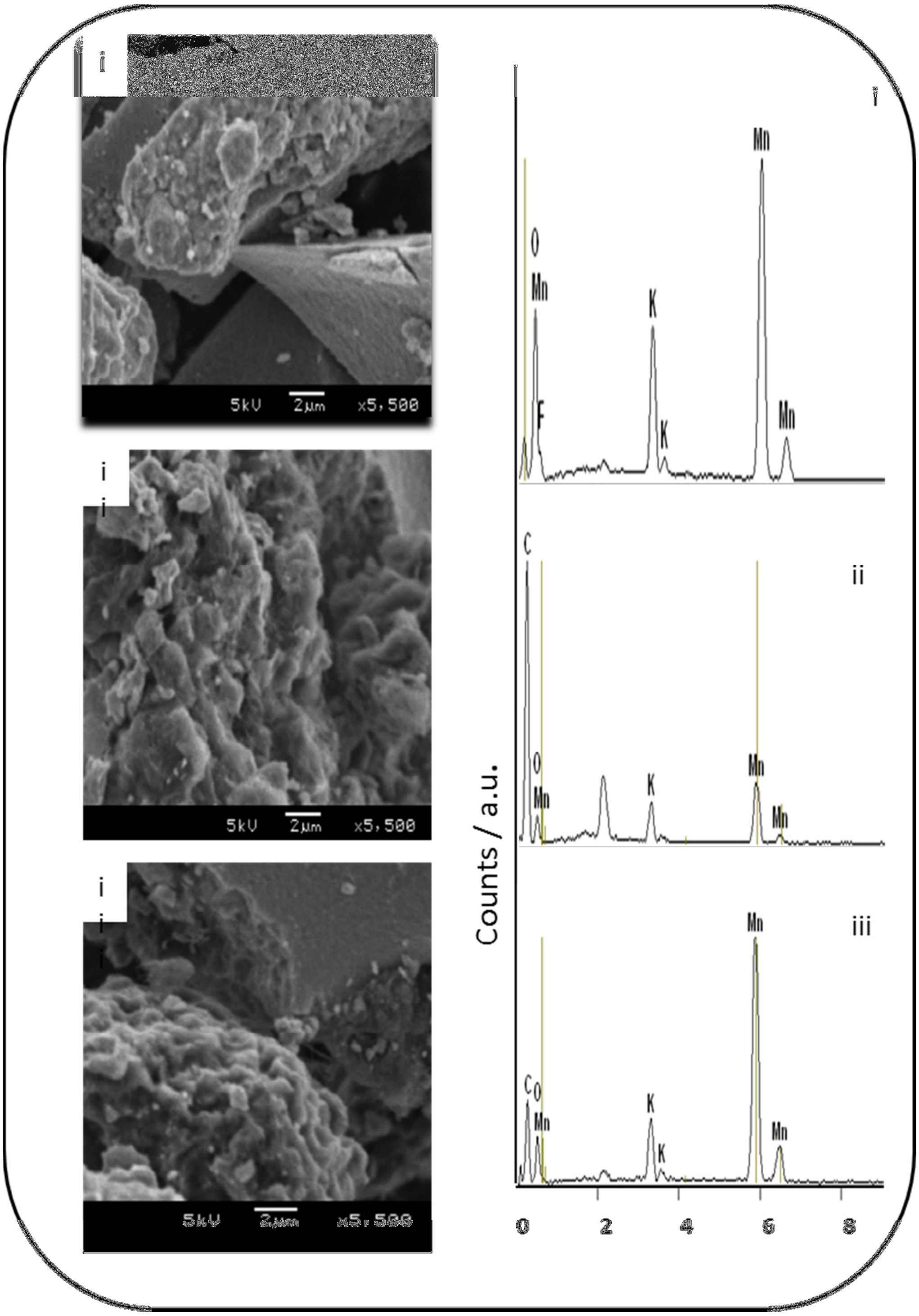

Figure 4.4: SEM images and EDX plots of (i) MnO_2, (ii) MWCNT(30%)-MnO_2 and (iii) MWCNT(15%)-MnO_2.

4.2. Electrochemical properties

4.2.1. Cyclic voltammetric experiments

Figure 4.5 shows cyclic voltammograms of MWCNTaf, MnO_2, MWCNT (30%)-MnO_2 and MWCNT (15%)-MnO_2 which were obtained between -0.2 V and 0.8 V in 1.0M Na_2SO_4 at a scan rate of 5 mV.s^{-1}. From the CV measurements, MWCNT (15%)-MnO_2 electrode exhibited a big current separation while MWCNTaf had the lowest current separation. The current separation trend for the studied materials is:

MWCNT (15%)-MnO_2 > MWCNT (30%)-MnO_2 > MnO_2 > MWCNT.

This observation is intriguing since the composite that contained 30% of MWCNT performed significantly less as compared to the composite with 15% MWCNT. Cyclic voltammograms of all materials are almost rectangular in shape; this indicates the excellent reversibility and ideal capacitive property of the electrodes (6).

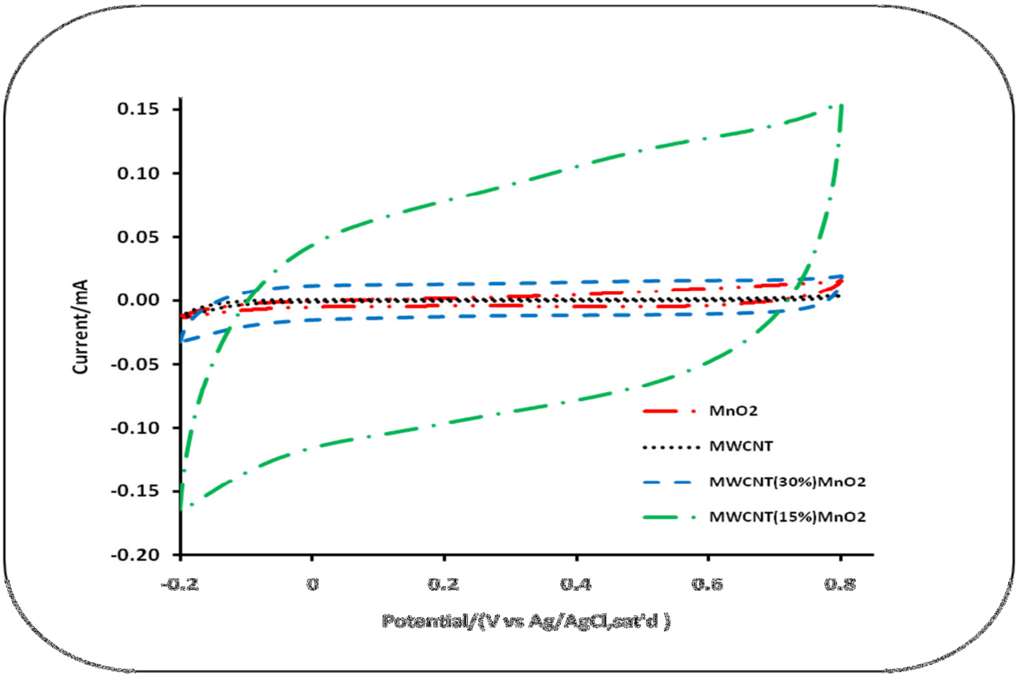

Figure 4.5: Comparative cyclic voltammograms of MnO_2, MWCNT and MWCNT-MnO_2 composite at 5 mV.s^{-1} using 1.0 M Na_2SO_4

The cyclic voltammogram curves of the composites and MnO_2 have a partially distorted rectangular shape due to the polarisation resistance. Polarisation resistance is due to poor conductivity of MnO_2. Cyclic voltammograms of acid functionalised MWCNT (Figure 4.6) at different scan rates maintain the rectangular shape and the cathodic and anodic are perfect mirror images of one another. The anodic and the cathodic current separation are the same at the middle of the potential range indicative of the good supercapacitive nature of the materials. The composites [MWCNT(15%)-MnO_2 and MWCNT(30%)-MnO_2], show a much better capacitive behaviour as compared to the pure systems (MnO_2 and MWCNT).

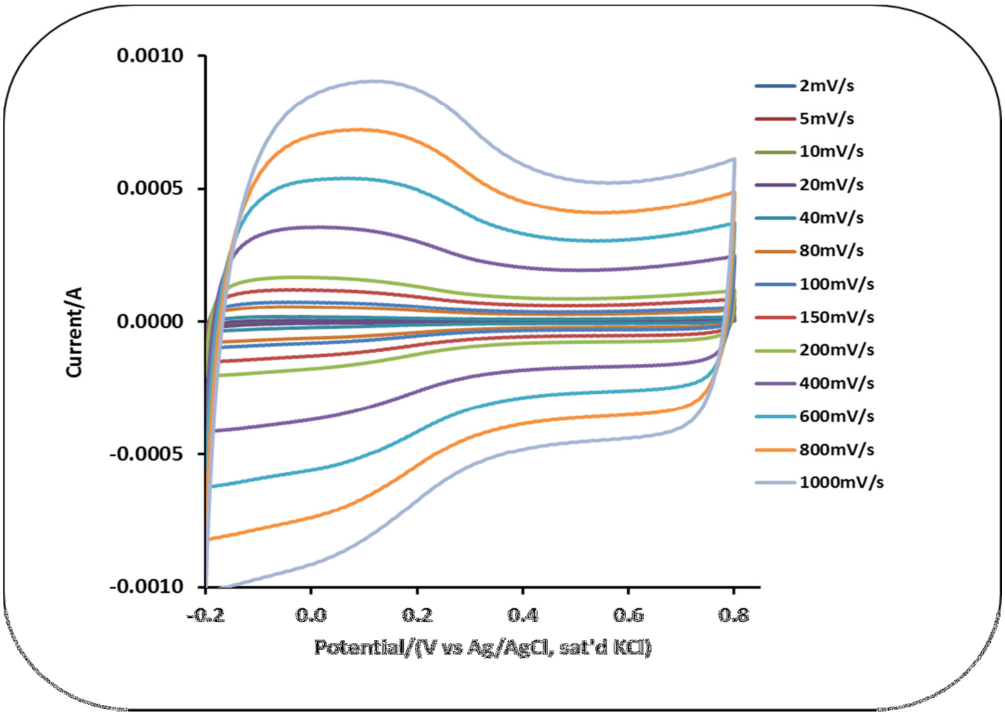

Figure 4.6: Cyclic voltammogram evolutions of acid functionalised MWCNTs in 1.0 M Na_2SO_4 at different scan rates.

Kelliher *et al* (7-9) proposed two charge storage mechanisms for MnO_2 in a neutral medium as follows:

(3.1)

where, M^+ = Li^+ , Na^+, K^+ or H_3O^+ or

(3.2)

Where, M^+ = Li^+, Na^+, K^+ or H_3O^+

The specific capacitance shown on figure 3.7 was obtained from the formula

—

(3.3)

where, is average current (A), v is the scan rate ($V.s^{-1}$) and m is the mass of the active electrode mass (g)

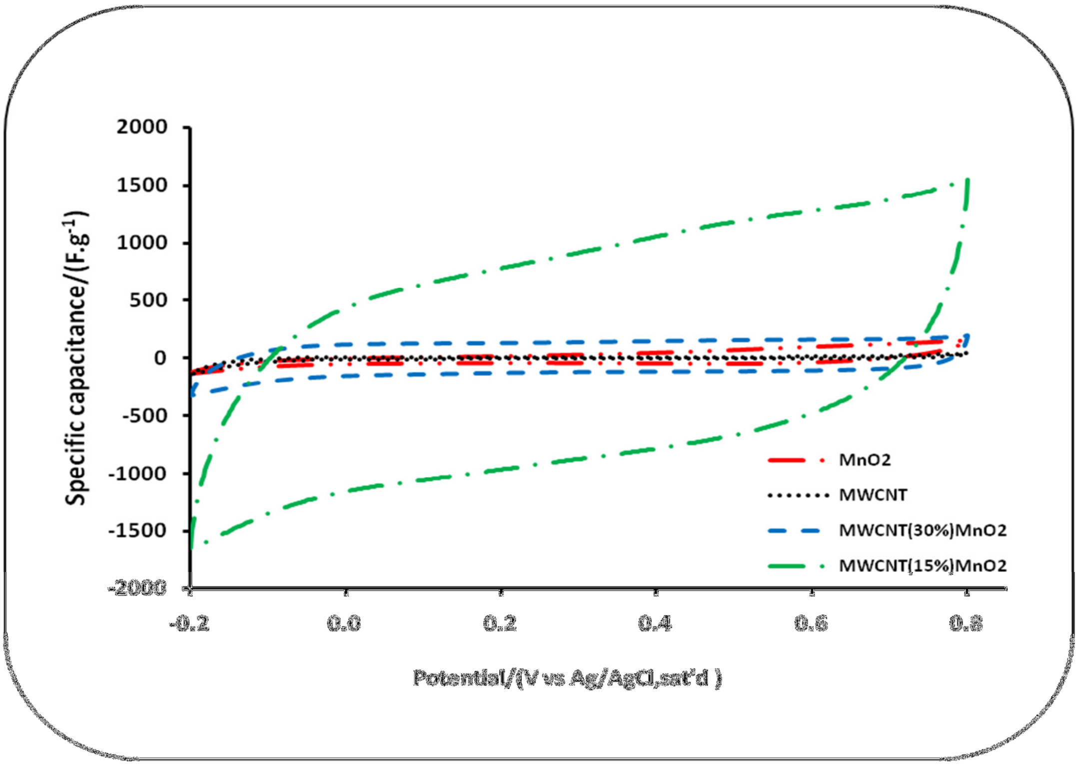

Figure 4.7: Comparative cyclic voltammograms of MnO_2, MWCNT and MWCNT(15%)-MnO_2 and MWCNT(30%)-MnO_2 in 1.0 M Na_2SO_4 at 5 $mV.s^{-1}$.

Table 4.1 shows specific capacitance values at various scan rates for the MnO_2 based systems. MWCNT(15%)-MnO_2 composite gave the highest capacitance of 885 $F.g^{-1}$ at 5 $mV.s^{-1}$. The specific capacitance results show that as the scan rate increases, the specific capacitance decreases. The large capacitance of MWCNT(15%)-MnO_2 can be attributed to the porous nature of the materials used (6). The interaction of individual materials in the composites is extraordinaire, especially where we have less amount of MWCNT.

The impact of scan rate on capacitance is shown in Figure 4.8. As the scan rate increases the voltammogram loops shrinks from the end of the potential range limits, thus showing increased resistivity as scan rate is increased. The inaccessibility of electrode material pores at high scan rate and the ionic resistivity contributes to the decrease in specific capacitance (1).

Table 4.1: Specific capacitance values of MnO2 based systems from CV.

Electrode	**Gravimetric Specific capacitance at various scan rates in 1.0M Na_2SO_4 electrolyte between -0.2 and 0.8 V**				
	2 $mV.s^{-1}$	**5 $mV.s^{-1}$**	**10 $mV.s^{-1}$**	**20 $mV.s^{-1}$**	**40$mV.s^{-1}$**
MnO_2	65	53	39	28	19
MWCNT	17	14	10	5	2
MWCNT(15%)-MnO_2	1099	885	723	578	448
MWCNT(30%)-MnO_2	138	135	130	120	106

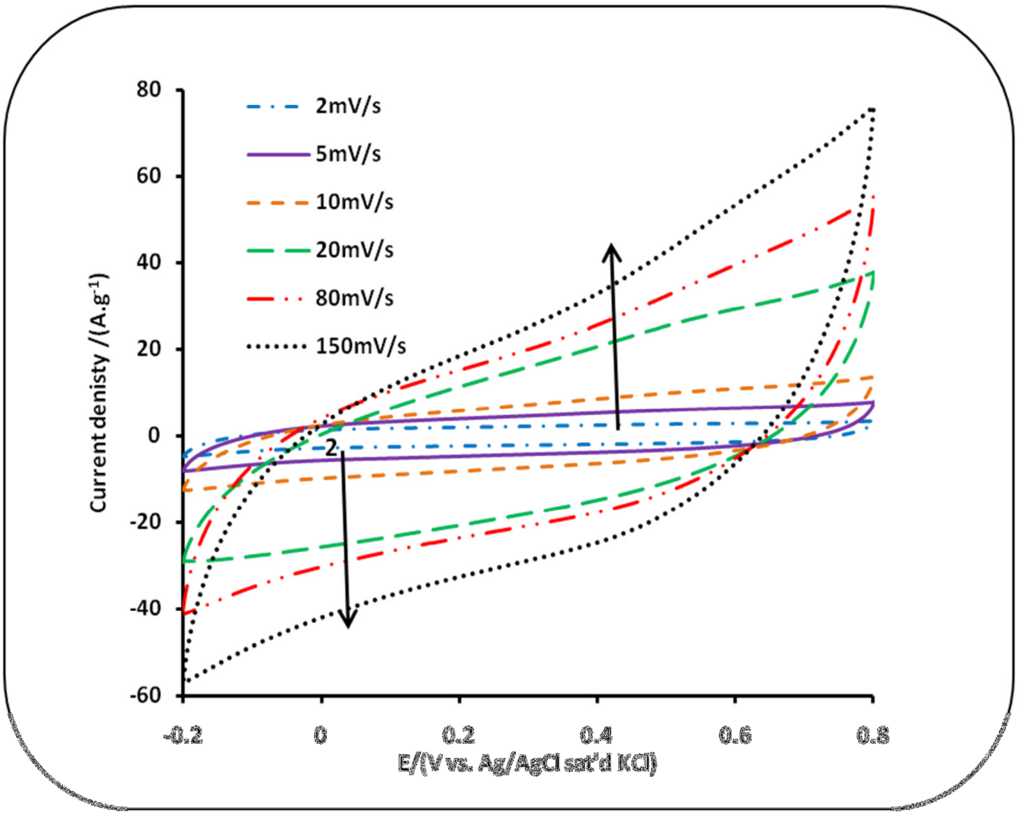

Figure 4.8: Cyclic voltammograms of MWCNT(15%)-MnO_2 at various potential scan rate from in 1.0 M Na_2SO_4

SEM images have shown that the MnO_2 is porous. At high scan rate the electrolyte ions do not have sufficient time to penetrate to the inner pores of the material. The interaction between the electrode and the electrolyte is mainly at the surface and therefore, capacitance decreases as scan rate increases (10). The capacitance of the MnO_2 pure system and composite in H_2SO_4 and alkaline medium could not be done due to the complexities in these electrolytes. MnO_2 has been found to dissolve in H_2SO_4 solution while in alkaline medium, it gives several irreversible redox peaks. The presence of adsorbed H_2O as confirmed by TGA and FTIR and the absence of noticeable redox peaks in the cyclic voltammogram curves suggest that the charge storage mechanism is in accordance with mechanism as shown by Equation 4.2.

Thus, the charge storage is a surface process. This suggests that for the composites, their storage of charges might be through both double layer capacitance and pseudocapacitance.

As outlined in Chapter 1, the pseudocapacitance storage mechanism is not essentially by redox process but proton intercalation that happens at the surface of the electrode (11) as presumed to be the case for the composites.

4.2.2. Galvanostatic charge-discharge experiments

Galvanostatic charge-discharge (c-d) has been found to be the best and accurate method for determination of specific capacitance (12). Figure 4.9(a)–(e) shows the galvanostatic charge-discharge curves of various electrodes of MnO_2 and MnO_2 composites in 1.0M Na_2SO_4 at the current density of 2 $A.g^{-1}$.

In Figure 4.9, c-d curves of all electrodes are almost symmetrical and mirror images of each other. The discharge curves are also linear in the entire potential range showing that the electrode materials used have good capacitive behaviour. The triangular shape of charge and discharge cycle is indicative that the electrodes have good capacitive behaviour and high reversibility. Specific capacitance was calculated from the Equation 4.4:

$$\frac{\quad}{\quad} \qquad (4.4)$$

where, I is the discharging current applied (A), Δt is the discharging time (s), m is the mass of the active electrode (g) and ΔE is the discharge voltage difference. The

Specific capacitances calculated from charge-discharge curves for MWCNTs, MnO_2 and the composites electrodes using equation 4.4 are given in Table 4.2.

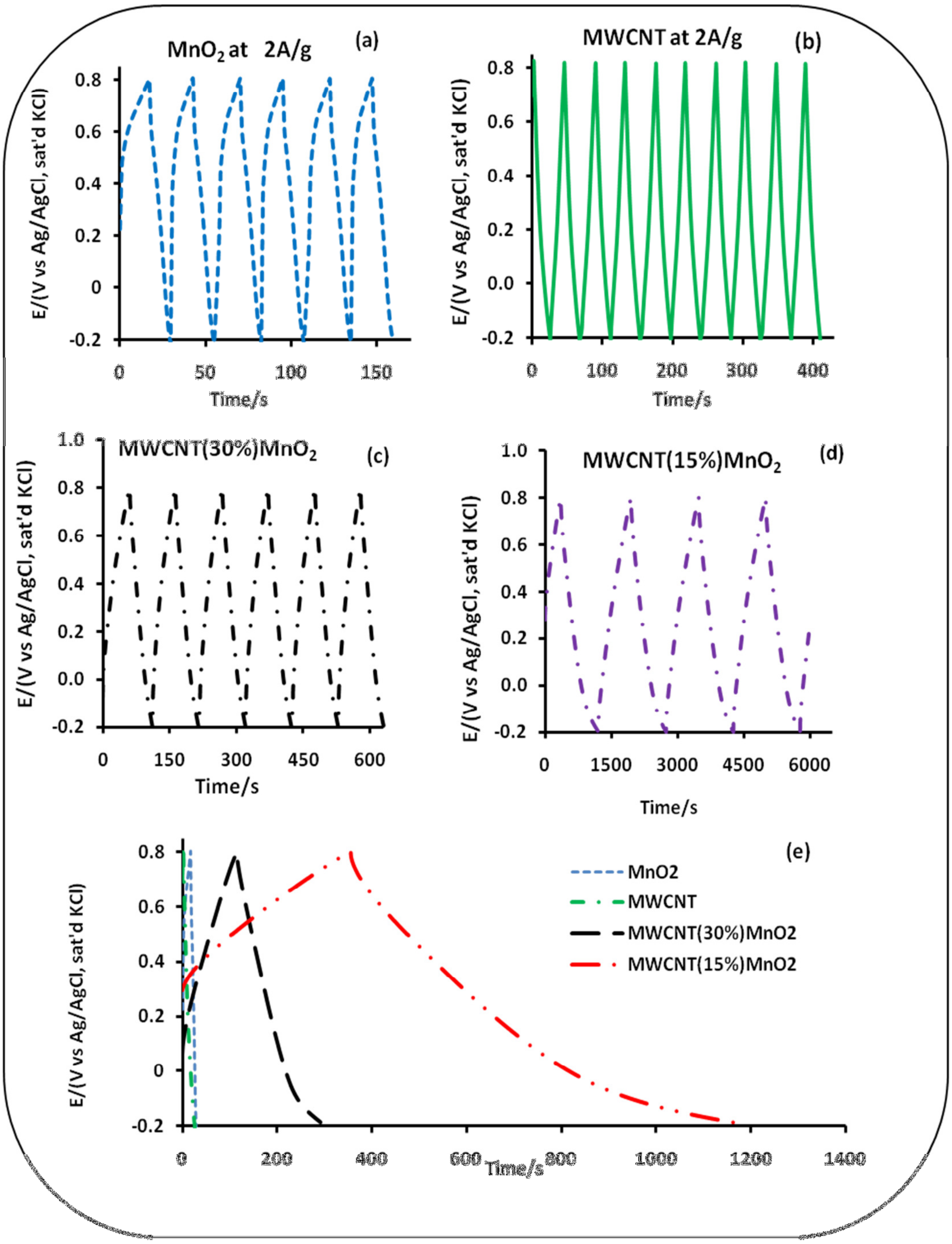

Figure 4.9: Galvanostatic charge-discharge curves of (a) MnO_2, (b) MWCNT, (c) MWCNT(30%)-MnO_2, (d) MWCNT(15%)-MnO_2 and (e) comparative electrodes at a current density of 2 $A.g^{-1}$ in 1.0 M Na_2SO_4.

Table 4.2: Supercapacitive parameters of MnO2 systems.

Electrode	Specific capacitance/($F.g^{-1}$)	Energy efficiency/%
MnO_2	45	97
MWCNT	44	99
MWCNT(30%)-MnO_2	207	101
MWCNT(15%)-MnO_2	1209	99

MWCNT(15%)-MnO_2 gave the highest capacitance of 1209 $F.g^{-1}$, which is six times higher than the value of the MWCNT(30%)-MnO_2. The high capacitance of MWCNT(15%)-MnO_2 composite can be attributed to the good surface area network provided by 15% MWCNT composition and to the moderate diffusion rate, moderate mobility in aqueous solutions and moderate adsorption-desorption rate of Na_2SO_4 (13). It can be assumed that the 15% of MWCNT is an ideal composition to give an entangled network that gives the best surface area and good conductivity (2). The energy deliverable efficiency was calculated using equation 1.18. All the electrodes have great energy efficiency which is above 97% and (Table 4.2) this indicates good electrochemical reversibility.

Current density studies were performed for MWCNT (15%)-MnO_2 (Figure 4.10). The results suggest that as current density increases, specific capacitance decreases. The decrease of specific capacitance is due to surface energy storage process of MnO_2 electrode. The hydrated Na^+ ions from the electrolyte have enough time at low current density to access the pores of the porous MnO_2 composites while at high current density, some pores become unreachable. In order to evaluate the electrochemical stability of the best performing MWCNT(15%)MnO_2 electrode suitability for good performance as a supercapacitor, galvanostatic charge-discharge measurements were performed in 1.0 M Na_2SO_4 between -0.2 V and 0.8 V. Figure 4.11 shows the cycle stability of MWCNT(15%)-MnO_2 at 2 $A.g^{-1}$. Greater loss of capacitance happened within 100 first cycle. This could be due to non-activation of the electrode prior to measurements. After 100th cycle the electrode lost 30% of its specific capacitance at cycle 500. Figure 4.11 shows a long cycle performance of MWCNT(15%)-MnO_2 electrode in 1.0 M Na_2SO_4 aqueous electrolyte at 2 $A.g^{-1}$.

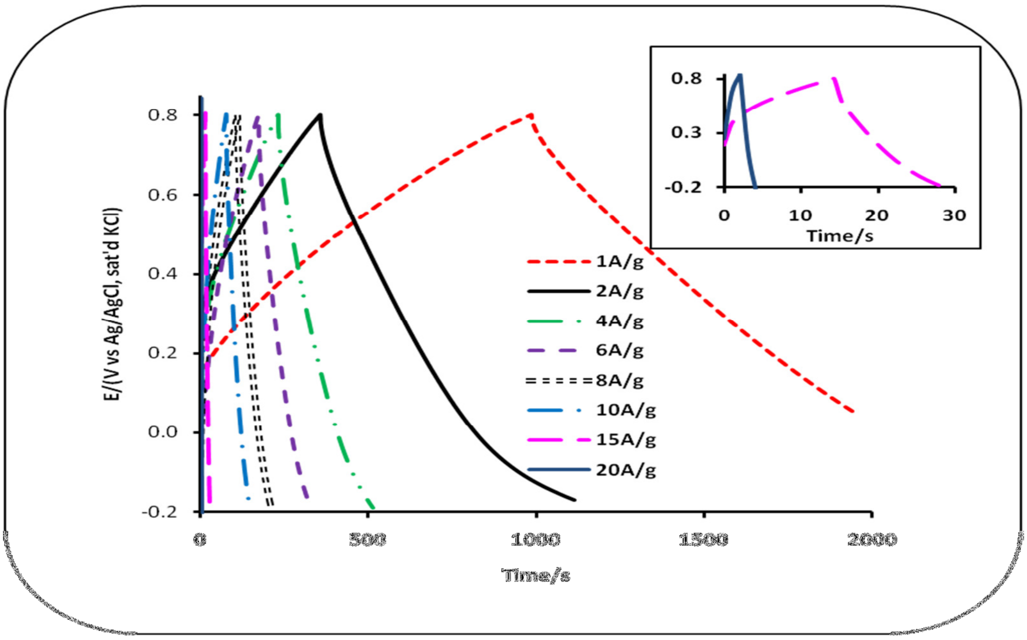

Figure 4.10: Galvanostatic charge-discharge of MWCNT(15%)-MnO_2 at different current densities.

For the first 100 cycles capacitance drops significantly and thereafter stabilises indicating that the electrode could be utilized for EC applications. The change of c-d profiles of the MWCNT(15%)-MnO_2 electrode at the 2nd and 500th cycle is shown in

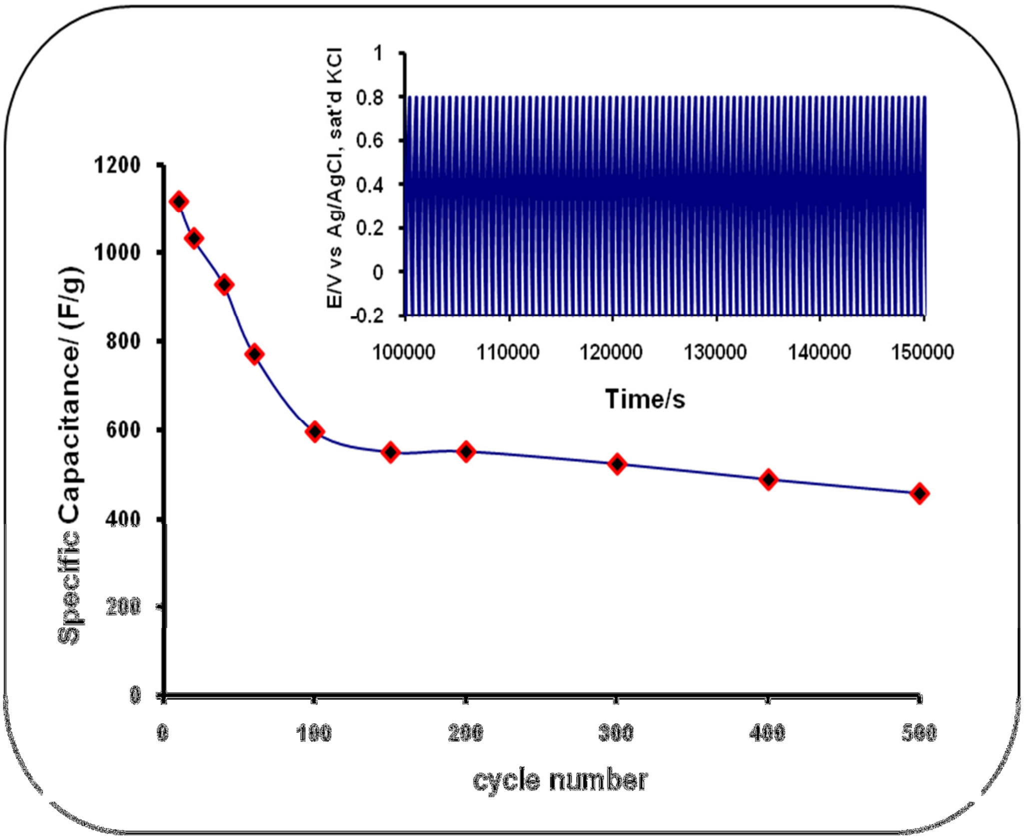

Figure 4.11: Cycle life of MWCNT(15%)-MnO_2 at current density of 2 $A.g^{-1}$. The inset shows the charge-discharge cycles around 500 cycles.

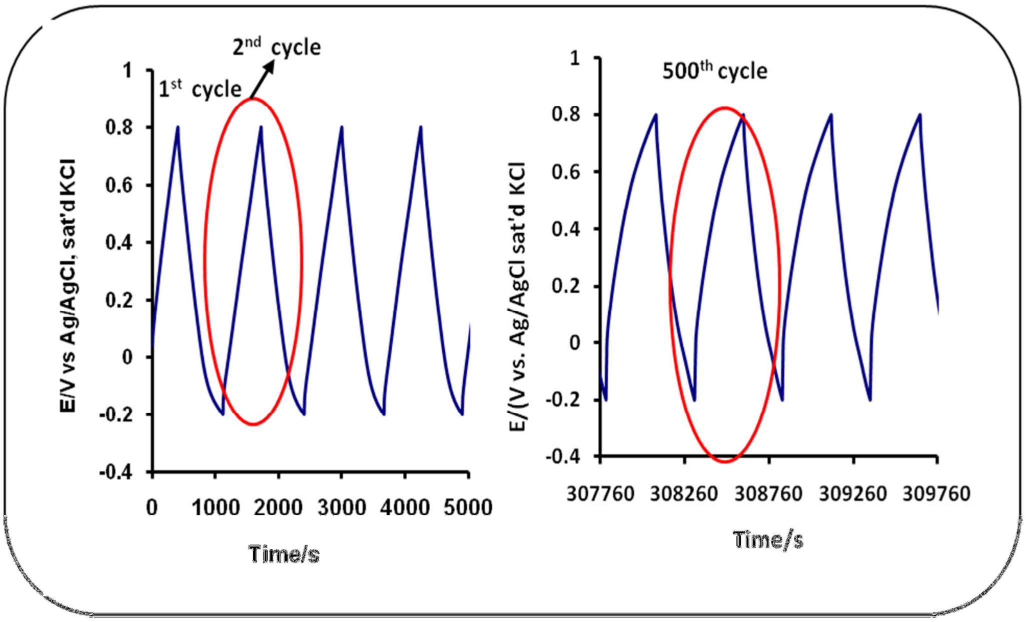

Figure 4.12: Charge-discharge curves for cycle 2 (a) and cycle 500 (b) at a current density of 2 $A.g^{-1}$.

4.2.3. Electrochemical Impedance spectroscopy (EIS) experiments

Electrochemical impedance spectroscopy (EIS) is the best method to interrogate and evaluate the electrical properties of the electrode materials such as electrical conduction, ion transfer and capacitance (10, 14). Nyquist (complex-plane impedance) plots at 0.3 V vs. Ag/AgCl for MWCNT, MnO_2, MWCNT(15%)-MnO_2 and MWCNT(30%)-MnO_2 are shown in Figure 4.13. For MWCNT the Nyquist plot exhibits a straight line perpendicular to the imaginary axis which implies that the MWCNT electrode is ideally polarizable. For the composites a depressed semicircle at a higher frequency and a slopping line is observed at low frequency.

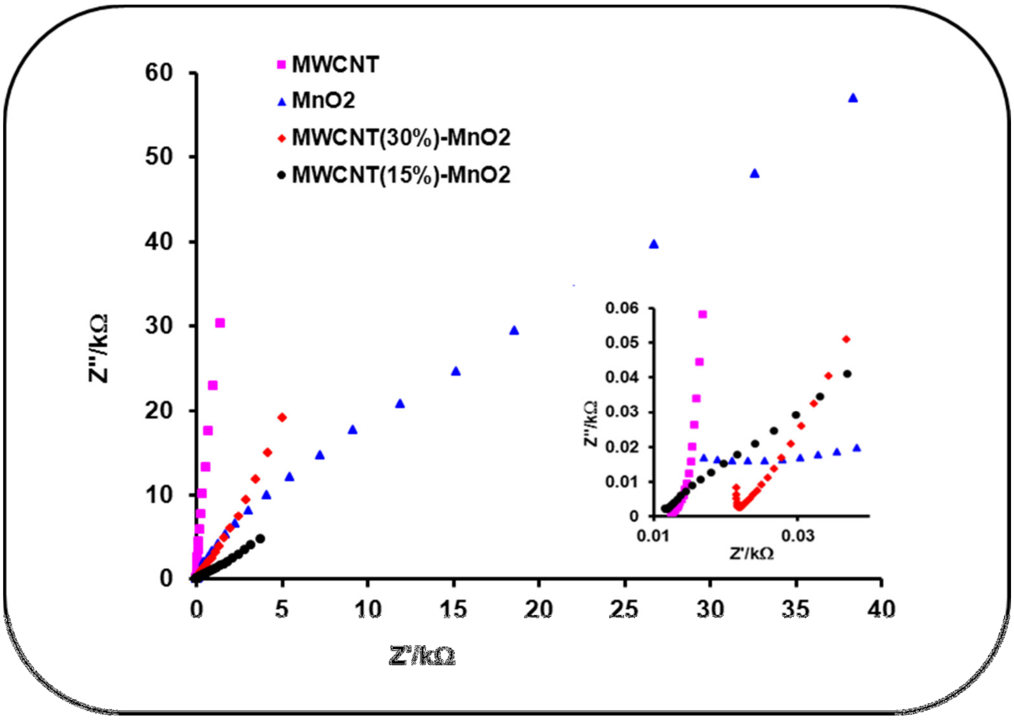

Figure 4.13: Nyquist plot of various electrodes in 1.0 M Na_2SO_4 measured at 0.3 V between 10 kHz to 10 MHz. Inset: expanded nyquist plots.

The inset of the Nyquist plots shows that the MWCNT(15%)-MnO_2 has smaller internal resistance than any other electrodes. Internal resistance consists of ionic resistance of an electrolyte, contact resistance between the electrode and current collector and intrinsic resistance of an electro-active material (2, 15). From the Nyquist plot the ionic resistance of MWCNT, MnO_2, MWCNT(30%)-MnO_2 and MWCNT(15%)-MnO_2 has been found to be about 12 Ω, 17 Ω, 22 Ω and 11 Ω, respectively. The latter electrode has the lowest ionic resistance, and this could have contributed to its high specific capacitance as compared to other electrodes.

This also confirms that the composite with 15% of MWCNT has better interconnectivity between MnO_2 particles. From Figure 4.13 and 4.14, knee frequency (which is a measure of charge transfer in an electrochemical reaction) has been found to be 0.48 kHz, 1.45 kHz, 1.10 kHz and 3.31 kHz for MnO_2, MWCNT, MWCNT(30%)-MnO_2 and MWCNT(15%)-MnO_2, respectively.

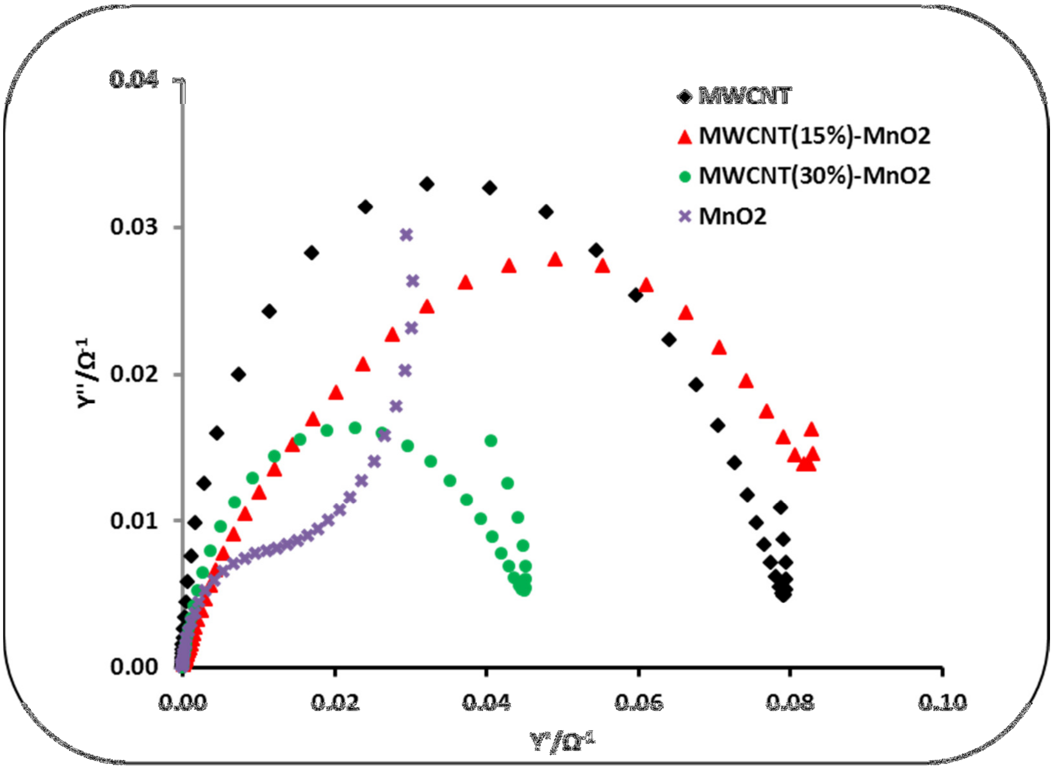

Figure 4.14: Admittance plots of MWCNT, MnO_2, MWCNT(15%)-MnO_2 and MWCNT(30%)-MnO_2

The higher knee frequency of the latter electrode implies a better electrochemical response and thus confirms c-d results already found that MWCNT(15%)-MnO_2 has highest specific capacitance.

Phase angle (Figure 4.15) of the electrodes follows the trend: MWCNT(15%)-MnO_2 < MWCNT(15%)-MnO_2 < MnO_2 < MWCNT. All the phase angle observed (Table 4.3) were above 45° indicating that all electrode materials are suitable for supercapacitor application (16). MWCNT(15%)-MnO_2 gave the best response time amongst all the electrodes studied. This indicates that the electrode can be charged and discharged at a rapid rate (16, 17).

Table 4.3: Supercapacitive parameters of MnO2 based systems from EIS.

Electrolyte: 1.0 M Na_2SO_4, Frequency range = 10 kHz – 10 mHz, amplitude = 5 mV

Electrode	**Specific capacitance/ $F.g^{-1}$**	**Knee frequency/ KHz**	**Phase angle/º**	**Response time /ms**
MnO_2	14	0.48	75	2
MWCNT	26	1.45	88	0.7
MWCNT(30%)-MnO_2	41	1.10	73	0.9
MWCNT(15%)-MnO_2	169	3.31	57	0.3

The specific capacitance (C_{sp}) from EIS was calculated according to the following equation (18-20):

3.5 where *Z″* is the imaginary part of the impedance and *f* is the measurement frequency.

MWCNT(15%)-MnO$_2$ gave highest specific capacitance of 169 F.g^{-1} as compared to the other electrodes.

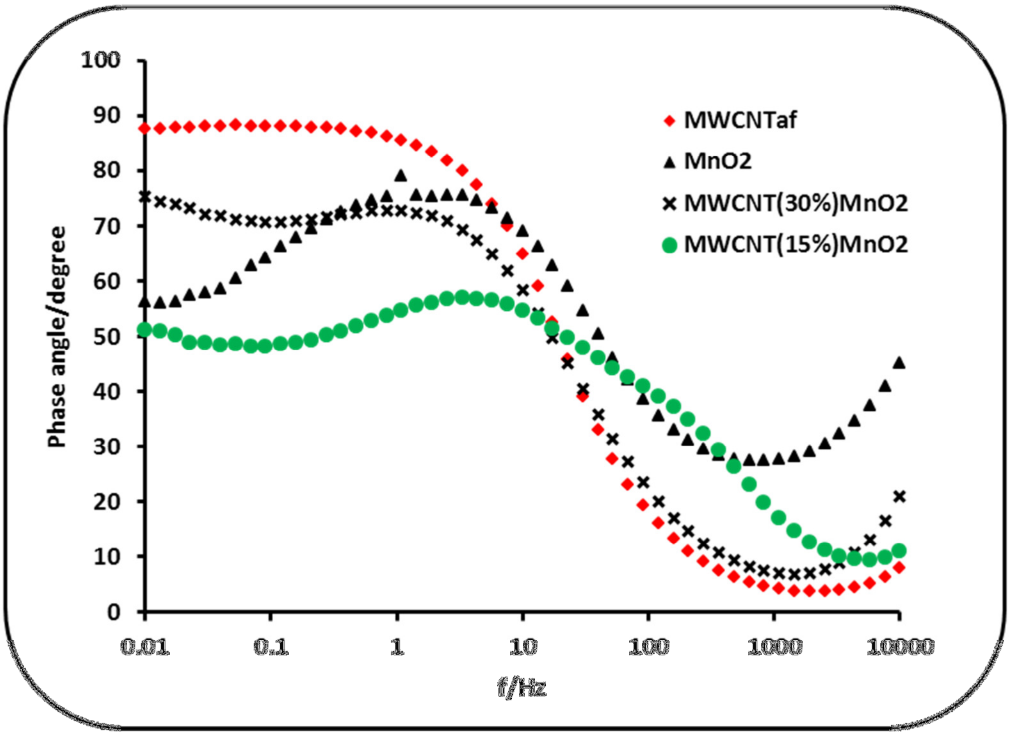

Figure 4.15: Bode plots of MWCNT, MnO$_2$, MWCNT(15%)-MnO$_2$ and MWCNT(30%)-MnO$_2$

Between 0.1 Hz and 1 Hz, Cs for MWCNT(15%)-MnO$_2$ decreases significantly with the increase in frequency. It can be assumed that at this frequency range, the Na$^+$ ions have greater accessibility into the material.

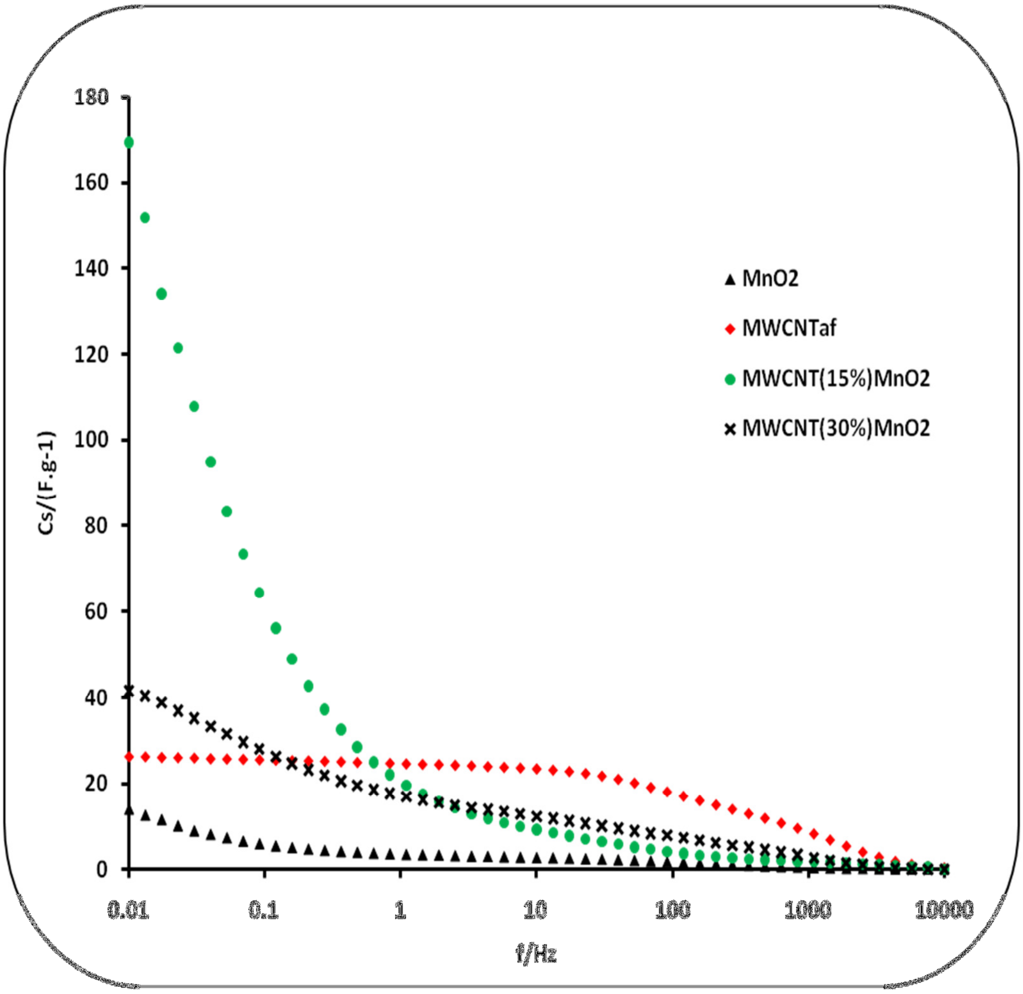

Figure 4.16: Frequency dependence of specific capacitance of MWCNT, MnO_2, MWCNT(15%)-MnO_2 and MWCNT(30%)-MnO_2

4.3. Conclusion

MnO_2, MWCNT(15%)-MnO_2 and MWCNT(30%)-MnO_2 were synthesised by reduction of $KMnO_4$ with aniline. The electrodes exhibited good capacitive behaviour. The specific capacitance of MWCNT(15%)-MnO_2 was 1209 $F.g^{-1}$, six times larger than the specific capacitance of MWCNT(30%)-MnO_2. This good electrochemical behaviour can be attributable to increase in conductivity in the composite, better interconnectivity among the MnO_2 particles and accessibility of MnO_2 particles (1, 10). The Cs of MWCNT(15%)-MnO_2 is a promising supercapacitor electrode material considering its good cycle stability, lowers internal resistance and good electrochemical reversebility. This MWCNT(15%)-MnO_2 electrode performs well at lower frequency as shown by EIS.

4.4. References.

1. Ragupathy P, Vasan HN, Munichandraiah N. Synthesis and Characterization of Nano-MnO2 for Electrochemical Supercapacitor Studies. Journal of The Electrochemical Society. 2008;155(1):A34-A40.

2. Xie X, Gao L. Characterization of a manganese dioxide/carbon nanotube composite fabricated using an in situ coating method. Carbon. 2007;45(12):2365-73.

3. Reddy RN, Reddy RG. Synthesis and electrochemical characterization of amorphous MnO_2 electrochemical capacitor electrode material. Journal of Power Sources. 2004;132(1-2):315-20.

4. Reyhani A, Mortazavi SZ, Golikand AN, Moshfegh AZ, Mirershadi S. The effect of various acids treatment on the purification and electrochemical hydrogen storage of multi-walled carbon nanotubes. Journal of Power Sources. 2008;183(2):539-43.

5. Jiang Q, Qu MZ, Zhou GM, Zhang BL, Yu ZL. A study of activated carbon nanotubes as electrochemical super capacitors electrode materials. Materials Letters. 2002;57(4):988-91.

6. Xiao W, Xia H, Fuh JYH, Lu L. Growth of single-crystal α-MnO_2 nanotubes prepared by a hydrothermal route and their electrochemical properties. Journal of Power Sources. 2009;193(2):935-8.

7. Pang S-C, Anderson MA, Chapman T, W. Novel Electrode Materials for Thin-Film Ultracapacitors: Comparison of Electrochemical Properties of Sol-Gel-Derived

and Electrodeposited Manganese Dioxide. Journal of The Electrochemical Society. 2000;147(2):444-50.

8. Lee HY, Goodenough JB. Supercapacitor Behavior with KCl Electrolyte. Journal of Solid State Chemistry. 1999;144(1):220-3.
9. Kelliher EM, Rose T, L. Simulation electrodes based on MnO_2 thin film: Electrical properties in carbonate buffered saline. MRS Fall Meeting; 1985; Boston, Massachusetts. MRS; 1985. p. 287.
10. Subramanian V, Zhu H, Wei B. Synthesis and electrochemical characterizations of amorphous manganese oxide and single walled carbon nanotube composites as supercapacitor electrode materials. Electrochemistry Communications. 2006;8(5):827-32.
11. Conway BE, Birss V, Wojtowicz J. The role and utilization of pseudocapacitance for energy storage by supercapacitors. Journal of Power Sources. 1997;66(1-2):1-14.
12. Conway BE. Electrochemical supercapacitors: scientific fundamentals and technological applications. Plenum Press; 1999.
13. Xu C, Li B, Du H, Kang F, Zeng Y. Supercapacitive studies on amorphous MnO_2 in mild solutions. Journal of Power Sources. 2008;184(2):691-4.
14. Guerrero DJ, Ren X, Ferraris JP. Preparation and Characterization of Poly(3-arylthiophene)s. Chemistry of Materials. 1994;6(8):1437-43.
15. Yan J, Fan Z, Wei T, Cheng J, Shao B, Wang K, et al. Carbon nanotube/MnO_2 composites synthesized by microwave-assisted method for supercapacitors

with high power and energy densities. Journal of Power Sources. 2009;194(2):1202-7.

16. Xu J, Gao L, Cao J, Wang W, Chen Z. Preparation and electrochemical capacitance of cobalt oxide (Co_3O_4) nanotubes as supercapacitor material. Electrochimica Acta. 2010;56(2):732-6.
17. Du C, Pan N. Supercapacitors using carbon nanotubes films by electrophoretic deposition. Journal of Power Sources. 2006;160(2):1487-94.
18. Kötz R, Carlen M. Principles and applications of electrochemical capacitors. Electrochimica Acta. 2000;45(15-16):2483-98.
19. Justin P, Meher SK, Rao GR. Tuning of Capacitance Behavior of NiO Using Anionic, Cationic, and Nonionic Surfactants by Hydrothermal Synthesis. The Journal of Physical Chemistry C. 2010;114(11):5203-10.
20. Meher SK, Justin P, Ranga Rao G. Microwave-Mediated Synthesis for Improved Morphology and Pseudocapacitance Performance of Nickel Oxide. ACS Applied Materials & Interfaces. 2011;3(6):2063-73.

CHAPTER 5

SUPERCAPACITIVE BEHAVIOUR OF CoTPyzPz-MWCNT NANOCOMPOSITES

5.1. Physical characterisation of CoTPyzPz-MWCNT nanocomposites

5.1.1. Comparative microscopic images

Figure 5.1 displays FESEM images of various MWCNTs, CoTPyzPz and CoTPyzPz at 1.00 keV after sonication in DMF. MWCNTaf are less entangled as compared to MWCNTPhNH$_2$.

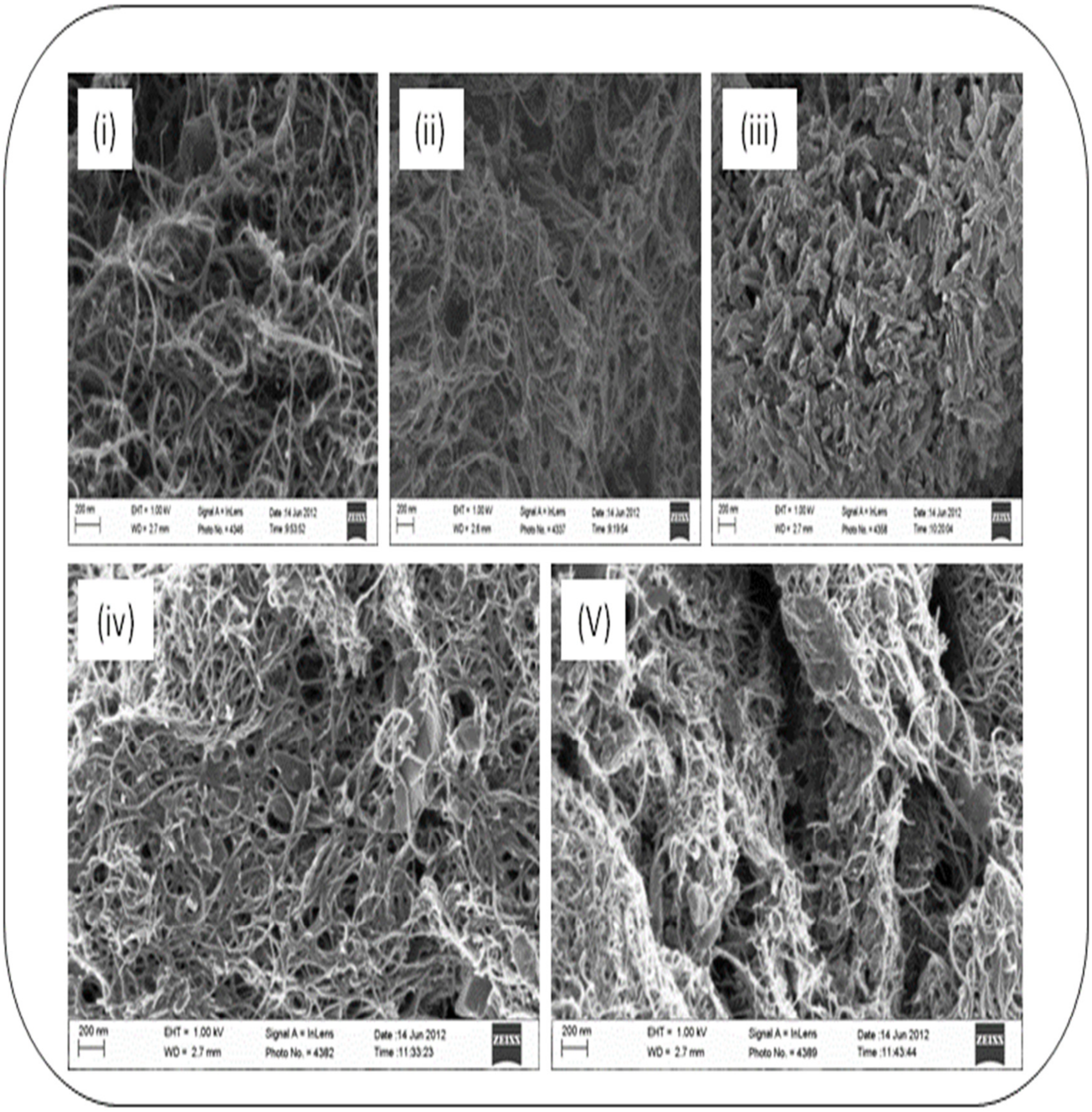

Figure 5.1: Typical FESEM images of (i) MWCNTaf, (ii) MWCNTPhNH$_2$, (iii) CoTPyzPz, (iv) MWCNTaf-CoTPyzPz and (v) MWCNTPhNH$_2$-CoTPyzPz.

From the micrographs, it can be seen that MWCNTaf provides interconnectivity between the CoTPyzPz particles and seems also to wrap around the particles. In Figure 5.1 (v), MWCNTPhNH$_2$-CoTPyzPz shows less entanglement and connectivity. MWCNTs interactions result in their entanglement when drying after their deposition onto a substrate (1). Du *et al.* (2) reported that open porous entangled CNTs with high surface area contribute to easy access of solvate ions to the electrode-electrolyte interface.

Figure 5.2 shows the energy dispersive X-ray (EDX) images of CoTPyPyz and MWCNTaf-CoTPyzPz and outlines that C, N and Co are major elemental composition of the material analysed. Elements such as thallium could be remnants of a starting reagent or deposits during gold plating of the sample for EDX analysis.

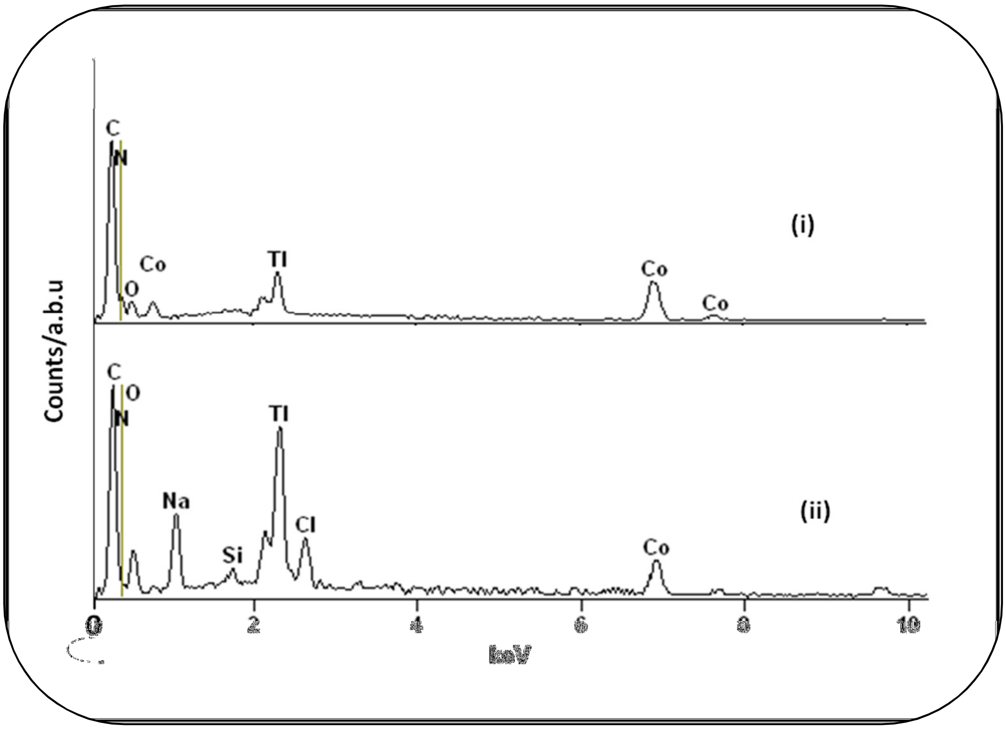

Figure 5.2: EDX spectra of (i) CoTPyzPz and (ii) MWCNTaf-CoTPyzPz.

5.1.2. Comparative FTIR

The FTIR spectra shown in Figure 5.3, depicts the functional groups found in MWCNTaf, MWCNTPhNH$_2$, CoTPyzPz, MWCNTaf-CoTPyzPz and MWCNTPhNH$_2$-CoTPyzPz. The peak at 3436 cm^{-1} can be ascribed to (O-H) stretching vibration in MWCNTaf and MWCNTaf-CoTPyzPz, and while a peak at 3447 cm^{-1} in MWCNTPhNH$_2$ and MWCNTPhNH$_2$-CoTPyzPz can be ascribed to N-H stretching vibration. The stretching (C-N) vibration at 1115 cm^{-1} in Figure 5.3 confirms the functionalization of MWCNT with phenylamine. Acid functionalization of MWCNTs is confirmed by the carbonyl peak around 1728 cm^{-1} in Figure 5.3.

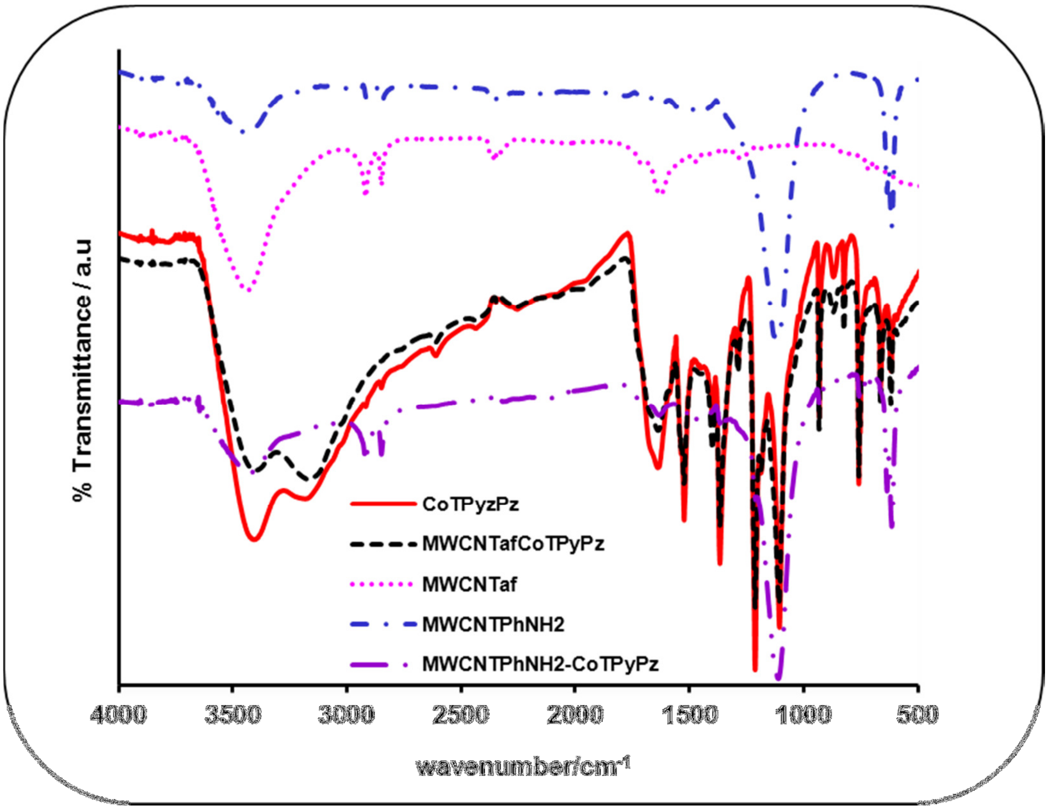

Figure 5.3: FTIR spectra of MWCNTPhNH$_2$, MWCNTPhNH$_2$-CoTPyzPz, MWCNTaf, MWCNTaf-CoTPyzPz and CoTPyzPz.

The metal ligand (M-N) vibration band is observed at around 823 $cm^{-1,}$ and this indicates strong bonding between the metal ion and the four surrounding nitrogen atoms in the pyrrole rings (3). Peaks at 1647 cm^{-1}, 1637 cm^{-1} and 1656 cm^{-1} for MWCNTPhNH$_2$-CoTPyzPz, MWCNTaf-CoTPyzPz and CoTPyzPz, respectively are indicative of C=N bond in porphyrazine core.(4)

5.1.3. Comparative UV-Vis analysis

Figure 5.4 shows the UV-Vis spectra of MWCNTaf, MWCNTPhNH$_2$, CoTPyzPz, MWCNTaf-CoTPyzPz and MWCNTPhNH$_2$-CoTPyzPz in DMF. The electronic spectra show an intense and broad peak around 624 nm, 630 nm and 628 nm for CoTPyzPz, MWCNTaf-CoTPyzPz and MWCNTPhNH$_2$-CoTPyzPz, respectively. These peaks are due to a transition and are ascribed as Q bands.

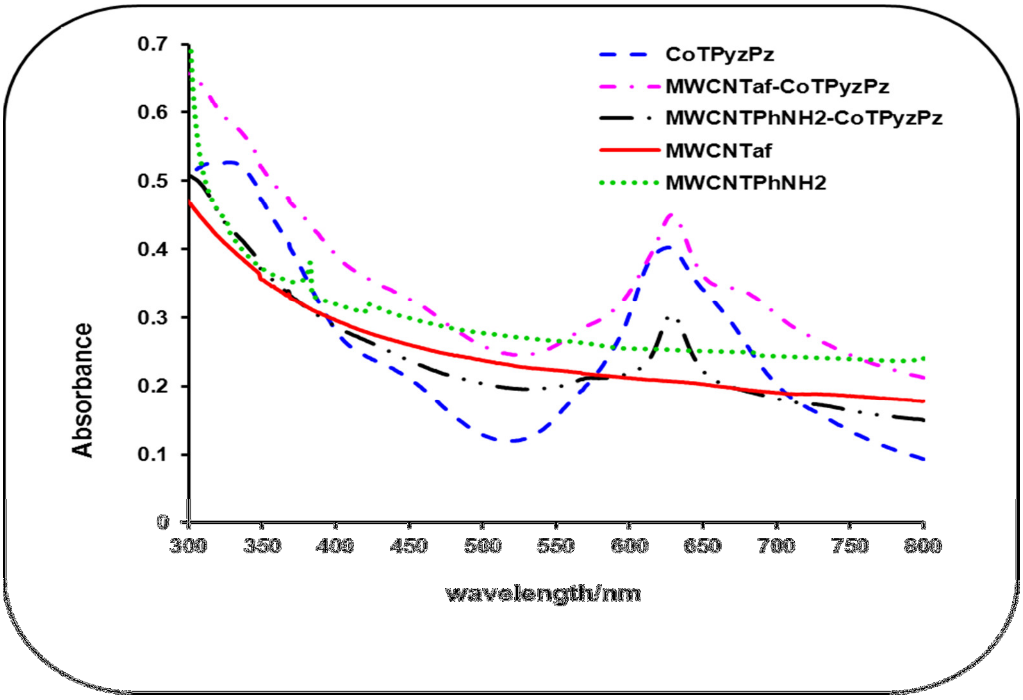

Figure 5.4: UV-Vis spectra of MWCNTaf, MWCNTPhNH$_2$, CoTPyzPz, MWCNTaf-CoTPyzPz and MWCNTPhNH$_2$-CoTPyzPz.

The Q band shifted to the red with about 4 nm and 6 nm, indicative of a smaller HOMO-LUMO (5, 6) gap in CoTPyzPz composites. This also indicates that the incorporation of the pyrazine rings expand the -conjugated system (7). The value of the Q band found is in comparable to the value found by Uslu Kobak *et al.* (8). No peaks are observed for MWCNTaf and MWCNTPhNH$_2$.

The Q-band has a red shift due an expansion of the π conjugated system (9). A single Q band depicts a tetrapyrrollic macrocycle with D_{4h} symmetry (10). Soret bands (B band) of CoTPyzPz, MWCNTaf-CoTPyzPz and MWCNTPhNH$_2$-CoTPyzPz were at 327 nm, 280 nm and 276 nm, respectively. The B-Bands of the CoTPyzPz composites are red-shifted. Onay *et al.* (11) reported that a broad band of metallated porphyrazine molecule is observable within 300 nm – 400 nm range as stipulated in literature for metallated porphyrazine. The Q-band is much broader which suggests that the molecules of CoTPyzPz and its composites had aggregated (12, 13).

5.1.4. Comparative Thermogravimetry

The TG and DTG curves of MWCNTaf, MWCNTPhNH$_2$, CoTPyzPz, MWCNTaf-CoTPyzPz and MWCNTPhNH$_2$-CoTPyzPz are shown in Figure 5.5(a). Physically and chemically adsorbed water molecules were released between 0 °C and 300 °C. The TG curves show that the materials have an average weight loss of 90% except for MWCNTPhNH$_2$ and CoTPyzPz which showed weight loss of 35 % and 70 %, respectively. From the results, the order of stability based on the initial decomposition of the compounds or composites is as follows:

$MWCNT_{af}$ > $MWCNTPhNH_2$ > MWCNTp > CoTPyPz > $MWCNTPhNH_2$-CoTPyzPz >

$MWCNYT_{af}$CoTPyPz

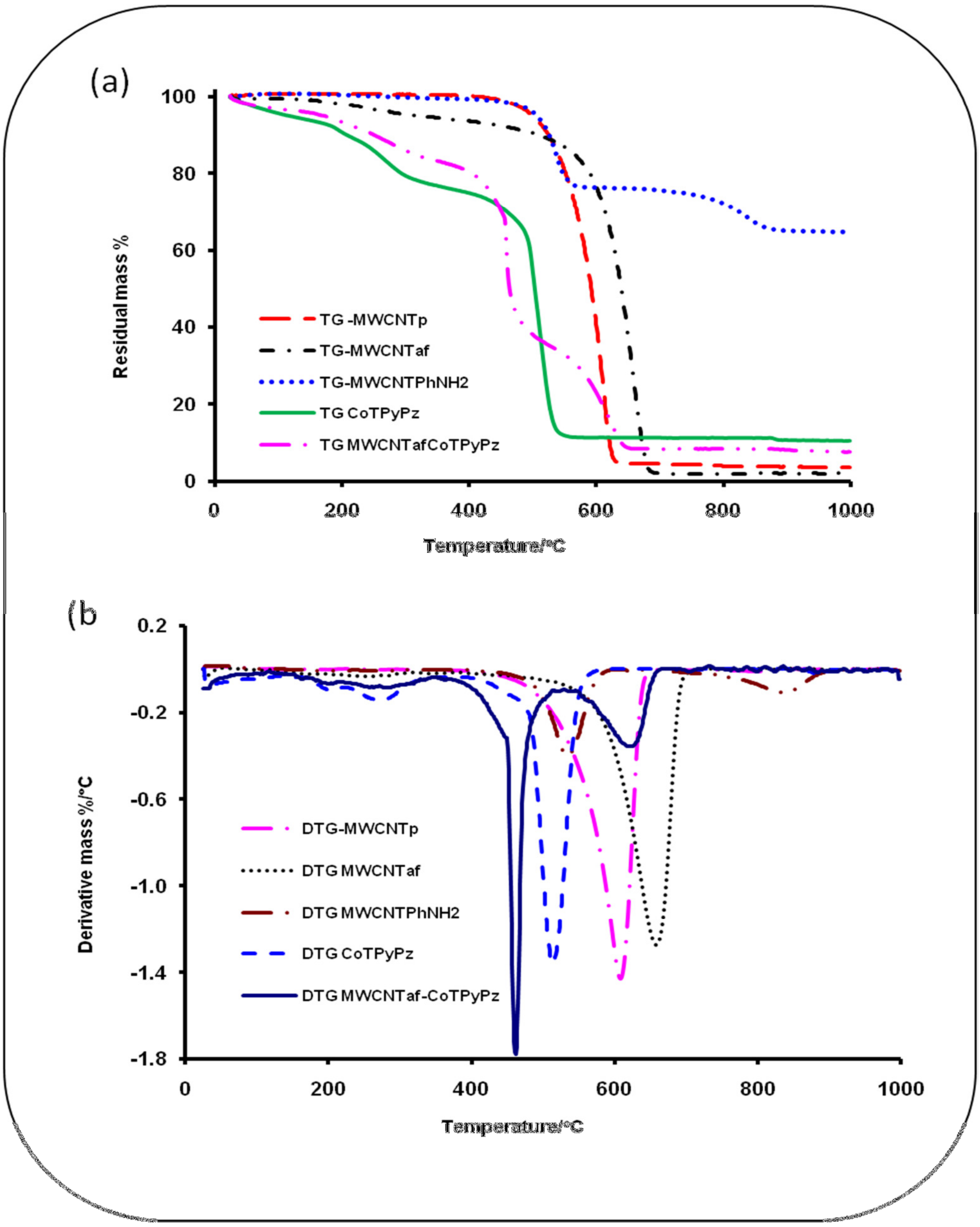

Figure 5.5: Thermogravimetric curves (a) and Differential Thermogravimetric curves (b) of MWCNT (pristine), MWCNTaf, ($MWCNTPhNH_2$, CoTPyzPz, $MWCNTPhNH_2$-CoTPyzPz and MWCNTaf-CoTPyzPz

All of the substances have about 90% residual weight loss except MWCNTPhNH$_2$ and MWCNTPhNH$_2$-CoTPyzPz, which have 35% and 70% residual weight loss respectively. The DTG curves [Figure 5.6(b)] of pristine and acid functionalised MWCNT decompose in a one step process while CoTPyPz, MWCNTPhNH$_2$ and composites undergo two or more thermal decomposition steps. From the results it can be deduced the highest stable material is MWCNTaf which has the highest onset temperature than the other materials (14).

5.2. Supercapacitive behaviour of MWCNT-CoTPyzPz

5.2.1. Cyclic voltammetry analysis

Figure 5.6 compares cyclic voltammetric evolutions of MWCNTaf, MWCNTPhNH$_2$, CoTPyzPz, MWCNTaf-CoTPyzPz and MWCNTPhNH$_2$-CoTPyzPz electrodes in 1.0 M H_2SO_4 at 10 mV.s^{-1} scan rates. Figure 5.7 shows the cyclic voltammetric evolutions of bare BPPG, MWCNTaf and MWCNTPhNH$_2$. CV evolutions of MWCNTaf and MWCNTPhNH$_2$ have deviated from a rectangular shape which depicts utilisation of EDL storage mechanism. The same phenomenon is observed for the same electrodes in 1.0 M Na_2SO_4 electrolyte (Figure 5.9). The current separation of MWCNTaf is bigger than of MWCNTPhNH$_2$ (Table 5.1). The current separation of these carbon electrodes is bigger in H_2SO_4 than in Na_2SO_4. The enhancement of capacitance can be attributed to the oxidative functionalization of MWCNTs. Oxidative functionalization introduces oxygen functionalities and increases MWCNTs wettability. Niu *et al.* (15) reported a value of 113 F.g^{-1} after CNT chemical oxidation.

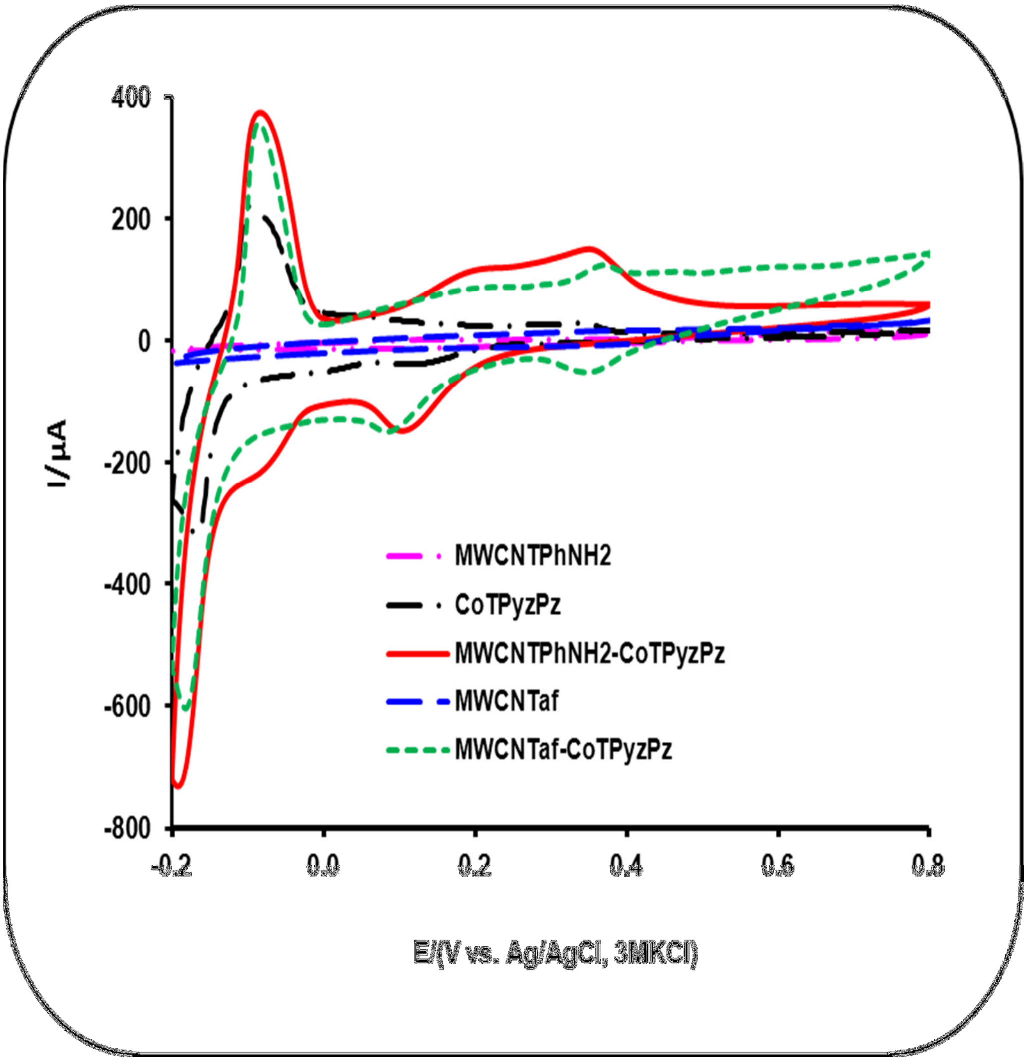

Figure 5.6: Comparative cyclic voltammograms of various electrodes in 1.0 M H_2SO_4 electrolyte at 10 mV.s^{-1}.

Capacitance of functionalised MWCNT can be increased by psuedocapacitance by some of the following redox reactions (16):

5.1

5.2

The curve for MWCNTPhNH$_2$ (Figure 5.7) is not perfectly rectangular, and the anodic region is not the mirror image of the cathodic region.

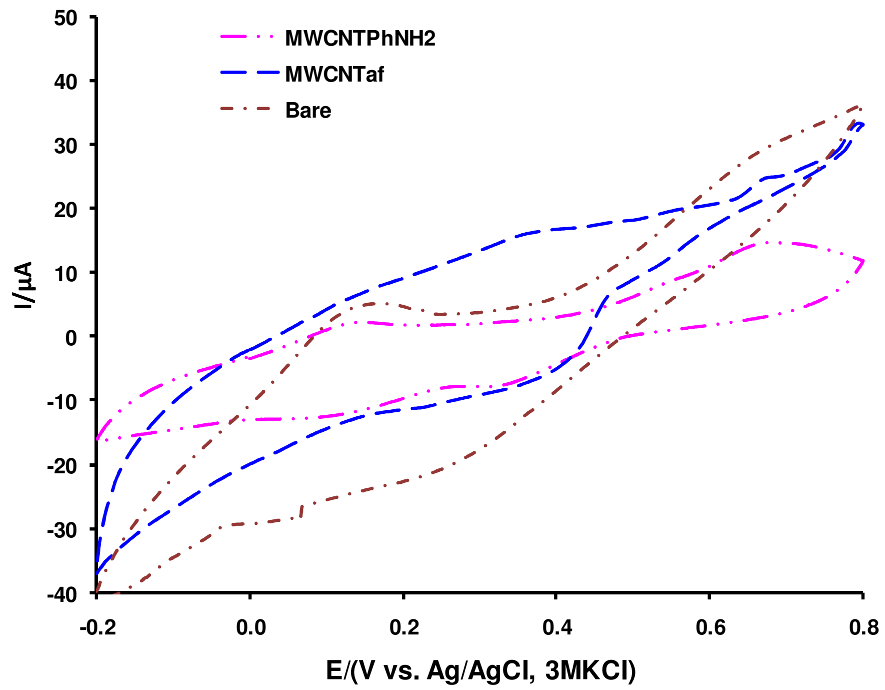

Figure 5.7: Comparative cyclic voltammograms of Bare BPPG, MWCNTaf and MWCNTPhNH$_2$ electrodes in 1.0 M H_2SO_4 electrolyte at 10 mV.s^{-1}.

Hulicova-Jurcakova *et al.* (17) concluded that nitrogen surface functionalities on MWCNT enhance capacitance in accordance with the following equations:

5.3

5.4

Cyclic voltammograms of CoTPyzPz, MWCNTaf-CoTPyzPz and MWCNTPhNH$_2$-CoTPyzPz (Figure 5.6) in 1.0 M H_2SO_4 are not rectangular-shaped, and the anodic scan is not a mirror image of the cathodic scan. The current separation of MWCNTaf-

CoTPyzPz CV is much bigger than the other electrode materials. The CV curves of CoTPyzPz, MWCNTaf-CoTPyzPz and MWCNTPhNH$_2$-CoTPyzPz (Figure 5.6) show several redox peaks. Peaks found on the CV curves are given in Table 5.1. There are two peaks, one anodic and the other cathodic that are prominent in 1.0 M H_2SO_4. Deviation of the CVs from rectangular shape and redox peaks illustrate that charge storage in these materials is enhanced by pseudocapacitance.

Table 5.1: CV data of various electrodes at 10 mV.s^{-1} in 1.0 M H_2SO_4.

	Redox Processes					
Electrode	**Anodic Peak/V**			**Cathodic peak/V**		
	I	II	III	IV	V	VI
CoTPyzPz	-0.100	-	0.334	-	0.107	-0.167
MWCNTPHNH$_2$-CoTPyzPz	-0.093	0.173	0.342	-	0.115	-0.185
MWCNTaf-CoTPyzPz	-0.097	-	0.356	0.361	0.097	-0.176

A redox process with the $E_{1/2}$ at -0.134, -0.139 and -0.137 for CoTPyzPz, MWCNTPhNH$_2$-CoTPyzPZ and MWCNTaf-CoTPyzPz respectively may be the attributed to the protonation and deprotonation of the complexes. Hulicova-Jurcakova *et al.* (17) reported that carbonised melamine mica composites have superior capacitance due to the pyridinic and pyrrolic nitrogen content. There are several types of nitrogens in tetrapyrazino porphyrazine (H_2TPyzPz) that are susceptible to protonation. Ledson *et al.* (18) and Beeby *et al.* (19) reported that azomethine nitrogens in phthalocyanine can be protonated in an acidic medium. Hulicova-Jurcakova *et al.* (17) assumed that protonation of H_2TPyzPz occurs first at azomethine nitrogens. They also concluded that H_2TPyzPz can be deprotonated. Theodoridis *et al.* (20) also confirmed that the high electronegativity of H_2TPyzPz is due to meso methine nitrogens. Villano *et al.* (21) reported that in macrocycle like H_2TPyzPz, stepwise one-electron reductions occur due to electron deficiency of the entire macrocycle. It can be assumed that a superior specific capacitance observed in 1.0 M H_2SO_4 electrolyte for electrode materials (CoTPyzPz, MWCNTaf-CoTPyzPz and MWCNTPhNH$_2$-CoTPyzPz) in the present study can be due to protonation and deprotonation process. MWCNTaf-CoTPyzPz gave the highest specific capacitance in acidic electrolyte of 723 F.g^{-1}. This specific capacitance is 5 times the value of CoTPyzPz and 10 times the value of MWCNTaf. As reported previously, MWCNTaf provides a porous network which is favourable for CoTPyzPz to form a composite that has good electrochemical performance. The values for the specific capacitance shown in Table 5.2 are calculated from the formula:

$$— \qquad 5.5$$

where average current is (A), ν is the scan rate (V.s^{-1}) and m is the mass of the active electrode mass (g). Figure 5.8 shows cyclic voltammograms of MWCNTaf, MWCNTPhNH$_2$, BPPG, CoTPyzPz, MWCNTPhNH$_2$-CoTPyzPz and MWCNTaf-CoTPyzPz while Figure 5.9 shows only the first three electrodes in 1.0 M Na_2SO_4 at 10 mV.s^{-1} scan rate. The last three electrodes exhibit cyclic voltammograms that are non-rectangular and unsymmetrical. This type of CVs with well-resolved anodic and cathodic peak depicts a contribution to specific capacitance by a pseudocapacitive storage mechanism. The redox couple at about $E_{1/2}$ = 0.169 V for MWCNTPhNH$_2$-CoTPyzPz in 1.0 M Na_2SO_4 might be due Na^+ ion incorporation in the porphyrazine complex. The high electronegative porphyrazine complex can also enhance the diffusion of the Na^+ into its surface. Good reversibility of the fast charge-discharge response is illustrated by the increasing peak current as scan rate increases (22) (Figure 5.10).

Table 5.2: Specific capacitance of CoTPyzPz based systems from CV at various scan rates in 1.0 M Na_2SO_4 and 1.0M H_2SO_4.

Electrode	**Gravimetric Specific capacitance at various scan rates in two electrolytes between -0.2 and 0.8 V.**					
	2 mV.s^{-1}		**10 mV.s^{-1}**		**25 mV.s^{-1}**	
	1.0 M Na_2SO_4	**1.0 M H_2SO_4**	**1.0 M Na_2SO_4**	**1.0 M H_2SO_4**	**1.0 M Na_2SO_4**	**1.0 M H_2SO_4**
MWCNTPhNH$_2$	23	90	19	37	11	20
MWCNTaf	34	69	27	39	20	25
CoTPyzPz	68	144	22	92	19	66
MWCNTPhNH$_2$-CoTPyzPz	219	455	86	249	68	168
MWCNTaf-CoTPyzPz	369	723	116	270	60	177

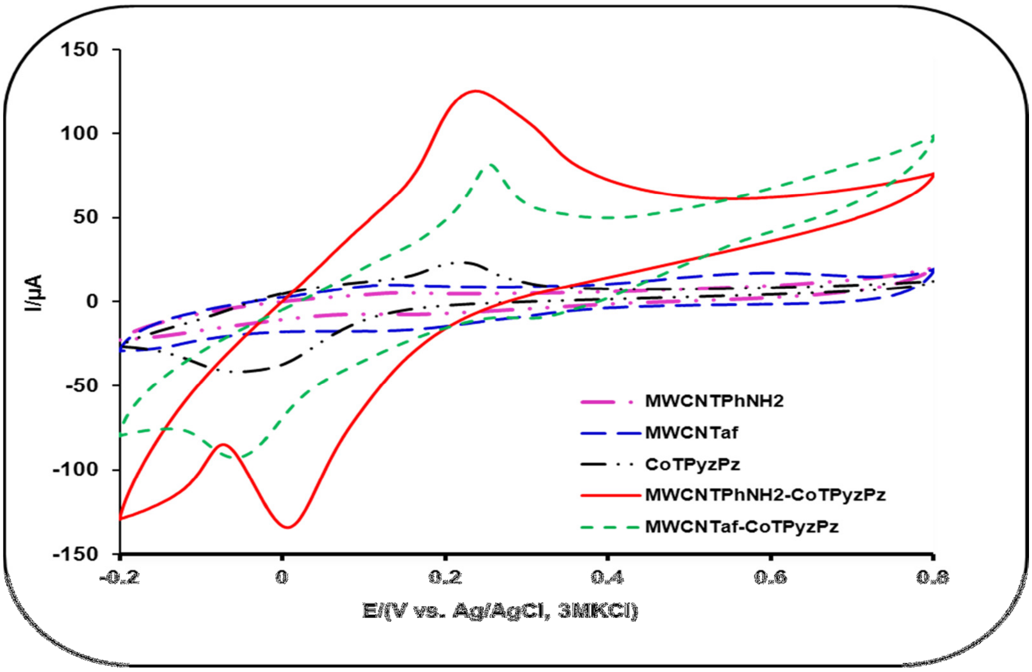

Figure 5.8: Comparative cyclic voltammograms of Bare BPPG, MWCNTaf, MWCNTPhNH$_2$, MWCNTaf-CoTPyzPz and MWCNTPhNH$_2$-CoTPyzPz electrodes in 1.0 M Na$_2$SO$_4$ electrolyte at 10 mV.s^{-1}.

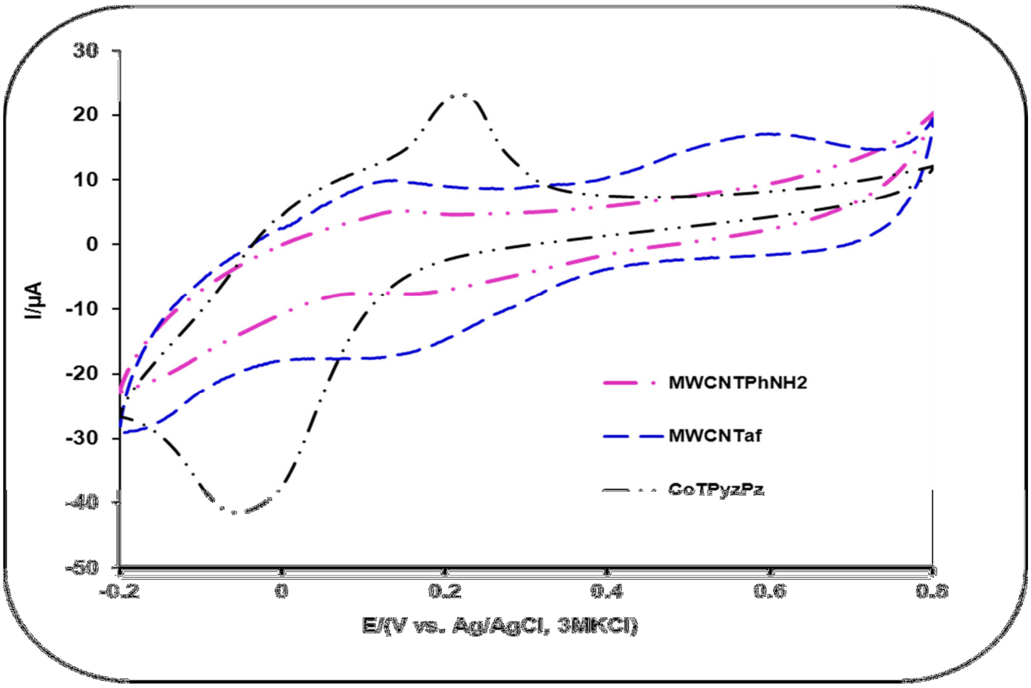

Figure 5.9: Comparative cyclic voltammograms of MWCNTaf, MWCNTPhNH$_2$ and CoTPyzPz electrodes in 1.0 M Na$_2$SO$_4$ electrolyte at 10 mV.s^{-1}.

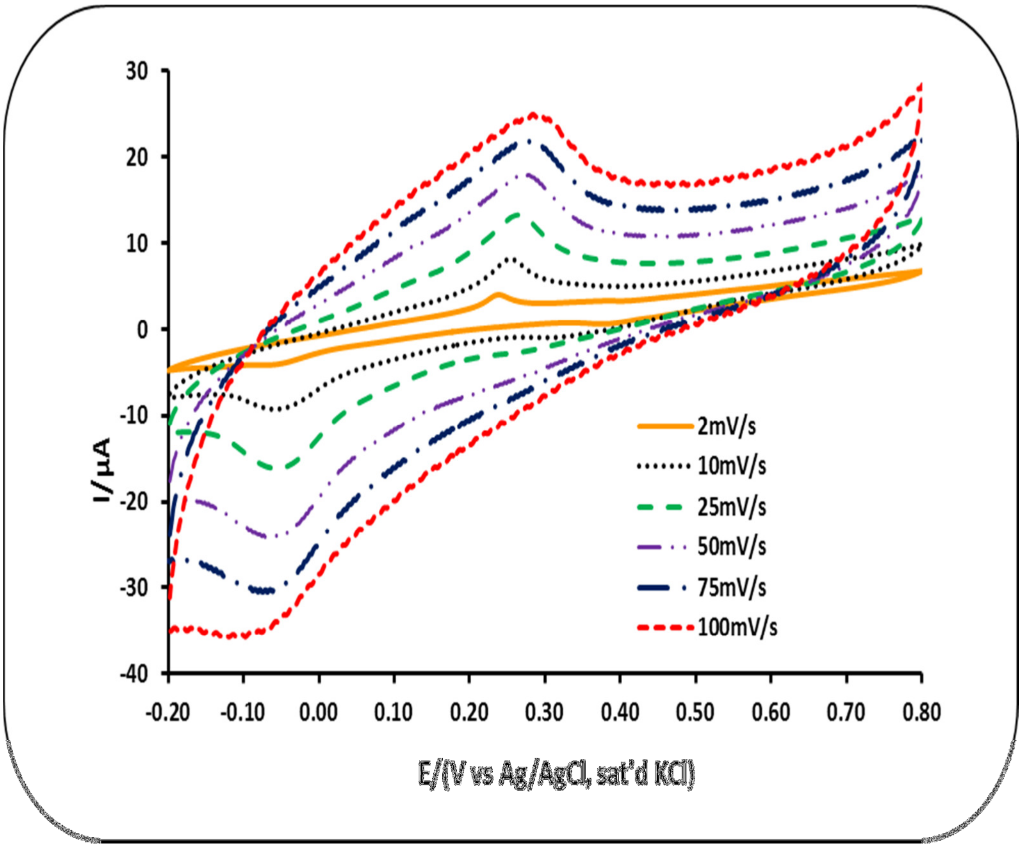

Figure 5.10: Cyclic voltammogram evolutions of $MWCNTPhNH_2$-CoTPyzPz in 1.0 M Na_2SO_4 at different scan rates.

5.2.2. Galvanostatic charge-discharge analysis

Galvanostatic charge-discharge measurements were done in 1.0 M H_2SO_4 and 1.0 M Na_2SO_4 to evaluate the electrochemical properties of the functionalised MWCNTs and composites of CoTPyzPz. Figure 5.11 displays comparative charge-discharge curves of MWCNTs and CoTPyzPz composites electrodes measured at a current density of 1 $A.g^{-1}$ in 1.0 M Na_2SO_4 with potential varied from -0.2 V to 0.8 V versus Ag/AgCl. MWCNTaf and $MWCNTPhNH_2$ electrodes have linear charge-discharge curves, indicating double layer capacitor behaviour.

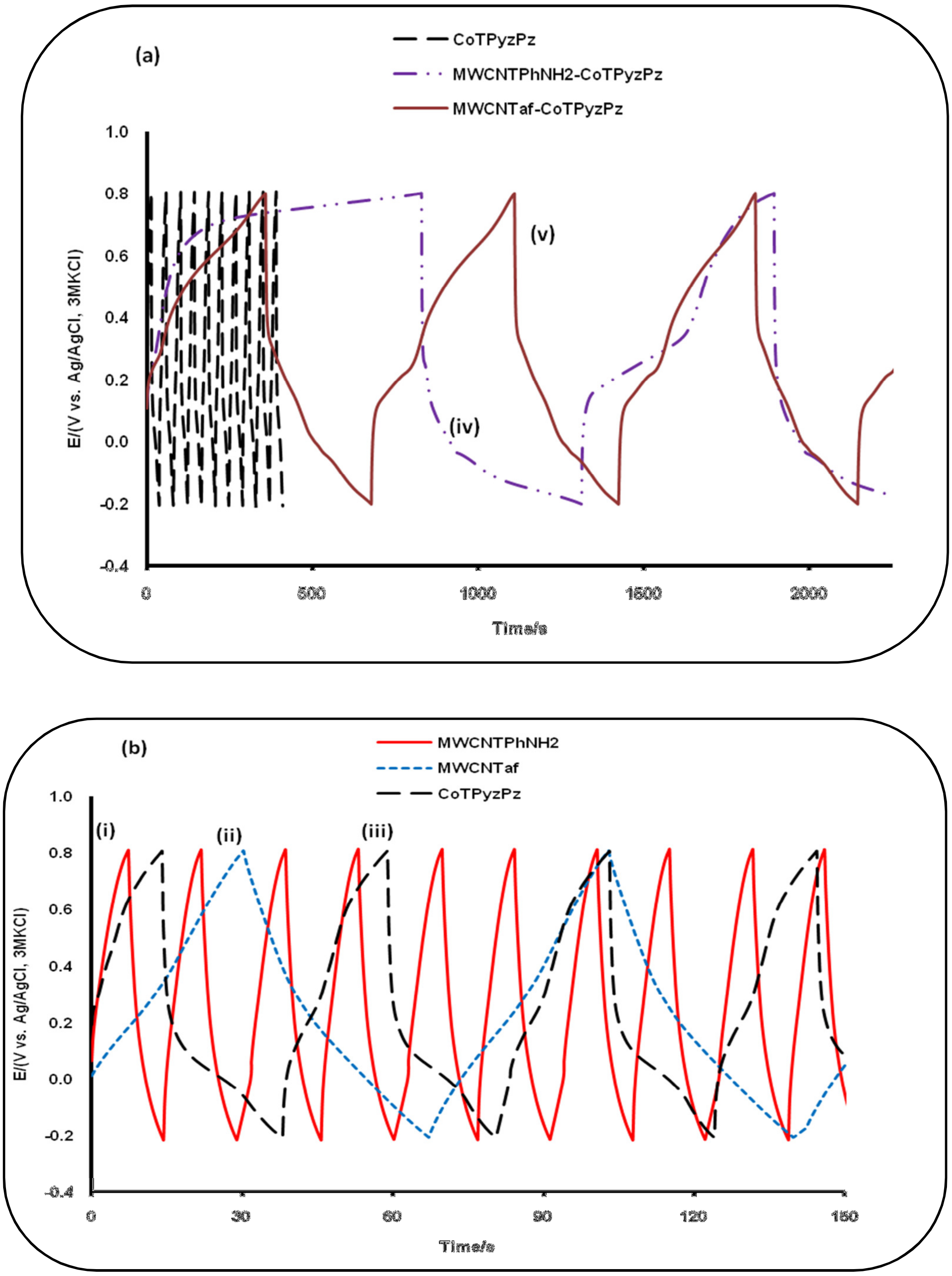

Figure 5.11: (a) Charge-discharge (c-d) curves of (iv) MWCNTPhNH$_2$-CoTPyzPz and (v) MWCNTaf-CoTPyzPz in 1.0 M Na$_2$SO$_4$ at 1 A.g^{-1}. (b) c-d curves of (i) MWCNTPhNH$_2$, (ii) MWCNTaf and (iii) CoTPyzPz.

MWCNTaf and MWCNTPhNH$_2$ electrodes show good reversibility since their charge and discharge curves are mirror images of other. MWCNTPhNH$_2$-CoTPyzPz and MWCNTaf-CoTPyzPz c-d curves are non-linear, typical for electrodes that exhibit pseudocapacitor behaviour. The curves depict a non-linear dependence of voltage on time. The Specific capacitance of the electrodes was estimated from the equation:

——— 5.6

where, I is the discharging current applied (A), Δt is the discharging time (s), m is the mass of the active electrode (g) and ΔE is the discharge voltage difference. The specific capacitance values in Na_2SO_4 for all the electrodes are shown in Table 5.3:

Table 5.3: Supercapacitive parameters of CoTPyzPz based systems in neutral electrolyte from charge-discharge

	Electrolyte: 1.0 M Na_2SO_4, current density = 1 $A.g^{-1}$			
Electrode	**Specific capacitance/ ($F.g^{-1}$)**	**Energy efficiency/ %**	**Specific Energy/ $Whkg^{-1}$**	**Specific Power/ Wkg^{-1}**
$MWCNTPhNH_2$	7	80	7.0	1007
MWCNTaf	37	97	10	995
CoTPyzPz	20	91	5.7	1011
$MWCNTPhNH_2$-CoTPyzPz	351	83	97	1000
MWCNTaf-CoTPyzPz	299	76	83	1001

From the above results it can be seen that the combination of MWCNTs and CoTPyzPz in 1:1 mass ratio enhances specific capacitance drastically. The tenfold increase of specific capacitance of the composites can be attributable to interconnectivity of CoTPyzPz particles by MWCNTs as seen from the SEM images (figure 5.1). It should be noted that MWCNTs possess high surface area, and they are highly porous; thus the electrolyte ions can easily penetrate and interact with CoTPyzPz molecules, which are embedded within the MWCNTs network. Figure 5.12 displays comparative charge-discharge curves of MWCNTs and CoTPyzPz composites electrodes measured at a current density of 1 $A.g^{-1}$ in 1.0 M H_2SO_4 with voltage varied from -0.2 to 0.8 V. Charge-discharge curves of MWCNTaf and $MWCNTPhNH_2$ deviate slightly from linearity, where potential is time dependent. This outlines that MWCNTs show a double layer capacitive behaviour. The c-d curves of CoTPyzPz, MWCNTaf-CoTPyzPz and $MWCNTPhNH_2$-CoTPyzPz show non uniform linearity between 0.8 V and 0.1 V with a significant deviation from linearity between -0.2 V and 0.1 V. Non-linearity of charge–discharge curves of MWCNTaf-CoTPyzPz clearly outlines the pseudocapacitance behaviour of the material in the voltage range -0.2 V to 0.8 V. The pseudocapacitive behaviour of the electrodes confirms the result found from CV studies. The charge-discharge profiles of CoTPyzPz, MWCNTaf-CoTPyzPz and $MWCNTPhNH_2$-CoTPyzPz electrodes show a plateau between -0.2 V and 0 V. Seel *et al.* (23) have reported that the intercalation and de-intercalation of PF_6^- ion into graphite is indicated by plateau (24) on the charge-discharge profile.

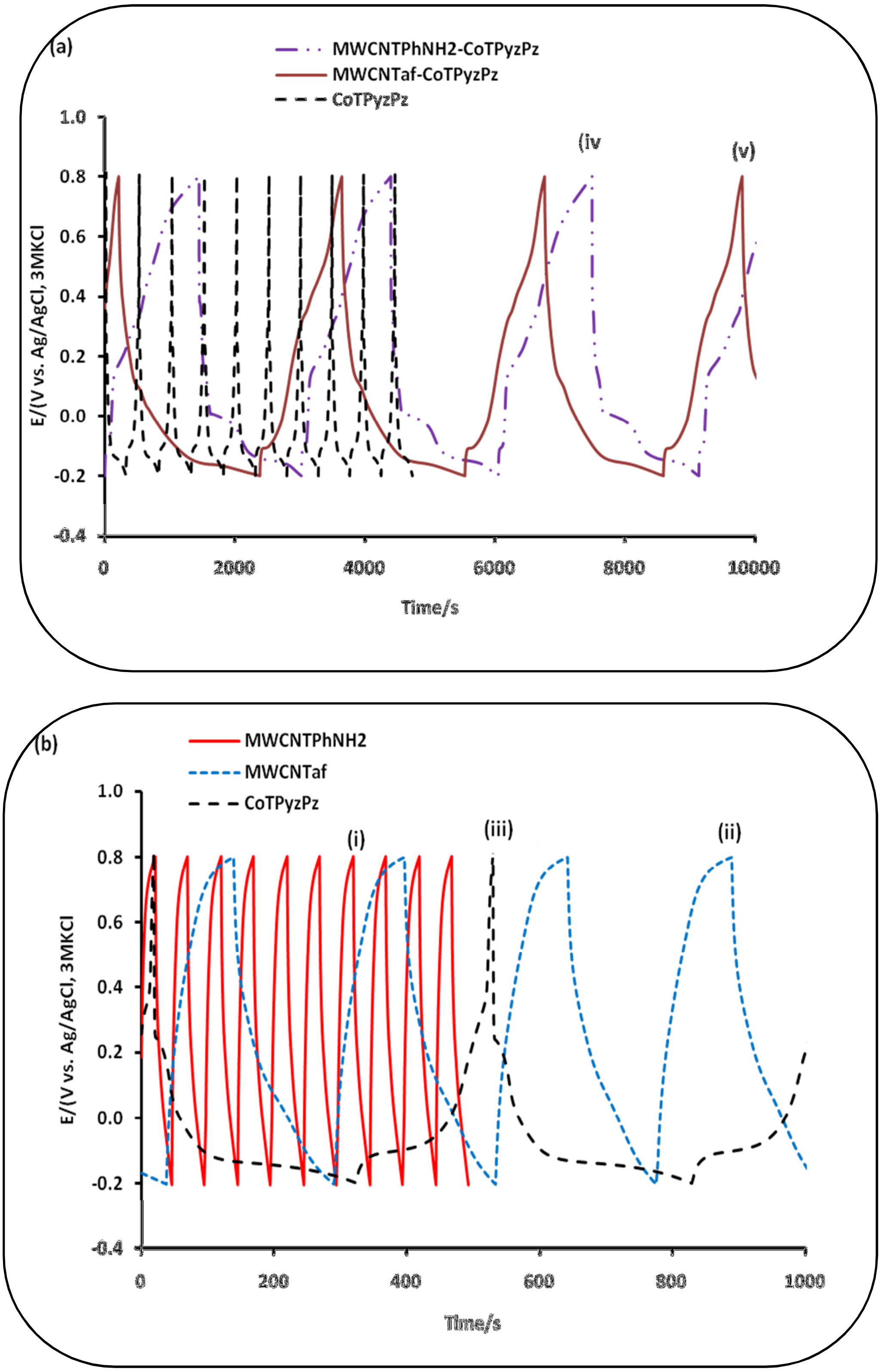

Figure 5.12: Charge-discharge curves of (iv) MWCNTPhNH$_2$-CoTPyzPz and (v) MWCNTaf-CoTPyzPz in 1.0 M H_2SO_4 at 1 A.g^{-1}. (b) Charge-discharge curves of (i) MWCNTPhNH2, (ii) MWCNTaf and (iii) CoTPyzPz in 1M H_2SO_4 at 1 A.g^{-1}.

The observed plateau in the studied electrodes is assumed to be due to the protonation and deprotonation of the porphyrazine macromolecule. The specific capacitance values in H_2SO_4 were found to increase in the following order:

MWCNTPhNH$_2$-CoTPyzPz (1902 F.g^{-1}) > MWCNTaf-CoTPyzPz (1642 F.g^{-1}) > CoTPyzPz (287 F.g^{-1}) > MWCNTPhNH$_2$ (132 F.g^{-1}) > MWCNTaf (25 F.g^{-1})

It should be noted that the capacitance of MWCNTPhNH$_2$ exceeded that of MWCNTaf. This could be due to the wettability of the electrode material because of the incorporation of the phenylamine groups. Both composites, MWCNTaf-CoTPyzPz and MWCNTPhNH$_2$-CoTPyzPz gave highest specific capacitances as compared to other materials. The Specific capacitances of these composites are about 6 times higher than the specific capacitance of CoTPyzPz. The high specific capacitance may be due to increased wettability and or the increased surface area of the electroactive material when mixed with open tubular network of MWCNTs. Several authors gave several possibilities that explained the increased specific capacitance in the composites they studied. Chidembo *et al.* (25) reported that the high specific capacitance (981 F.g^{-1}) of MWCNT-NiTAPc composite may be due to high surface area, porous nature of the nanocomposite and the incorporation of amine groups on the phthalocyanine ring. Zhang *et al.* (26) reported that CNTs open tubular network makes them a good support for active materials. Obreja *et al.* (27) reported that MWCNTs in an aqueous electrolyte have threefold increase in capacitance due to their hydrophilicity caused by functionalization of MWCNTs with surface hydroxyl groups. Yuan *et al.* (28) summarised the enhancement of capacitance of hybrid composites of CNTs and pseudocapacitive materials as due to (i) synergy between EDLCs and pseudocapacitors (ii) open mesoporous network formed by the entanglement of CNTs that allow ions to diffuse into the active surface, which lowers ESR and high resilience of CNTs. Hall *et al.* (29) reported that incorporation of heteroatoms on CNTs increases wettability.

Figure 5.13 shows that specific capacitance of MWCNTaf-CoTPyzPz decreases as current density increases.

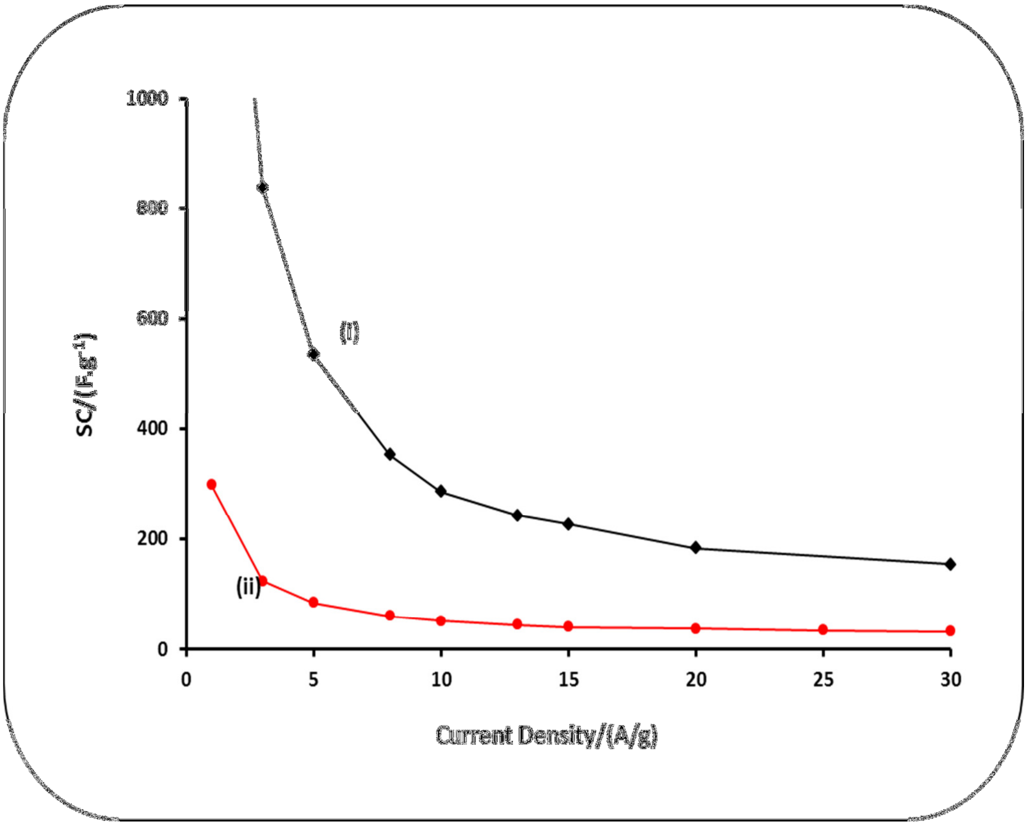

Figure 5.13: Specific capacitance of MWCNTaf-CoTPyzPz in (i) 1.0 M H_2SO_4 and (ii) 1.0 M Na_2SO_4 at different current densities.

The following equation was used to obtain the energy deliverable or Coulombic efficiency (η):

$$- \qquad (5.7)$$

where t_d and t_c are discharging time and charging time respectively. The η / % values are given in Table 5.3 and 5.4. The electrodes in neutral electrolyte take more time to charge and less to discharge since all η values in Na_2SO_4 are all below 100 %. A different trend is observed in H_2SO_4, at 1.0 $A.g^{-1}$ the η values are above 100% with the exception of MWCNTPhNH$_2$ electrode. For MWCNTaf-CoTPyzPz in H_2SO_4, the η value decrease from 150 % to 95 % as current density increased from 1 $A.g^{-1}$ to 10 $A.g^{-1}$. This 95 % value at 10 $A.g^{-1}$ of MWCNTaf-CoTPyzPz suggests that the redox activity of the electrode is feasible even at high current density (30).

The specific power (SP) and specific energy (SE) of the various electrodes calculated using equation 1.10 and 1.11 are given in Table 5.3 and 5.4. The specific power is about 1000 $W.Kg^{-1}$ for all the electrodes in 1.0 M Na_2SO_4 and 1.0 M H_2SO_4. For all the electrodes SE was higher in 1.0 M H_2SO_4 electrolyte than in 1.0 M Na_2SO_4 electrolyte. MWCNTaf-CoTPyzPz gave the highest SE of 472 $Wh.kg^{-1}$. The SE value obtained for MWCNTaf-CoTPyzPz was far greater than 10 $Wh.kg^{-1}$, a minimum value required for electrochemical supercapacitors. This values compares well with higher SE values reported for MWCNT-NiTAPc (134 $Wh.kg^{-1}$) (25) and MWCNT-polyNiTAPc (140 $Wh.kg^{-1}$) (31). The specific energy and the specific power calculated with the three electrode system is not the true reflection of the capability of the electrode materials.

Table 5.4: Supercapacitive parameters of CoTPyzPz based systems in acidic electrolyte from charge-discharge

	Electrolyte: 1.0 M H_2SO_4, current density = 1 A.g^{-1}			
Electrode	Specific capacitance/ (F.g^{-1})	Energy efficiency/ %	Specific Energy/ Whkg^{-1}	Specific Power/ Wkg^{-1}
MWCNTPhNH$_2$	132	98	2.1	1014
MWCNTaf	24.9	116	37	1001
CoTPyzPz	287	137	79	1007
MWCNTPhNH$_2$-CoTPyzPz	1642	114	456	1000
MWCNTaf-CoTPyzPz	1902	150	472	938

5.2.3. Electrochemical impedance analysis

The Nyquist plots in Figure 5.14 and 5.15 show an incomplete semicircle at high frequency while a straight sloping line is observed at low frequencies. At lower frequencies, the deviation of the vertical line from the imaginary impedance axis signifies the level of diffusion resistance of the electrolyte into the pores of the electrode material (32). The slope of the 45° portion of the curve is called the Warburg resistance (Z_W) and is a result of the frequency dependence of ion diffusion/transport in the electrolyte to the electrode surface (33). From the Nyquist plot (Figure 5.14), MWCNTaf has the least diffusion resistance which can be attributable to its porous network structure (34) while CoTPyPyz has the highest diffusion resistance due to the aggregation as seen in the SEM images (Figure 5.1). It can be seen that blending of MWCNTaf and CoTPyzPz results in a composite that has a reduced diffusion resistance which is due to the porous network of the entangled MWCNTaf. From figure 5.15 the "knee" frequency values are 3.73 kHz, 268 Hz, 838 Hz and 373 Hz for CoTPyzPz, MWCNTaf, MWCNTPhNH$_2$-CoTPyzPz and MWCNTaf-CoTPyzPz respectively. Most of the energy stored in MWCNTaf-CoTPyzPz will be accessible at 373 Hz. This knee frequency denotes the maximum frequency at which capacitive behaviours is dominant, and is an indication of the power capability of a supercapacitor (2). The time response of the electrodes is given in Table 5.5 where CoTPyzPz has the smallest time response of 0.268 ms. Most commercial supercapacitors have a "knee" of less than 1 Hz. While the value obtained for MWCNTaf-CoTPyzPz (373 Hz) is almost 4 times the value reported by Niu *et al.* for mats of MWCNTs (15) and 2 times the value reported by Hughes *et al.* for MWCNT-PPy (35).

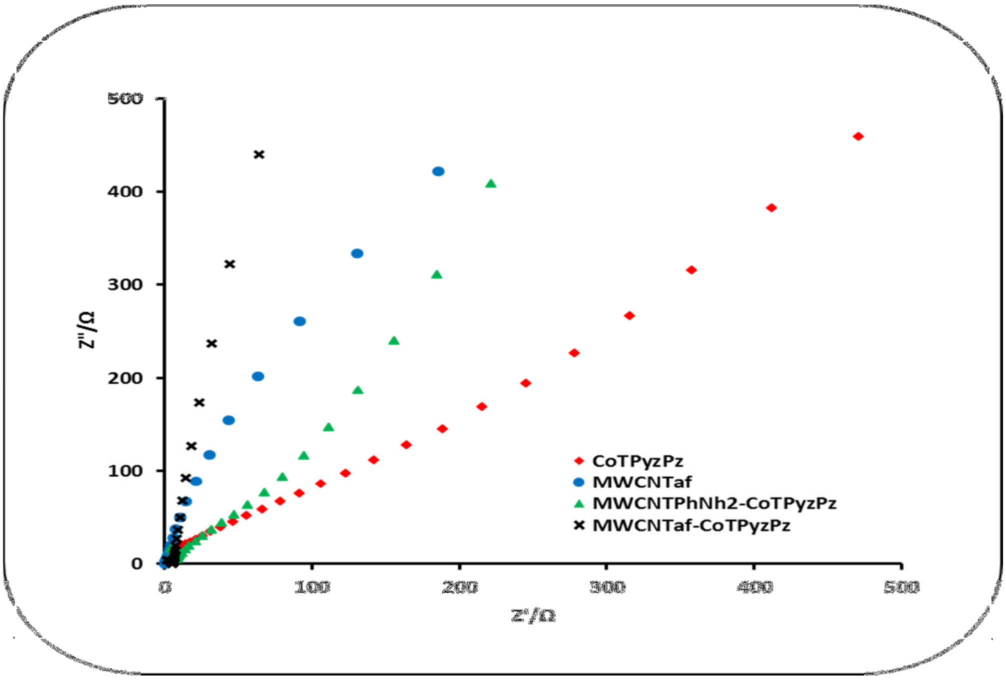

Figure 5.14: Nyquist plot of MWCNTaf, MWCNTPhNH$_2$, MWCNTaf-CoTPyzPz and MWCNTPhNH$_2$- CoTPyzPz in 1.0 M H$_2$SO$_4$ measured at 0.42 V.

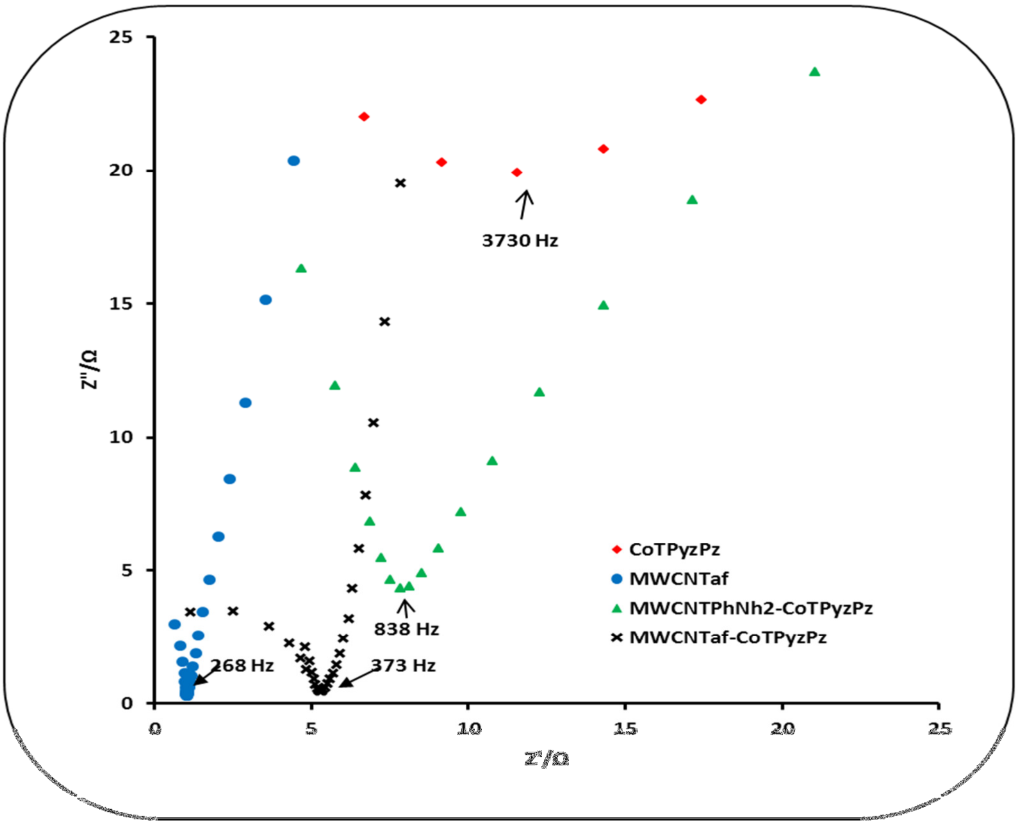

Figure 5.15: Expanded Nyquist plot of MWCNTaf, MWCNTPhNH$_2$, MWCNTaf-CoTPyzPz and MWCNTPhNH$_2$- CoTPyzPz in 1.0 M H_2SO_4 measured at 0.42V.

The phase angle of the electrodes has been reported in Table 5.5. MWCNTPhNH$_2$-CoTPyzPz shows two angles, one at 65° and another one at 48°. Bode plots (Figure 5.15) shows the deviation from the normal trend where at high frequency the electrode material are not resistive and behaves like a pure capacitor at lowest frequencies.

Table 5.5: Supercapacitive parameters of -CoTPyzPz based systems from EIS.

	Electrolyte: 1.0 M H_2SO_4, Frequency range = 10 kHz –10 mHz			
Electrode	**Specific capacitance/ (F.g^{-1})**	**Knee frequency/ kHz**	**-Phase angle / °**	**Response time / ms**
MWCNTaf	21	0.268	78	3.72
CoTPyzPz	70	3.73	59	0.268
MWCNTPhNH$_2$-CoTPyzPz	159	0.838	65	1.19
MWCNTaf-CoTPyzPz	176	0.373	82	2.68

The specific capacitance values obtained for EIS are showing large deviation from the values obtained by both CV and galvanostatic charge/discharge.

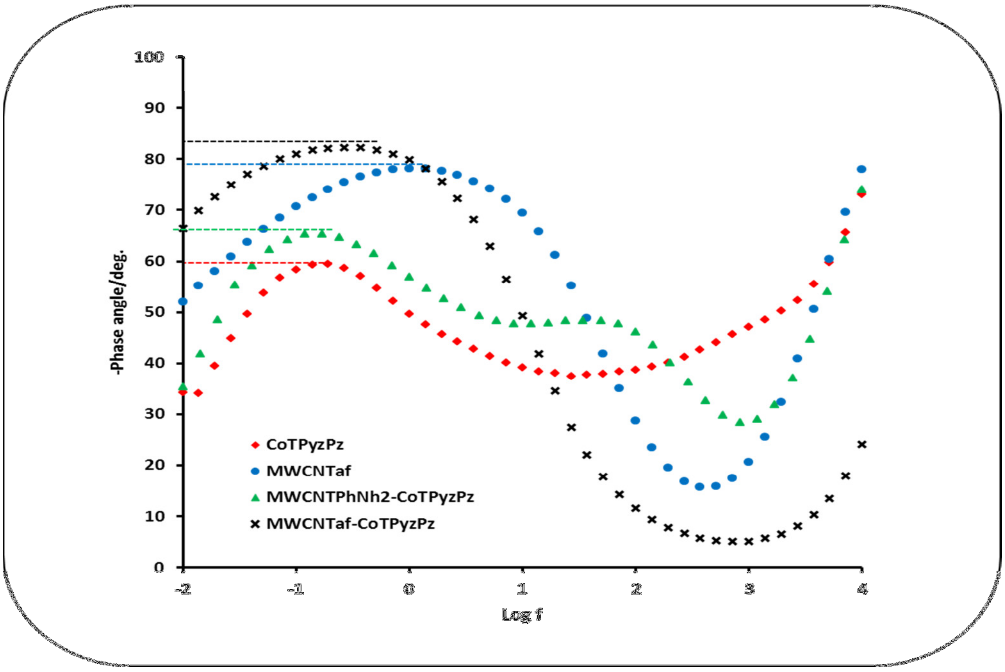

Figure 5.16: Bode plot of MWCNTaf, MWCNTPhNH$_2$, MWCNTaf-CoTPyzPz and MWCNTPhNH$_2$-CoTPyzPz in 1.0 M H_2SO_4 measured at 0.42 V.

This discrepancy in specific capacitance may be due to (i) redox switching "hysteresis" (36), (ii) involvement of heterogeneous functionalities(2), (iii) limited electrolyte access (35), (iv) immobility of ions during impedance experiment (37, 38) and (v) morphology of materials e.g. thick films (39, 40).

5.3. The electrochemical characterization of MWCNTs-CoTPyzPz//CB-MWCNTs asymmetric capacitors

To further evaluate the MWCNTPhNH2-CoTPyzPz and MWCNTaf-CoTPyzPz composites for real device application, asymmetric capacitors using activated carbon as a negative electrode were fabricated. It has been reported that asymmetric capacitor systems has larger electrochemical windows which leads to an increase in capacitance, energy density and power density (41-44).

Figure 5.17(a) shows CV curves of MWCNTPhNH_2-CoTPyzPz//CB-MWCNTPhNH_2 and MWCNTaf-CoTPyzPz//CB-MWCNTaf asymmetric supercapacitors at a scan rate of 20 mV.s^{-1} using 1.0 M Na_2SO_4 electrolyte. The asymmetric supercapacitors exhibit a reasonable capacitive behaviour with a quasi-rectangular CV curves with redox humps between -0.2 V and 0.8 V. The quasi rectangular shape and redox humps of this CV curves suggest that the energy storage mechanism for these supercapacitors is a combination of pseudocapacitance and EDLC. As scan rate is increased, the cathodic peak shifts towards the positive direction and the anodic peaks shifts towards the negative direction due to ionic resistivity. The resistivity at high scan rates has been attributed to the depletion or saturation of protons in the electrolyte (45-47). Figure 5.17(a) also shows that the capacitance of MWCNTaf-CoTPyzPz//CB-

MWCNTaf is bigger than the capacitance of MWCNTPhNH$_2$-CoTPyzPz//CB-MWCNTPhNH$_2$. The galvanostatic charge-discharge at a current density 0.2 A.g^{-1} is shown in Figure 5.17(b). The charge-discharge profiles showed a slight deviation form perfect symmetrical triangular shape, indicative of a good capacitive behaviour. The shape of the c-d curve implies both MWCNTPhNH$_2$-CoTPyzPz//CB-MWCNTPhNH$_2$ and MWCNTaf-CoTPyzPz//CB-MWCNTaf use EDLC and pseudocapacitive mechanisms to store energy. The IR drop of both composites decreases as current density increases. The average internal resistance (ESR) of MWCNTaf-CoTPyzPz//CB-MWCNTaf and MWCNTPhNH$_2$-CoTPyzPz//CB-MWCNTPhNH$_2$ was calculated to be 18 Ω and 29 Ω respectively according to equation:

$$\frac{\quad}{\quad} \qquad 4.8$$

where V_c is the potential at the end of charging, V_d is the potential at the beginning of discharge, and I is the current applied. The values of the IR drop further shows that MWCNTaf-CoTPyzPz//CB-MWCNTaf is a better asymmetric capacitor as compared to MWCNTPhNH$_2$-CoTPyzPz//CB-MWCNTPhNH$_2$.

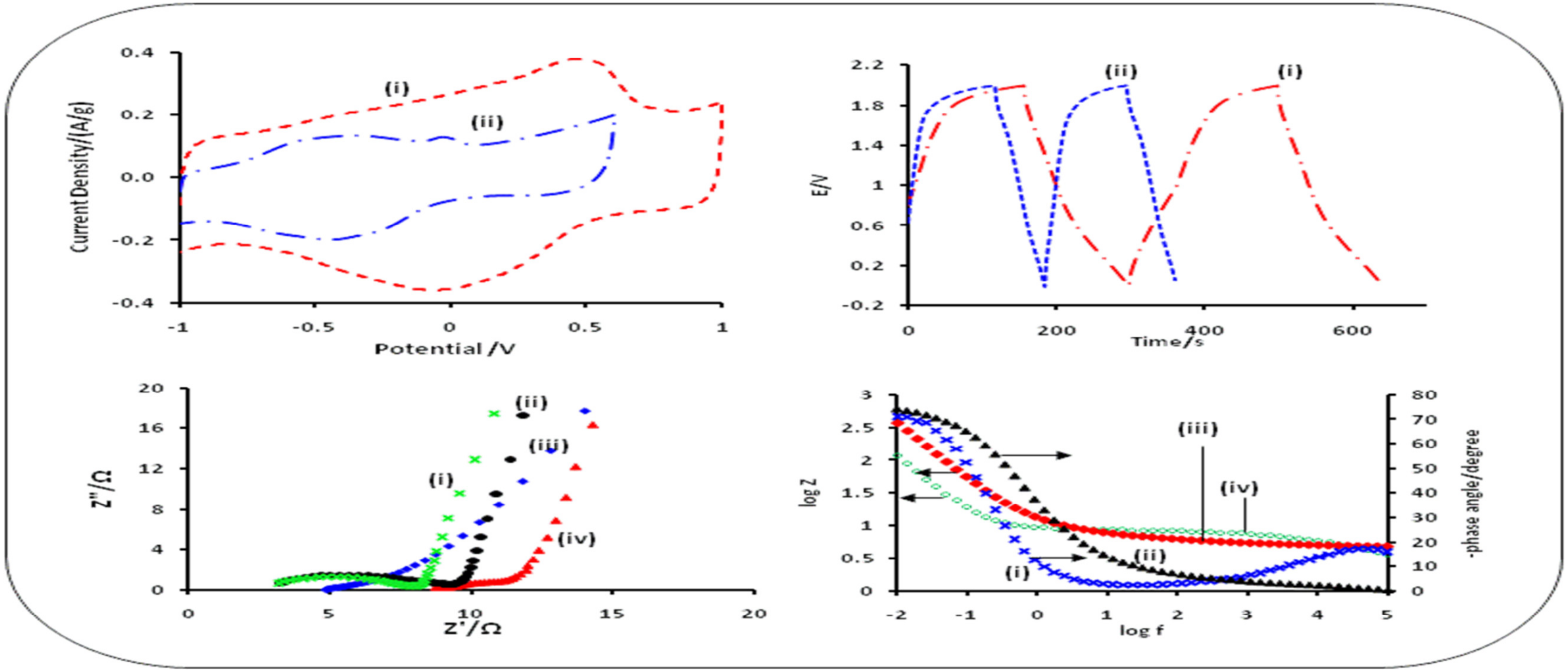

Figure 5.17:(a) Cyclic voltammograms of MWCNTaf-CoTPyzPz//CB- MWCNTaf (i) and MWCNTPhNH$_2$-CoTPyzPz//CB-MWCNTPhNH$_2$ (ii) in 1.0 M Na$_2$SO$_4$ at 20 mV.s^{-1}. (b) Charge-discharge profiles of MWCNTaf-CoTPyzPz//CB- MWCNTaf (i) and MWCNTPhNH$_2$-CoTPyzPz//CB-MWCNTPhNH$_2$ (ii) in 1.0 M Na$_2$SO$_4$ at 250 mA.g^{-1}. (c) Nyquist plot of MWCNTaf-CoTPyzPz//CB-MWCNTaf at -0.34 V (i), MWCNTaf-CoTPyzPz//CB- MWCNTaf at 0.20 V (ii), MWCNTPhNH$_2$-CoTPyzPz//CB-MWCNTPhNH$_2$ at 0.20 V (iii) and MWCNTPhNH$_2$-CoTPyzPz//CB-MWCNTPhNH$_2$ at -0.34 V in 1.0 M Na$_2$SO$_4$ in the frequency range 100 kHz to 10 MHz. (d) Bode plots of MWCNTaf-CoTPyzPz//CB- MWCNTaf (i) & (iv) and MWCNTPhNH$_2$-CoTPyzPz//CB-MWCNTPhNH$_2$ at 0.20 V (ii) & (iii) at 0.20 V in 1.0 M Na$_2$SO$_4$

Table 5.6 shows the specific capacitance calculated from c-d curves according to the equation:

$$\frac{\quad}{\quad} \qquad 4.5$$

$$\text{where } C = \frac{\quad}{\quad} \qquad 4.6$$

where I is the current (A), Δt is the discharging time, ΔV is the discharge voltage, m is the total mass of the positive electrode and the negative electrode. The C_{sp} of MWCNTaf-CoTPyzPz//CB-MWCNTaf is 70 $F.g^{-1}$ and of MWCNTPhNH$_2$-CoTPyzPz//CB-MWCNTPhNH$_2$ is 49 $F.g^{-1}$ at 0.2 $A.g^{-1}$.

Table 5.6: Supercapacitive behaviour parameters of MWCNTPhNH$_2$-CoTPyzPz//CB- MWCNTPhNH$_2$ and MWCNTaf-CoTPyzPz//CB- MWCNTaf supercapacitors

	Electrolyte: 1.0 M Na_2SO_4, current density = 250 $mA.g^{-1}$			
Electrode	**Specific capacitance / ($F.g^{-1}$)**	**Energy efficiency/ %**	**Specific Energy/Wh kg^{-1}**	**Specific Power/ Wkg^{-1}**
MWCNTPhNH$_2$-CoTPyzPz//CB-MWCNTPhNH$_2$	49	60	4.9	4968
MWCNTaf-CoTPyzPz//CB-MWCNTaf	70	86	8.5	4306

Figure 5.18 shows the Ragone plot of MWCNTaf-CoTPyzPz//CB-MWCNTaf at 2 V and of MWCNTPhNH$_2$-CoTPyzPz//CB-MWCNTPhNH$_2$ at two voltages. At a cell voltage of 2 V, MWCNTaf-CoTPyzPz//CB-MWCNTaf delivered an energy density of 8.5 Wh.kg^{-1} at a power density of 4306 W.kg^{-1} and maintained 5.9 Wh.kg^{-1} at 5.42 kW. kg^{1}, while MWCNTPhNH$_2$-CoTPyzPz//CB-MWCNTPhNH$_2$ has gave an energy density of 4.9 Wh.kg^{-1} at power density of 4968 W.kg^{-1} and maintaining 3.9 Wh.kg^{-1} at 5233 W.kg^{-1}. From Figure 5.18 it was observed that the energy density of MWCNTPhNH$_2$-CoTPyzPz//CB-MWCNTPhNH$_2$ is dependent on the cell voltages. The energy density values obtained is slightly higher to what commercial devices can achieve (48, 49). The energy density can be improved by mass balance of the electrodes (50).

The energy density results of this novel AEC cells are comparable to energy densities of other asymmetric supercapacitor cells. For example, the power and energy density of MnO$_2$ nanowire/Graphene composite is 7.0 Wh.kg^{-1}and 5000 W.kg^{-1}, respectively (51). The coulombic efficiency of MWCNTaf-CoTPyzPz//CB-MWCNTaf and MWCNTPhNH$_2$-CoTPyzPz//CB-MWCNTPhNH$_2$ was found to be 86 % and 60 % respectively.

The electrochemical impedance of MWCNTaf-CoTPyzPz//CB-MWCNTaf and MWCNTPhNH$_2$-CoTPyzPz//CB-MWCNTaf are displayed in Figure 5.17(c) and (d). The spectra show nearly vertical lines at low frequency which are a characteristic good capacitance performance of the electrode materials. The Internal resistance (ESR) of the cells at 0.2 V were found to be 9.63 Ω and 2.14 Ω for MWCNTPhNH$_2$-CoTPyzPz//CB-MWCNTPhNH$_2$ and MWCNTaf-CoTPyzPz//CB-MWCNTaf respectively. From Figure 5.17(c) it can be seen that the internal resistance does not increase even after 1000 cycles for MWCNTaf-CoTPyzPz//CB-MWCNTaf. From Figure 5.17(d) it can be seen that the phase angle of MWCNTaf-CoTPyzPz//CB-MWCNTaf and MWCNTPhNH$_2$-CoTPyzPz//CB-MWCNTPhNH$_2$ are 77.2° and 77.9° respectively. This confirms that the charge storage mechanism is a combination of pseudocapacitance and double layer capacitance since for a pure ideal EDLC the phase angle is 90 ° (31, 52).

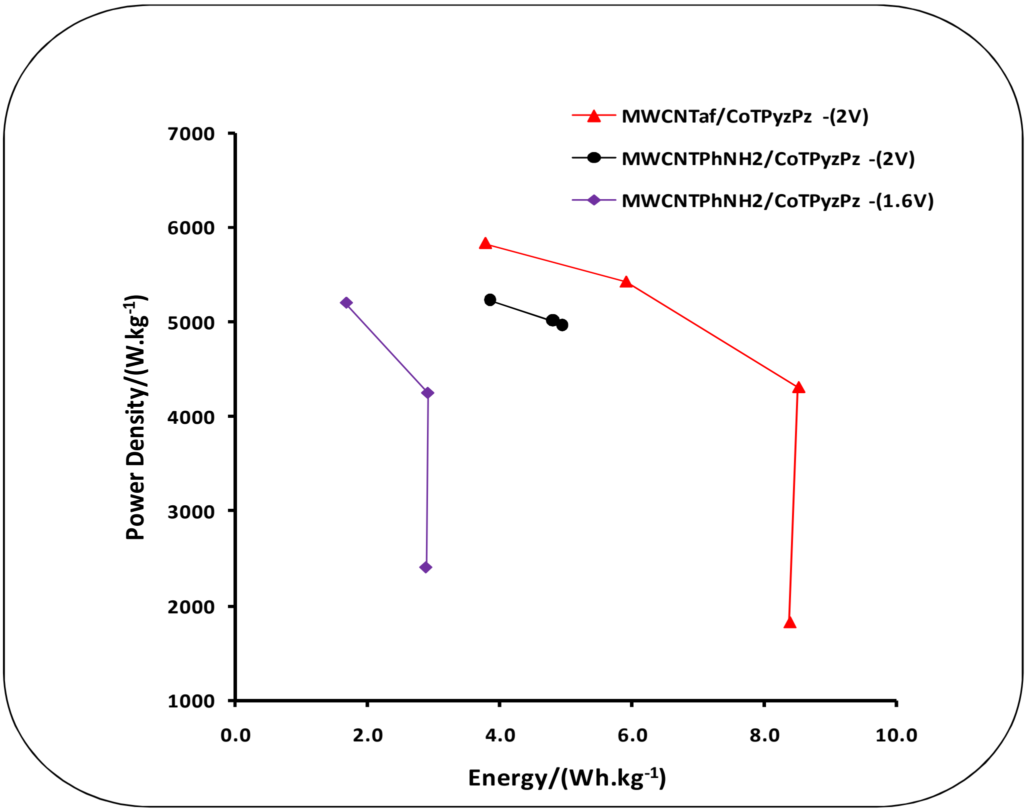

Figure 5.18: Ragone plot of MWCNTaf-CoTPyzPz//CB-MWCNTaf and MWCNTPhNH$_2$-CoTPyzPz// CB-MWCNTPhNH$_2$.

Based on the EIS data, the specific capacitance was found to be 45 F.g^{-1} and 26 F.g^{-1} decreasing to 35 F.g^{-1} and 15 F.g^{-1} for MWCNTaf-CoTPyzPz//CB-MWCNTaf and MWCNTPhNH$_2$-CoTPyzPz//CB-MWCNTPhNH$_2$, respectively after 1000 cycles. The values of C_{sp} obtained from EIS confirm that MWCNTaf-CoTPyzPz//CB-MWCNTaf performs better as compared to $MWCNTPhNH_2$-CoTPyzPz//CB-$MWCNTPhNH_2$ cell. The loss of capacitance in both asymmetric capacitor cells may be due to the loss of electrode materials, gas evolution during cycling and imperfect contact between electrode surface and the current collector (53, 54).

Figure 5.19 shows the plot of C_{sp} versus frequency before and after stability experiment. C_{sp} of the AEC cells decreased after stability cycling. MWCNTaf-CoTPyzPz// CB-MWCNTaf AEC cell gave the highest C_{sp} of 45 $F.g^{-1}$.

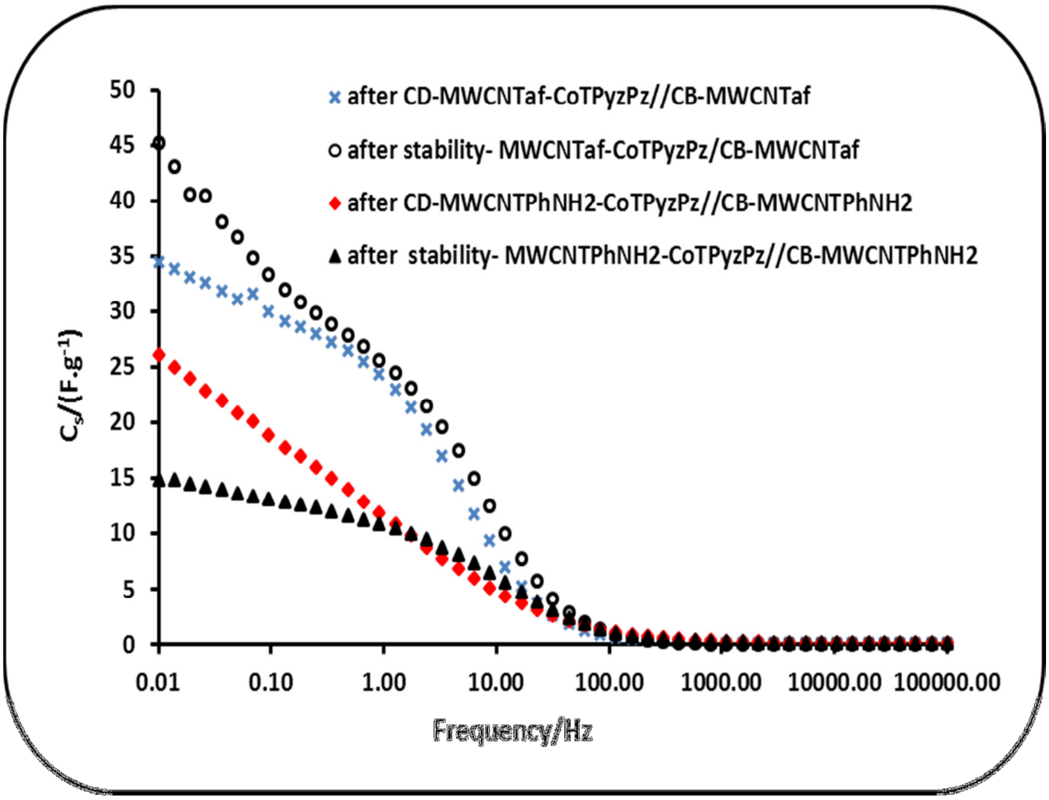

Figure 5.19: Comparison of specific capacitance of MWCNTaf-CoTPyzPz//CB-MWCNTaf and $MWCNTPhNH_2$-CoTPyzPz//CB-$MWCNTPhNH_2$ from EIS data.

Figure 5.20 shows the stability of the asymmetric capacitor cells. It was found that there is a decrease of capacitance of 32 % and 47 % of MWCNTaf-

CoTPyzPz//CB-MWCNTaf and MWCNTPhNH$_2$-CoTPyzPz//CB-MWCNTPhNH$_2$ respectively without considering first cycles as activation process of the studied materials. Capacitance of the cells decreases with about 11 % and 14 % for MWCNTaf-CoTPyzPz//CB-MWCNTaf and MWCNTPhNH$_2$-CoTPyzPz//CB-MWCNTPhNH$_2$ respectively after 1000 charge-discharge cycles. From the results a significant decrease occurred in the first 100 cycles, which were considered activation cycles. Thus, also from capacitance it can be seen that MWCNTaf-CoTPyzPz//CB-MWCNTaf cell perform better; thus MWCNTaf-CoTPyzPz electrode composite material can be a suitable electrode material.

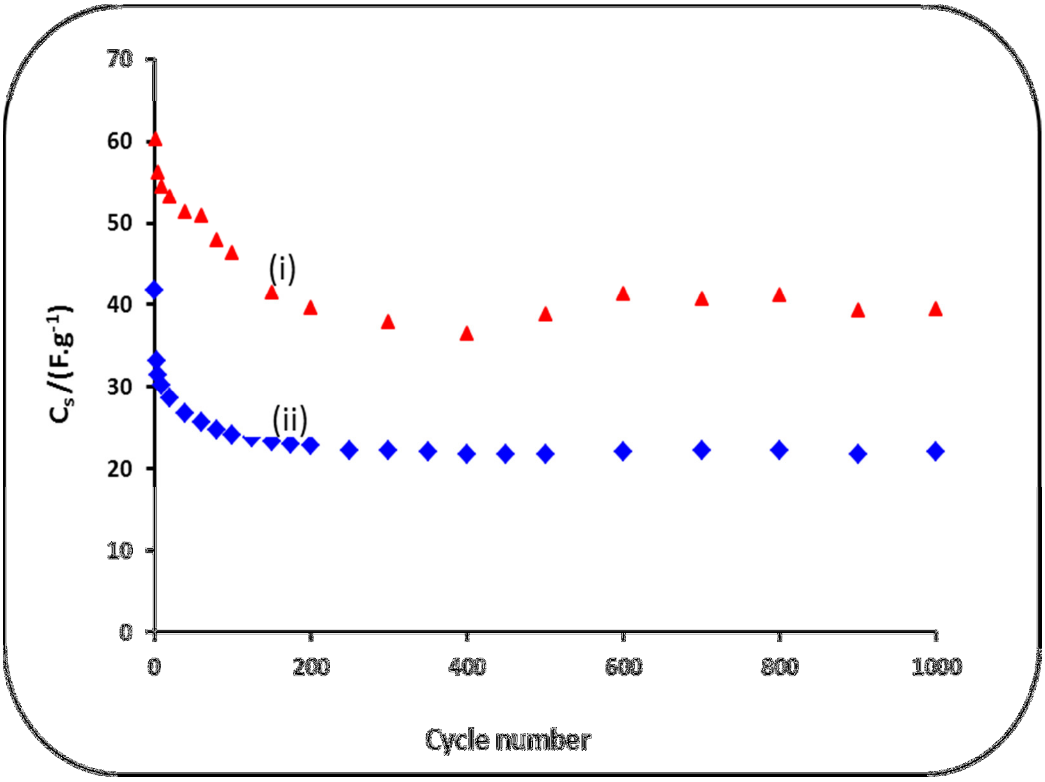

Figure 5.20: Cycling stability of MWCNTaf-CoTPyzPz//CB-MWCNTaf and MWCNTPhNH2-CoTPyzPz//CB-MWCNTPhNH2 from charge-discharge curves at 200 mA.g^{-1}.

5.4. Conclusion

In a three electrode system, MWCNTaf-CoTPyzPz and MWCNTPhNH$_2$-CoTPyzPz exhibited good electrochemical specific capacitance in H_2SO_4 electrolyte than in Na_2SO_4. Specific capacitance of BPPG electrode modified with MWCNTaf-CoTPyzPz particles in H_2SO_4 was 1902 F.g^{-1}. The value obtained in acidic electrolyte is ten times more to the value obtained in Na_2SO_4 electrolyte. This phenomenon in acidic electrolyte is attributable to the protonation and deprotonation due to the basicity of the nitrogen atoms in the porphyrazine molecules. These electrodes also exhibited good electrochemical behaviour with good energy deliverable efficiency, good cycle stability and lower charge transfer resistance. MWCNTaf-CoTPyzPz//CB-MWCNTaf and MWCNTPhNH$_2$-CoTPyzPz//CB-MWCNTPhNH$_2$ asymmetric cells have good cycling stability with a loss of about 10 % loss specific capacitance after 1000 cycles. These asymmetric cells have a specific energy density of 4.9 Wh.kg^{-1} and 8.5 Wh.kg^{-1} for MWCNTaf-CoTPyzPz//CB-MWCNTaf and MWCNTPhNH$_2$-CoTPyzPz//CB-MWCNTPhNH$_2$ respectively.

5.5. References

1. Yang D-Q, Rochette J-F, Sacher E. Functionalization of Multiwalled Carbon Nanotubes by Mild Aqueous Sonication. The Journal of Physical Chemistry B. 2005;109(16):7788-94.

2. Du C, Pan N. Supercapacitors using carbon nanotubes films by electrophoretic deposition. Journal of Power Sources. 2006;160(2):1487-94.

3. Ahmad A, Collins RA. FTIR characterization of triclinic lead phthalocyanine. Journal of Physics D: Applied Physics. 1991;24(10):1894.

4. Bilgin A, Ertem B, Gök Y. Novel porphyrazines containing peripherally functionalized macrocyclic (N_2O_2, N_2S_2) units: Synthesis and characterization. Dyes and Pigments. 2009;80(1):187-93.

5. Guo L, Ellis DE, Hoffman BM, Ishikawa Y. Ligand Substitution Effect on Electronic Structure and Optical Properties of Nickel Porphyrazines. Inorganic Chemistry. 1996;35(18):5304-12.

6. Petit L, Quartarolo A, Adamo C, Russo N. Spectroscopic Properties of Porphyrin-Like Photosensitizers:Insights from Theory. The Journal of Physical Chemistry B. 2006;110(5):2398-404.

7. Musil Z, Zimcik P, Miletin M, Kopecky K, Lenco J. Synthesis, Separation and UV/Vis Spectroscopy of Pyrazino-quinoxalino-porphyrazine Macrocycles. European Journal of Organic Chemistry. 2007;2007(27):4535-42.

8. Uslu Kobak RZ, Öztürk ES, Koca A, Gül A. The synthesis and cyclotetramerisation reactions of aryloxy-, arylalkyloxy-substituted pyrazine-2,3-dicarbonitriles and

spectroelectrochemical properties of octakis(hexyloxy)-pyrazinoporphyrazine. Dyes and Pigments. 2010;86(2):115-22.

9. Kobayashi N, Miwa H, Nemykin VN. Adjacent versus Opposite Type Di-Aromatic Ring-Fused Phthalocyanine Derivatives: Synthesis, Spectroscopy, Electrochemistry, and Molecular Orbital Calculations. Journal of the American Chemical Society. 2002;124(27):8007-20.
10. Sakellariou EG, Montalban AG, Beall SL, Henderson D, Meunier HG, Phillips D, et al. Novel peripherally functionalized seco-porphyrazines: synthesis, characterization and spectroscopic evaluation. Tetrahedron. 2003;59(46):9083-90.
11. Onay H, Esat B, Öztürk R. The symmetrical porphyrazine with annulated six membered rings. Polyhedron. 2010;29(4):1314-6.
12. Zimcik P, Miletin M, Novakova V, Kopecky K, Nejedla M, Stara V, et al. Effective Monofunctional Azaphthalocyanine Photosensitizers for Photodynamic Therapy. Australian Journal of Chemistry. 2009;62(5):425-33.
13. Lee BH, Jaung JY, Jang SC, Yi SC. Synthesis and optical properties of push-pull type tetrapyrazinoporphyrazines. Dyes and Pigments. 2005;65(2):159-67.
14. Allan JR, Paton AD, Turvey K, Gerrard DL, Hoey S. Thermal and electrical studies on porphyrin compounds of cobalt(II), copper(II) and zinc(II). Thermochimica Acta. 1989;143(0):67-74.

15. Niu C, Sichel EK, Hoch R, Moy D, Tennent H. High power electrochemical capacitors based on carbon nanotube electrodes. Applied Physics Letters. 1997;70(11):1480-2.

16. Nian Y-R, Teng H. Nitric Acid Modification of Activated Carbon Electrodes for Improvement of Electrochemical Capacitance. Journal of The Electrochemical Society. 2002;149(8):A1008-14.

17. Hulicova-Jurcakova D, Seredych M, Lu GQ, Bandosz TJ. Combined Effect of Nitrogen- and Oxygen-Containing Functional Groups of Microporous Activated Carbon on its Electrochemical Performance in Supercapacitors. Advanced Functional Materials. 2009;19(3):438-47.

18. Ledson DL, Twigg MV. Acid-base behaviour of phthalocyanine. Inorganica Chimica Acta. 1975;13(0):43-6.

19. Beeby A, FitzGerald S, Stanley CF. Protonation of Tetrasulfonated Zinc Phthalocyanine in Aqueous Acetonitrile Solution. Photochemistry and Photobiology. 2001;74(4):566-9.

20. Theodoridis A, Maigut J, Puchta R, Kudrik EV, van Eldik R. Novel Iron(III) Porphyrazine Complex. Complex Speciation and Reactions with NO and H_2O_2. Inorganic Chemistry. 2008;47(8):2994-3013.

21. Villano M, Amendola V, Sandonà G, Donzello MP, Ercolani C, Meneghetti M. Excited State Dynamics and Nonlinear Absorption of a Pyrazinoporphyrazine Macrocycle Carrying Externally Appended Pyridine Rings. The Journal of Physical Chemistry B. 2006;110(48):24354-60.

22. Xu J, Gao L, Cao J, Wang W, Chen Z. Preparation and electrochemical capacitance of cobalt oxide (Co_3O_4) nanotubes as supercapacitor material. Electrochimica Acta. 2010;56(2):732-6.

23. Seel JA, Dahn JR. Electrochemical Intercalation of PF_6 into Graphite. Journal of The Electrochemical Society. 2000;147(3):892-8.

24. Amatucci GG, Badway F, Pasquier AD, Zheng T. An Asymmetric Hybrid Nonaqueous Energy Storage Cell. Journal of The Electrochemical Society. 2001;148(8):A930-A9.

25. Chidembo AT, Ozoemena KI, Agboola BO, Gupta V, Wildgoose GG, Compton RG. Nickel(ii) tetra-aminophthalocyanine modified MWCNTs as potential nanocomposite materials for the development of supercapacitors. Energy & Environmental Science. 2010;3(2):228-36.

26. Zhang LL, Zhao XS. Carbon-based materials as supercapacitor electrodes. Chemical Society Reviews. 2009;38(9):2520-31.

27. Obreja VVN. On the performance of supercapacitors with electrodes based on carbon nanotubes and carbon activated material-A review. Physica E: Low-Dimensional Systems and Nanostructures. 2008;40(7):2596-605.

28. Yuan CZ, Gao B, Shen LF, Yang SD, Hao L, Lu XJ, et al. Hierarchically structured carbon-based composites: Design, synthesis and their application in electrochemical capacitors. Nanoscale. 2010;3(2):529-45.

29. Hall PJ, Mirzaeian M, Fletcher SI, Sillars FB, Rennie AJR, Shitta-Bey GO, et al. Energy storage in electrochemical capacitors: designing functional materials to improve performance. Energy & Environmental Science. 2010;3(9):1238-51.

30. Meher SK, Justin P, Rao GR. Pine-cone morphology and pseudocapacitive behavior of nanoporous nickel oxide. Electrochimica Acta. 2010;55(28):8388-96.

31. Chidembo AT, Ozoemena KI. Electrochemical Capacitive Behaviour of Multiwalled Carbon Nanotubes Modified with Electropolymeric Films of Nickel Tetraaminophthalocyanine. Electroanalysis. 2010;22(21):2529-35.

32. Justin P, Ranga Rao G. CoS spheres for high-rate electrochemical capacitive energy storage application. International Journal of Hydrogen Energy. 2010;35(18):9709-15.

33. Yan J, Fan Z, Wei T, Qian W, Zhang M, Wei F. Fast and reversible surface redox reaction of graphene-MnO_2 composites as supercapacitor electrodes. Carbon. 2010;48(13):3825-33.

34. Justin P, Meher SK, Rao GR. Tuning of Capacitance Behavior of NiO Using Anionic, Cationic, and Nonionic Surfactants by Hydrothermal Synthesis. The Journal of Physical Chemistry C. 2010;114(11):5203-10.

35. Hughes M, Chen GZ, Shaffer MSP, Fray DJ, Windle AH. Electrochemical capacitance of a nanoporous composite of carbon nanotubes and polypyrrole. Chemistry of Materials. 2002;14(4):1610-3.

36. Xu G, Wang W, Qu X, Yin Y, Chu L, He B, et al. Electrochemical properties of polyaniline in p-toluene sulfonic acid solution. European Polymer Journal. 2009;45(9):2701-7.

37. Tanguy J, Mermilliod N, Hoclet M. Charging capacitive effect in conducting polymers in relation with the electrochemical doping. Synthetic Metals. 1987;18(1-3):7-12.

38. Bisquert J. Analysis of the kinetics of ion intercalation: Ion trapping approach to solid-state relaxation processes. Electrochimica Acta. 2002;47(15):2435-49.

39. Mohamedi M, Takahashi D, Uchiyama T, Itoh T, Nishizawa M, Uchida I. Explicit analysis of impedance spectra related to thin films of spinel LiMn2O4. Journal of Power Sources. 2001;93(1-2):93-103.

40. Niessen RAH, de Jonge J, Notten PHL. The Electrochemistry of Carbon Nanotubes. Journal of The Electrochemical Society. 2006;153(8):A1484-91.

41. Li J, Gao F. Analysis of electrodes matching for asymmetric electrochemical capacitor. Journal of Power Sources. 2009;194(2):1184-93.

42. Brousse T, Belanger D. A Hybrid FeO-MnO Capacitor in Mild Aqueous Electrolyte. Electrochemical and Solid-State Letters. 2003;6(11):A244-8.

43. Khomenko V, Raymundo-Piñero E, Béguin F. A new type of high energy asymmetric capacitor with nanoporous carbon electrodes in aqueous electrolyte. Journal of Power Sources. 2010;195(13):4234-41.

44. Wang Y-g, Xia Y-y. A new concept hybrid electrochemical supercapacitor: Carbon/LiMn2O4 aqueous system. Electrochemistry Communications. 2005;7(11):1138-42.

45. Conway BE, Pell WG, editors. Efficiency Aspects of Charge/Discharge Cycling at Porous Capacitors Electrodes:

Behavior of a Hardware Model Circuit. The 8th International Seminar on DLC and Similar Energy Storage Devices; 1998 7- 9 December; Deerfield Beach, Florida, USA.

46. Wu F-C, Tseng R-L, Hu C-C, Wang C-C. The capacitive characteristics of activated carbons: comparisons of the activation methods on the pore structure and effects of the pore structure and electrolyte on the capacitive performance. Journal of Power Sources. 2006;159(2):1532-42.

47. Subramanian V, Hall SC, Smith PH, Rambabu B. Mesoporous anhydrous RuO2 as a supercapacitor electrode material. Solid State Ionics. 2004;175(1-4):511-5.

48. Schiffer J, Linzen D, Sauer DU. Heat generation in double layer capacitors. Journal of Power Sources. 2006;160(1):765-72.

49. Guillemet P, Scudeller Y, Brousse T. Multi-level reduced-order thermal modeling of electrochemical capacitors. Journal of Power Sources. 2006;157(1):630-40.

50. Pell WG, Conway BE. Peculiarities and requirements of asymmetric capacitor devices based on combination of capacitor and battery-type electrodes. Journal of Power Sources. 2004;136(2):334-45.

51. Wu Z-S, Ren W, Wang D-W, Li F, Liu B, Cheng H-M. High-Energy MnO2 Nanowire/Graphene and Graphene Asymmetric Electrochemical Capacitors. ACS Nano. 2010;4(10):5835-42.

52. Adekunle AS, Ozoemena KI. Electrosynthesised Metal (Ni, Fe, Co) Oxide Films on Single-Walled Carbon Nanotube Platforms and Their Supercapacitance in Acidic and Neutral pH Media. Electroanalysis. 2011;23(4):971-9.

53. Wang J-G, Yang Y, Huang Z-H, Kang F. A high-performance asymmetric supercapacitor based on carbon and carbon-MnO2 nanofiber electrodes. Carbon. 2013;61(0):190-9.

54. Yu G, Hu L, Liu N, Wang H, Vosgueritchian M, Yang Y, et al. Enhancing the Supercapacitor Performance of Graphene/MnO2 Nanostructured Electrodes by Conductive Wrapping. Nano Letters. 2011 2014/01/18;11(10):4438-42.

CHAPTER 6

SUPERCAPACITIVE BEHAVIOUR OF FeTPyzPz-MWCNT NANOCOMPOSITES

6.1. Physical characterisation of FeTPyzPz-MWCNT nanocomposites

6.1.1. Comparative microscopic images

FESEM images of MWCNTs and FeTPyzPz-MWCNTs composites as depicted in Figure 6.1 show a porous entangled morphology of all the electrode materials. Images of FeTPyzPz show lumps surrounded by small aggregated particles.

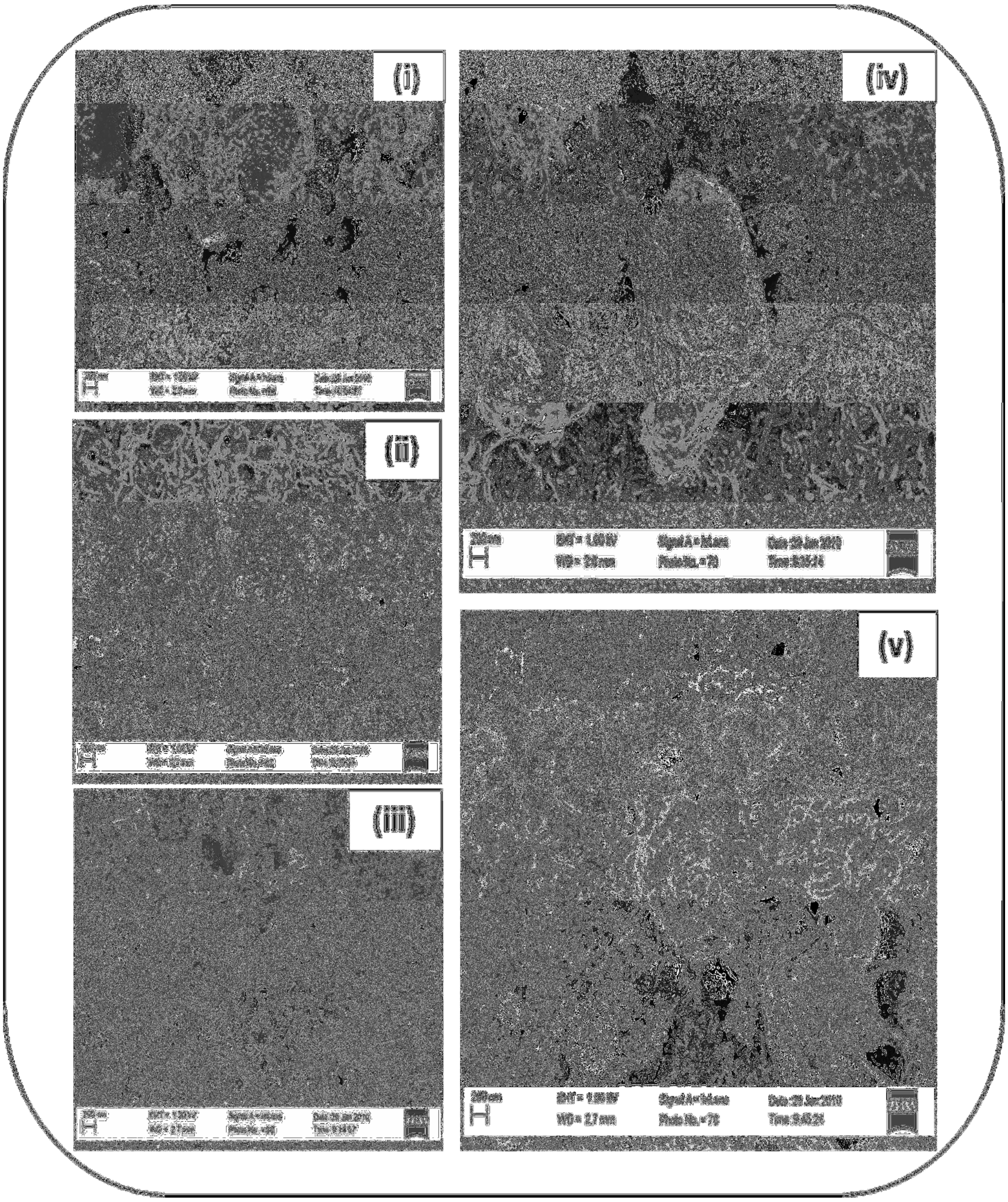

Figure 6.1: Typical FESEM images of (i) FeTPyzPz, (ii) MWCNTPhNH$_2$, (iii) MWCNTaf, (iv) MWCNTaf-FeTPyzPz and (v) MWCNTPhNH$_2$-FeTPyzPz.

The MWCNTs seem to wrap around the FeTPyzPz particles. Špitalsky*et al*. (1) have reported that MWCNTs form dense morphology that has intra and inter bundle porosity. According to Yuen (2), functionalized MWCNTs appear to be curled and entangled with a porous network. Iijima *et al*. (3) discovered that MWCNTs are thread like tangles and curls as they form bundles.

6.1.2. Comparative EDX

EDX profiles of FeTPyzPz, MWCNTaf-FeTPyzPz and MWCNTPhNH$_2$-FeTPyzPz shown in Figure 6.2 gives the analytical details of the electrodes elemental composition. Major elements found are C, N and Fe. Other elements found in the sample are sodium and oxygen which might be from synthesis. A pronounced peak of thallium could be from gold plating of the sample holder.

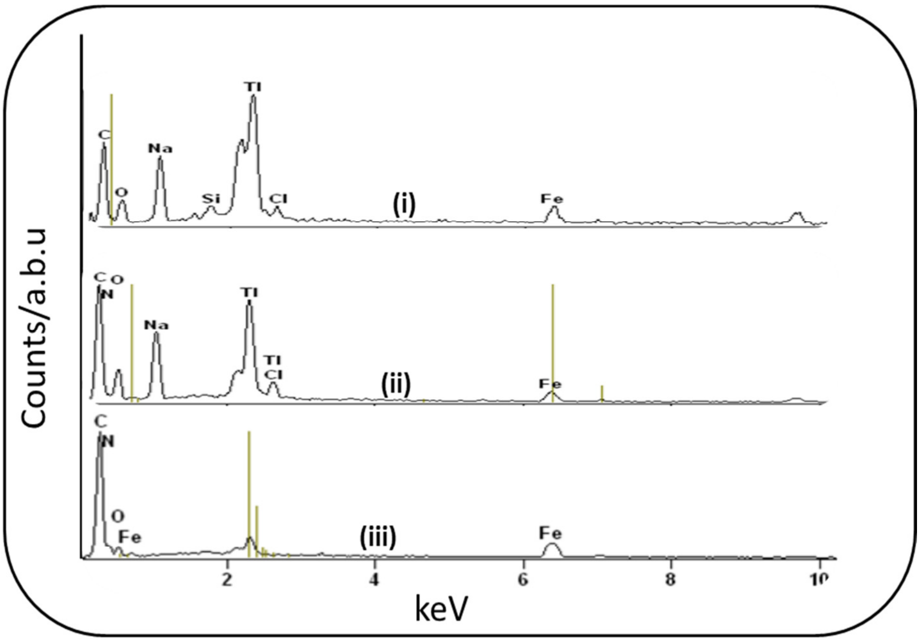

Figure 6.2: EDX spectra of (i) MWCNTPhNH$_2$-FeTPyzPz and (ii) MWCNTaf-FeTPyzPz and (iii) FeTPyzPz.

6.1.3. Comparative FTIR

Figure 6.3 shows FTIR spectra overlay of MWCNTs, FeTPyzPz and FeTPyzPz-MWCNTs composites. FeTPyzPz and the composites show a peak at around 1619 cm^{-1} that is attributed to the C—N stretching vibrations of the bond in the porphyrazine core (4). Acid functionalization of MWCNTs was confirmed by the presence of CO stretching vibration at 1712 cm^{-1} in MWCNTaf and MWCNTaf-FeTPyzPz spectra. The broad peaks that appear around 3436 cm^{-1} are due to OH stretching frequency in acid functionalized MWCNTs and N-H stretching vibrations in MWCNTPhNH$_2$.

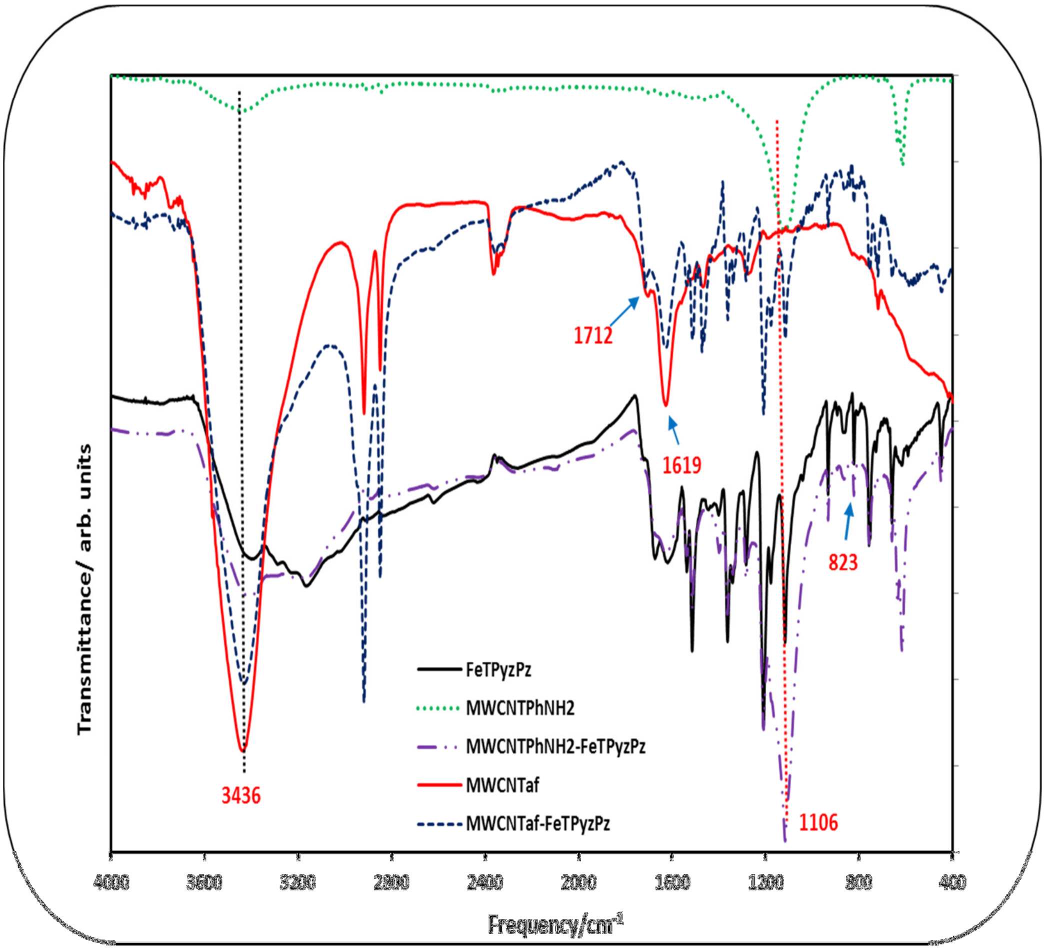

Figure 6.3: FTIR spectra of MWCNTPhNH$_2$, MWCNTPhNH$_2$-FeTPyzPz, MWCNTaf, MWCNTaf-FeTPyzPz and FeTPyzPz.

6.1.4. Comparative UV-Vis analysis

Figure 6.4 shows the UV-Vis spectra of MWCNTs, FeTPyzPz and FeTPyzPz-MWCNTs composites in DMF. The electronic spectrum for FeTPyzPz shows a monomeric Q-band peak at 621 nm with a shoulder at 640 nm. The Q band of FeTPyzPz is characteristic of a tetrapyrrollic macrocycle with a D_{4h} symmetry (5). Peaks at 374 nm and 490 nm show ligand to metal charge transfer transitions of the type a_{2u}(ring) → e_g(metal) (5). MWCNTaf-FeTPyzPz and MWCNTPhNH$_2$-FeTPyzPz composite material show a similar trend as FeTPyzPz with suppressed Q band. This similarity means the composite electronic structures were not altered significantly. MWCNTaf and MWCNTPhNH$_2$ spectra have no peak, an indication of MWCNTs functionalization (6-8). Another weak band observed (Figure 6.4) at 374 nm, 370 nm and 364 nm for FeTPyzPz, MWCNTPhNH$_2$-FeTPyzPz and MWCNTaf-FeTPyzPz respectively is classified as a B band (Soret band).

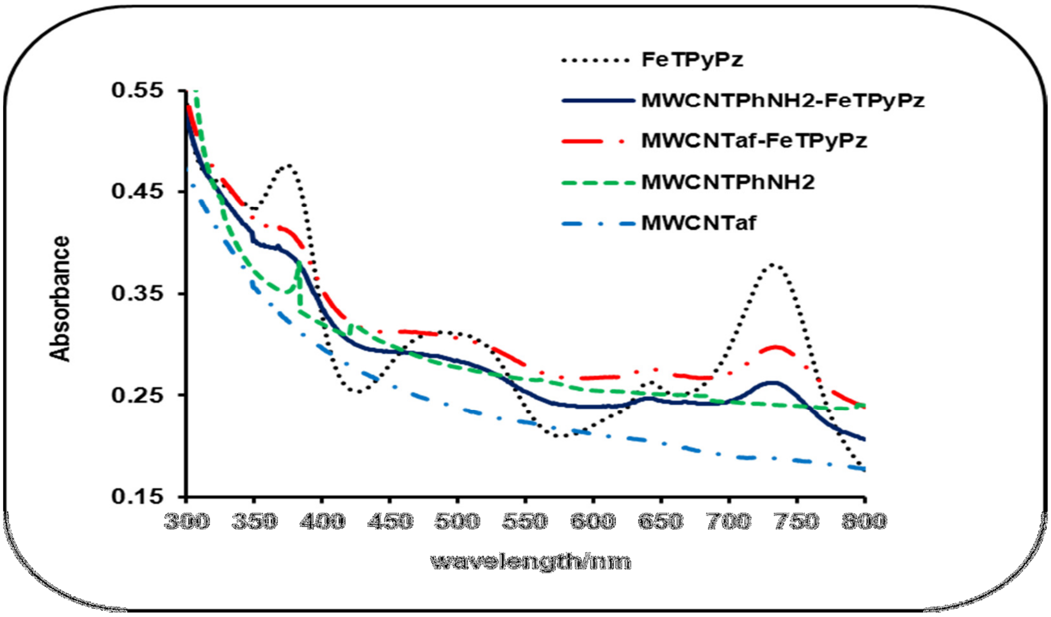

Figure 6.4: UV-VIS spectra of MWCNTaf, MWCNTPhNH$_2$, FeTPyzPz, MWCNTPhNH$_2$-FeTPyzPz and MWCNTaf-FeTPyzPz.

This B band is characteristic of the tetrapyrrollic derivatives and shows that there is coupling between nonbonding lone pair electrons and the macrocyclic system (4, 9).

6.1.5. Comparative Thermogravimetry

Figure 6.5 and 6.6 displays the TG and DTG curves of MWCNTaf, MWCNTPhNH$_2$, MWCNTp, FeTPyzPz, MWCNTaf-FeTPyzPz and MWCNTPhNH$_2$-FeTPyzPz materials heated in air from 25°C to 1000 °C. Between one to three major mass loss steps are distinguishable on TG and further elucidated by the DTG (Figure 6.6).MWCNTp, MWCNTaf and MWCNTPhNH$_2$ show no significant mass loss between 25°C to 350 °C. At the same temperature range, FeTPyzPz and composites show mass loss of about 20% due to the physisorbed and chemisorbed water (10).MWCNTp and MWCNTaf show one major mass loss at 612 °C and 657 °C respectively. MWCNTPhNH$_2$ show one major mass loss at 537 °C and a minor mass loss 834 °C. A major mass loss for FeTPyzPz occurred at 473 °C. MWCNTPh$_2$-FeTPyzPz exhibited a major mass loss at 388 °C, 430 °C and 534 °C. MWCNTaf-FeTPyzPz showed two major mass losses at 416 °C and 625 °C. The incorporation of the MWCNTs into FeTPyzPz lowers the onset temperature for the decomposition of the macrocycle. These results suggest that the composites exhibit lower oxidation resistance than FeTPyzPz. The order of stability based on the initial decomposition temperature of the porphyrazine is as follows:

MWCNTaf > MWCNTPhNH$_2$>MWCNTp>FeTPyPz> MWCNTPhNH$_2$-FeTPyzPz > MWCNTaf-FeTPyPz

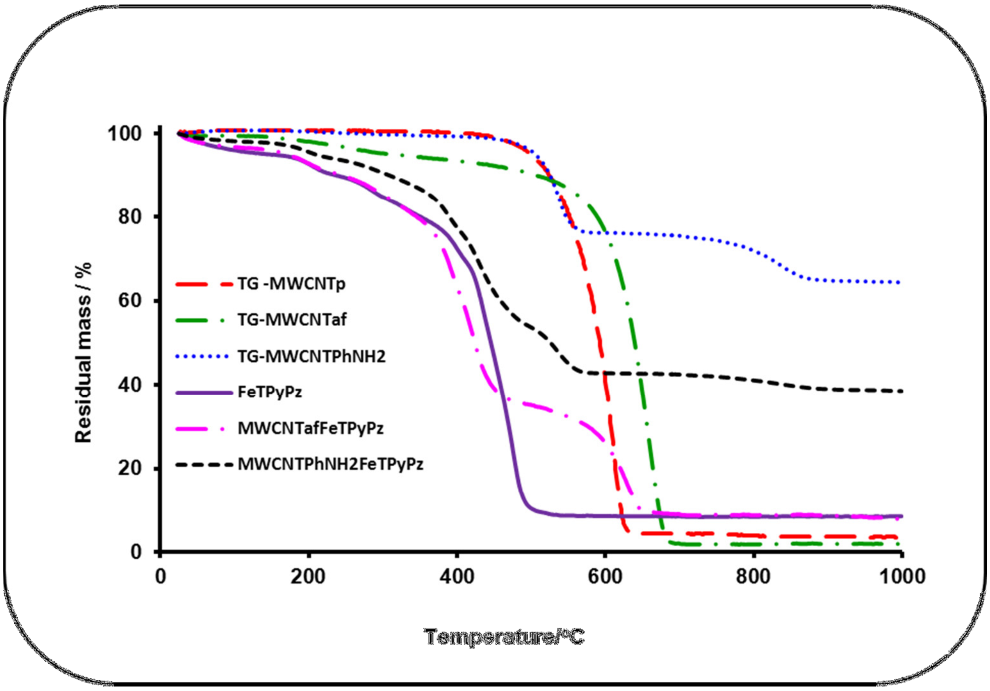

Figure 6.5: Thermogravimetric curves of MWCNTPhNH$_2$, MWCNTaf, MWCNT (pristine), FeTPyzPz, MWCNTPhNH$_2$-FeTPyzPz and MWCNTaf-FeTPyzPz.

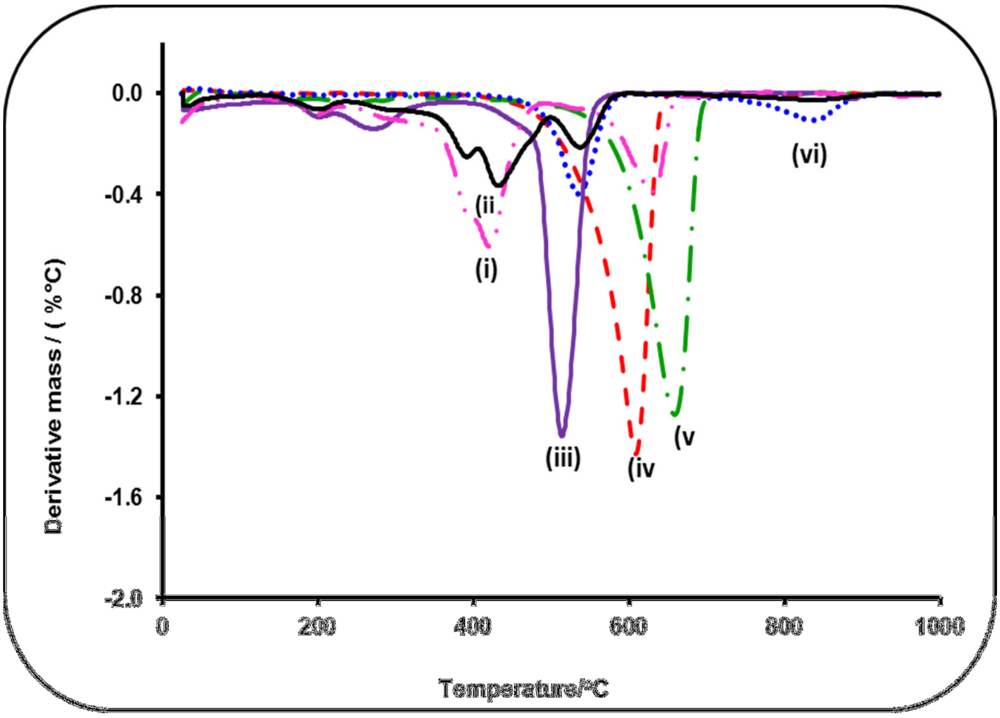

Figure 6.6: Differential thermogravimetric curves of (i) (MWCNTPhNH$_2$, (ii) MWCNTaf (iii) MWCNT (pristine), FeTPyzPz, MWCNTPhNH$_2$-FeTPyzPz and MWCNTaf-FeTPyzPz.

6.2. Supercapacitive behaviour of MWCNT-FeTPyzPz

Cyclic voltammetry is one of the diagnostic tools that can be used to investigate the electrochemical properties of materials such as capacitive behaviour. The shape of the cyclic voltammogram depicts an energy storage mechanism which an electrode material utilizes. A rectangular shape suggests a double layer storage mechanism while a distorted rectangular shape with redox peaks outlines a pseudo-capacitive storage mechanism (11-15).

6.2.1. Cyclic voltammetry analysis

Figure 6.7 shows the CV curves of BPPG, MWWCNTPhNH$_2$, MWCNTaf, FeTPyzPz, MWCNTPhNH$_2$-FeTPyzPz and MWCNTaf-FeTPyzPz electrodes at 10 mV.s^{-1} using 1.0 M H_2SO_4 electrolyte. The inset shows that the cyclic voltammograms of BPPG, MWCNTPhNH$_2$ and MWCNTaf are not perfectly rectangular, andthis signifies deviation from ideal double layer supercapacitive behaviour. Some redox humps on the CVs indicate that functionalization of MWCNTs enhances capacitance through pseudocapacitance. MWCNTaf and MWCNTPhNH$_2$ have been found to contain oxygen and nitrogen functional groups respectively, which enhance capacitance in acidic electrolytes through charge transfer reactions (15-18). The redox process on the MWCNT occurs through the following previously proposed reactions such as (16, 19-21):

6.1

6.2

where C* is the carbon framework.

Specific capacitance from the CVs was calculated according to the equation 5.3 (22-24):

— 6.3

where is average current (A), ν is the scan rate ($V.s^{-1}$) and m is the mass of the active electrode mass (g). Specific capacitance values from comparative cyclic voltammograms in 0.1 M H_2SO_4 at 10 $mV.s^{-1}$ follows the trend:

MWCNTaf-FeTPyzPz (502 $F.g^{-1}$) > MWCNTPhNH$_2$-FeTPyzPz (408 $F.g^{-1}$) > FeTPyzPz (127 $F.g^{-1}$) > MWCNTaf (39 $F.g^{-1}$) > MWCNTPhNH$_2$ (37 $F.g^{-1}$).

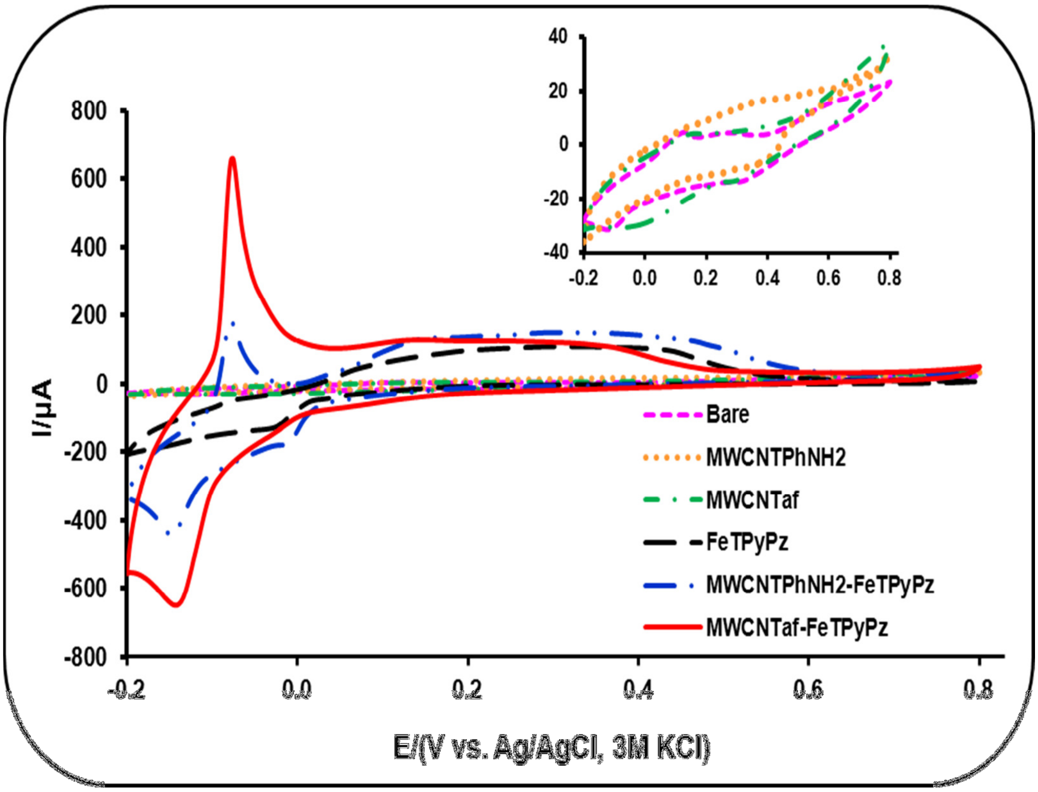

Figure 6.7: Cyclic voltammograms of Bare, MWCNTPhNH$_2$, MWCNTaf, FeTPyzPz, MWCNTPhNH$_2$-FeTPyzPz and MWCNTaf-FeTPyzPz in 1.0 M H_2SO_4 at a scan rate of 10 $mV.s^{-1}$. Inset: Cyclic voltammograms of Bare, MWCNTPhNH$_2$, MWCNTaf.

The high C_{sp} values found for the composites suggest that there are good synergistic effects in the combination of functionalized MWCNTs and FeTPyzPz. The MWCNTS seems to provide a porous network that connects the FeTPyzPz particles that undergo faradaic reactions. It has been reported that composites such MWCNT-NiTAPc (18), NiO/CNT(10%) (25), PPy/MWCNT (26) and MWCNT/PANI (27) gave a superior C_{sp} than individual electrode materials. Figure 6.7 and 6.8 show CV curves of MWCNTaf-FeTPyzPz and MWCNTPhNH$_2$-FeTPyzPz at different scan rates. The CV curves (Figure 6.9) depict that the redox couple is quasi-reversible due to the shifting of anodic and cathodic peaks as scan rate increases (28, 29).

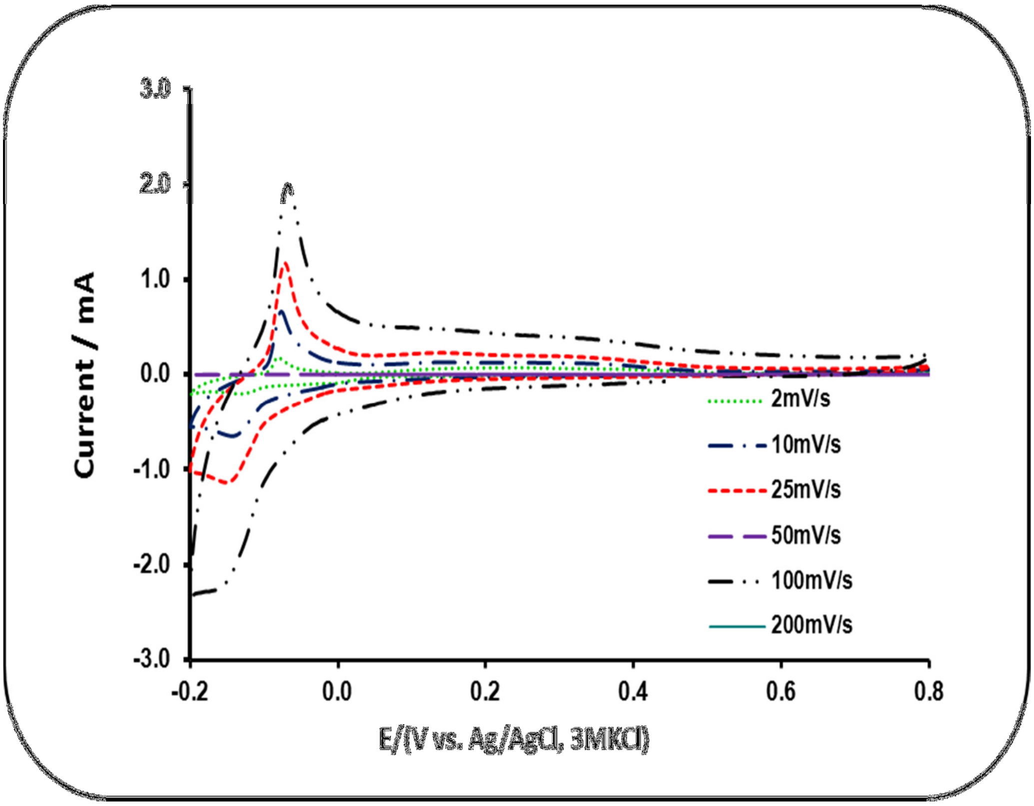

Figure 6.8: Cyclic voltammogram evolutions of MWCNTaf-FeTPyzPz in 1.0 M H_2SO_4 at different scan rates.

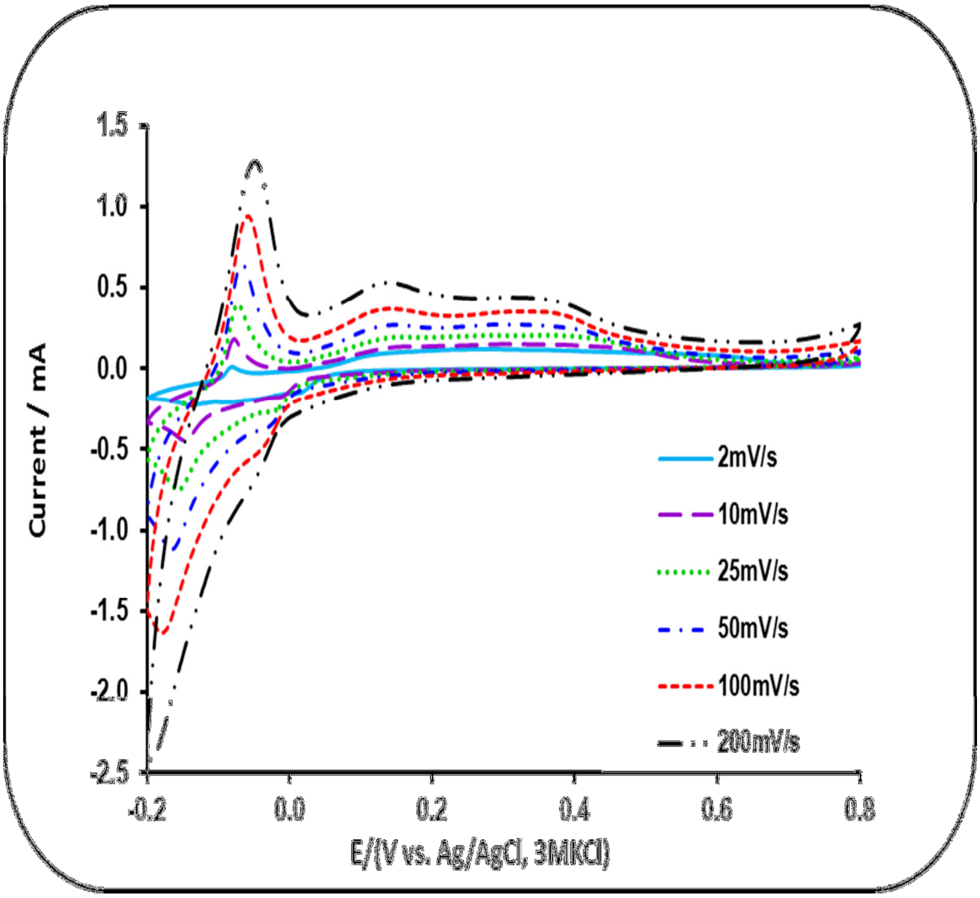

Figure 6.9: Cyclic voltammogram evolutions of MWCNTPhNH$_2$-FeTPyzPz in 1.0 M H$_2$SO$_4$ at different scan rates.

6.2.2. Galvanostatic charge-discharge analysis

Figure 6.10 shows the galvanostatic charge-discharge curves obtained for MWCNTPhNH$_2$, MWCNTaf, FeTPyzPz, MWCNTPhNH$_2$-FeTPyzPz and MWCNTaf-FeTPyzPz at a current density of 3 A.g^{-1} in 1.0 M H$_2$SO$_4$. The charge-discharge curves of are mostly linear showing an ideal capacitor behaviour while the non-linear charge-discharge curves of FeTPyzPz, MWCNTPhNH$_2$-FeTPyzPz and MWCNTaf-FeTPyzPz indicates that the redox process occurs at the electrode (30). The specific capacitance was calculated from the equation:

—— 6.4

where, I is the discharging current applied (A),Δt is the discharging time (s), m is the mass of the active electrode (g) and ΔE is the discharge voltage difference. Table 6.1 shows the specific capacitance, energy efficiency, specific energy and specific power for the electrodes studied at 3 A.g^{-1} in 1.0 M H_2SO_4. The specific capacitances for the composites were bigger; MWCNTaf-FeTPyzPz gave the highest specific capacitance of 410 F.g^{-1}. The mixing of MWCNT and FeTPyzPz provides a porous network that allows electrolyte ions to have access to the FeTPyzPz particles. The high conductivity of the MWCNTs enhances electron transport between FeTPyzPz molecules.

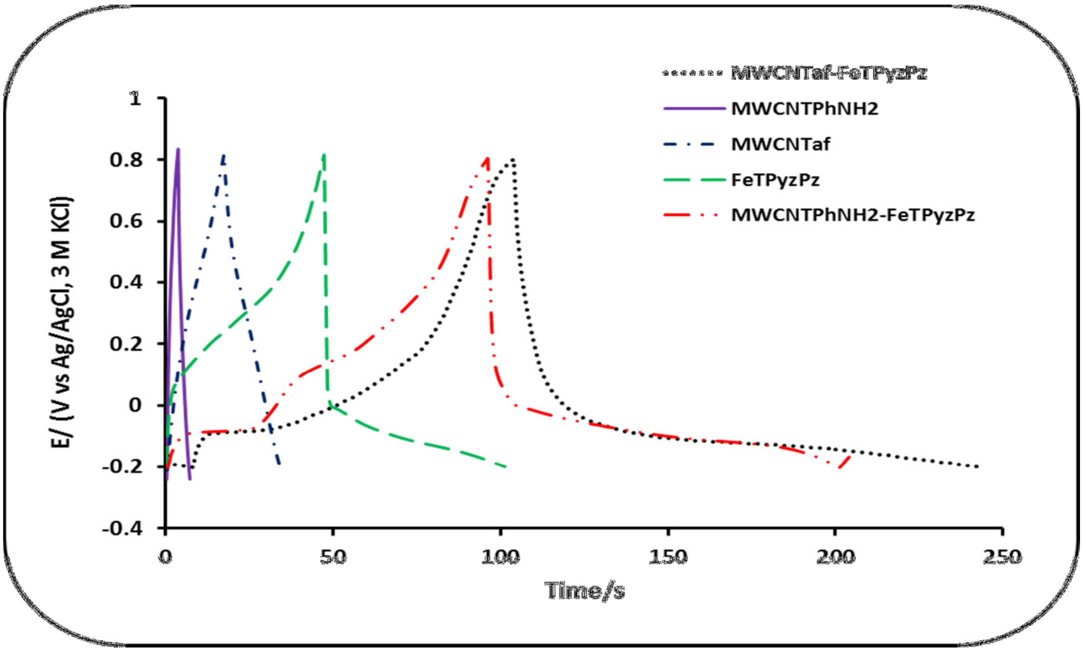

Figure 6.10: Charge-Discharge curves of $MWCNTPhNH_2$, MWCNTaf, FeTPyzPz, $MWCNTPhNH_2$-FeTPyzPz and MWCNTaf-FeTPyzPz in 1.0 M H_2SO_4 at a current density of 3 A.g^{-1}.

Table 6.1: Supercapacitive parameters of FeTPyzPz based systems from c-d measurements

Electrode	Electrolyte: 1.0 M H_2SO_4, current density = 3 $A.g^{-1}$			
	Specific capacitance/ ($F.g^{-1}$)	**Energy efficiency/ %**	**Specific Energy/ $Whkg^{-1}$**	**Specific Power/W kg^{-1}**
$MWCNTPhNH_2$	10	98	3	3032
MWCNTaf	50	116	15	3097
FeTPyzPz	156	109	45	3042
$MWCNTPhNH_2$-FeTPyzPz	309	107	87	3020
MWCNTaf-FeTPyzPz	410	140	115	3010

The high specific capacitance in MWCNTaf-FeTPyzPz can be attributed to the heteroatoms functionalities that increases wettability of the electrode surface and introduce redox active sites (11).

The enhancement of the capacitance could be following the same mechanism (Figure 5.11) as proposed by Lota *et al.* (31) due to the pyridinic N present in the porphyrazine molecules.

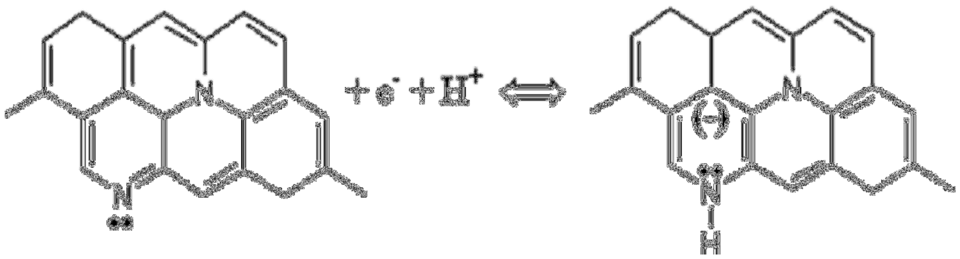

Figure 5.11: Scheme of possible redox reactions based on presence of pyridinic groups (31).

6.2.3. Electrochemical impedance spectroscopy analysis

EIS measurements were done to understand the fundamental behaviour of the electrodes. Figure 6.12(a) shows a Nyquist plot of MWCNTPhNH$_2$-FeTPyzPz and MWCNTaf-FeTPyzPz electrodes measured in the frequency range of 100 kHz to 10 MHz in 1.0 M H_2SO_4 aqueous electrolyte. The inset of Figure 6.12(a) shows a partial semicircle. The Nyquist plot shows that both MWCNTaf-FeTPyzPz and MWCNTPhNH$_2$-FeTPyzPz have a lower charge transfer resistance. This suggests that the electrodes can offer a good rate performance (32). At lower frequencies, the Nyquist plots are not parallel to the y axis, and this indicates that the electrodes are not purely EDLC, but that the storage of charges happens through both pseudocapacitance and EDLC.

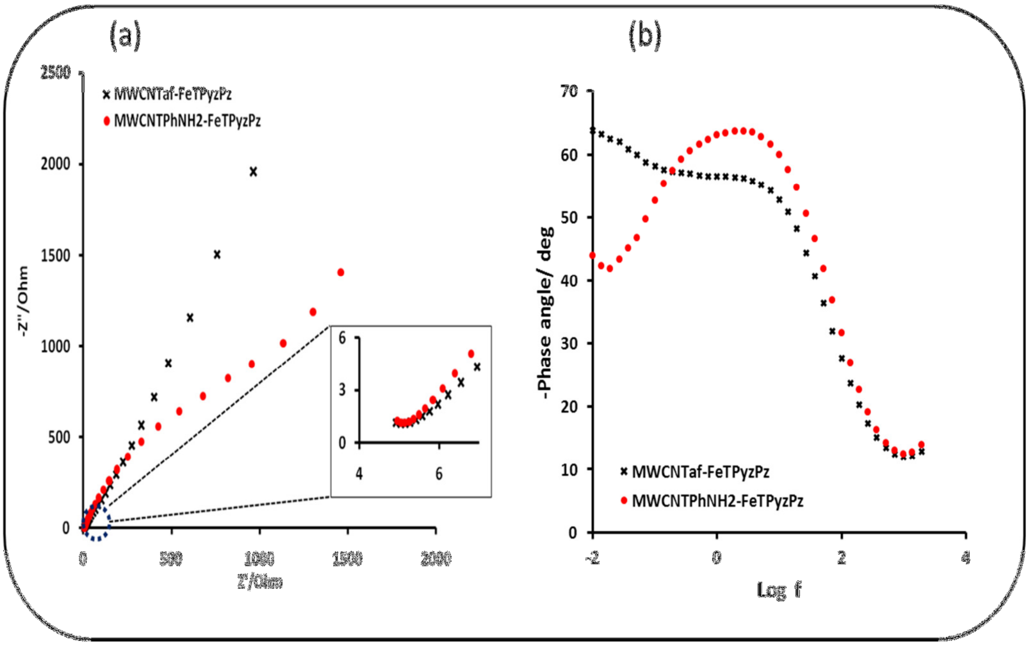

Figure 6.12: (a) Nyquist plot (inset: expansion of Nyquist at high frequency) plot and Bode plot of MWCNTPhNH$_2$-FeTPyzPz and MWCNTaf-FeTPyzPz in 1.0 M H_2SO_4.

Figure 6.13 shows a plot of specific capacitance versus frequency of MWCNTPhNH$_2$-FeTPyzPz and MWCNTaf-FeTPyzPz. Specific capacitance from impedance data was obtained using equation 2.23. From the graph it can be seen that at higher frequency both composites have almost same behaviour while between 0.1 Hz and 10 Hz, MWCNTaf-FeTPyzPz performs better than MWCNTPhNH$_2$-FeTPyzPz. At lower frequency MWCNTPhNH$_2$-FeTPyzPz exhibit a specific capacitance of about 660 F.g^{-1}.

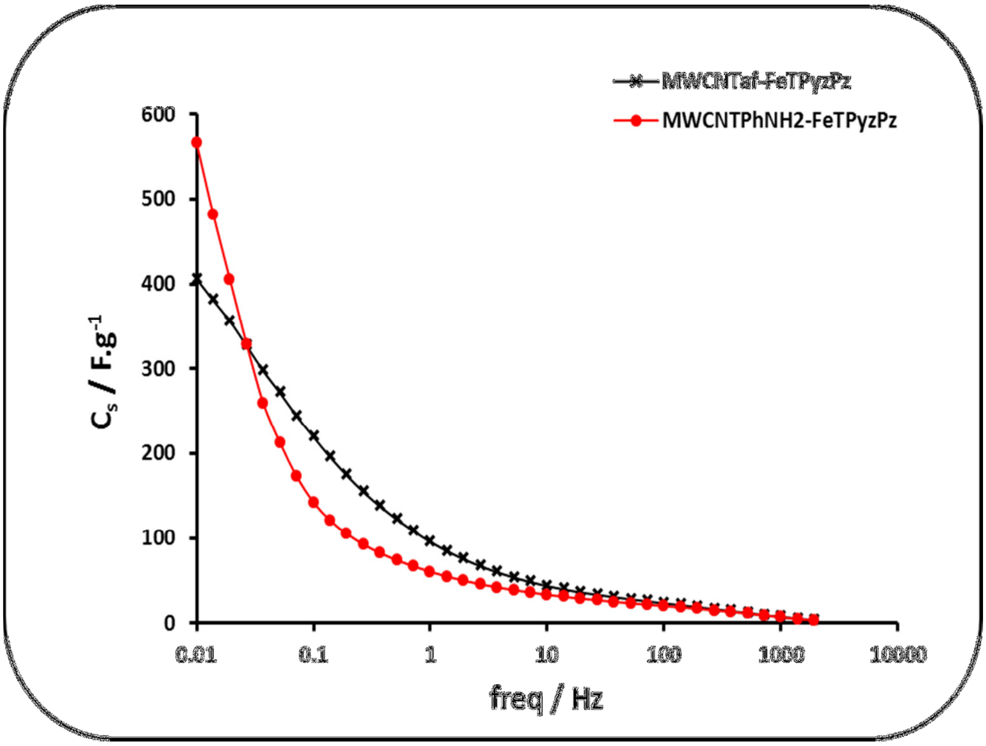

Figure 6.13: Frequency dependent specific capacitance of MWCNTPhNH$_2$-FeTPyzPz and MWCNTaf-FeTPyzPz in 1.0 M H_2SO_4.

6.3. The electrochemical characterisation of MWCNTs/FeTPyzPz asymmetric supercapacitors.

Asymmetric supercapacitors are more favourable for aqueous electrolyte since they give high energy density due to their large electrochemical potential window. Figure

6.14 shows CV evolutions of MWCNTaf-FeTPyzPz//CB-MWCNTaf and MWCNTPhNH$_2$-FeTPyzPz//CB-MWCNTPhNH$_2$AECs at 5 mV.s^{-1} using 1.0 M Na$_2$SO$_4$ electrolyte. The CV curves of both asymmetric supercapacitors exhibit a rectangular-like shape with slight observable redox peaks between -0.4 V and 0.2 V. This depicts that the asymmetric supercapacitor charge storage is a combination of EDLC and pseudocapacitance. Figure 6.15 shows that as the scan rate is increased, the CV profiles of the both asymmetric supercapacitors are not distorted indicating a desirable fast charging-discharging characteristic of the devices (33, 34).

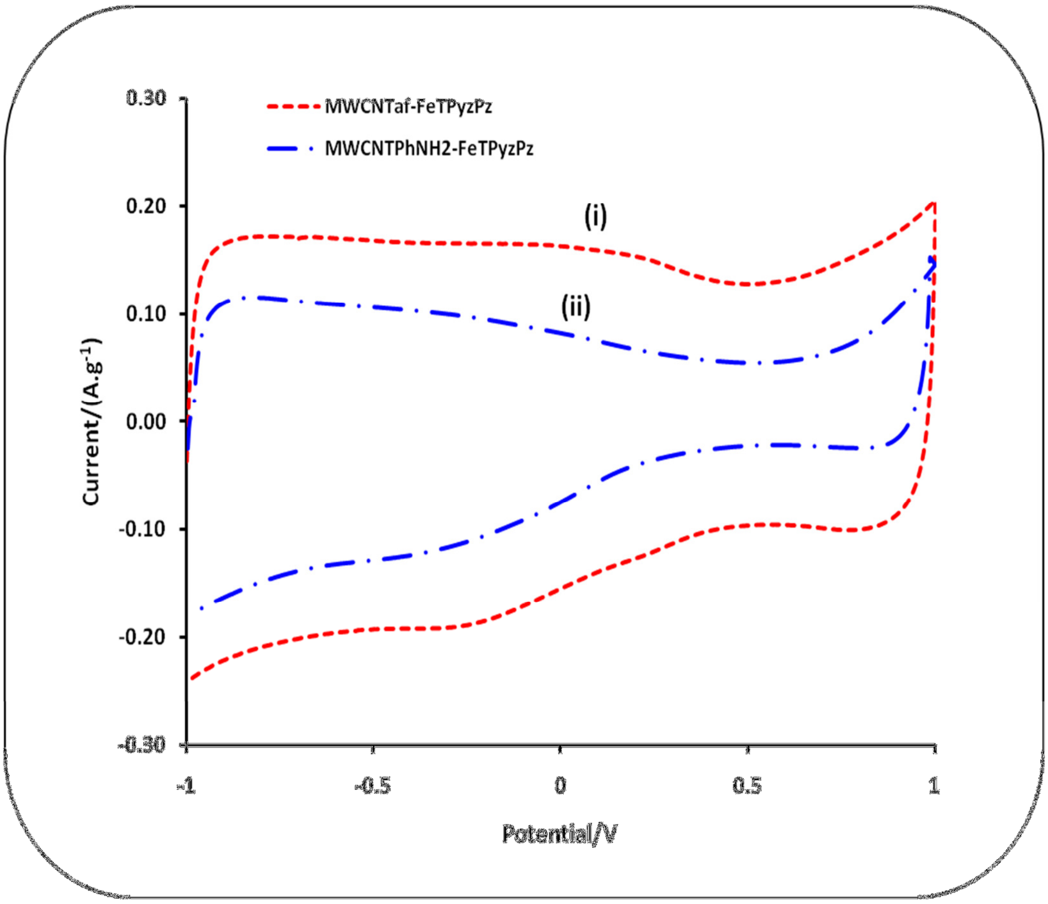

Figure 5.14: CV curve of (i) MWCNTaf-FeTPyzPz//CB-MWNTaf and (ii) MWCNTPhNH$_2$-FeTPyzPz//CB-MWCNTPhNH$_2$AECsat 5 mV.s^{-1} in 1.0 M Na$_2$SO$_4$ electrolyte.

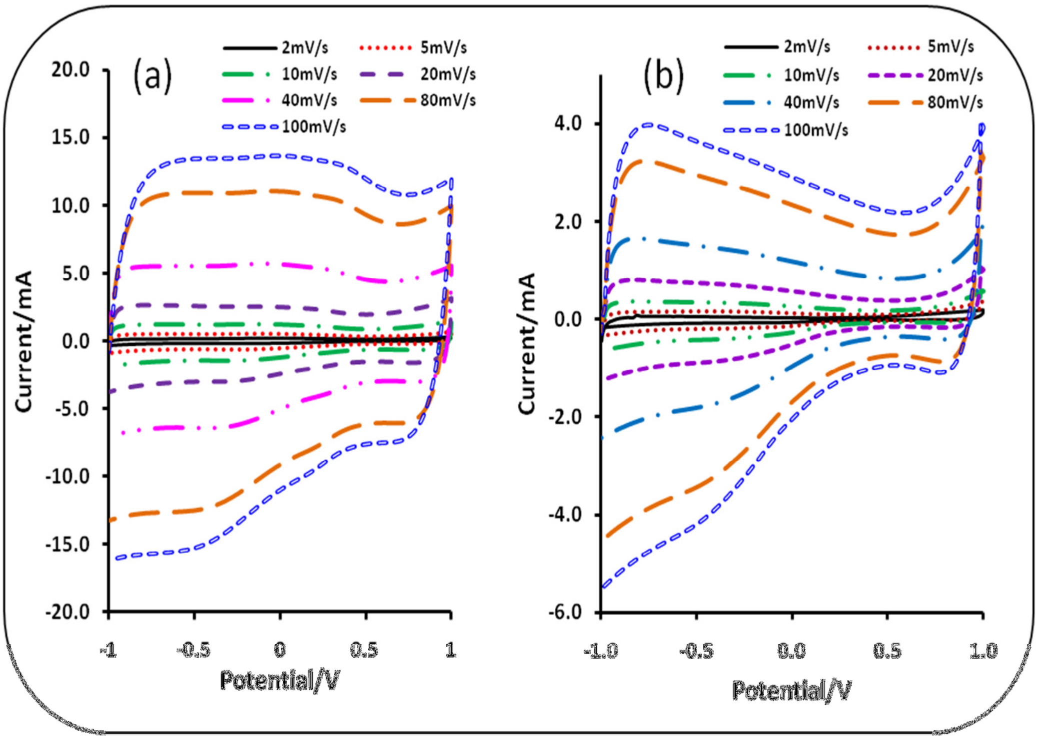

Figure 6.15: CV curves of (a) MWCNTaf-FeTPyzPz//CB-MWCNTaf and (b) MWCNTPhNH$_2$-FeTPyzPz//CB-MWCNTPhNH$_2$ asymmetric ECs at different scan rates in 1.0 M Na$_2$SO$_4$ electrolyte.

Figure 6.16 shows galvanostatic charge-discharge curves of MWCNTaf-FeTPyzPz//CB-MWCNTaf and MWCNTPhNH$_2$-FeTPyzPz//CB-MWCNTPhNH$_2$ at a current density of 300 mA.g^{-1} using 1.0 M Na$_2$SO$_4$ aqueous electrolyte. At a potential window of 1.8 V, the charge and discharge curves of MWCNTaf-FeTPyzPz//CB-MWCNTaf are symmetrical, indicating a good coulombic efficiency and excellent chemical reversibility. Comparing the ESR of the two supercapacitors calculated from the IR drop, it was found that MWCNTaf-FeTPyzPz//CB-MWCNTaf had smaller ESR of 10.4 Ω as compared to ESR of MWCNTPhNH$_2$-FeTPyzPz//CB-MWCNTPhNH$_2$ (25.75 Ω). Figure 6.17 shows that as current density increases, the specific capacitance of both asymmetric cells decrease. Specific capacitance of MWCNTaf-FeTPyzPz//CB-

MWCNTaf and MWCNTPhNH$_2$-FeTPyzPz//CB-MWCNTPhNH$_2$ at different density is shown in Figure 6.18.

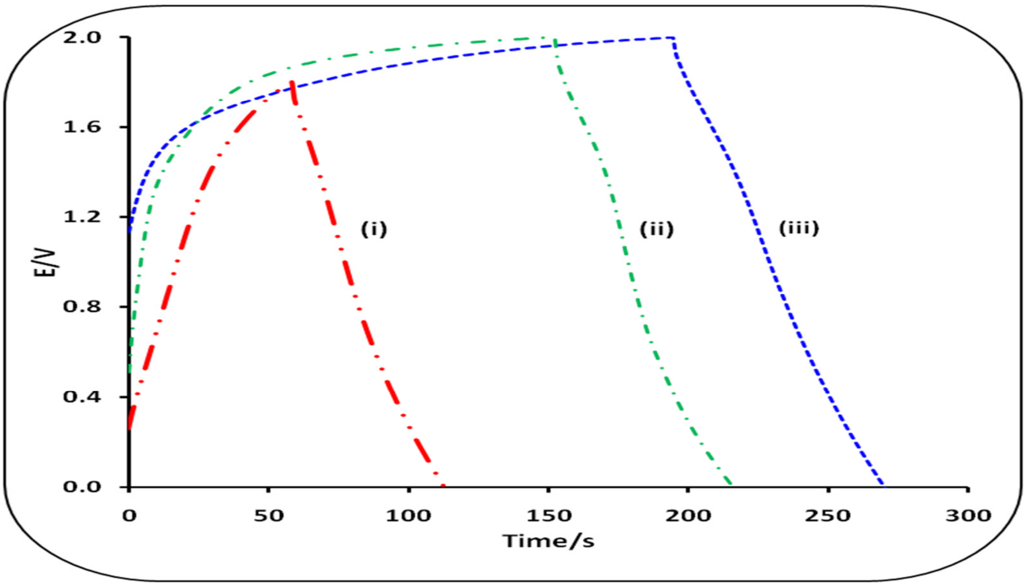

Figure 6.16: C-D curves at 300 mA.g^{-1} of (i) MWCNTaf-FeTPyzPz//CB-MWCNTaf with cell voltage of 1.8 V, (ii) MWCNTPhNH$_2$-FeTPyzPz//CB-MWCNTPhNH$_2$ with cell voltage of 2.0 V and (iii) MWCNTaf-FeTPyzPz//CB-MWCNTaf with cell voltage of 2.0 V in 1.0 M Na_2SO_4 electrolyte.

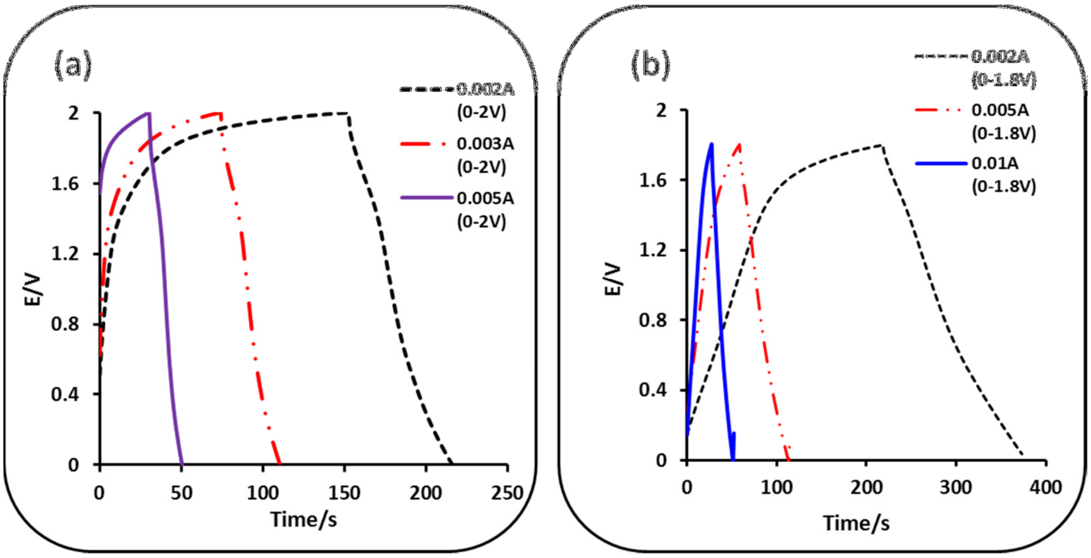

Figure 6.17: C-D curves at different current densities of (a) MWCNTPhNH$_2$-FeTPyzPz//CB-MWCNTPhNH$_2$ with cell voltage of 2.0 V and (b) MWCNTaf-FeTPyzPz//CB-MWCNTaf with cell voltage of 1.8 V in 1.0 M Na_2SO_4 electrolyte.

This increase in capacitance after 1000 charge-discharge cycles may be attributed to the electro-activation of the electrode (35). This implies that the electrolyte ions were more able to penetrate the electrode surface due to increased wettability of the electrode. The specific capacitance of MWCNTPhNH$_2$-FeTPyzPz//CB-MWCNTPhNH$_2$ asymmetric cell after 1000 charge-discharge cycles increased by 59 % at 300 mA.g^{-1} in a potential window of 2.0 V. Figure 6.18 also shows that specific capacitance decreases as current density increases.

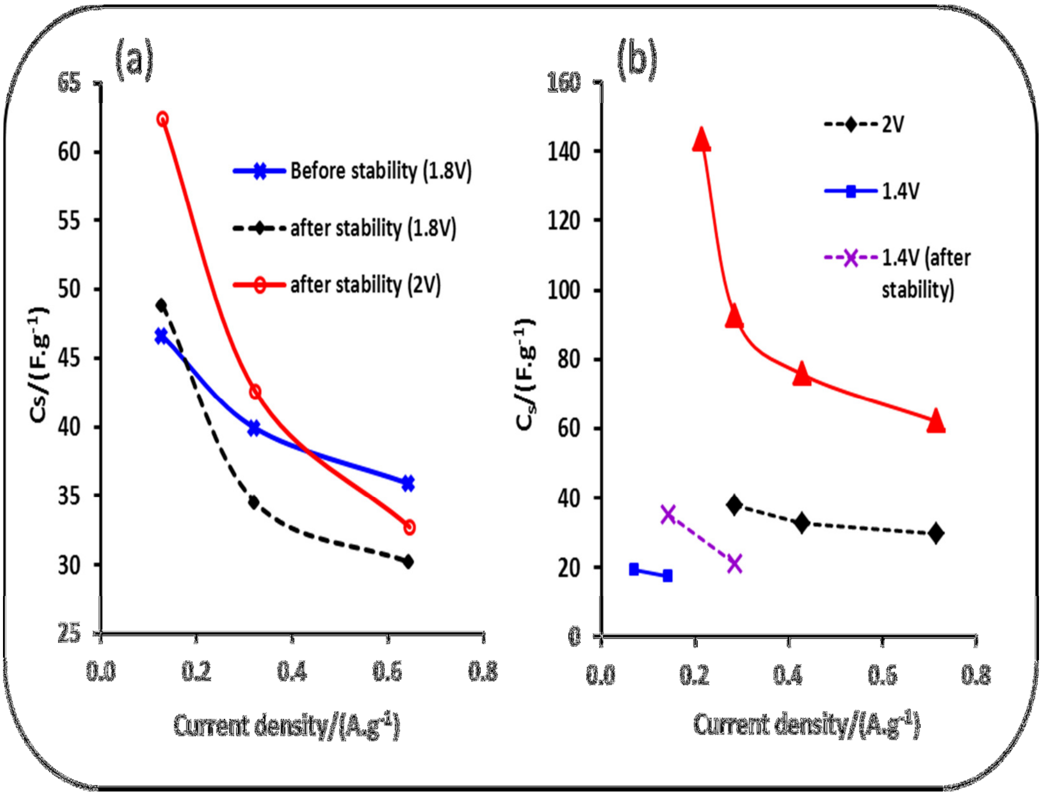

Figure 6.18: Specific capacitance of (a) MWCNTaf-FeTPyzPz//CB-MWCNTaf asymmetric supercapacitor cell before and after stability test and (b) MWCNTPhNH$_2$-FeTPyzPz//CB-MWCNTPhNH$_2$.

Figure 6.19 shows the Ragone plots of asymmetric supercapacitor cells relating energy density and power density at different potential windows. At cell potential of 2.0 V, the energy density for MWCNTaf-FeTPyzPz//CB-MWCNTaf asymmetric supercapacitor cell reaches 8.2 Wh.kg^{-1} where power density was 6.2 kW.kg^{-1}. At lower cell potential of 1.8 V, energy density decreases to 5.0 Wh.kg^{-1} at power density of 5.8 kW.kg^{-1}. For MWCNTPhNH$_2$-FeTPyzPz//CB-MWCNTPhNH$_2$ asymmetric cell the best energy density of 16 Wh.kg^{-1} at a power density of 1.6 kW.kg^{-1}was obtained after 1000 cycle performance. It was observed that at lower potential windows, the energy density as well as power density values were very small.

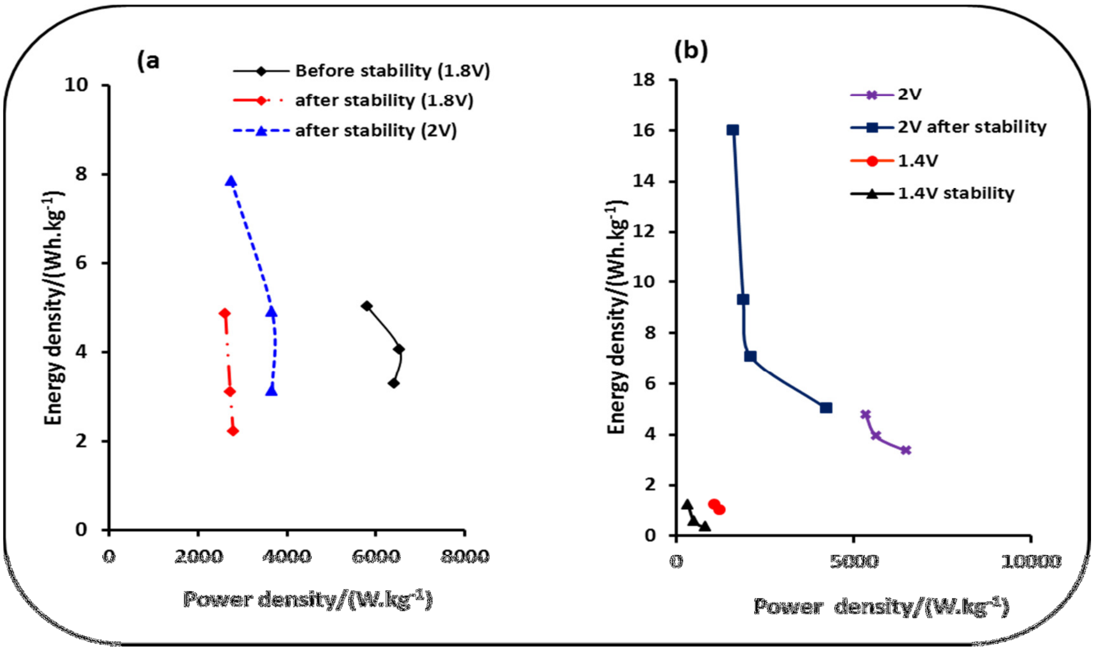

Figure 6.19: Ragone plot of (a) MWCNTaf-FeTPyzPz//CB-MWCNTaf asymmetric supercapacitor cell before and after stability test and (b) MWCNTPhNH$_2$-FeTPyzPz//CB-MWCNTPhNH$_2$ asymmetric supercapacitor cell before and after stability test in 1.0 M Na$_2$SO$_4$ electrolyte.

Figure 6.20 shows the Nyquist plot for MWCNTaf-FeTPyzPz//CB-MWCNTaf and MWCNTPhNH$_2$-FeTPyzPz//CB-MWCNTPhNH$_2$ asymmetric cells. At high frequency, MWCNTaf-FeTPyzPz//CB-MWCNTaf asymmetric cell shows a pronounced semi-circle while MWCNTPhNH$_2$-FeTPyzPz//CB-MWCNTPhNH$_2$ asymmetric cell does not have a well-defined semi-circle. MWCNTaf-FeTPyzPz//CB-MWCNTaf and MWCNTPhNH$_2$-FeTPyzPz//CB-MWCNTPhNH$_2$ asymmetric cell gave an internal cell resistance of 2.1 Ω and 4.2 Ω, respectively. At low frequency, the Nyquist plot of MWCNTaf-FeTPyzPz//CB-MWCNTaf asymmetric cell is more vertically linear as compared to the Nyquist plot of MWCNTPhNH$_2$-FeTPyzPz//CB-MWCNTPhNH$_2$ asymmetric cell. This indicates that MWCNTaf-FeTPyzPz and CB-MWCNTaf can perform well as electrode materials for supercapacitors. Since the plots at low frequency are not vertical linear, this indicates that the materials used are not purely EDLC but a combination of both EDLC and pseudocapacitance.

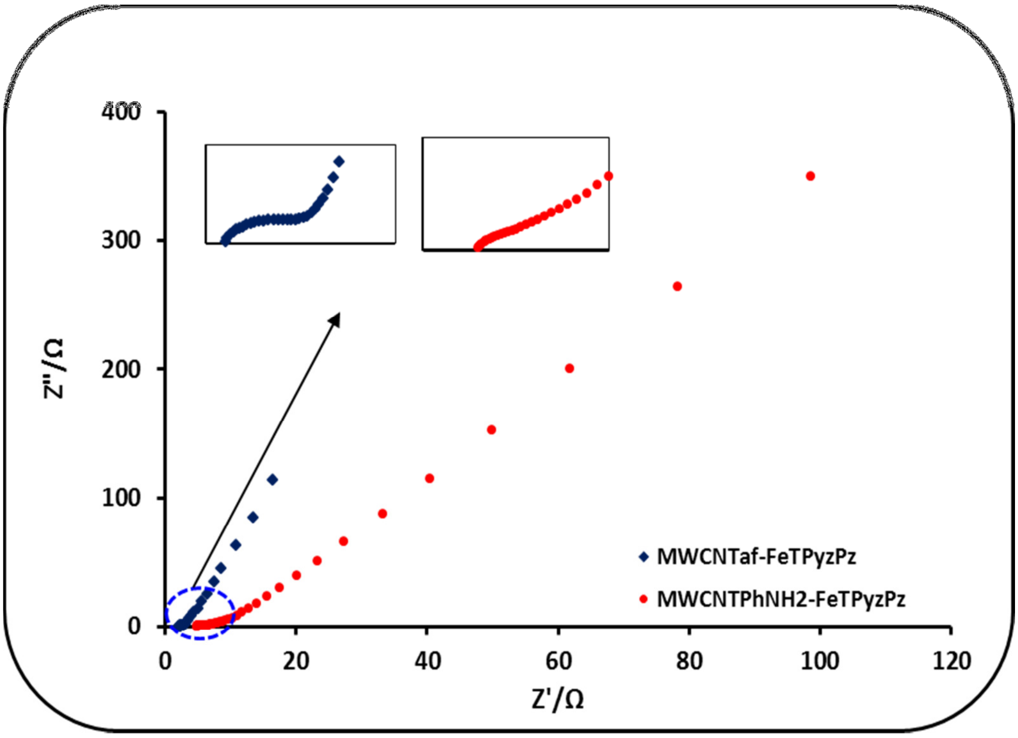

Figure 6.20: Nyquist plots of MWCNTaf-FeTPyzPz//CB-MWCNTaf and MWCNTPhNH$_2$-FeTPyzPz//CB-MWCNTPhNH$_2$ asymmetric supercapacitors in 1.0 M Na_2SO_4 at 0.2 V.

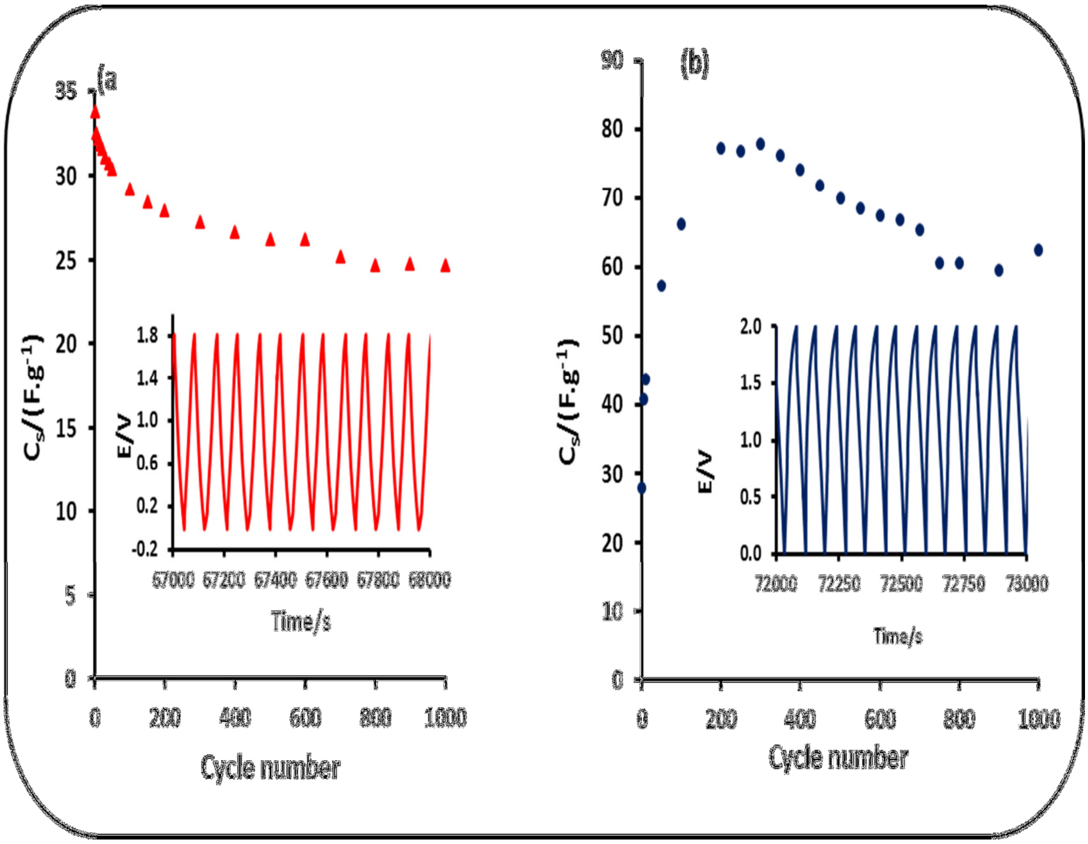

Figure 6.21: Cycling performance of MWCNTaf-FeTPyzPz//CB-MWCNTaf and MWCNTPhNH$_2$-FeTPyzPz//CB-MWCNTPhNH$_2$ AECs at 5 mA.

Galvanostatic charge-discharge was used to investigate the long term cycling performance of the asymmetric cells. Figure 6.21 shows capacitance as a function of a number of cycles for both asymmetric cells. The specific capacitance of MWCNTaf-FeTPyzPz//CB-MWCNTaf decreased by 26 %, whilst that of MWCNTPhNH$_2$-FeTPyzPz//CB-MWCNTPhNH$_2$ first increased by 38 % and thereafter decreased by 19 %.

6.4. Conclusion

In a three electrode system it was found that the composite MWCNTaf-FeTPyzPz electrode gave a superior specific capacitance of 410 F.g^{-1} at 3 A.g^{-1} as compared to the other composite MWCNTPhNH2-FeTPyzPz electrode. It was established that when functionalised MWCNTs are incorporated into FeTPyzPz, the specific capacitance atleast doubles. The composites exhibited good electrochemical behaviour with lower charge transfer resistance in Na_2SO_4 electrolyte. Both MWCNTaf-FeTPyzPz//CB-MWCNTaf and $MWCNTPhNH_2$-FeTPyzPz//CB-$MWCNTPhNH_2$ asymmetric attained reasonable specific capacitance of 62 $F.g^{-1}$ and 143 $F.g^{-1}$ respectively after stability tests at 300 $mA.g^{-1}$. MWCNTaf-FeTPyzPz//CB-MWCNTaf has good cycle stability. MWCNTaf-FeTPyzPz//CB-MWCNTaf and $MWCNTPhNH_2$-FeTPyzPz//CB-$MWCNTPhNH_2$ asymmetric cells gave a reasonable energy density of between 8 $Wh.kg^{-1}$ and 16 $Wh.kg^{-1}$ respectively.

6.5. References

1. Špitalskỳ Z, Aggelopoulos C, Tsoukleri G, Tsakiroglou C, Parthenios J, Georga S, et al. The effect of oxidation treatment on the properties of multi-walled carbon nanotube thin films. Materials Science and Engineering: B. 2009;165(3):135-8.

2. Yuen S-M, Ma C-CM, Lin Y-Y, Kuan H-C. Preparation, morphology and properties of acid and amine modified multiwalled carbon nanotube/polyimide composite. Composites Science and Technology. 2007;67(11-12):2564-73.

3. Iijima S, Ichihashi T. Single-shell carbon nanotubes of 1-nm diameter. Nature. 1993;363(6430):603-5.

4. Bilgin A, Ertem B, Gök Y. Novel porphyrazines containing peripherally functionalized macrocyclic (N2O2, N2S2) units: Synthesis and characterization. Dyes and Pigments. 2009;80(1):187-93.

5. Sakellariou EG, Montalban AG, Beall SL, Henderson D, Meunier HG, Phillips D, et al. Novel peripherally functionalized seco-porphyrazines: synthesis, characterization and spectroscopic evaluation. Tetrahedron. 2003;59(46):9083-90.

6. Bahr JL, Tour JM. Highly Functionalized Carbon Nanotubes Using in Situ Generated Diazonium Compounds. Chemistry of Materials. 2001;13(11):3823-4.

7. Peng H, Alemany LB, Margrave JL, Khabashesku VN. Sidewall Carboxylic Acid Functionalization of Single-Walled Carbon Nanotubes. Journal of the American Chemical Society. 2003;125(49):15174-82.

8. Liu L, Barber AH, Nuriel S, Wagner HD. Mechanical Properties of Functionalized Single-Walled Carbon-Nanotube/Poly(vinyl alcohol) Nanocomposites. Advanced Functional Materials. 2005;15(6):975-80.

9. Onay H, Esat B, Öztrük R. The symmetrical porphyrazine with annulated six membered rings. Polyhedron. 2010;29(4):1314-6.

10. Seoudi R, El-Bahy GS, El Sayed ZA. FTIR, TGA and DC electrical conductivity studies of phthalocyanine and its complexes. Journal of Molecular Structure. 2005;753(1-3):119-26.

11. Frackowiak E, Béguin F. Carbon materials for the electrochemical storage of energy in capacitors. Carbon. 2001;39(6):937-50.

12. Toupin M, Bélanger D, Hill IR, Quinn D. Performance of experimental carbon blacks in aqueous supercapacitors. Journal of Power Sources. 2005;140(1):203-10.

13. Lang J, Yan X, Xue Q. Facile preparation and electrochemical characterization of cobalt oxide/multi-walled carbon nanotube composites for supercapacitors. Journal of Power Sources. 2011;196(18):7841-6.

14. Chang J-K, Chen Y-L, Tsai W-T. Effect of heat treatment on material characteristics and pseudo-capacitive properties of manganese oxide prepared by anodic deposition. Journal of Power Sources. 2004;135(1-2):344-53.

15. Byon HR, Lee SW, Chen S, Hammond PT, Shao-Horn Y. Thin films of carbon nanotubes and chemically reduced graphenes for electrochemical micro-capacitors. Carbon. 2011;49(2):457-67.

16. Andreas HA, Conway BE. Examination of the double-layer capacitance of an high specific-area C-cloth electrode as titrated from acidic to alkaline pHs. Electrochimica Acta. 2006;51(28):6510-20.

17. Okajima K, Ohta K, Sudoh M. Capacitance behavior of activated carbon fibers with oxygen-plasma treatment. Electrochimica Acta. 2005;50(11):2227-31.

18. Chidembo AT, Ozoemena KI, Agboola BO, Gupta V, Wildgoose GG, Compton RG. Nickel(ii) tetra-aminophthalocyanine modified MWCNTs as potential nanocomposite materials for the development of supercapacitors. Energy & Environmental Science. 2010;3(2):228-36.

19. Hulicova-Jurcakova D, Seredych M, Lu GQ, Bandosz TJ. Combined Effect of Nitrogen- and Oxygen-Containing Functional Groups of Microporous Activated Carbon on its Electrochemical Performance in Supercapacitors. Advanced Functional Materials. 2009;19(3):438-47.

20. Hsieh C-T, Teng H. Influence of oxygen treatment on electric double-layer capacitance of activated carbon fabrics. Carbon. 2002;40(5):667-74.

21. Frackowiak E. Carbon materials for supercapacitor application. Physical Chemistry Chemical Physics. 2007;9(15):1774-85.

22. Hu C-C, Huang Y-H. Cyclic Voltammetric Deposition of Hydrous Ruthenium Oxide for Electrochemical Capacitors. Journal of The Electrochemical Society. 1999;146(7):2465-71.

23. Hu C-C, Tsou T-W. Ideal capacitive behavior of hydrous manganese oxide prepared by anodic deposition. Electrochemistry Communications. 2002;4(2):105-9.

24. Hu C-C, Chang K-H. Cyclic voltammetric deposition of hydrous ruthenium oxide for electrochemical capacitors: effects of codepositing iridium oxide. Electrochimica Acta. 2000;45(17):2685-96.

25. Lee JY, Liang K, An KH, Lee YH. Nickel oxide/carbon nanotubes nanocomposite for electrochemical capacitance. Synthetic Metals. 2005;150(2):153-7.

26. Lin X, Xu Y. Facile synthesis and electrochemical capacitance of composites of polypyrrole/multi-walled carbon nanotubes. Electrochimica Acta. 2008;53(15):4990-7.

27. Mengqiang W, Liping Z, Dongmei W, Jiahui G, Shuren Z. Electrochemical capacitance of MWCNT/polyaniline composite coatings grown in acidic MWCNT suspensions by microwave-assisted hydrothermal digestion. Nanotechnology. 2007;18(38):385603.

28. Kong L-B, Lang J-W, Liu M, Luo Y-C, Kang L. Facile approach to prepare loose-packed cobalt hydroxide nano-flakes materials for electrochemical capacitors. Journal of Power Sources. 2009;194(2):1194-201.

29. Qing X, Liu S, Huang K, Lv K, Yang Y, Lu Z, et al. Facile synthesis of Co3O4 nanoflowers grown on Ni foam with superior electrochemical performance. Electrochimica Acta. 2011;56(14):4985-91.

30. Wang G, Qu M, Yu Z, Yuan R. LiNi0.8Co0.2O2/MWCNT composite electrodes for supercapacitors. Materials Chemistry and Physics. 2007;105(2-3):169-74.

31. Lota G, Grzyb B, Machnikowska H, Machnikowski J, Frackowiak E. Effect of nitrogen in carbon electrode on the supercapacitor performance. Chemical Physics Letters. 2005;404(1-3):53-8.

32. Lei Z, Zhang J, Zhao XS. Ultrathin MnO2 nanofibers grown on graphitic carbon spheres as high-performance asymmetric supercapacitor electrodes. Journal of Materials Chemistry. 2012;22(1):153-60.

33. Wang H, Holt CMB, Li Z, Tan X, Amirkhiz BS, Xu Z, et al. Graphene-nickel cobaltite nanocomposite asymmetrical supercapacitor with commercial level mass loading. Nano Research. 2012:1-13.

34. Fan Z, Yan J, Wei T, Zhi L, Ning G, Li T, et al. Asymmetric Supercapacitors Based on Graphene/MnO2 and Activated Carbon Nanofiber Electrodes with High Power and Energy Density. Advanced Functional Materials. 2011;21(12):2366-75.

35. Cheng Q, Tang J, Ma J, Zhang H, Shinya N, Qin L-C. Graphene and nanostructured MnO2 composite electrodes for supercapacitors. Carbon. 2011;49(9):2917-25.

CHAPTER 7

Supercapacitive behaviour of GO-CoTPyzPz nanocomposites

7.1. Physical characterisation of GO/CoTPyzPz nanocomposites

7.1.1. Comparative microscopic images

FESEM images of GO, CoTPyzPz and GO/CoTPyzPz are shown in Figure 7.1. From the micrographs of the GO/CoTPyzPz it can be seen that the graphene oxide sheet is spread on top of CoTPyzPz particles creating a porous network. This morphology of the GO/CoTPyzPz composite enhances the electrical conductivity of the composite.

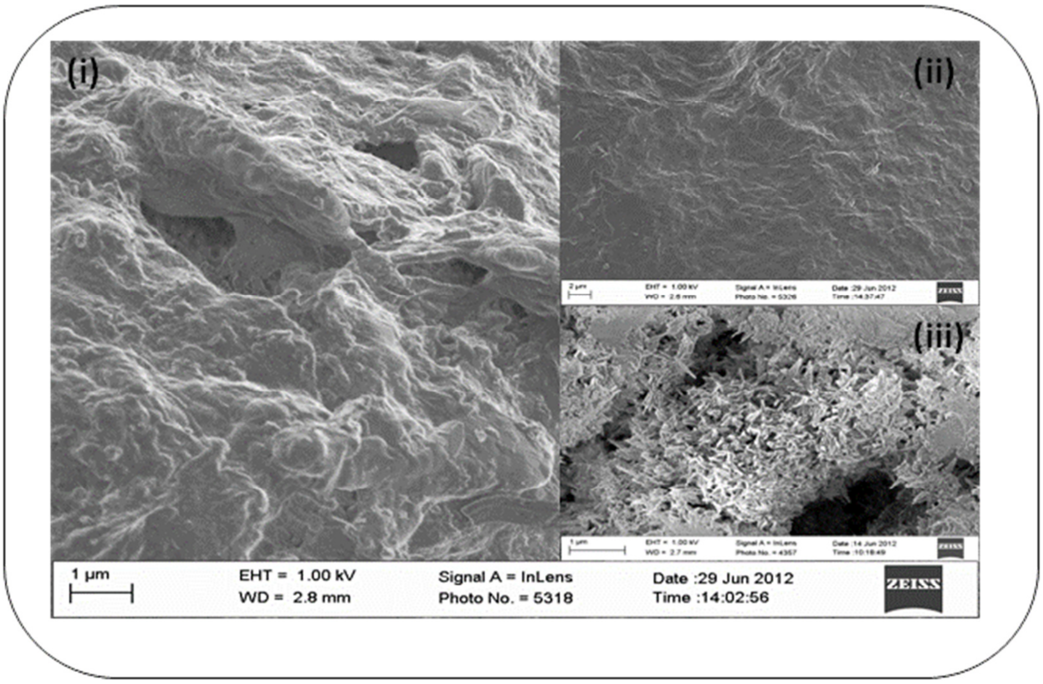

Figure 7.1: Typical FESEM images of (i) GO/CoTPyzPz, (ii) GO and (iii) CoTPyzPz.

7.1.2. Comparative FTIR

Figure 7.2 shows the FTIR spectra of GO, CoTPyzPz and GO/CoTPyzPz. The spectra depicts the nature of the chemical groups found the GO, CoTPyzPz and GO/CoTPyzPz. From the FTIR spectra, the broad band between 3600 and 3100 cm^{-1} is attributable to O-H stretching band for GO, N-H stretching vibrations in CoTPyzPz and O-H or N-H vibrations in the GO/CoTPyzPz. A peak at 1715 cm^{-1} confirms the presence of C=O in GO. The C=N pyrazine ring stretching for CoTPyzPz and GO/CoTPyzPz appeared at 1633 cm^{-1}. The composite shows the strong M-N vibration band (metal ion and the four nitrogen atoms in pyrrole) at 756 cm^{-1}. Strong band at 2874 cm^{-1} is assigned to aliphatic carbons in GO, CoTPyzPz and GO/CoTPyzPz.

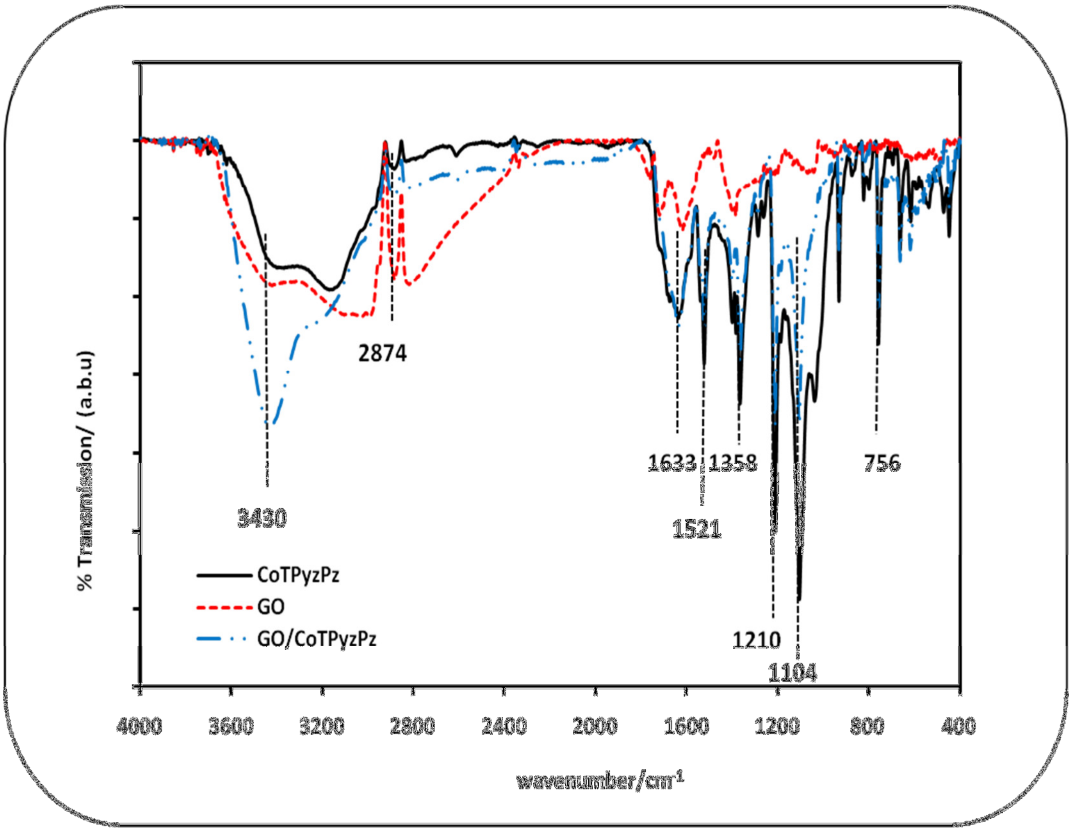

Figure 7.2: FTIR spectra of (i) GO/CoTPyzPz, (ii) GO and (iii) CoTPyzPz.

7.1.3. Comparative Raman analysis

From the Raman spectra (Figure 7.3), both GO and GO/CoTPyzPz show same peak positions for the D and G peaks at 1344 cm^{-1} and 1593 cm^{-1}, respectively. However, there is a marginal increase in the D to G band intensity ratio, D/G, from 0.87 to 0.91 upon integration with the CoTPyzPz. The increased D band intensity reflects a disorder in the carbon structure. The stronger D peak intensity observed in the GO/CoTPyzPz is related to the smaller size of the GO/CoTPyzPz compared to the pristine GO, which is a reflection of more defects. The strongest peak at 1530 cm^{-1} for CoTPyzPz mainly involves stretching of C–N–C and C–N bonds coupling with expanding of pyrroles (1). The second strongest peak at 1327 cm^{-1} for CoTPyzPz mainly involves stretching of the pyrroles and N–Co bonds coupling with C–H and C–N–C bonds in-plane bending. The weak peak at 655 cm^{-1} for CoTPyzPz can be attributed to an expansion of pyrrole rings and stretching of N–Co bond. The shoulder vibration mode at 455 cm^{-1} is typical N–H vibrations. The integration with the GO led to an enhanced, but a broad vibration mode at 671 cm^{-1} for the GO/CoTPyzPz, suggesting more expanded pyrrole rings and stretching of the N–Co bond (2).

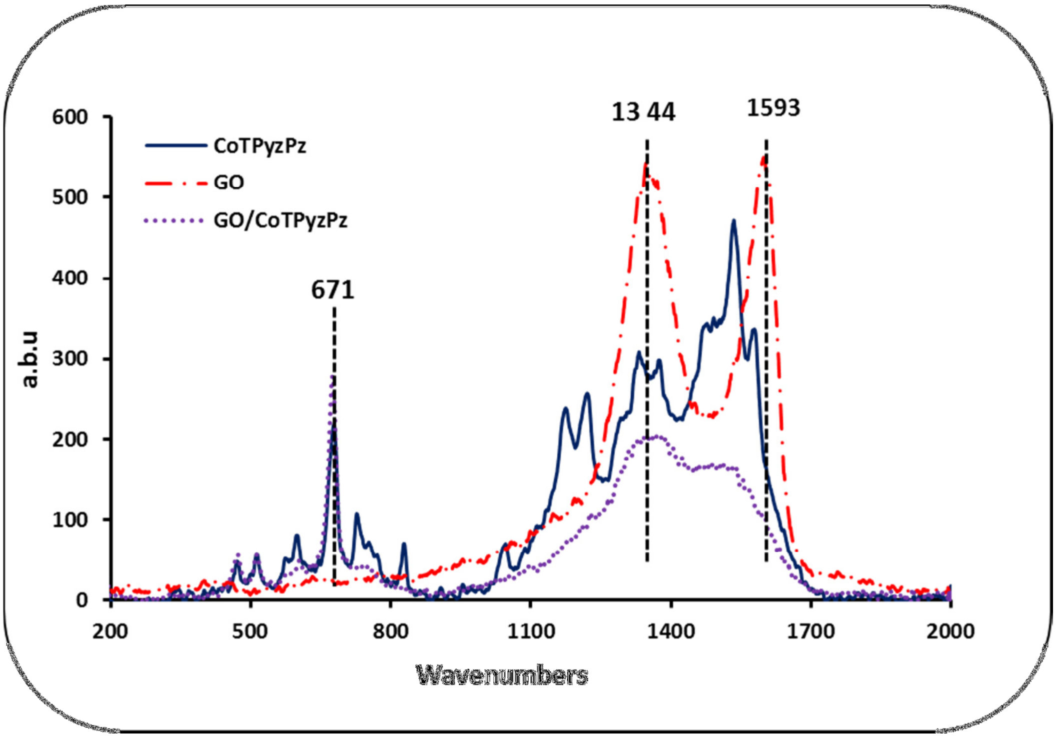

Figure 7.3: Raman spectra of GO/CoTPyzPz, GO and CoTPyzPz.

7.1.4. Comparative UV-Vis analysis

Figure 7.4 shows the UV/Vis spectra of GO, CoTPyzPz, and GO/CoTPyzPz in DMF. The GO spectrum presented an adsorption peak around 260 nm (π-π* transition). The CoTPyzPz showed the characteristic Q band at 630 nm with a shoulder at 730 nm due to aggregation (1), a vibrational Q_{0-0} band at 577 nm, a weak band around 430 nm due to metal-ligand-charge-transfer (MLCT) transition, and a B band at 345 nm. Upon integration with the GO, the original Q-band of the CoTPyzPz at 630 nm almost disappeared, slightly blue-shifted to 621 nm, while the peak at 730 nm became broader and more pronounced.

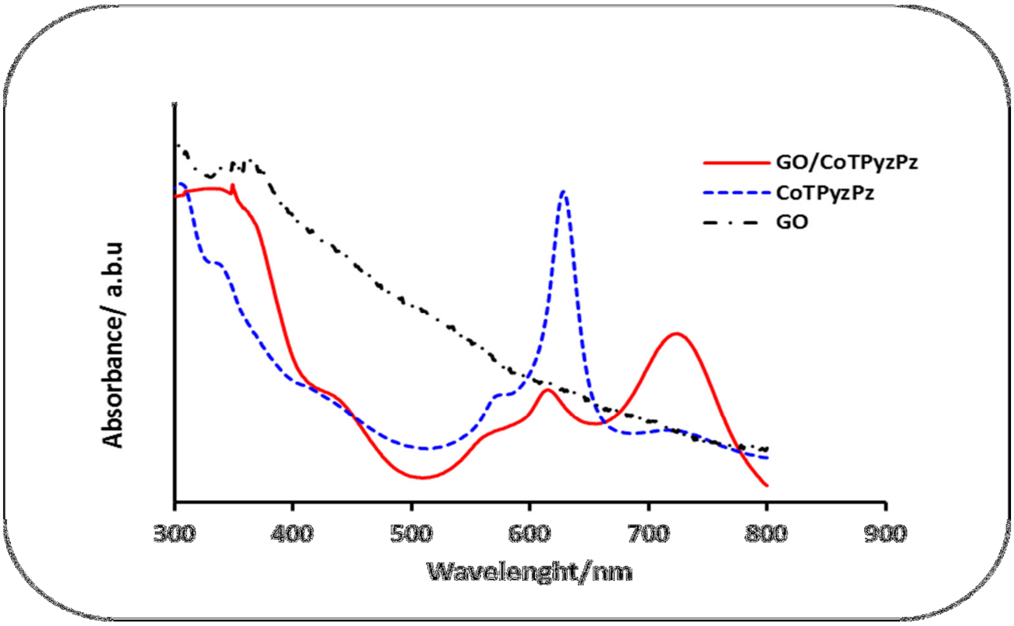

Figure 7.4: UV-VIS spectra of (i) GO/CoTPyzPz, (ii) GO and (iii) CoTPyzPz.

This incredible change in the UV-Vis spectrum is a clear indication of the interaction between the GO and the CoTPyzPz via strong co-facial aggregation (face-to-face assembly). The slight blue shift suggests that the energy gap between the HOMO and LUMO of the GO/CoTPyzPz hybrid has become wider than that of the CoTPyzPz (3, 4). The co-facial aggregation should result in maximum contact between the CoTPyzPz molecules and the graphene sheet, thus leading to a fast electron transport through the graphene during the faradaic redox reaction.

7.2. Supercapacitive behaviour of GO/CoTPyzPz

Figure 7.5(i) shows the CV curves of GO, CoTPyzPz and GO/CoTPyzPz composite at 20 mV.s^{-1}. The CV curve of GO electrode shows a nearly rectangular shape with no observable redox peaks.

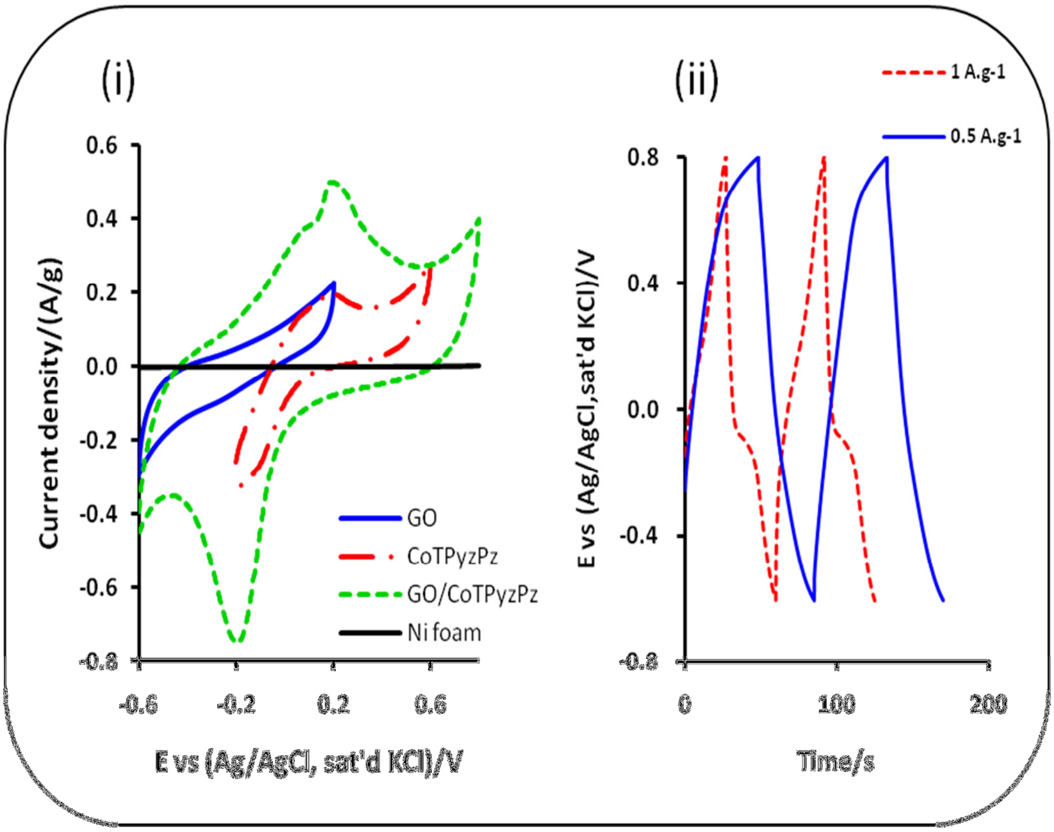

Figure 7.5: Electrochemical properties of electrode materials using a three-electrode system in 1.0 M Na_2SO_4 electrolyte. (i) CV curves of GO, CoTPyzPz and GO/CoTPyzPz on nickel foam electrodes at a scan rate of 20 mV.s^{-1}. (ii) Galvanostatic charge-discharge curves of GO/CoTPyzPz at different charge density.

This indicates that the GO electrode exhibit an EDL capacitive behaviour. The CV curve of CoTPyzPz exhibits a redox peaks between -0.2 V and 0.2 V which are attributable to the Na^+ ion insertion into the electronegative porphyrazine molecule. This pseudocapacitive behaviour is greatly enhanced in the GO/CoTPyzPz composite.

The well-defined redox peaks can be attributed to the enhancement of electron mobility through the highly conductive GO that has formed a porous network over CoTPyzPz molecules. Figure 7.5(ii) shows galvanostatic charge-discharge curves of GO/CoTPyzPz electrode in 1.0 M Na_2SO_4 electrolyte solution at different current density. The c-d curve at 0.5 $A.g^{-1}$ is linear and symmetrical while at 1.0 $A.g^{-1}$, the c-d curve shows a hump between -0.2 V and 0 V indicative of a pseudocapacitive behaviour.

7.3. Asymmetric supercapacitive behaviour of GO/CoTPyzPz//CB-GO cell.

To further evaluate GO/CoTPyzPz composite for real device application, an asymmetric supercapacitor was made with activated carbon as the negative electrode and GO/CoTPyzPz as a positive electrode using 1.0 M Na_2SO_4 as an electrolyte. Activated carbon was used as to extend the cell voltage to 1.6 V. Figure 7.6(i) shows the CV curves of GO/CoTPyzPz//CB-GO asymmetric supercapacitor at different scan rates in 1.0 M Na_2SO_4 aqueous electrolyte. The CV curves are quasi rectangular shaped with redox peaks, this depicts that the charge storage mechanism is a combination of EDLC and psuedocapacitance. As the potential scan a rate is increased, CV curves still retain their shape indicating a desirable fast charge-discharge phenomenon.

Galvanostatic charge-discharge was used to further evaluate the performance of an asymmetric cell. Figure 7.6 (ii) shows galvanostatic charge-discharge curves of GO/CoTPyzPz//CB-GO cell at different current density in 1.0 M Na_2SO_4 aqueous electrolyte. The charge and discharge curves are symmetrically. This indicates that the cell has an excellent electrochemical reversibility and good columbic efficiency.

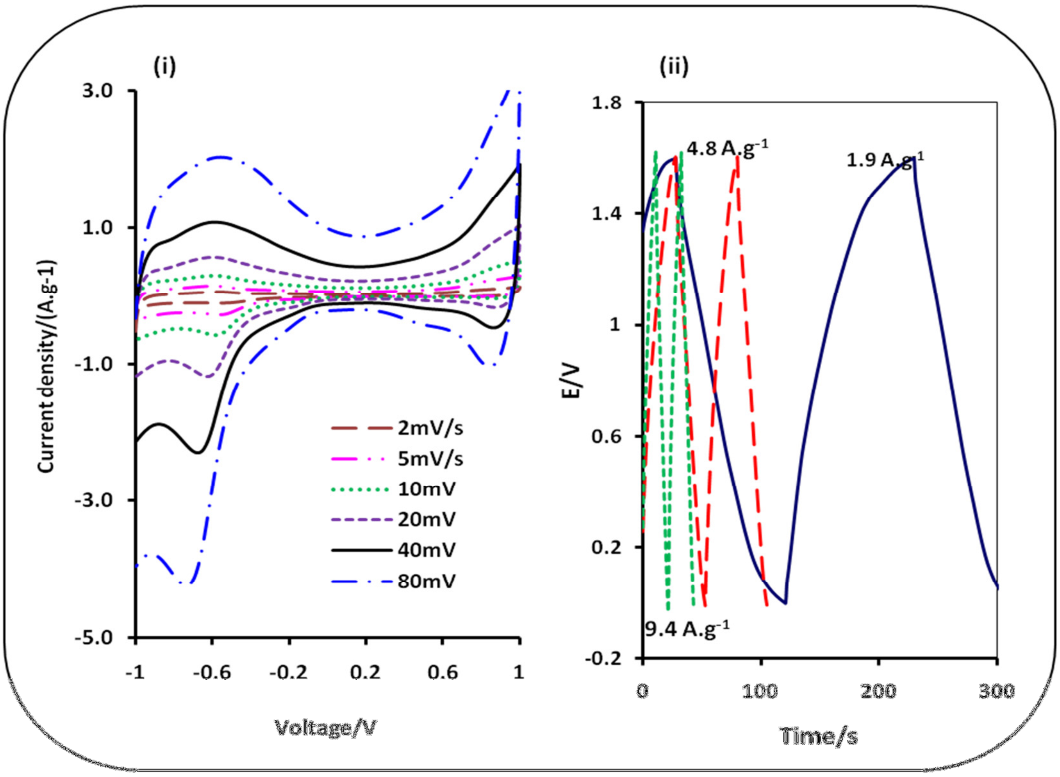

Figure 7.6: CV curves of GO/CoTPyzPz//CB-GO asymmetric supercapacitor at a different scan rate between -1.0 V and 1.0 V in 1.0 M Na_2SO_4 aqueous electrolyte (ii) Galvanostatic charge-discharge curves of GO/CoTPyzPz//CB-GO at different charge density.

The specific capacitance was evaluated from discharge curve according to Equations (4):

— 7.1

— 7.2

where C is the capacitance, Csp is the specific capacitance, Δt is the change in the discharge time, ΔV is the change in the discharge voltage after the IR drop and M is the total mass of the anode and the cathode electrode materials. The Specific capacitance of the cell was found to be 399 $F.g^{-1}$ at a current density of 1.9 $A.g^{-1}$ decreasing to 275 $F.g^{-1}$ at 9.5 $F.g^{-1}$ (table 7.1). Energy deliverable efficiency was found to increase from 83 % to 96 % with the increase in current density.

Figure 7.7(i) shows a Ragone plot of GO/CoTPyzPz//CB-GO asymmetric cell. The power density (P_{max}) and energy density (E) were calculated according to the following equations (4):

— 7.3

— 7.4

where V is the applied voltage, m is the total mass of active materials in both the anode and the cathode and R_{ir} is the internal resistance calculated from the voltage drop of the discharge curve according the equation (4):

— 7.5

where ΔV_{iR} is a potential difference of the discharge curve from the end of the iR drop to the end of discharge. From the Ragone plot it can be seen that GO/CoTPyzPz//CB-GO asymmetric cell possesses the energy density of 36 $Wh.kg^{-1}$ at a power density of 31 kW. kg^{-1}, and still maintains the energy density of 24 $Wh.kg^{-1}$ at power density of 41 $kW.kg^{-1}$.

Table 7.1: Supercapacitive behaviour parameters of GO/CoTPyzPz//CB-GO asymmetric cell at different current densities

Electrolyte: 1.0 M Na_2SO_4				
Current density/ $A.g^{-1}$	**Specific capacitance /($F.g^{-1}$)**	**Energy efficiency /%**	**Specific Energy/W hkg^{-1}**	**Specific Power/k Wkg^{-1}**
1.9	399	83	36	31
4.8	315	92	28	37
9.5	275	96	24	41

The energy density obtained for the GO/CoTPyzPz//CB-GO asymmetric capacitor cell is higher than other Na_2SO_4 aqueous electrolyte based asymmetric ECs, such as MGC//graphene (30 $Wh.kg^{-1}$) (5), GHCS–MnO2//GHCS (22$Wh.kg^{-1}$) (6), GNCC//AC (20 $Wh.kg^{-1}$) (7) and MnO_2-coated graphene//graphene (11 $Wh.kg^{-1}$) (8). The energy density value obtained is higher than the energy range of the electrochemical capacitors (~ 0.2 to 10 $Wh.kg^{-1}$) (9). A long cycling stability is one of the important performance requirements for supercapacitor applications. Figure 7.7 (ii) shows a specific capacitance versus cycle number. The long term cycling performance was evaluated from charge-discharge curves of GO/CoTPyzPz//CB-GO asymmetric capacitor cell. The specific capacitance in the first 300 cycles decreased slightly and thereafter decreased significantly until it normalized at about 300 F.g^{-1}. The stability study proves that the device can charge and discharge continuously at a very high current density with little or no significant loss in efficiency.

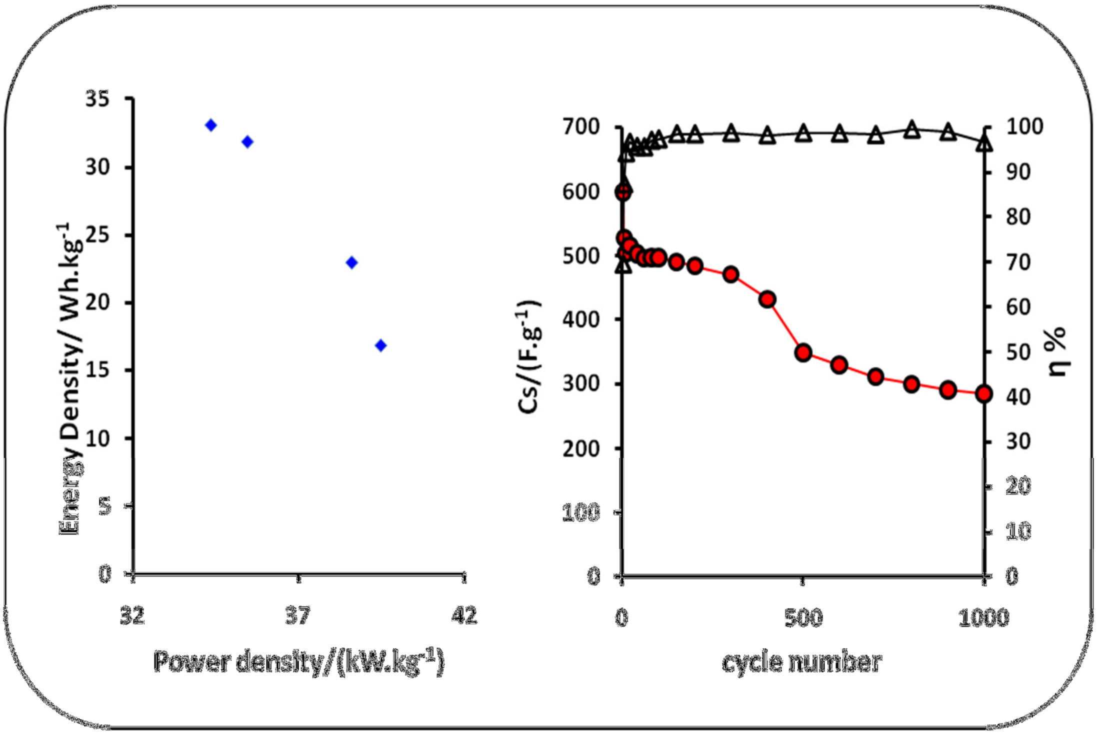

Figure 7.7: (i) Ragone plot of GO/CoTPyzPz//CB-GO asymmetric supercapacitor in 1.0 M Na_2SO_4 aqueous electrolyte (ii) cycle performance of GO/CoTPyzPz//CB-GO asymmetric cell with a voltage window of 1.6V at a current density of 2.4 A.g^{-1} in 1.0 M $NaSO_4$ aqueous electrolyte.

Figure 7.8(i) shows the Nyquist plot of GO/CoTPyzPz//CB-GO asymmetric supercapacitor before and after stability performance. An inset shows the high frequency range of the Nyquist plot.

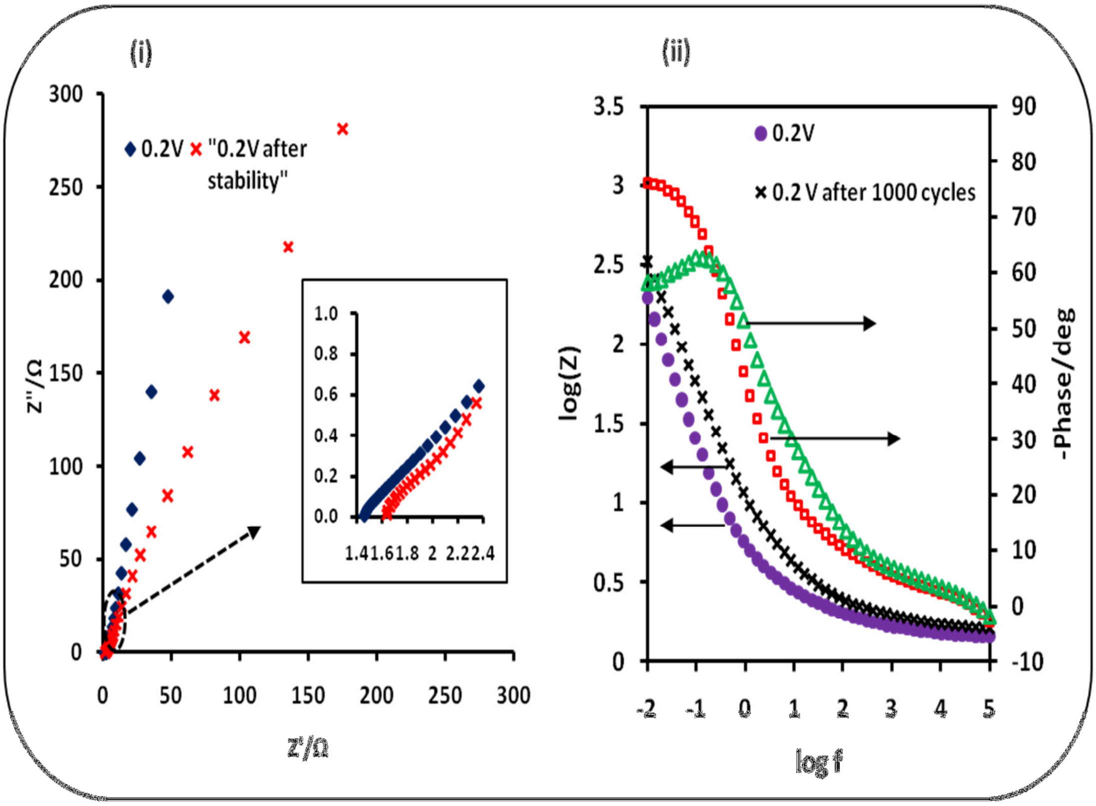

Figure 7.8: (i) Nyquist plot of GO/CoTPyzPz//CB-GO asymmetric supercapacitor in 1.0 M Na_2SO_4 aqueous electrolyte (ii) Bode plot of GO/CoTPyzPz//CB-GO asymmetric supercapacitor in 1.0 M Na_2SO_4 aqueous electrolyte**.**

The plot shows that there is no obvious or well defined semi-circle before and after the cycle stability tests. The equivalent series resistance (ESR) before and after stability test have is 1.46 Ω and 1.63 Ω. This low ESR indicates that the EC cell can be utilized for high power density applications (6). From the Bode plots, the phase angle decreased from 76 to 62 degrees, indicating further transition to more pseudocapacitive properties (figure 7.8(ii)). There is also a slight change in the polarisation resistance after 1000 cycles (from 0.34 to 0.50 Ω), which may be due to loss of adhesion of some active material with the current collector, and/or corrosion of the current collector caused by the dissolved oxygen in electrolytes during the charge/discharge cycling.

7.4. **Conclusion**

The electrochemical capacitive properties of a novel aqueous asymmetric electrochemical capacitor based on a GO/CoTPyzPz nanocomposite have been reported. Electrochemical tests revealed that GO/CoTPyzPz nanocomposite had good electrochemical capacitance behaviour in the potential window of 0V to 1.6V. The GO/CoTPyzPz//CB-GO asymmetric cell gave a high specific capacitance of 275 $F.g^{-1}$ at a high current density of 9.5 $A.g^{-1}$. A high energy density of 36 $Wh.kg^{-1}$ was obtained at power density of 31 $kW.kg^{-1}$. The obtained specific energy is highly comparable to values obtained other asymmetric supercapacitors of between 30 $Wh.kg^{-1}$ and 50 $Wh.kg^{-1}$ (5, 6, 10, 11). These asymmetric cells have shown excellent energy deliverable efficiency.

7.5. References

1. Kobayashi N, Adachi, A., Osa, T. Some Spectroscopic, Electrochemical and Spectroelectrochemical Properties of Tetrapyrazinoporphyrazine and Its Iron and Cobalt Complexes. Analytical Sciences. 1990;6(3):449-53.

2. Liu Z, Zhang X, Zhang Y, Jiang J. The molecular, electronic structures and IR and Raman spectra of metal-free, N,N-dideuterio, and magnesium tetra-2,3-pyrazino-porphyrazines: Density functional calculations. Vibrational Spectroscopy. 2007;43(2):447-59.

3. Nakai K, Ishii K, Kobayashi N, Yonehara H, Pac C. Theoretical Calculations of the Electronic Absorption Spectra of Oxotitanium(IV) Phthalocyanine in the Solid State. The Journal of Physical Chemistry B. 2003 2012/09/14;107(36):9749-55.

4. Khomenko V, Raymundo-Piñero E, Béguin F. Optimisation of an asymmetric manganese oxide/activated carbon capacitor working at 2 V in aqueous medium. Journal of Power Sources. 2006;153(1):183-90.

5. Wu Z-S, Ren W, Wang D-W, Li F, Liu B, Cheng H-M. High-Energy MnO2 Nanowire/Graphene and Graphene Asymmetric Electrochemical Capacitors. ACS Nano. 2010;4(10):5835-42.

6. Lei Z, Zhang J, Zhao XS. Ultrathin MnO2 nanofibers grown on graphitic carbon spheres as high-performance asymmetric supercapacitor electrodes. Journal of Materials Chemistry. 2012;22(1):153-60.

7. Wang H, Holt CMB, Li Z, Tan X, Amirkhiz BS, Xu Z, et al. Graphene-nickel cobaltite nanocomposite asymmetrical supercapacitor with commercial level mass loading. Nano Research. 2012:1-13.

8. Cheng Q, Tang J, Ma J, Zhang H, Shinya N, Qin L-C. Graphene and nanostructured MnO2 composite electrodes for supercapacitors. Carbon. 2011;49(9):2917-25.

9. Kötz R, Carlen M. Principles and applications of electrochemical capacitors. Electrochimica Acta. 2000;45(15-16):2483-98.

10. Xiao J, Yang S. Bio-inspired synthesis of NaCl-type CoxNi1-xO (0 [less-than-or-equal] x < 1) nanorods on reduced graphene oxide sheets and screening for asymmetric electrochemical capacitors. Journal of Materials Chemistry. 2012;22(24):12253-62.

11. Yu G, Hu L, Vosgueritchian M, Wang H, Xie X, McDonough JR, et al. Solution-Processed Graphene/MnO2 Nanostructured Textiles for High-Performance Electrochemical Capacitors. Nano Letters. 2011;11(7):2905-11.

CONCLUSION AND RECOMMENDATIONS

8.1. Conclusion

The composites, MWCNT(30%)-MnO_2 and MWCNT(15%)-MnO_2 were synthesised and characterised successfully. The composites were found to be hydrated. MWCNT(15%)-MnO_2 immobilized onto BPPGE gave the highest C_{sp} of 1209 $F.g^{-1}$ while the C_{sp} of MWCNT(30%)-MnO_2 was 207 $F.g^{-1}$. The incorporation of the MWCNTs provides connectivity between individual MnO_2 molecules thereby increasing conductivity and specific area. This leads to an enhancement of specific capacitance of MWCNT(15%)-MnO_2 by 27 fold as compared to specific capacitance of MNO_2 and MWCNTs. MWCNT(15%)-MnO_2 showed excellent specific capacitance (1209 $F.g^{-1}$), excellent energy efficiency (101%) and excellent cycle stability after activation. Therefore, the synthesised MWCNT(15%)-MnO_2 composite is a promising electrode material for supercapacitors.

From the novel study of the composites of CoTPyzPz and MWCNTs, it was found that porphyrazine composites have excellent supercapacitive behaviour in H_2SO_4 than in Na_2SO_4. The porphyrazine composites exhibited a dominantly pseudocapacitive behaviour. This could be attributed to the hydrogen protonation and deprotonation on the azomethine nitrogens or nitrogens on the pyrazine ring. The acid functionalized MWCNTs porphyrazine composites performed better than phenylamine functionalized MWCNTs porphyrazine composites. MWCNTaf-CoTPyzPz was found to be a promising supercapacitor electrode material. From two-electrode system, MWCNTaf-CoTPyzPz//CB-MWCNTaf exhibited an excellent energy density, power density and better cycle stability. Therefore, it was found to be the best supercapacitor cell studied. This study reported for the first time an asymmetric capacitor that utilizes porphyrazine molecules. This makes the composites of metallotetrapyrazinoporphyrazine and MWCNTs to be promising electrode materials for supercapacitors. GO/ CoTPyzPz nanocomposites interrogated for the first time showed a superior capacitive behaviour. An assembled GO/ CoTPyzPz//CB-GO asymmetric supercapacitor cell exhibited energy density comparable to NiMH batteries and a high power to these NiMH batteries currently used in hybrid vehicles like Toyota Prius.

This study has successfully used electrochemical methods to characterise manganese oxides composites and porphyrazine composites. The suitability of these materials for supercapacitor applications was determined, and they exhibited excellent supercapacitive behaviours. The introduction of nanocarbons such as functionalized MWCNTs and GO was found to enhance the capacitive behaviour of the materials.

8.2. Recommendations

To further explore these materials for use in commercial supercapacitor applications it is recommended that:

- New methods should be employed of making these composites material with the aim of increasing stability.
- More methods of analysis such as XPS and BET should be done, to further elucidate the physical properties of the composites.

- Energy storage mechanism in the porphyrazine macrocycle molecules should be fully explored.
- Electrode fabrication without current collectors should be made. This will enable determine the effect of the current collector on capacitance.

APPENDIX

List of Publications and Conference Presentations

Publications

1. Joel N. Lekitima, Kenneth I. Ozoemena, Charl J. Jafta, Nagao Kobayashi, Yang Song, Dennis Tong, Shaowei Chen and Munetaka Oyama, "Ultrahigh-Performance Asymmetric Electrochemical Capacitor Based on Graphene Oxide/Cobalt(II)-tetrapyrazinoporphyrazine Nanocomposites", *Journal of Material Chemistry A*, 2013, **1**, 2821- 2826.
2. Joel Lekitima, Kenneth I. Ozoemena and Nagao Kobayashi, "Electrochemical Capacitors Based on Nitrogen-Enriched Cobalt (II) Phthalocyanine/Multi-walled Carbon Nanotube nanocomposites", *Electrochemical Transactions* 2013, **50**, 125-132.

Conference Presentations

1. **Joel N. Lekitima** and Kenneth I. Ozoemena, Functionalized Carbon Nanotubes/Nano MnO_2 Hybrids as Novel Materials for use as Electrochemical Supercapacitor, NanoAfrica 2009, 3rd International Conference on Nanoscience and Nanotechnology, CSIR International Convention Centre, Pretoria, South Africa, 1 - 4 February, 2009 (Oral).

2. **Joel N. Lekitima**, Kenneth I. Ozoemena, MWCNT/porphyrazine macrocycle nanocomposite for energy storage systems, 11th International Conference on Frontiers of Polymers and Advanced Materials, University of Pretoria, Pretoria, South Africa, 22 - 27 May, 2011 (Oral).

3. **Joel N. Lekitima** and Kenneth I. Ozoemena, Supercapacitive behaviour of MWCNTs and Iron(II) tetrapyrazinoporphyrazine composites, 2nd International Symposium on Electrochemistry, Electrochemistry for Energy, University of Western Cape, Cape Town, South Africa, 19-20 July, 2012 (Oral).

4. **Joel N. Lekitima** and Kenneth I. Ozoemena, Electrochemical Performance of MWCNTs-CoTPyzPz//CB-MWCNTs Asymmetric Capacitors, 13th Topical Meeting of the International Society of Electrochemistry, CSIR International Convention Centre - Pretoria, South Africa, 07-10 April, 2013 (oral).

5. Kenneth I. Ozoemena and **Joel Lekitima**, Aqueous Asymmetric Electrochemical Capacitors Based on Nitrogen-enriched Metallophthalocyanines / Graphene Oxide Composites, International Conference on Advanced Capacitors (ICAC 2013), Osaka, Japan, 27 – 30 May, 2013 (Oral).

6. Kenneth I. Ozoemena, **Joel Lekitima**, Katlego Makgopa, Charl J. Jafta, and Shaowei Chen Nitrogen-Enriched Metallophthalocyanine/Graphene Oxide Nanocomposites for High-Energy Asymmetric Electrochemical Capacitors in Aqueous Electrolytes, Honolulu PRiME, Honolulu, Hawaii, 7 –12 October, 2012 (Poster).

Mass of positive and negative electrodes of different asymmetric cell

MWCNTaf-CoTPyzPz//CB- MWCNTaf cell

	Mass of active materials/mg	
	Positive electrode	Negative electrode
MWCNTaf-CoTPyzPz	*6.4*	
CB- MWCNTaf		*6.5*

MWCNTPhNH$_2$-CoTPyzPz//CB- MWCNT PhNH$_2$ cell

	Mass of active materials/mg	
	Positive electrode	Negative electrode
MWCNT PhNH$_2$-CoTPyzPz	*2.0*	
CB- MWCNT PhNH$_2$		*5.0*

MWCNTaf-FeTPyzPz//CB- MWCNTaf cell

	Mass of active materials/mg	
	Positive electrode	Negative electrode
MWCNTaf-CoTPyzPz	*6.5*	
CB- MWCNTaf		*9.0*

MWCNTPhNH$_2$-FeTPyzPz//CB- MWCNT PhNH$_2$ cell

	Mass of active materials/mg	
	Positive electrode	Negative electrode
MWCNTPhNH$_2$-FeTPyzPz	*1.0*	
CB- MWCNT PhNH$_2$		*6.0*

GO/CoTPyzPz//CB-GO cell

	Mass of active materials/mg	
	Positive electrode	Negative electrode
GO/CoTPyzPz	*0.6*	
CB-GO		*1.5*